

# **Phase diagrams of exceptional and supersymmetric lattice gauge theories**

## Dissertation

zur Erlangung des akademischen Grades  
doctor rerum naturalium (Dr. rer. nat.)

vorgelegt dem Rat der Physikalisch-Astronomischen Fakultät  
der Friedrich-Schiller-Universität Jena

von Dipl.-Phys. Björn-Hendrik Wellegehausen,  
geboren am 03.07.1983 in Großburgwedel

## **Gutachter**

1. Prof. Dr. A. Wipf, Jena
2. Prof. Dr. Uwe-Jens Wiese, Bern, Schweiz
3. Prof. Dr. Simon Hands, Swansea, UK

*Tag der Disputation:* 10.07.2012

# Contents

<b>1</b>	<b>Introduction</b>	<b>3</b>
<b>2</b>	<b>The exceptional gauge group <math>G_2</math></b>	<b>7</b>
<b>3</b>	<b>Algorithmic considerations</b>	<b>11</b>
3.1	The IHMC algorithm for semi-simple Lie algebras . . . . .	11
3.2	The rHMC algorithm for fermions . . . . .	20
3.3	Conclusions . . . . .	24
<b>4</b>	<b>Exceptional confinement</b>	<b>25</b>
4.1	The deconfinement transition in $G_2$ Yang-Mills . . . . .	27
4.2	The deconfinement transition in three dimensions . . . . .	29
4.3	Conclusions . . . . .	30
<b>5</b>	<b>Exceptional gluodynamics at zero temperature</b>	<b>31</b>
5.1	Exponential error reduction for Wilson loops . . . . .	33
5.2	Casimir scaling and string breaking in $G_2$ gluodynamics . . . . .	36
5.3	Conclusions . . . . .	46
<b>6</b>	<b>The <math>G_2</math> Yang-Mills Higgs model</b>	<b>47</b>
6.1	The phase diagram of the $G_2$ Higgs model: overview . . . . .	48
6.2	The transition lines away from the triple point . . . . .	54
6.3	The transition lines near the triple point . . . . .	57
6.4	Conclusions . . . . .	63
<b>7</b>	<b>A QCD-like theory with fermionic baryons</b>	<b>65</b>
7.1	Continuum formulation of $G_2$ -QCD . . . . .	66
7.2	Lattice formulation and thermodynamic observables . . . . .	73
7.3	The phase diagram of $G_2$ -QCD . . . . .	75
7.4	Conclusions . . . . .	89
<b>8</b>	<b>Supersymmetric lattice gauge theories</b>	<b>90</b>
8.1	$\mathcal{N} = 1$ supersymmetric Yang-Mills theory in 4 dimensions . . . . .	90
8.2	Supersymmetric quantum mechanics . . . . .	93
8.3	$\mathcal{N} = 2$ supersymmetric Yang-Mills theory in 3 dimensions . . . . .	95
8.4	Conclusions . . . . .	97
<b>9</b>	<b>Summary and outlook</b>	<b>98</b>

<b>A</b>	<b>Conventions</b>	<b>101</b>
<b>B</b>	<b>Additional information about Lie groups</b>	<b>102</b>
B.1	The exceptional Lie group $G_2$ . . . . .	102
B.2	The exceptional Lie groups $F_4$ and $E_6$ . . . . .	104
<b>C</b>	<b><math>G_2</math> Yang-Mills at zero temperature: tables</b>	<b>105</b>
<b>D</b>	<b>Lattice results for <math>G_2</math>-QCD: raw data</b>	<b>106</b>
D.1	Zero temperature . . . . .	107
D.2	Finite temperature . . . . .	108
<b>E</b>	<b>Supersymmetric Yang-Mills theories on the lattice</b>	<b>109</b>
E.1	$\mathcal{N} = 2$ SYM in three dimensions in the continuum . . . . .	109
E.2	$\mathcal{N} = 2$ SYM in three dimensions on the lattice . . . . .	110

# 1 Introduction

Since the discovery of the principles of quantum mechanics in the first half of the twentieth century [1–3], it is widely believed that elementary particles are not only the fundamental building blocks of matter, but also the carrier of all fundamental interactions observed in nature [4]. The most prominent example of such an elementary *force particle* is the photon, the mediator of the electromagnetic force. The common framework of describing particle physics is relativistic quantum field theory, the unification of quantum mechanics, classical field theory and special relativity [5–7]. Since there has never been a confirmed experimental observation, violating either the laws of quantum mechanics or the laws of special relativity, the principles of quantum mechanics and relativistic spacetime symmetries are common to all serious fundamental models of nature.

But quantum field theory by itself is only a tool, providing methods to obtain information out of a given system. During the last century it turned out that not only spacetime symmetries, i.e. Poincare invariance, are an at least approximate symmetry realized in nature, but also internal symmetries play an important role. Moreover, these internal symmetries, often indirectly found in experiments, are the guideline for building mathematical descriptions of the phenomena observed. Through a long process of development, the internal symmetries led to the standard model of particle physics, today the most successful theory describing physics below an energy scale of one TeV, in excellent agreement with the measurements [8–13].

The standard model incorporates the electromagnetic interaction with local *gauge symmetry*  $U(1)$ , the weak interaction with gauge group  $SU(2)$  [9, 10, 13] and the strong interaction based on the gauge group  $SU(3)$  [11]. Thus, three of the four fundamental interactions in nature are unified in the local gauge group  $SU(3) \times SU(2) \times U(1)$ . Only the unification with gravity is an outstanding task and may lead to new physics beyond the standard model.

Although the standard model was invented more than forty years ago, many features, as for example *confinement* [14, 15] or the generation of mass [16], are not fully understood and subject of intensive research, in experiments as well as theoretical investigations. An important discovery in experiments is the scale dependence of the strength of the interaction [17]. In the underlying quantum field theory this manifests in the scale dependence of the coupling constants, i.e. the free parameters of the proposed model, and can be described within the renormalization group [18–21]. But, at the end of the day, a finite number of free parameters have to be fixed by experiments to get a predictive theory of nature, known as renormalization. These scale dependence of coupling constants already indicates that perturbation theory, i.e. an expansion in terms of the coupling constants, will not hold on all scales and therefore different approaches are necessary. For instance, quantum electrodynamics (QED) is very weakly coupled in the infrared, while the scale dependent coupling, i.e. the observed charge of the electron, increases at smaller distances or higher energies. QED is not an asymptotically free theory, and at some scale, perturbation theory will miserably fail [22]. Contrary, quantum chromodynamics (QCD) is an asymptotically free theory that is strongly-coupled in the infrared and weakly coupled in the ultraviolet [23–26]. Therefore,

perturbation theory is only valid for small distances or high energies.

QCD is the theory describing the interaction of the 8 gluons, the force particles of the strong interaction, with the fundamental constituents of matter, coming in three families: the *up* and *down*, the *charm* and *strange*, and the *top* and *bottom* quark. In contrast to the photons of the abelian gauge theory QED, the gluons interact directly with each other, and this non-abelian property leads to the observed phenomena of confinement and colour-charge screening [15]. At low energy scales quarks and gluons are confined in mesons and baryons and are not seen as asymptotic states of the strong interaction. Understanding the dynamics of this confinement mechanism is one of the challenging problems in strongly-coupled gauge theories. Confinement is lost under extreme conditions: when temperature reaches the QCD energy scale or the density rises to the point, where the average inter-quark separation is less than 1 fm, then hadrons are melted into their constituent quarks. Confinement is a highly non-perturbative effect that cannot be understood within the framework of perturbation theory. So far the most successful approach to the non-perturbative aspects of QCD and Yang-Mills theories are Monte-Carlo simulations on discrete spacetime lattices [14, 27]. Employing this method, the finite temperature phase transition was studied with much effort in [28–35], and for physical quark masses a crossover from the confined to the unconfined phase between 150 and 200 MeV was found, in quite good agreement with the experimental value of 160 to 170 MeV [36, 37].

Another important aspect of QCD is its phase diagram at finite net baryon density [38]. It is also subject of many large-scale experiments, as for instance at the Large Hadron Collider (LHC) at Cern, the Relativistic Heavy Ion Collider (RHIC) at Brookhaven or the future Facility for Antiproton and Ion Research (FAIR) at the GSI in Darmstadt, where especially the nature of the deconfinement and chiral phase transition is probed and the proposed existence of a critical point in the QCD phase diagram is examined. At low temperatures and high baryon densities experiments are still not feasible nowadays, but the result for the thermodynamic equations of state are extremely important in many research areas, as for instance in nuclear-matter physics or astrophysics, such as for the formation of compact stellar objects. At very large densities, where the fermionic nature of baryons becomes important, exotic phases like quarkionic phases or colour superconductivity are expected [39–41]. Unfortunately, current lattice algorithms are not applicable at this point due to the fermion sign problem [42], and the only reliable results so far are obtained from functional methods or model calculations, that crucially rely on truncations or model building [43–45]. Therefore, first principle calculations are still unavoidable to verify the obtained results. Although there are different promising approaches to circumvent the fermion sign problem, they still all suffer from various shortcomings [46–50].

A different strategy is to investigate QCD-like theories without a sign problem, having as many features in common with QCD as possible. An example for such a theory is two-colour QCD, where its phase diagram as a function of temperature and net baryon density has recently extensively been investigated [51–56]. Although it contains many aspects that are interesting by itself, this theory does not contain fermionic bound states, and might therefore behave qualitatively differently compared to QCD, especially at high baryon density where the fermionic nature of baryons becomes important.

In this work a different theory, that does not suffer from this drawback, is proposed and investigated. Based on recent works of the group in Bern [57, 58], the gauge group  $SU(3)$  of the strong interaction is

replaced by the exceptional Lie group  $G_2$ . In many aspects,  $G_2$  is very similar to  $SU(3)$ ; in particular, pure  $G_2$  gauge theory coupled to fundamental fermions ( $G_2$ -QCD) contains fermionic baryons. However, it turns out that this QCD-like theory does not suffer from a fermion sign problem. Here,  $G_2$  gauge theories are investigated in detail with and without fundamental scalars and fermions, employing lattice Monte-Carlo methods. It is shown that already  $SU(3)$  and  $G_2$  pure gauge theories have indeed inspiring connections and behave in many aspects very similar to each other. In this context, first simulations of a QCD-like theory with fermionic baryons and quarks in the fundamental representation of the gauge group are performed, and the resulting phase diagram is discussed as a function of temperature and net baryon density.

Although the standard model is extremely successful in describing physics below an energy scale of one TeV, it is expected to be replaced by a more fundamental theory on higher energy scales. The most often discussed extensions are supersymmetric theories, which also play an important role in string theory. In a mathematical context, supersymmetry is the only possible (spacetime) extension of the Poincare algebra [59,60]. Roughly speaking, every particle of the standard model gets a supersymmetric partner particle with the same properties, except for a difference in spin of one half. These theories allow to solve, or at least weaken, various shortcomings of the standard model, for instance the hierarchy problem and the strong CP problem, and provide possible candidates for dark matter [61–63]. Another argument for supersymmetry is the unification of interactions. Employing supersymmetry, at a certain energy scale, all interactions are of equal strength and can be described within a single gauge group. The most trivial unification leads to the minimal supersymmetric standard model (MSSM) [64, 65]. Ongoing experiments, in particular at the Large Hadron Collider (LHC), aim at the direct or indirect discovery of supersymmetry. In any case, so far no supersymmetric particles have been observed. If supersymmetry exists, it must be spontaneously broken at low energy scales. An important ingredient of the MSSM are supersymmetric Yang-Mills (SYM) theories and especially its simplest version with a single supersymmetry,  $\mathcal{N} = 1$  SYM in four spacetime dimensions [66]. It describes the interaction of gluons with its fermionic superpartners, the gluinos. Since supersymmetry is a spacetime symmetry, it is explicitly broken by the lattice regularization, due to the failure of the Leibniz rule on the lattice [67]. In [68] it has been shown that the only SUSY breaking operator is the gluino condensate, making chiral Ginsparg-Wilson fermions [69] the optimum choice, but also Wilson fermions together with a fine-tuning of the gluino mass are feasible, in particular since they are much cheaper in computation time.  $\mathcal{N} = 1$  SYM theory has recently been investigated on the lattice, considering different formulations, but so far the results are not conclusive [70–75].

In the present work the lattice formulation of  $\mathcal{N} = 1$  SYM theory and its dimensional reduced theories to three and one spacetime dimensions are investigated, employing Wilson fermions. The main aspect here focuses on the possibility to restore supersymmetry in the continuum limit, to pave the way for future work on the mass spectrum of  $\mathcal{N} = 1$  SYM theory in four dimensions, as suggested from low energy effective actions [68].

In detail, the work is organized as follows: In chapter 2 the relevant properties of the exceptional Lie group  $G_2$  are reviewed. To simulate  $G_2$  Yang-Mills theory on the lattice, in chapter 3 a Monte-Carlo update algorithm based on a local HMC algorithm is developed for arbitrary Lie groups and a

new and highly efficient implementation for  $G_2$  is presented. Also algorithms to simulate QCD and supersymmetric Yang-Mills theories are reviewed. In chapter 4 properties associated to confinement for arbitrary gauge groups are discussed, and pure  $G_2$  gluodynamics at finite temperature is investigated. It is shown that, similar to  $SU(3)$  gauge theory, a first order phase transition separates the confined from the deconfined phase. Additionally, for the first time the deconfinement phase transition in  $F_4$  and  $E_6$  gluodynamics is explored and compared to other gauge groups. Especially the gauge group  $E_6$  is an interesting candidate in various grand unified theory (GUT) scenarios [76, 77]. The assumptions made about exceptional confinement are then confirmed in chapter 5, where the dynamics of the flux tube between a quark and an anti-quark at zero temperature in different representations of the gauge group  $G_2$  is studied. Casimir scaling of the confining string can be verified for different representations of the gauge group to a high precision, and for the first time string breaking in  $G_2$  gauge theory is observed. The results are compared to results from bosonic string theory and different approaches to Yang-Mills theory in three and four dimensions, where for instance Casimir scaling and string breaking are predicted. In [57] it turned out that  $G_2$ -Yang-Mills theory coupled to a fundamental scalar field has an intriguing connection to  $SU(3)$ -Yang-Mills theory. By tuning the mass of the scalar field it is possible to interpolate between both theories. Therefore, in chapter 6 the phase diagram of the  $G_2$  gauge Higgs theory as a function of the scalar field mass and the gauge coupling is investigated with high-precision simulations. It is shown, that the former first-order phase transition of  $G_2$  gauge theory turns into a crossover, if the scalar field mass is fine-tuned to a small window in parameter space. This feature by itself is very similar to ordinary QCD, where the transition is weakened by fundamental quarks. Having shown that  $G_2$  and  $SU(3)$  pure gauge theory share many features,  $G_2$  gauge theory coupled to fundamental fermions is studied in chapter 7. It is shown that the fermion determinant is non-negative for any value of the gauge coupling and chemical potential, making Monte-Carlo simulations feasible. Furthermore, the chiral properties are explored and finally first results of Monte-Carlo simulations are presented, opening an interesting playground for future investigations. In chapter 8,  $\mathcal{N} = 1$  supersymmetric Yang-Mills theory on the lattice is investigated in the Wilson formulation. In one dimension the spectrum of the Dirac operator is studied and the continuum limit is performed, showing that supersymmetry can be restored on the lattice. Additionally, first results of simulations in three spacetime dimensions are presented. Finally, in chapter 9 the obtained results are summarized and various interesting problems for future investigations are addressed. Parts of this work have already been published [78–80] and presented at international conferences [81, 82].

*The compilation of this work is solely due to the author. However, parts of this work have been done in collaboration with colleagues from the research groups on quantum field theory in Jena and Darmstadt. The investigations of  $G_2$  gauge theories in chapter 5 and 6 have been done together with Christian Wozar and the investigations on  $G_2$ -QCD in chapter 7 have been performed in collaboration with Axel Maas, Andreas Wipf and Lorenz von Smekal.*

## 2 The exceptional gauge group $G_2$

The main part of this thesis deals with gauge theories, where the gauge group is the exceptional Lie group  $G_2$ . To understand the dynamics, it is necessary to know about the structure of the Lie group, especially its construction and representation theory. In the present chapter some of the relevant properties of the exceptional Lie group  $G_2$  are reviewed.

### General properties and construction

$G_2$  is the smallest of the five exceptional simple Lie groups and it is also the smallest simple and simply connected Lie group which has a trivial centre. As  $SU(3)$ , the gauge group of strong interaction, it has rank 2 and the fundamental representations are the 7-dimensional and the 14-dimensional adjoint representation with Dynkin labels

$$(7) = [1, 0], \quad (14) = [0, 1]. \quad (2.1)$$

It is also the automorphism group of the octonion algebra or, equivalently, the subgroup of  $SO(7)$  that preserves any vector in its 8-dimensional real spinor representation [83]. This means that the 8-dimensional real spinor representation of  $\text{Spin}(7)$  branches into the trivial representation and the 7-dimensional fundamental representation of  $G_2$ . The 14-dimensional fundamental representation of  $G_2$  arises in the branching of the adjoint of  $SO(7)$  according to  $(21) \rightarrow (7) \oplus (14)$ . The elements of  $G_2$  can be viewed as elements of  $SO(7)$  subject to seven independent cubic constraints for the 7-dimensional matrices  $g$  representing  $SO(7)$  [57, 84]:

$$T_{abc} = T_{def} g_{da} g_{eb} g_{fc}. \quad (2.2)$$

Here,  $T$  is a total antisymmetric tensor given by

$$T_{127} = T_{154} = T_{163} = T_{235} = T_{264} = T_{374} = T_{576} = 1. \quad (2.3)$$

The constraints (2.2) for the group elements reduce the 21 generators of  $SO(7)$  to 14 generators of the group  $G_2$ . Its Weyl group is the dihedral group  $D_6$  of order 12. Additionally,  $G_2$  is connected to  $SU(3)$  through the embedding of  $SU(3)$  as a subgroup of  $G_2$  according to [85, 86]

$$G_2/SU(3) \sim SO(7)/SO(6) \sim S_6. \quad (2.4)$$

This means that every element  $\mathcal{U}$  of  $G_2$  can be written as

$$\mathcal{U} = \mathcal{S} \cdot \mathcal{V} \quad \text{with} \quad \mathcal{S} \in G_2/SU(3) \quad \text{and} \quad \mathcal{V} \in SU(3), \quad (2.5)$$

and this decomposition is used to speed up the numerical simulations. With respect to the subgroup  $SU(3)$  the fundamental representations (7) and (14) branch into the following irreducible  $SU(3)$  representations:

$$(7) \longrightarrow (3) \oplus (\bar{3}) \oplus (1) \quad \text{and} \quad (14) \longrightarrow (8) \oplus (3) \oplus (\bar{3}). \quad (2.6)$$

representation $\mathcal{R}$	[0, 0]	[1, 0]	[0, 1]	[2, 0]	[1, 1]	[3, 0]	[0, 2]	[4, 0]	[2, 1]
dimension $d_{\mathcal{R}}$	1	7	14	27	64	77	77'	182	189
Casimir eigenvalue $\mathcal{C}_{\mathcal{R}}$	0	12	24	28	42	48	60	72	64
Casimir ratio $\mathcal{C}'_{\mathcal{R}}$	0	1	2	7/3	3.5	4	5	6	16/3

**Table 2.1** Representations of  $G_2$  with corresponding dimensions and Casimir values.

Any irreducible representation of  $G_2$  is characterized by its highest weight vector  $\mu$ , which is a linear combination of the fundamental weights,  $\mu = p\mu_{(1)} + q\mu_{(2)}$ , with non-negative integer coefficients  $p, q$  called Dynkin labels. The dimension of an arbitrary irreducible representation  $\mathcal{R} = [p, q]$  can be calculated with the help of Weyl's dimension formula and is given by

$$d_{\mathcal{R}} \equiv \dim_{p,q} = \frac{1}{120}(1+p)(1+q)(2+p+q)(3+p+2q)(4+p+3q)(5+2p+3q). \quad (2.7)$$

In what follows, mainly the 'physics-convention' is used, where a representation is denoted by its dimension. For example, the fundamental representations are denoted by  $[1, 0] = (7)$  and  $[0, 1] = (14)$ . However, this notation is ambiguous, since there exist different representations with the same dimension. For example  $[3, 0] = (77)$  and  $[0, 2] = (77')$  have the same dimension. The Dynkin labels of the lowest-dimensional representations are given by

$$\begin{aligned} (1) &= [0, 0], & (7) &= [1, 0], & (14) &= [0, 1], & (27) &= [2, 0], & (64) &= [1, 1], \\ (77) &= [3, 0], & (77') &= [0, 2], & (182) &= [4, 0], & (189) &= [2, 1]. \end{aligned} \quad (2.8)$$

An irreducible representation of  $G_2$  can also be characterized by the values of the two Casimir operators of degree 2 and 6. In chapter 5 the eigenvalues of the quadratic Casimir operator in a representation  $[p, q]$  are needed. They are given by

$$\mathcal{C}_{\mathcal{R}} \equiv \mathcal{C}_{p,q} = 2p^2 + 6q^2 + 6pq + 10p + 18q. \quad (2.9)$$

For an easy comparison these 'raw' Casimir values can be normalized with respect to the defining representation by  $\mathcal{C}'_{p,q} = \mathcal{C}_{p,q}/\mathcal{C}_{1,0}$ . The normalized Casimir values for the lowest-dimensional representations are given in Tab. 2.1. Since  $G_2$  is a subgroup of  $SO(7)$ , all representations are real and one can always choose a real basis for the Lie algebra. A possible real representation for the 14 generators is given in the appendix B, cf. also [87].

## Fundamental region and Haar measure

In effective theories for the gauge invariant (traced) Polyakov loops in the fundamental representations, only the reduced Haar measure is needed. Based on [87, 88], this measure can be given for a parametrisation of the conjugacy classes either by angular variables or alternatively by the fundamental characters,

$$d\mu \propto J^2 d\varphi_1 d\varphi_2 = J d\chi_7 d\chi_{14}. \quad (2.10)$$

The density  $J^2$  can be expressed in terms of the fundamental characters,

$$J^2 = (4\chi_7^3 - \chi_7^2 - 2\chi_7 - 10\chi_7\chi_{14} + 7 - 10\chi_{14} - \chi_{14}^2) \times (7 - \chi_7^2 - 2\chi_7 + 4\chi_{14}), \quad (2.11)$$

where the characters are given in terms of (particularly chosen) angular variables  $\varphi_{1,2}$  as

$$\begin{aligned} \chi_7 &= 1 + 2\cos(\varphi_1) + 2\cos(\varphi_2) + 2\cos(\varphi_1 + \varphi_2), \\ \chi_{14} &= 2(1 + \cos(\varphi_1) + \cos(\varphi_1 - \varphi_2) + \cos(\varphi_2) \\ &\quad + \cos(\varphi_1 + \varphi_2) + \cos(2\varphi_1 + \varphi_2) + \cos(\varphi_1 + 2\varphi_2)). \end{aligned} \quad (2.12)$$

The boundary of the fundamental domain is determined by  $J = 0$  and thus is parametrised by the three curves (see Fig. 2.1)

$$\chi_{14} = \frac{1}{4}(\chi_7 + 1)^2 - 2, \quad \chi_{14} = -5(\chi_7 + 1) \pm 2(\chi_7 + 2)^{3/2}. \quad (2.13)$$

Note that the reduced  $G_2$  Haar measure is maximal not at the origin but for  $(\chi_7, \chi_{14}) = (-1/5, -2/5)$ . The fundamental domain has no symmetries at all and this expresses the fact that the centre of  $G_2$  is trivial. In Fig. 2.1, the Haar measure of  $G_2$  is compared to the Haar measure of  $SU(3)$  with centre  $\mathbb{Z}(3)$ , where the centre symmetry is clearly visible.

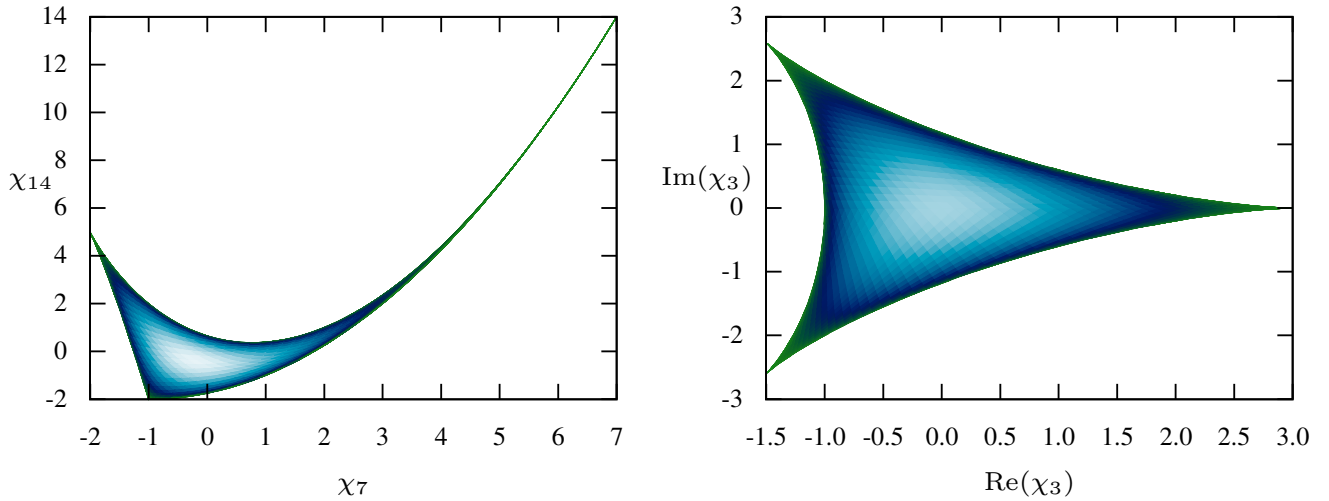


**Figure 2.1** Haar measure and fundamental domain of  $G_2$  (left panel), compared to Haar measure and fundamental domain of  $SU(3)$  (right panel). Lighter regions indicate a larger value of the Haar measure.

## Representation theory

Tensor products of irreducible representations are important to understand the formation of possible colourless bound states (singlets under the action of the gauge group) in  $G_2$  gluodynamics. Quarks in  $G_2$  transform under the 7-dimensional fundamental representation, gluons under the 14-dimensional fundamental representation. The decomposition of tensor products of the lowest-dimensional representations

into irreducible representations is given by

$$\begin{aligned}
(7) \otimes (7) &= (1) \oplus (7) \oplus (14) \oplus (27), \\
(7) \otimes (7) \otimes (7) &= (1) \oplus 4 \cdot (7) \oplus 2 \cdot (14) \oplus 3 \cdot (27) \oplus 2 \cdot (64) \oplus (77'), \\
(14) \otimes (14) &= (1) \oplus (14) \oplus (27) \oplus (77) \oplus (77'), \\
(14) \otimes (14) \otimes (14) &= (1) \oplus (7) \oplus 5 \cdot (14) \oplus 3 \cdot (27) \oplus \dots, \\
(7) \otimes (14) \otimes (14) \otimes (14) &= (1) \oplus \dots.
\end{aligned} \tag{2.14}$$

The character  $\chi_{\mathcal{R}}(\mathcal{U}) = \text{tr}_{\mathcal{R}}(\mathcal{U})$  of any irreducible representation  $\mathcal{R}$  is a polynomial of the characters  $\chi_7$  and  $\chi_{14}$  of the two fundamental representations 7 and 14. For example, the first two decompositions in (2.14) imply

$$\begin{aligned}
\chi_{27} &= \chi_7 \cdot \chi_7 - \chi_1 - \chi_7 - \chi_{14}, \\
\chi_{64} &= \chi_7 \cdot \chi_{14} - \chi_7 - \chi_{27} = \chi_7 \chi_{14} - \chi_7^2 + \chi_1 + \chi_{14},
\end{aligned} \tag{2.15}$$

and yield the characters of the representations (27) and (64) as polynomials of  $\chi_7$  and  $\chi_{14}$ . From further tensor products of irreducible representations one can calculate the polynomial in  $\chi_{\mathcal{R}} = \text{Pol}_{\mathcal{R}}(\chi_7, \chi_{14})$  for any irreducible representation  $\mathcal{R}$ . For a fast implementation of some of the used algorithms it is also useful to consider the ‘branchings’ of  $SO(7)$  representations to  $G_2$ . The 27 dimensional representations of  $SO(7)$  acting on symmetric traceless 2-tensors remains irreducible under  $G_2$ . Additionally, the following relations will be needed:

$$(7) \rightarrow (7), \quad (21) \rightarrow (14) \oplus (7), \quad (27) \rightarrow (27), \quad (35) \rightarrow (27) \oplus (7) \oplus (1), \quad (77) \rightarrow (77). \tag{2.16}$$

In particular the reducible representations

$$(7 \otimes 7)_s, (7 \otimes 7 \otimes 7)_s, (7 \otimes 7 \otimes 7 \otimes 7)_s, (7 \otimes 7)_s \otimes 14, \tag{2.17}$$

are useful, where the subscript ‘s’ denotes the symmetrized part of the respective tensor product. Comparing the reduction of representations for  $SO(7)$  and  $G_2$  and mapping representations from  $SO(7)$  to  $G_2$  the following characters of reducible representations can be computed

$$\begin{aligned}
\chi_{(7 \otimes 7)_s} &= \chi_{27} + \chi_1, \quad \chi_{(7 \otimes 7 \otimes 7)_s} = \chi_{77} + \chi_7, \quad \chi_{(7 \otimes 7 \otimes 7 \otimes 7)_s} = \chi_{182} + \chi_{27} + \chi_1, \\
\chi_{(7 \otimes 7)_s \otimes 14} &= \chi_{189} + \chi_{77} + \chi_{27} + \chi_{64} + 2\chi_{14} + \chi_7.
\end{aligned} \tag{2.18}$$

Altogether the following relations are used to compute the characters of the 8 lowest-dimensional representations

$$\begin{aligned}
\chi_7, \quad \chi_{14}, \quad \chi_{27} &= \chi_{(7 \otimes 7)_s} - \chi_1, \quad \chi_{64} = \chi_{7 \otimes 14} - \chi_{(7 \otimes 7)_s} - \chi_7 + \chi_1, \\
\chi_{77} &= \chi_{(7 \otimes 7 \otimes 7)_s} - \chi_7, \quad \chi_{77'} = \chi_{14 \otimes 14} - \chi_{(7 \otimes 7 \otimes 7)_s} - \chi_{(7 \otimes 7)_s} - \chi_{14} + \chi_7, \\
\chi_{182} &= \chi_{(7 \otimes 7 \otimes 7 \otimes 7)_s} - \chi_{(7 \otimes 7)_s}, \quad \chi_{189} = \chi_{(7 \otimes 7)_s \otimes 14} - \chi_{(7 \otimes 7 \otimes 7)_s} - \chi_{7 \otimes 14} + \chi_7 - 2\chi_{14}.
\end{aligned} \tag{2.19}$$

For the algorithms used in this work, it is important that the relations are linear in the (reducible) representations on the right hand side of the equations. In this case the representation trace commutes with the ensemble average of Polyakov or Wilson lines, which is necessary for an efficient computation of sublattice expectation values in chapter 5. Additional information on  $G_2$  and on the construction of the exceptional Lie groups  $F_4$  and  $E_6$  can be found in the appendix B.

# 3 Algorithmic considerations

In the present work, purely bosonic theories as well as theories containing fermions are investigated. Since many features of these strongly-coupled theories are perturbatively not accessible, non-perturbative tools are needed, and the method of choice here are Monte-Carlo simulations on discrete spacetime lattices. In the following, the lattice formulation of theories, investigated below, is briefly reviewed and the Monte-Carlo algorithms are discussed in a general way. Details depending on the implementation and special features of the model will be discussed later in the corresponding chapter. Mainly two algorithms are presented, the (local) Hybrid Monte-Carlo algorithm ((l)HMC) for purely bosonic theories on arbitrary semi-simple and simply connected Lie groups, and the rational Hybrid Monte-Carlo (rHMC) extension for fermionic degrees of freedom.

The Euclidean path integral or the partition function of a system is given by

$$\mathcal{Z} = \int_{\mathcal{M}} \mathcal{D}\phi e^{-S_E[\phi]}, \quad (3.1)$$

where  $S_E$  is the Euclidean action on the discrete spacetime lattice  $\Lambda$ . The fields  $\phi(x)$  are mappings from  $\Lambda$  to some manifold  $\mathcal{M}$ . For details on the lattice regularization of path integrals see [27, 89, 90]. Observables  $\mathcal{O}$  are calculated as an ensemble average

$$\langle \mathcal{O} \rangle_p = \int_{\mathcal{M}} p[\phi] \mathcal{O}[\phi], \quad p[\phi] = \frac{\mathcal{D}\phi e^{-S_E[\phi]}}{\mathcal{Z}}. \quad (3.2)$$

The goal of the Markov chain Monte-Carlo method (MCMC) is now to generate a Markov chain for the probability function  $p$  such that field configurations  $\mathcal{C}[\phi]$  are distributed with respect to  $p[\phi]$ . Then the expectation value can be written as a sum over field configurations,

$$\langle \mathcal{O} \rangle_p \approx \frac{1}{N} \sum_{n=1}^N \mathcal{O}[\mathcal{C}_n]. \quad (3.3)$$

For details on Markov chain Monte-Carlo methods and statistical error estimation of observables see [91]. In the present work statistical errors are calculated with the Jackknife method and in some cases a bias correction for derived quantities and non-Gaussian distributions [91–94], as for instance the expectation values of masses, is applied.

## 3.1 The IHMC algorithm for semi-simple Lie algebras

A common algorithm for generating such a Markov chain is the Hybrid Monte-Carlo algorithm (HMC), introduced in [95]. The first class of models investigated here are purely bosonic theories, where the dynamic fields are Lie algebra valued, e.g. pure gauge theories or non-linear sigma models. In simulations of pure gauge field theories different algorithms are in use. For  $SU(N_c)$  gluodynamics heat-bath algorithms based on the Cabibbo-Marinari  $SU(2)$  subgroup updates [96], often improved by over-relaxation

steps, have proven to be fast and reliable. For the exceptional gauge group  $G_2$  there exists a modification of the heat-bath update [58], which combines the heat-bath update for a  $SU(3)$  subgroup with randomly distributed  $G_2$  gauge transformations to rotate the  $SU(3)$  subgroup through  $G_2$ . In the present work instead a *local* version of the HMC algorithm, based on [97], where single links are evolved in a HMC style, is used for several good reasons: The formulation is given entirely in terms of Lie group and Lie algebra elements and there is no need to back-project onto the group  $\mathcal{G}$ . The autocorrelation time can be controlled (in certain ranges) by the integration time in the molecular dynamics part of the HMC algorithm. The inclusion of a (normalized) Higgs field is straightforward and does not suffer from a low Metropolis acceptance rate (even for large hopping parameters) and finally the extension to a HMC algorithm coupled to fundamental or adjoint fermions is obvious. The IHMC algorithm has been essential for obtaining the results in the present work. Here and in the accompanying (journal) publication [80], the first implementation for  $G_2$  is developed. It is therefore useful to explain the technical details for this exceptional group. However, the algorithm is applicable to any semi-simple and simply connected Lie group, since it depends only on a choice for the generators  $T$  of the corresponding Lie algebra. In the following it is assumed that the generators of the Lie algebra are normalized according to

$$(T^a, T_b) = \text{tr}(T^a T_b) = \delta_b^a. \quad (3.4)$$

Additionally, they are chosen to be Hermitian,  $T_a^\dagger = T_a$ . Now consider a field configuration  $\mathcal{C}(\{\mathcal{U}\})$  on the lattice with  $\mathcal{U}_i \in \mathcal{G}$ . Then, as for any HMC algorithm, the transition to a new configuration  $\mathcal{C}'(\{\mathcal{U}'\})$  is based on a fictitious dynamics for the variables on the group manifold. The ‘free evolution’ on a semi-simple group  $\mathcal{G}$  is the Riemannian geodesic motion with respect to the Cartan-Killing metric

$$ds_{\mathcal{G}}^2 \sim \text{tr}(d\mathcal{U}\mathcal{U}^{-1} \otimes d\mathcal{U}\mathcal{U}^{-1}), \quad \mathcal{U} \in \mathcal{G}. \quad (3.5)$$

In the fictitious dynamics the interaction term is given by the action  $S[\mathcal{U}]$  of the lattice theory and hence it suggests itself to derive the dynamics from the Lagrangian

$$L = \frac{1}{2} \sum_i \text{tr} \left( i \dot{\mathcal{U}}_i \mathcal{U}_i^{-1} \right)^2 - S[\mathcal{U}], \quad (3.6)$$

where ‘dot’ denotes the derivative with respect to the fictitious time parameter  $\tau$ . The Lie algebra valued fictitious ‘conjugated momentum’  $\mathfrak{P} \in \mathfrak{g}$  is given by

$$\mathfrak{P}_i = i \frac{\partial L}{\partial \left( i \dot{\mathcal{U}}_i \mathcal{U}_i^{-1} \right)} = i \mathcal{U}_i \frac{\partial L}{\partial \dot{\mathcal{U}}_i} = -i \dot{\mathcal{U}}_i \mathcal{U}_i^{-1}, \quad (3.7)$$

and via a Legendre transform yields the pseudo-Hamiltonian

$$H = \frac{1}{2} \sum_i \text{tr} \mathfrak{P}_i^2 + S[\mathcal{U}]. \quad (3.8)$$

Since  $\mathfrak{P}$  is Hermitian, the kinetic term is always positive. For real  $\mathcal{U}_i$  the momenta are antisymmetric and therefore purely imaginary. The equations of motion for the momenta are obtained by varying the Hamiltonian with respect to the fictitious time parameter  $\tau$ . Hence one obtains

$$\delta H = \sum_i \text{tr} \{ \mathfrak{P}_i \delta \mathfrak{P}_i \} + \delta S[\mathcal{U}] = \sum_i \text{tr} \mathfrak{P}_i \left\{ \dot{\mathfrak{P}}_i - F_i \right\} \delta \tau = 0, \quad (3.9)$$

where the HMC ‘force’  $F$  is defined as a solution to the equation

$$\delta S[\mathcal{U}] = -\text{tr}(\mathfrak{P}F) \delta\tau. \quad (3.10)$$

Here one already notices that the solution is not unique and the remaining freedom can always be used to assure that  $\mathfrak{P} \in \mathfrak{g}$ . Then the variational principle implies that the projection of the term between curly brackets in (3.9) onto the Lie algebra  $\mathfrak{g}$  vanishes,

$$\dot{\mathfrak{P}}_i = F_i|_{\mathfrak{g}}. \quad (3.11)$$

Choosing a trace-orthonormal basis  $\{T_a\}$  of  $\mathfrak{g}$ , the equations for the (1)HMC dynamics can be written as follows,

$$\dot{\mathfrak{P}}_i = \sum_a \text{tr}(F_i T_a) T_a \quad \text{and} \quad \dot{\mathcal{U}}_i = i \mathfrak{P}_i \mathcal{U}_i, \quad (3.12)$$

with the ‘force’  $F_i$  defined in (3.10). Now it is possible to consider two different algorithms to obtain a new configuration  $\mathcal{C}'$  in the Markov chain, starting from a configuration  $\mathcal{C}$ . The original HMC algorithm is given by a Gaussian draw of all momenta, followed by a (numerical) integration of the equations of motion from HMC ‘time’  $\tau = 0$  to  $\tau = t_{\text{HMC}}$ . To ensure detailed balance, a final Metropolis acceptance step is performed. The pseudocode is shown in Alg. 1. Due to the numerical integration of the equations of motion, the energy is not exactly conserved and  $\delta H$  is proportional to the number of degrees of freedom  $N$ . Therefore, with increasing  $N$ , the integration step size  $\delta\tau$  has to be adjusted to ensure a constant acceptance rate in the Metropolis step. The second possibility is the IHMC algorithm (Alg. 2). Here, every single variable is evolved in a HMC-style. This local version of the HMC does not suffer from an extensive  $\delta H \propto N$  problem, such that in many cases already a second-order symplectic (leap frog) integrator allows for sufficiently large time-steps  $\delta\tau$ . A test for the algorithm is its ability to reproduce the Haar measure of the group. In Fig. 3.1 the Haar measure in the fundamental domain for  $SU(3)$ ,  $G_2$ ,  $F_4$  and  $E_6$  is shown as a scatter plot, where the  $\mathbb{Z}(3)$  centre symmetry of  $SU(3)$  and  $E_6$  is seen, while the fundamental domains for  $G_2$  and  $F_4$  do not possess any symmetry at all.

---

#### Algorithm 1 HMC algorithm

---

**Require:** Configuration  $\mathcal{C}(\{\mathcal{U}\})$ ,  $N$  degrees of freedom, symplectic integrator  $I(\tau)$

- 1: **for**  $i = 1$  **to**  $N$  **do**
  - 2:   Draw momentum  $\mathfrak{P}_i$  Gaussian distributed
  - 3: **end for**
  - 4: **for**  $\tau = 0$  **to**  $t_{\text{HMC}}$  **step**  $\delta\tau$  **do**
  - 5:   Integrate the equations of motion (3.12) for  $\{\mathfrak{P}\}$  and  $\{\mathcal{U}\}$  with integrator  $I(\tau)$ .
  - 6: **end for**
  - 7: Accept the new configuration with probability  $p = \min(1, \exp\{H(\mathcal{C}) - H(\mathcal{C}')\})$
  - 8: **return** Configuration  $\mathcal{C}'(\{\mathcal{U}'\})$
-

---

**Algorithm 2** IHMC algorithm

**Require:** Configuration  $\mathcal{C}(\{\mathcal{U}\})$ ,  $N$  degrees of freedom, symplectic integrator  $I(\tau)$

- 1: **for**  $i = 1$  **to**  $N$  **do**
  - 2:   Draw momentum  $\mathfrak{P}_i$  Gaussian distributed
  - 3:   **for**  $\tau = 0$  **to**  $t_{\text{HMC}}$  **step**  $\delta\tau$  **do**
  - 4:     Integrate the equations of motion (3.12) for  $\mathfrak{P}_i$  and  $\mathcal{U}_i$  with integrator  $I(\tau)$ .
  - 5:   **end for**
  - 6:   Accept the time evolution with probability  $p = \min(1, \exp\{H(\mathcal{C}) - H(\mathcal{C}')\})$
  - 7: **end for**
  - 8: **return** Configuration  $\mathcal{C}'(\{\mathcal{U}'\})$
- 

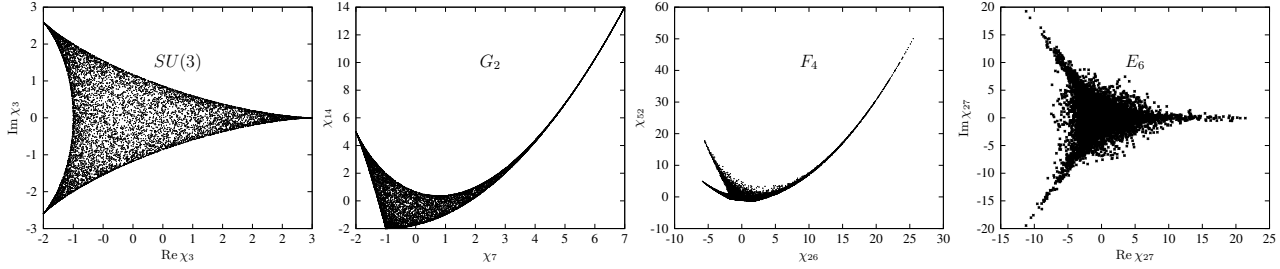


**Figure 3.1** Fundamental domains for  $SU(3)$  and  $G_2$  and its projection to the lowest-dimensional representations for  $F_4$  and  $E_6$ , as obtained with the local HMC algorithm.

### 3.1.1 Symplectic integration and multiple time scales

In order to assure the detailed balance condition, the integrator used in the HMC algorithm has to be time reversible. To get a large acceptance rate, the energy should be conserved (at least to some order in the time step  $\delta\tau$ ). For these purposes a large class of integrators (so called symplectic integrators) exist. The simplest possible integration scheme is the leap-frog scheme [98]. With a definition of time evolution operators  $T_{\mathcal{U}}$  and  $T_S$  according to

$$\begin{aligned}\mathfrak{P}_i(\tau + \delta\tau) &= T_S(\delta\tau) \mathfrak{P}_i(\tau) = \mathfrak{P}_i(\tau) + \delta\tau \dot{\mathfrak{P}}_i(\tau) \\ \mathcal{U}_i(\tau + \delta\tau) &= T_{\mathcal{U}}(\delta\tau) \mathcal{U}_i(\tau) = \exp\left\{i \delta\tau \mathfrak{P}_i\left(\tau + \frac{1}{2}\delta\tau\right)\right\} \mathcal{U}_i(\tau),\end{aligned}\tag{3.13}$$

the time evolution from  $\tau = 0$  to  $\tau = t_{\text{HMC}}$  with the leap-frog time evolution operator  $T_{\text{LF}}$  can be written as

$$T(t_{\text{HMC}}, \delta\tau) = T_{\text{LF}}(\delta\tau)^n, \quad T_{\text{LF}}(\delta\tau) = T_S\left(\frac{1}{2}\delta\tau\right) T_{\mathcal{U}}(\delta\tau) T_S\left(\frac{1}{2}\delta\tau\right), \quad n = \frac{t_{\text{HMC}}}{\delta\tau}.\tag{3.14}$$

It is proven that this integration scheme is of order 2 in  $\delta\tau$ , i.e. it conserves the energy up to  $\delta H \propto \delta\tau^2$ . Although in the (l)HMC algorithm the discretization errors within the leap-frog scheme are often already small enough, especially for theories containing fermions, a significant improvement can be achieved by using so called minimized norm integrators. An improved second-order integrator is given by the Sexton-Weingarten scheme [99],

$$T_{\text{SW}}(\delta\tau) = T_S\left(\frac{\delta\tau}{6}\right) T_{\mathcal{U}}\left(\frac{\delta\tau}{2}\right) T_S\left(\frac{2\delta\tau}{3}\right) T_{\mathcal{U}}\left(\frac{\delta\tau}{2}\right) T_S\left(\frac{\delta\tau}{6}\right).\tag{3.15}$$

A fourth order integrator is given by [100]

$$T_4(\delta\tau) = T_S(\rho\delta\tau) T_U(\lambda\delta\tau) T_S(\theta\delta\tau) T_U\left(\left(1 - 2\lambda\right)\frac{\delta\tau}{2}\right) T_S\left(\left(1 - 2(\theta + \rho)\right)\delta\tau\right) \times \\ \times T_U\left(\left(1 - 2\lambda\right)\frac{\delta\tau}{2}\right) T_S(\theta\delta\tau) T_U(\lambda\delta\tau) T_S(\rho\delta\tau), \quad (3.16)$$

with  $\rho = 0.1786178958448091$ ,  $\theta = 0.06626458266981843$  and  $\lambda = 0.7123418310626056$ . Higher order integrators are constructed in [101]. Further improvement can be achieved by integration on multiple time scales [102]. For this purpose an arbitrary integrator  $T_s$  (here  $s$  stands for the integration scheme) is written as a function of the basic time evolution operators  $T_S$  and  $T_U$  and the integration step size  $\delta\tau$ ,  $T_s = T_s(T_S, T_U, \delta\tau)$ . If the action can be written as a sum of contributions  $S_j$ , i.e.  $S = \sum_j S_j$ , then multiple time scale integration can be defined by the recursion relation

$$T_{s_j}^j(T_{S_j}, T_U, \delta\tau_j) = T_{s_j}^j(T_{S_j}, [T_{s_{j-1}}^{j-1}(T_{S_{j-1}}, T_U, \delta\tau_j/n_j)]^{n_j}, \delta\tau_j), \quad (3.17)$$

where  $S_j$  denotes the subset of the action that should be taken into account in the computation of the ‘force’ on the  $j$ -th time scale with step size  $\delta\tau_j$ . An example of a two time scale integration often used in this work is the combination of the Sexton-Weingarten scheme with the leap-frog scheme,

$$T(\delta\tau) = T_{S_0}\left(\frac{\delta\tau}{2}\right) T_{SW}(T_{S_1}, T_U, \delta\tau) T_{S_0}\left(\frac{\delta\tau}{2}\right) \\ = T_{S_0}\left(\frac{\delta\tau}{2}\right) T_{S_1}\left(\frac{\delta\tau}{6}\right) T_U\left(\frac{\delta\tau}{2}\right) T_{S_1}\left(\frac{2\delta\tau}{3}\right) T_U\left(\frac{\delta\tau}{2}\right) T_{S_1}\left(\frac{\delta\tau}{6}\right) T_{S_0}\left(\frac{\delta\tau}{2}\right). \quad (3.18)$$

Here, the ‘force’ according to  $S_1$  has to be calculated twice as often as the ‘force’ belonging to  $S_0$ . Another scheme often used is the combination of a fourth order integrator with the Sexton-Weingarten scheme or with the simple leap-frog scheme. Usually, multiple-time-scale integration is efficient if parts of the action with large contribution to the HMC ‘force’ are cheap in computation time.

### 3.1.2 Computation of the exponential map

In pure gauge theories, the most time-consuming step in the IHMC algorithm is the computation of the exponential map  $\mathfrak{g} \mapsto \mathcal{G}$ . Although there is no need to calculate the exponential map exactly, the approximation used in the symplectic integrator has to respect time reversibility. For the different Lie groups discussed in this work, different strategies to obtain the most efficient algorithm are used.

**The exponential map for  $SU(2)$  and  $SU(3)$**  can be computed exactly with the Cayley-Hamilton theorem and exact expressions for the needed eigenvalues in the Lie algebra. For  $SU(2)$ , for instance, the exponential map is given by

$$\exp(i\mathfrak{P}) = \exp(ip_a T^a) = \cos(r)\mathbb{1} + i\frac{\sin(r)}{r}\mathfrak{P}, \quad r = \sqrt{p_a p^a}. \quad (3.19)$$

**The exponential map of  $G_2$**  For an efficient and fast computation of the exponential map of  $G_2$  the real embedding of the  $SU(3)$  representation  $3 \oplus \bar{3}$  into  $G_2$ , given by

$$\mathcal{V}(\mathcal{W}) = \Omega^\dagger \begin{pmatrix} 1 & 0 & 0 \\ 0 & \mathcal{W} & 0 \\ 0 & 0 & \mathcal{W}^* \end{pmatrix} \Omega \in G_2 \quad \text{with} \quad \mathcal{W} \in SU(3), \quad (3.20)$$

is used. One can choose the unitary matrix  $\Omega$  to have block diagonal form with  $\Omega_{11} = 1$ . A possible choice for  $\Omega$  is

$$\Omega = \begin{pmatrix} 1 & 0 \\ 0 & VQ \end{pmatrix} \quad \text{with} \quad Q = \begin{pmatrix} 0 & 0 & 0 & 0 & 0 & 1 \\ 0 & 0 & 1 & 0 & 0 & 0 \\ 1 & 0 & 0 & 0 & 0 & 0 \\ 0 & 0 & 0 & 0 & 1 & 0 \\ 0 & 0 & 0 & 1 & 0 & 0 \\ 0 & 1 & 0 & 0 & 0 & 0 \end{pmatrix}, \quad V = \frac{1}{\sqrt{2}} \begin{pmatrix} 1 & i \\ i & 1 \end{pmatrix} \otimes \mathbb{1}_3. \quad (3.21)$$

Every element  $\mathcal{U}$  of  $G_2$  can, according to (2.4) and (2.5), be factorized as

$$\mathcal{U} = \mathcal{S} \cdot \mathcal{V}(\mathcal{W}) \quad \text{with} \quad \mathcal{S} \in G_2/SU(3). \quad (3.22)$$

For a given time-step  $\delta\tau$  in the molecular dynamics this factorization will be expressed in terms of the Lie algebra elements with the help of the exponential maps,

$$\exp\{\delta\tau \mathbf{u}\} = \exp\{\delta\tau \mathfrak{s}\} \cdot \exp\{\delta\tau \mathfrak{v}\} \quad \text{with generators} \quad \mathbf{u} \in \mathfrak{g}_2, \quad \mathfrak{v} \in \mathcal{V}_*(\mathfrak{su}(3)), \quad (3.23)$$

fulfilling the commutation relations

$$[\mathfrak{v}, \mathfrak{v}'] = \mathfrak{v}'', \quad [\mathfrak{v}, \mathfrak{s}] = \mathfrak{s}', \quad \text{and} \quad [\mathfrak{s}, \mathfrak{s}'] = \mathfrak{v}' + \mathfrak{s}''. \quad (3.24)$$

The generators  $\mathfrak{s}$  are orthogonal to the generators of the really embedded  $SU(3)$  subgroup. To simplify the notation, the time step  $\delta\tau$  is absorbed in the Lie algebra elements. The last exponential map in (3.23) can be calculated with the help of the embedding (3.20) and the exponential map for  $SU(3)$ ,  $\mathcal{W} = \exp(\mathfrak{w})$ , which follows from the Cayley-Hamilton theorem for  $SU(3)$  generators, see [103]. The result can be expressed in terms of the imaginary eigenvalues  $w_1, w_2, w_3$  of  $\mathfrak{w}$  and the differences  $\delta_1 = w_2 - w_3$ ,  $\delta_2 = w_3 - w_1$  and  $\delta_3 = w_1 - w_2$  by

$$\mathcal{W} = \exp(\mathfrak{w}) = -\frac{1}{\delta_1\delta_2\delta_3} (\alpha_{\mathbb{1}} \mathbb{1} + \alpha_{\mathfrak{w}} \mathfrak{w} + \alpha_{\mathfrak{w}^2} \mathfrak{w}^2), \quad (3.25)$$

with expansion coefficients

$$\alpha_{\mathbb{1}} = \sum_{i=1}^3 \delta_i w_{i+1} w_{i+2} e^{w_i}, \quad \alpha_{\mathfrak{w}} = \sum_{i=1}^3 \delta_i w_i e^{w_i}, \quad \alpha_{\mathfrak{w}^2} = \sum_{i=1}^3 \delta_i e^{w_i}, \quad (3.26)$$

wherein one identifies  $w_{3+i}$  and  $w_i$ . For the generators  $\{\mathbf{u}_1, \dots, \mathbf{u}_{14}\}$  of  $G_2$  the real representation, given in [104], is used. The  $\mathfrak{su}(3)$  subalgebra formed by the elements  $\{\mathbf{u}_1, \dots, \mathbf{u}_8\}$  generates the really

embedded  $3 \oplus \bar{3}$  of  $SU(3)$  and the remaining generators  $\{u_9, \dots, u_{14}\}$  generate the coset elements  $\mathcal{S}$  in the factorization (3.22). With this choice for the generators the real embedding (3.20) reads

$$\mathcal{V}(\mathcal{W}) = \begin{pmatrix} 1 & 0 \\ 0 & \mathcal{V}_\perp \end{pmatrix}, \quad \mathcal{V}_\perp = \begin{pmatrix} a_{33} & -b_{33} & a_{32} & -b_{32} & -b_{31} & a_{31} \\ b_{33} & a_{33} & b_{32} & a_{32} & a_{31} & b_{31} \\ a_{23} & -b_{23} & a_{22} & -b_{22} & -b_{21} & a_{21} \\ b_{23} & a_{23} & b_{22} & a_{22} & a_{21} & b_{21} \\ b_{13} & a_{13} & b_{12} & a_{12} & a_{11} & b_{11} \\ a_{13} & -b_{13} & a_{12} & -b_{12} & -b_{11} & a_{11} \end{pmatrix}, \quad (3.27)$$

where the entries are the real and imaginary parts of the elements of the  $SU(3)$  matrix,  $\mathcal{W}_{ij} = a_{ij} + i b_{ij}$ . Finally, to parametrize the elements of the coset space the remaining exponential map,

$$\mathcal{S} = \exp \{ \mathfrak{s} \} \quad \text{with} \quad \mathfrak{s} = \sum_{i=1}^6 s_i u_{8+i}, \quad (3.28)$$

is calculated. The result depends on the real parameter  $\sigma = \|\vec{s}\|$  and the 6-dimensional unit-vector  $\hat{s} = \vec{s}/\|\vec{s}\|$ . In a  $1 \times 6$ -block notation the map takes the form

$$\mathcal{S} = \begin{pmatrix} \cos 2\sigma & -\sin 2\sigma \hat{s}^\top \\ \sin 2\sigma \hat{s} & \mathcal{S}_\perp \end{pmatrix} \quad (3.29)$$

with 6-dimensional matrix

$$\mathcal{S}_\perp = \cos \sigma \mathbb{1} + \sin \sigma \hat{s}_\perp + (\cos 2\sigma - \cos \sigma) \hat{s} \hat{s}^\top + (1 - \cos \sigma) \hat{v} \hat{v}^\top. \quad (3.30)$$

The matrix  $\hat{s}_\perp$  is the  $6 \times 6$  right-lower block of  $\mathfrak{s}$  in (3.28). The unit-vector  $\hat{v}^\top = (\hat{s}_2, -\hat{s}_1, \hat{s}_4, -\hat{s}_3, -\hat{s}_6, \hat{s}_5)$  defining the last projector in (3.30) is orthogonal to the unit-vector  $\hat{s}$  defining the projector  $\hat{s} \hat{s}^\top$ . In the numerical integration the exponential map for elements  $\mathfrak{u}$  in  $\mathfrak{g}_2$  is needed. They are related to the generators used in the factorization by the Baker-Campbell-Hausdorff formula,

$$\delta\tau \mathfrak{u} = \delta\tau (\mathfrak{s} + \mathfrak{v}) + \frac{1}{2} \delta\tau^2 [\mathfrak{s}, \mathfrak{v}] + \dots \quad (3.31)$$

Depending on the order of the symplectic integrator, this relation for  $\mathfrak{s}$  and  $\mathfrak{v}$  must be solved up to the corresponding order in  $\delta\tau$ . For a second-order integrator, mostly used in this work, this can be done analytically [105], since the commutator  $[\mathfrak{s}, \mathfrak{v}]$  does not contain any contribution of the subalgebra  $\mathfrak{su}(3)$ . The integrator used in the (l)HMC algorithm must be time reversible. It can be verified that time reversibility holds to every order in this expansion. To summarize, for a second-order integrator the approximation (3.31) is used in the exponentiation needed to calculate  $\mathcal{V}$  and  $\mathcal{S}$ . This approximation leads to a violation of energy conservation, which is of the same order as the violation one finds with a second-order integrator. In comparison to the exponentiation via the usual spectral decomposition, the method based on the factorization (3.22) is more than ten times faster. It is also much faster than computing the exponential map for  $SO(7)$  (and therefore the exponential map for  $G_2$ ) via the Cayley-Hamilton theorem.

The exponential map of  $SO(N)$  is calculated with the Caley-Hamilton theorem. The needed eigenvalues are obtained numerically.

**The exponential map of  $F(4)$ ,  $E(6)$  and other Lie groups** In the case of larger matrices, a series expansion of the exponential map is more efficient, since for small  $\delta\tau$  it converges rather fast to machine precision. Fig. 3.2 shows the convergence for a randomly chosen Lie algebra element (Gaussian distributed), where  $r(n) = \left\| \exp(i\delta\tau\mathfrak{P}) - \sum_{k=0}^n \frac{(i\delta\tau\mathfrak{P})^k}{k!} \right\|$ . In the simulations of  $F(4)$  and  $E(6)$  gauge theory, the first 15 terms ( $\delta\tau = 0.1$ ) in the expansion of the exponential map are used.

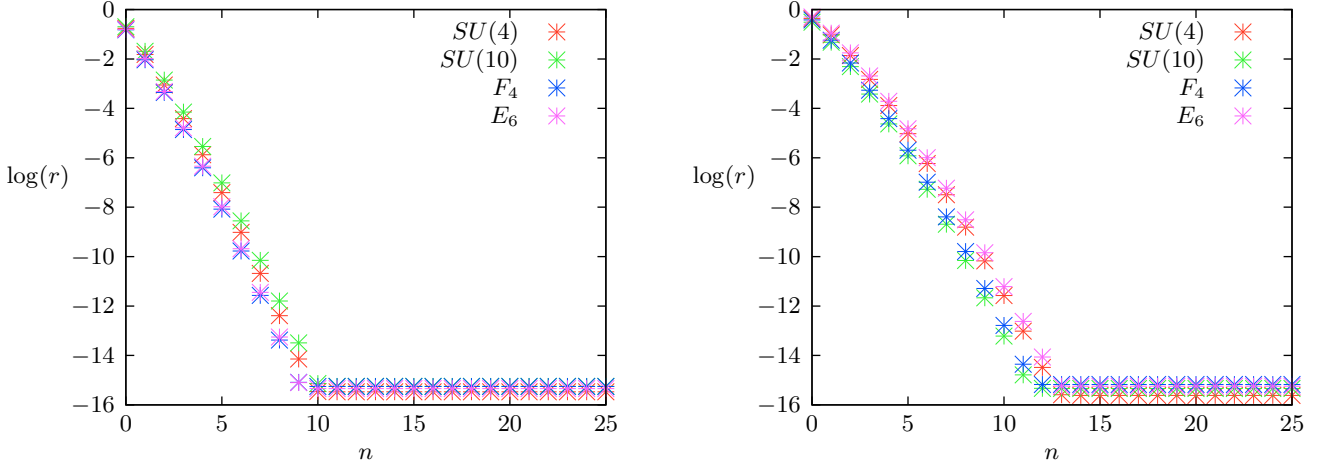


**Figure 3.2** Convergence of the exponential map for  $\delta\tau = 0.10$  (left panel) and  $\delta\tau = 0.25$  (right panel).

### 3.1.3 Non-linear $O(N)$ sigma models

The lattice action of the  $O(N)$  symmetric non-linear sigma model in  $d$  dimensions is given by

$$S[\Phi] = \kappa \sum_{\langle xy \rangle} \Phi_x^T \cdot \Phi_y, \quad \Phi_x^T \cdot \Phi_x = 1, \quad \Phi_x \in S^{N-1} \subset \mathbb{R}^N, \quad (3.32)$$

where the sum is over all nearest neighbour pairs  $\langle xy \rangle$  on the lattice and  $\Phi$  is an  $N$ -component normalized real scalar field. To update the normalized field  $\Phi$  one has to get rid of the explicit non-linear constraint equation. Therefore,  $\Phi$  is written as

$$\Phi_x = \mathcal{O}_x \Phi_0 \quad \text{with} \quad \mathcal{O}_x \in SO(N) \quad (3.33)$$

with constant  $\Phi_0$ . The change of variables  $\Phi_x \rightarrow \mathcal{O}_x$  converts the induced measure on  $S^{N-1} \subset \mathbb{R}^N$  into the Haar measure of  $SO(N)$ . Then the ‘force’ is given by

$$F_x = \kappa \Phi_x \left( \sum_{y:x} \Phi_y \right)^T, \quad (3.34)$$

where the sum extends over all nearest neighbours  $y$  of  $x$ . This expression is later used in the simulations of the  $G_2$  gauge Higgs model at infinitely large lattice gauge coupling where all gauge fields are frozen out. For  $O(N)$  non-linear sigma models also a cluster algorithm exists [106].

### 3.1.4 Pure gauge theories

In the case of pure Yang-Mills theory the standard Wilson lattice action [14],

$$S[\mathcal{U}] = \frac{\beta}{2N_c} \sum_{\square} \left( 2N_c - \text{tr}(\mathcal{U}_{\square} - \mathcal{U}_{\square}^{\dagger}) \right), \quad \beta = \frac{2N_c}{ag^2}, \quad (3.35)$$

is used. The sum extends over all plaquette variables  $\mathcal{U}_{\square}$ , the path ordered product of the fundamental link variables  $\mathcal{U}_{x,\mu}$  around a plaquette on the lattice. The ‘force’ is then given by

$$F_{x,\mu} = \frac{\beta}{2N_c} (\mathcal{U}_{x,\mu} R_{x,\mu} - R_{x,\mu}^{\dagger} \mathcal{U}_{x,\mu}^{\dagger}), \quad (3.36)$$

where the staple variable  $R_{x,\mu}$  is the sum of triple products of elementary link variables closing to a plaquette with the chosen link variable. According to [107], the cost for the local hybrid Monte-Carlo (IHMC) is about three times more than for a combined heat-bath and overrelaxation (HOR) scheme for the case of  $SU(N_c)$  gluodynamics. For a large range of Wilson couplings  $\beta$  in the simulations, an integration length of  $T = 0.75$  with a step size of  $\delta\tau = 0.25$  is optimal for minimal autocorrelation times and a small number of thermalization sweeps. Acceptance rates of more than 90% are reached. In the case of gauge theories coupled to fundamental or adjoint fermions the tree-level improved Symanzik gauge action [108, 109] is used, given as a special choice of constants  $c_i$  in the more general gauge action

$$S[\mathcal{U}] = \frac{\beta}{N_c} \left\{ c_0 \sum_{\square} \text{tr}(1 - \text{Re}\mathcal{U}_{\square}) + c_1 \sum_{\square\square} \text{tr}(1 - \text{Re}\mathcal{U}_{\square\square}) + c_2 \sum_{\square\square\square} \text{tr}(1 - \text{Re}\mathcal{U}_{\square\square\square}) \right\}. \quad (3.37)$$

Here,  $\mathcal{U}_{\square}$  stands for the plaquette variable,  $\mathcal{U}_{\square\square}$  for a rectangular path around two plaquettes and  $\mathcal{U}_{\square\square\square}$  for a shape around three plaquettes. Possible choices for the coefficients are  $c_0 = 1$  and  $c_1 = c_2 = 0$  for the Wilson action or  $c_0 = 1 - 8c_1$ ,  $c_1 = -1/2$ , and  $c_2 = 0$  for the tree-level improved Symanzik gauge action [110, 111]. The HMC ‘force’ is then given by (3.36), but with a different staple variable, obtained from (3.37) and (3.10).

### 3.1.5 The $G_2$ gauge Higgs model

The lattice action of the  $G_2$  gauge Higgs model is given by

$$S[\mathcal{U}, \Phi] = \beta \sum_{\square} \left( 1 - \frac{1}{7} \text{tr} \text{Re}\mathcal{U}_{\square} \right) - \kappa \sum_{x,\mu} \Phi_{x+\hat{\mu}}^{\dagger} \mathcal{U}_{x,\mu} \Phi_x, \quad \Phi_x^{\dagger} \cdot \Phi_x = 1, \quad (3.38)$$

where  $\Phi$  is a 7-component real scalar field. The HMC ‘force’ reads

$$F_{x,\mu} = \frac{\beta}{14} (\mathcal{U}_{x,\mu} R_{x,\mu} - R_{x,\mu}^{\dagger} \mathcal{U}_{x,\mu}^{\dagger}) + \kappa (\mathcal{U}_{x,\mu} \Phi_x) \Phi_{x+\mu}^{\dagger}, \quad G_x = \kappa \Phi_x \left( \sum_{y:x} \mathcal{U}_{xy} \Phi_y \right)^{\dagger}, \quad (3.39)$$

where the last sum extends over all nearest neighbours  $y$  of  $x$ . This leads to the equations of motion for the gauge and Higgs sector,

$$\dot{\mathfrak{P}}_{x,\mu} = F_{x,\mu} \Big|_{\mathfrak{g}_2}, \quad \dot{\mathfrak{Q}}_x = G_x \Big|_{\mathfrak{so}(7)}. \quad (3.40)$$

where  $\mathfrak{P}$  are the conjugate momenta to the link variables  $\mathcal{U}$  and  $\mathfrak{Q}$  are conjugate momenta to the  $SO(7)$  rotations  $\mathcal{O}$ .

## 3.2 The rHMC algorithm for fermions

For QCD and supersymmetric gauge theories the global version of the HMC algorithm is used together with a rational approximation for the inverse of the fermion matrix (rHMC) [112]. In the case of Dirac fermions the path integral is given by <sup>a</sup>

$$\mathcal{Z}_D = \int \mathcal{D}\Psi \mathcal{D}\bar{\Psi} \mathcal{D}\mathcal{U} \exp\{-S[\mathcal{U}] - \text{tr} \bar{\Psi} D[\mathcal{U}] \Psi\} = \mathcal{N} \int \mathcal{D}\mathcal{U} \det(D[\mathcal{U}]) \exp\{-S[\mathcal{U}]\}, \quad (3.41)$$

where  $D$  is the fermion operator. For Majorana fermions the integration over the fermionic variables yields the Pfaffian instead of the determinant of  $D$  (here  $\text{tr} \bar{\lambda} D[\mathcal{U}] \lambda = \text{tr} \lambda^\top (-C^{-1} D[\mathcal{U}]) \lambda$  is used)

$$\mathcal{Z}_M = \int \mathcal{D}\lambda \mathcal{D}\mathcal{U} \exp\{-S[\mathcal{U}] - \text{tr} \bar{\lambda} D[\mathcal{U}] \lambda\} = \mathcal{N} \int \mathcal{D}\mathcal{U} \text{Pf}(CD[\mathcal{U}]) \exp\{-S[\mathcal{U}]\}. \quad (3.42)$$

Up to a phase the Pfaffian is the square root of the determinant and  $C$  is the charge conjugation matrix. Therefore, in both cases the partition function can be written as

$$\mathcal{Z} = \mathcal{N} \int \mathcal{D}\mathcal{U} \text{sign}(D) \left| (\det M)^{\frac{1}{n}} \right| \exp\{-S[\mathcal{U}]\}, \quad (3.43)$$

where  $M = D^\dagger D$  is a Hermitian and positive operator. For Dirac fermions one has  $n = 2$  while for Majorana fermions  $n = 4$ . The sign-function can in general be a complex phase, leading to the fermion sign problem [113]. Standard Monte-Carlo techniques are only applicable if the probability measure is positive. Therefore, in the following discussion of the rHMC algorithm, it is assumed that  $\text{sign} D = 1$ . Introducing  $N_{\text{PF}}$  complex-valued pseudofermions  $\phi$  [114], one can write the partition function as

$$\mathcal{Z} = \int \mathcal{D}\mathcal{U} \mathcal{D}\phi \exp\{-S_B[\mathcal{U}, \phi]\} \quad \text{with} \quad S_B[\mathcal{U}, \phi] = S[\mathcal{U}] + \text{tr} \sum_{p=1}^{N_{\text{PF}}} \phi_p^\dagger M^{-q} \phi_p, \quad (3.44)$$

where  $S_B$  is the bosonic action and  $q$  is given by  $q = \frac{1}{nN_{\text{PF}}}$ . In the rHMC dynamics  $M^{-q}$  is replaced by a rational approximation according to

$$r(x) = x^{-q} \approx \alpha_0 + \sum_{r=1}^{N_R} \frac{\alpha_r}{x + \beta_r}. \quad (3.45)$$

For any rational number  $q$  the coefficients  $\alpha$  and  $\beta$  can be calculated with the Remez algorithm [115]. The numerical accuracy of the approximation in the interval  $x \in \{x_{\text{Min}}, x_{\text{Max}}\} = I$  depends on the order  $N_R$  of the used polynomial and the numerical accuracy of the coefficients  $\alpha$  and  $\beta$ . In the following  $r_S(x)$ ,  $S = \{I, \epsilon, q\}$  denotes a rational approximation of the function  $x^{-q}$  with  $\epsilon = \sup_{x \in I} \|r(x) - x^{-q}\|$ . In order to obtain an exact update algorithm, the bosonic action is written in the form

$$S_B[\mathcal{U}, \phi] = S[\mathcal{U}] + S_{\text{md}}(M) + S_{\text{acc}}(M) + S_{\text{rw}}(M), \quad (3.46)$$

where the different contributions are given by

$$\begin{aligned} S_{\text{md}}(M) &= \text{tr} \sum_{p=1}^{N_{\text{PF}}} \phi_p^\dagger r_{S_{\text{md}}}(M) \phi_p, & S_{\text{acc}}(M) &= \text{tr} \sum_{p=1}^{N_{\text{PF}}} \phi_p^\dagger (r_{S_{\text{acc}}}(M) - r_{S_{\text{md}}}(M)) \phi_p, \\ \text{and} \quad S_{\text{rw}}(M) &= \text{tr} \sum_{p=1}^{N_{\text{PF}}} \phi_p^\dagger (M^{-q} - r_{S_{\text{acc}}}(M)) \phi_p. \end{aligned} \quad (3.47)$$

---

<sup>a</sup>Below,  $\text{tr}$  denotes the integral over  $d$ -dimensional spacetime and the trace over all internal degrees of freedom.

---

**Algorithm 3** rHMC algorithm

---

**Require:** Configuration  $\mathcal{C}(\{\mathcal{U}\})$ ,  $N$  degrees of freedom, symplectic integrator  $I(\tau)$ , rational approximations  $r_{\mathcal{S}_{\text{pf}}}$ ,  $r_{\mathcal{S}_{\text{acc}}}$ ,  $r_{\mathcal{S}_{\text{md}}}$ ,  $N_{\text{PF}}$  pseudofermion fields  $\phi_i$

- 1: **for**  $i = 1$  **to**  $N$  **do**
- 2:   Draw momentum  $\mathfrak{P}_i$  Gaussian distributed
- 3: **end for**
- 4: **for**  $i = 1$  **to**  $N_{\text{PF}}$  **do**
- 5:   Draw complex vector  $\eta_i$  Gaussian distributed
- 6:   Calculate  $\phi_i = r_{\mathcal{S}_{\text{pf}}}\eta_i$
- 7: **end for**
- 8: **for**  $\tau = 0$  **to**  $t_{\text{HMC}}$  **step**  $\delta\tau$  **do**
- 9:   Integrate the equations of motion for  $\{\mathfrak{P}\}$  and  $\{\mathcal{U}\}$  with integrator  $I(\tau)$  and use the rational approximation  $r_{\mathcal{S}_{\text{md}}}$  for the inversion of the fermion matrix  $M$ .
- 10: **end for**
- 11: Accept the new configuration with probability  $p = \min(1, \exp\{H(\mathcal{C}) - H(\mathcal{C}')\})$  and use  $r_{\mathcal{S}_{\text{acc}}}$  for the inversion of the fermion matrix  $M$ .
- 12: **return** Configuration  $\mathcal{C}'(\{\mathcal{U}'\})$

---

The sum  $S[\mathcal{U}] + S_{\text{md}}(M)$  is used in the calculation of the HMC molecular dynamics, the sum  $S[\mathcal{U}] + S_{\text{md}}(M) + S_{\text{acc}}(M)$  in the Metropolis acceptance step of the HMC algorithm and the last term  $S_{\text{rw}}(M)$  in a reweighting step to assure an exact update algorithm. In practice, the reweighting step is not necessary since it is more efficient to choose  $r_{\mathcal{S}_{\text{acc}}}$  such that it approximates  $M^{-q}$  up to machine precision. For the generation of the pseudofermion fields from a Gaussian distributed vector the square root of  $M^q$  is needed, too. This is achieved by an approximation  $r_{\mathcal{S}_{\text{pf}}}(M) \approx M^{q/2}$ . To obtain an exact update algorithm, in this work the following choices are made,

$$r_{\mathcal{S}_{\text{pf}}}(M) = \{I \supseteq \Sigma(M), 10^{-16}, -q/2\} \quad \text{and} \quad r_{\mathcal{S}_{\text{acc}}}(M) = \{I \supseteq \Sigma(M), 10^{-16}, q\}, \quad (3.48)$$

where  $\Sigma(M) = \{\lambda_{\min}, \lambda_{\max}\}$  is the spectral range of the Hermitian operator  $M$ . In most of the simulations, an approximation for the pseudofermion and acceptance step approximation of degree  $N_{\text{R}} = 25$  is used in an interval  $I = \{10^{-7}, 10\}$ . The rHMC algorithm is shown as pseudocode in Alg. 3. The free parameters left to optimize the algorithm are the integration scheme used in the molecular dynamics and the degree and approximation range of the molecular dynamics rational approximation  $r_{\mathcal{S}_{\text{md}}}(M)$ . The inversions of the matrix  $M$  in the rational approximations are calculated with a multiple-mass conjugate gradient solver (MMCG) [116] which is able to compute all terms of (3.45) within a single inversion of the fermion matrix  $M$ .

### 3.2.1 Optimization of the rHMC algorithm

The efficiency of the rHMC algorithm depends crucially on the lowest eigenvalues, i.e. the condition number  $\kappa \approx \lambda_{\max}/\lambda_{\min}$ , of the Hermitian operator used in the rational approximation. In the left panel

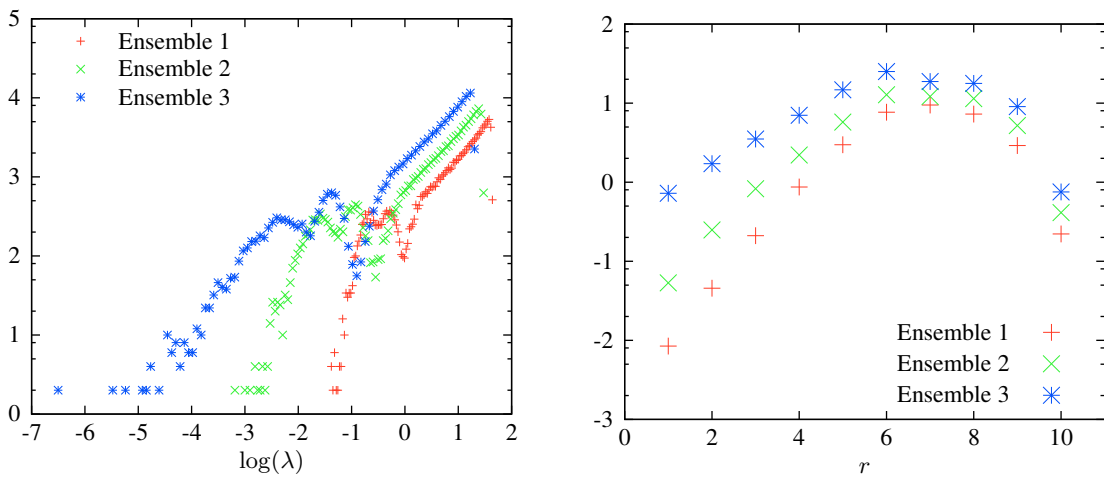


**Figure 3.3** *Left panel:* Histogram (absolute frequency, logarithmic) of the lowest eigenvalues of the Hermitian operator  $M$  for three different ensembles in the later discussed supersymmetric Yang-Mills theory. *Right panel:* Corresponding average force contribution from the  $r$ -th term in the rational approximation, sorted by increasing  $\beta_r$ .

of Fig 3.3 a histogram of the lowest eigenvalues of the operator  $M = D^\dagger D$  for three different ensembles is shown. The number of total inversion steps for a given precision  $\delta_{\max}$  (the inversion precision for the lowest mass, i.e. the lowest value of  $\beta_r$ ) in the MMCG solver increases significantly with decreasing values of the constants  $\beta_r$  in the rational approximation. Fortunately, the force contribution in the rHMC algorithm is for small constants also significantly lower than for larger constants (the reason is that  $\alpha_r$  decreases also with decreasing  $\beta_r$ ). Only in the case of very small eigenvalues, the force from these lowest eigenmodes becomes more important, see right panel of Fig. 3.3. This feature of the rHMC algorithm can now be used to optimize the algorithm with respect to computation time. Two different strategies are useful: The first is to integrate the terms with smaller  $\beta_r$  on a coarser time scale than the terms with larger  $\beta_r$ , i.e. larger force. The second is to increase the lower bound of the approximation interval, resulting in larger values of  $\beta_r$  and a possibly smaller degree of the rational function used for the molecular dynamics. This reduces the number of CG-steps for a given inversion precision  $\delta_{\max}$  significantly. Further optimization can be achieved by increasing the precision  $\delta_{\max}$  used for the inversion, leading also to a significantly reduced number of CG-steps. The best choice of course depends on the given problem and is in general a mixture of both strategies. Table 3.1 shows the used parameters for the three ensembles in Fig 3.3 and the resulting computation time and CG-steps. These parameters are a common choice used for most simulation results presented in this work. In the fourth column an example from a *realistic* simulation of  $G_2$ -QCD is shown. For all *test* ensembles, the force contribution from the bosonic action is much larger than the contribution from the fermion determinant. Therefore a two-time-scale integrator was used with a fourth order integrator for the bosonic action and a second-order integrator for the rational approximation of  $M$ . This setup, or the improved second-order integrator, is used for most of the simulations involving fermions. Further optimization used in this work involves even-odd preconditioning [117] as well as an exact computation of a few lowest eigenvalues in the MMCG solver. According to [118], the optimal number of pseudofermions is roughly given by the condition number of the fermion

	Ensemble 1	Ensemble 2	Ensemble 3	$G_2$ -QCD
Matrix dimension	1536	1536	1536	1835008
Degree $N_R r_{S_{\text{pf}}}, r_{S_{\text{acc}}} / r_{S_{\text{md}}}$	25 / 10	25 / 10	25 / 10	25 / 10
Power $q r_{S_{\text{pf}}} / r_{S_{\text{acc}}} / r_{S_{\text{md}}}$	$-\frac{1}{8} / \frac{1}{4} / \frac{1}{4}$	$-\frac{1}{8} / \frac{1}{4} / \frac{1}{4}$	$-\frac{1}{8} / \frac{1}{4} / \frac{1}{4}$	$-\frac{1}{4} / \frac{1}{2} / \frac{1}{2}$
Interval $I r_{S_{\text{pf}}}, r_{S_{\text{acc}}}$	$\{10^{-6}, 10\}$	$\{10^{-6}, 10\}$	$\{10^{-6}, 10\}$	$\{10^{-5}, 2000\}$
Interval $I r_{S_{\text{md}}}$	$\{10^{-3}, 10\}$	$\{10^{-3}, 10\}$	$\{10^{-3}, 10\}$	$\{10^{-4}, 2000\}$
Av. CG-steps / $\delta_{\text{max}} r_{S_{\text{pf}}}$	102 / $10^{-16}$	126 / $10^{-16}$	146 / $10^{-16}$	17270 / $10^{-16}$
Av. CG-steps / $\delta_{\text{max}} r_{S_{\text{acc}}}$	101 / $10^{-16}$	125 / $10^{-16}$	145 / $10^{-16}$	17020 / $10^{-16}$
Av. CG-steps / $\delta_{\text{max}} r_{S_{\text{md}}}$	46 / $10^{-2}$	61 / $10^{-2}$	82 / $10^{-2}$	2060 / $10^{-2}$
Total CG-steps / config	663	861	1111	116690
HMC acceptance	0.99	0.98	0.98	0.33

**Table 3.1** rHMC simulation parameters for three different *test* ensembles and a *realistic* ensemble ( $G_2$ -QCD, lattice  $16^4$ ,  $\beta = 1.00$ ,  $\mu = 1.00$ ). For the *test* ensembles the HMC parameters are  $t_{\text{HMC}} = 0.6$  and  $N_{\text{HMC}} = 10$  and a leap-frog integrator. For the  $G_2$ -QCD ensemble is  $t_{\text{HMC}} = 0.6$  and  $N_{\text{HMC}} = 20$  and an improved second-order integrator (2 force calculations per time step) is used. This ensemble represents the worst case considered in this work.

matrix,  $N_{\text{PF}}^{\text{opt}} \approx \frac{1}{n} \ln \kappa(M)$ . In the  $G_2$ -QCD simulations only one pseudofermion is used, while in the case of the investigated supersymmetric Yang-Mills theories more pseudofermions are favourable.

### 3.2.2 Fermionic correlation functions

The generating functional for  $n$ -point correlation functions of Majorana fermions  $\lambda$  is given by

$$Z[J] = \int \mathcal{D}U \mathcal{D}\lambda \exp(-S_{\text{B}} - S_{\text{F}} - \text{tr} J^{\text{T}} \lambda) \quad \text{with} \quad S_{\text{F}} = -\frac{1}{2} \text{tr} \lambda^{\text{T}} C^{-1} D \lambda = -\frac{1}{2} \text{tr} \lambda^{\text{T}} \tilde{D} \lambda. \quad (3.49)$$

With  $S_{\text{eff}} = S_{\text{B}} - \log \text{Pf}[\tilde{D}]$  the  $n$ -point correlation function is computed as

$$\langle \text{T} \lambda_{\alpha_1} \dots \lambda_{\alpha_n} \rangle = \left\langle \frac{\delta^n}{\delta J_{\alpha_1} \dots \delta J_{\alpha_n}} \frac{Z[J]}{Z[0]} \right\rangle_{J=0} = \left\langle \frac{\delta^n}{\delta J_{\alpha_1} \dots \delta J_{\alpha_n}} \exp\left(\frac{1}{2} \text{tr} J^{\text{T}} \tilde{\Delta} J\right) \right\rangle_{\text{eff}, J=0}, \quad (3.50)$$

where the indices  $\alpha$  and  $\beta$  are a short notation for spacetime, spinor, colour and flavour indices, i. e.  $\alpha = (x, i, a, n)$ , and  $\tilde{\Delta} = \tilde{D}^{-1}$  is the inverse fermion matrix, i.e. the propagator. Here,  $\langle \dots \rangle_{\text{eff}}$  denotes averaging with respect to  $e^{-S_{\text{eff}}}$ . The two-point function reads

$$\langle \text{T} \lambda_{\alpha_1} \lambda_{\alpha_2} \rangle = \left\langle \tilde{\Delta}_{\alpha_1 \alpha_2} \right\rangle_{\text{eff}}, \quad (3.51)$$

while the four-point function is given by

$$\begin{aligned} \langle \text{T} \lambda_{\alpha_1} \lambda_{\alpha_2} \lambda_{\alpha_3} \lambda_{\alpha_4} \rangle &= \left\langle \overbrace{\lambda_{\alpha_1} \lambda_{\alpha_2} \lambda_{\alpha_3} \lambda_{\alpha_4}} + \overbrace{\lambda_{\alpha_1} \lambda_{\alpha_2} \lambda_{\alpha_3} \lambda_{\alpha_4}} + \overbrace{\lambda_{\alpha_1} \lambda_{\alpha_2} \lambda_{\alpha_3} \lambda_{\alpha_4}} \right\rangle \\ &= \left\langle \tilde{\Delta}_{\alpha_1 \alpha_2} \tilde{\Delta}_{\alpha_3 \alpha_4} + \tilde{\Delta}_{\alpha_1 \alpha_4} \tilde{\Delta}_{\alpha_2 \alpha_3} - \tilde{\Delta}_{\alpha_1 \alpha_3} \tilde{\Delta}_{\alpha_2 \alpha_4} \right\rangle_{\text{eff}}. \end{aligned} \quad (3.52)$$

To compute masses of particles, correlation functions of operators like  $O_{\alpha,\beta}(x) = \lambda_{\alpha,x}\lambda_{\beta,x}$  are needed. According to (3.52), they are given by

$$C_{\alpha,\beta,\gamma,\delta}(x, y) = \langle O_{\alpha,\beta}(x)O_{\gamma,\delta}(y) \rangle = \left\langle \tilde{\Delta}_{\alpha\beta}^{xx}\tilde{\Delta}_{\gamma\delta}^{yy} + \tilde{\Delta}_{\alpha\delta}^{xy}\tilde{\Delta}_{\beta\gamma}^{xy} - \tilde{\Delta}_{\alpha\gamma}^{xy}\tilde{\Delta}_{\beta\delta}^{xy} \right\rangle_{\text{eff}} \quad (3.53)$$

A graphical representation of the four-point correlation function is shown in Fig. 3.4. For the com-

$$C_{\alpha,\beta,\gamma,\delta}(x, y) = \left\langle \begin{array}{c} \text{Diagram 1: Disconnected part} \\ \text{Diagram 2: Connected part} \\ \text{Diagram 3: Connected part} \end{array} \right\rangle_{\text{eff}}$$

**Figure 3.4** The fermionic four-point correlation function consists of a disconnected part (first diagram) and a connected contribution (last two diagrams).

putation of the connected part of the correlation function, the fermion matrix is inverted on a point-like *source* in space and time at a randomly chosen lattice point  $y$ , leading to the point-to-all propagator. Here,  $N_c \times N_s$  (number of colours times dimension of the representation of the Clifford algebra) inversions of the fermion matrix with the CG solver have to be made. To improve the overlap with the vacuum state, Jacobi smearing for the *source* and *sink* can be applied [119, 120]. The disconnected diagrams, and for instance observables like the chiral condensate or the quark number density, are calculated with the stochastic estimator technique (SET) [121, 122]. Here every element of the fermion propagator is calculated as an ensemble average over a noisy estimator  $\eta$ ,

$$\tilde{\Delta}_{ij} = \lim_{N_{\text{est}} \rightarrow \infty} \left\langle \eta_j^\dagger \chi_i \right\rangle \quad \text{with} \quad \chi = \tilde{\Delta} \eta \quad \text{and} \quad \lim_{N_{\text{est}} \rightarrow \infty} \left\langle \eta_i^\dagger \eta_j \right\rangle = \delta_{ij}. \quad (3.54)$$

In practice, the ensemble average is built over a finite number of  $N_{\text{est}}$  noisy estimators, where the *source*  $\eta$  is given by Gaussian or  $\mathbb{Z}(2)$  noise, satisfying the last equation in (3.54). The *sink* is again calculated with a CG solver, making a total of  $N_{\text{est}}$  matrix inversions to obtain an estimator for every matrix element of the propagator. In the case of local lattice averaged observables like condensates, a number of  $N_{\text{est}} \approx 10$  estimators is sufficient to get a reliable result. For the disconnected part of four-point correlation functions more estimators are necessary.

### 3.3 Conclusions

In the present chapter Monte-Carlo algorithms used to simulate pure gauge theories, as well as gauge theories coupled to fundamental and adjoint fermions, have been discussed. The simulations, presented in the next chapters, have been carried out on the clusters Doppler and Omega at the TPI in Jena as well as on the LOEWE cluster at the Center for Scientific Computing in Frankfurt. To obtain the results, in total more than 20 million CPU hours were needed, mostly for the simulations of  $G_2$ -QCD and supersymmetric gauge theories at the LOEWE cluster.

# 4 Exceptional confinement

Although known for more than 30 years, the confinement problem is one of the most challenging and still unsolved problems in particle physics [123]. In experiments quarks and gluons do not show up as asymptotic states of strong interaction. Only colourless states, colour singlets, can be observed at low temperatures. The theory of strong interaction is quantumchromodynamics (QCD), given by the continuum action in Minkowski spacetime,

$$S[A, \psi] = \int d^4x \left( -\frac{1}{4} \text{tr} F_{\mu\nu} F^{\mu\nu} + \bar{\psi} (i \not{D} + m) \psi \right). \quad (4.1)$$

The microscopic degrees of freedom are the 8 massless gluons  $A_\mu$  in the adjoint representation of  $SU(3)$  and 6 flavours of massive quarks  $\Psi$  in the fundamental representation of  $SU(3)$ . At low temperatures and densities these constituents are confined in mesons, baryons and glueballs. It is believed that the confining mechanism is already a property of pure *gluodynamics*, described by the Yang-Mills action

$$S_{\text{YM}}[A] = -\frac{1}{4} \int d^4x \text{tr} F_{\mu\nu} F^{\mu\nu}. \quad (4.2)$$

In the following not only Yang-Mills theories with gauge group  $SU(3)$  are discussed, but also with different gauge groups  $\mathcal{G}$  at finite temperature. For the Euclidean theory, temperature  $T$  is introduced via periodic boundary conditions for the gauge fields in temporal direction. The Yang-Mills action is then invariant under local gauge transformations

$$A_\mu \mapsto \Omega A_\mu \Omega^{-1} - \frac{1}{g} (\partial_\mu \Omega) \Omega^{-1}, \quad \Omega \in \mathcal{G}, \quad (4.3)$$

as well as under global centre transformations arising from the twisted boundary conditions of the gauge fields on a torus [124]. For a gauge group with non-trivial centre the trace of the Polyakov loop in representation  $\mathcal{R}$

$$P_{\mathcal{R}}(\vec{x}) = \text{tr}_{\mathcal{R}} \mathcal{P}(\vec{x}), \quad \mathcal{P}(\vec{x}) = \frac{1}{N_c} \left( \exp i \int_0^{\beta_T} A_0(\tau, \vec{x}) d\tau \right), \quad \beta_T = \frac{1}{T}, \quad (4.4)$$

transforms under *centre transformations* like  $P_{\mathcal{R}}(\vec{x}) \mapsto z^k P_{\mathcal{R}}(\vec{x})$ , where  $z \in \mathcal{Z}(\mathcal{G})$  is an element of the centre of the gauge group and  $k$  is the  $N$ -ality of the representation  $\mathcal{R}$ . In a pure gauge theory the only dynamical degrees of freedom are gluons in the adjoint centre-blind representation. Therefore, the Polyakov loop in any representation with non-zero  $N$ -ality is an order parameter for the spontaneous breaking of centre symmetry. On the other hand the vacuum expectation value of the Polyakov loop is related to the difference in free energy  $F_{\mathcal{R}}$  due to an infinitely heavy test quark in the gluonic bath,

$$\langle P_{\mathcal{R}} \rangle \propto e^{-\beta_T F_{\mathcal{R}}}. \quad (4.5)$$

In a confined phase the free energy of a test quark is infinite, while it takes a finite value in the deconfined phase. Consequently, in the confined phase centre symmetry is unbroken, while it is spontaneously

group $\mathcal{G}$	$A_r$	$B_r$	$C_r$	$D_r, r \text{ even}$	$D_r, r \text{ odd}$	$E_6$	$E_7$	$E_8$	$F_4$	$G_2$
centre $\mathcal{Z}$	$\mathbb{Z}(r+1)$	$\mathbb{Z}(2)$	$\mathbb{Z}(2)$	$\mathbb{Z}(2) \times \mathbb{Z}(2)$	$\mathbb{Z}(4)$	$\mathbb{Z}(3)$	$\mathbb{Z}(2)$	$\mathbb{1}$	$\mathbb{1}$	$\mathbb{1}$

**Table 4.1** Centres  $\mathcal{Z}$  of simple Lie groups.

broken in the deconfined phase. The Polyakov loop in every representation with non-zero N-ality is an order parameter for the transition from the confined to the unconfined phase, such that  $\langle P_{\mathcal{R}} \rangle \neq 0$  in the unconfined high-temperature phase and  $\langle P_{\mathcal{R}} \rangle = 0$  in the confined low-temperature phase. Below the critical temperature  $\mathcal{P}(\vec{x})$  is uniformly distributed over the group manifold. Above the critical temperature it lies in the neighborhood of a centre element. On a microscopic scale confinement means that the charges of test quarks in representations with non-zero N-ality cannot be screened and the inter-quark potential is linearly rising up to arbitrary long distances. In representations with zero N-ality, as for example the colour singlet or adjoint representation, the charges can be screened by gluons. At some distance, when the energy stored in the flux tube between the test charges is large enough to pop gluons out of the vacuum, the potential will become flat.

With matter in the fundamental representation, as for example QCD, the centre symmetry is *explicitly broken*. For all temperatures  $P_{\mathcal{R}}$  has a non-zero expectation value and points in the direction of a particular centre element. Thus in the strict sense the Polyakov loop ceases to be an order parameter for the centre symmetry. On a microscopic scale this is attributed to the breaking of the string, connecting a static ‘quark anti-quark pair’, when trying to separate the static charges [123]. It breaks via the spontaneous creation of dynamical quark anti-quark pairs which in turn screen the individual static charges. In every representation  $\mathcal{R}$  of the gauge group the potential becomes flat at larger asymptotic distances. But it is still expected that QCD confines colour in the sense that charges of test quarks are screened by dynamical light quarks. This also means that below the string breaking distance the inter-quark potential is still linearly rising.

Although in pure gauge theories confinement and deconfinement are related to the spontaneous breaking of centre symmetry, colour confinement survives if the centre symmetry is explicitly broken. Thus, to clarify the relevance of the centre symmetry for confinement, it suggests itself to compare confinement in gauge groups with different centres. From Tab. 4.1, taken from [125], one reads off the centres of all simple Lie groups. For gauge groups with *trivial centres* like  $G_2$ ,  $F_4$  or  $E_8$ , the Polyakov loop ceases to be an order parameter even in the absence of dynamical matter, since the strings connecting external charges can break via the spontaneous creation of dynamical gluons [58]. Again, on a microscopic scale confinement is seen as a linearly rising inter-quark potential at intermediate distances and string breaking in every representation at larger distances. Similar to QCD, one characterizes confinement as the absence of free colour charges in the physical spectrum [104, 126]. In this sense pure gauge theories with a trivial centre share an important feature with QCD and may give interesting insights into the confinement mechanism.

In this chapter it is confirmed that  $G_2$  Yang-Mills theory deconfines at a first order phase transition and confinement for different exceptional gauge groups in three spacetime dimensions is investigated.

	$G_2$	$SU(3)$	
quark / antiquark	$(7) / (\bar{7})$	$(3) / (\bar{3})$	fermion
gluon	$(14)$	$(8)$	boson
meson / diquark	$(7) \otimes (\bar{7}) / (7) \otimes (7)$	$(3) \otimes (\bar{3}) / -$	boson
(fermionic) baryon	$(7) \otimes (\bar{7}) \otimes (7)$	$(3) \otimes (\bar{3}) \otimes (3)$	fermion
glueballs	$(14) \otimes (14), (14) \otimes (14) \otimes (14)$	$(8) \otimes (8), (8) \otimes (8) \otimes (8)$	boson
hybrid	$(7) \otimes (14) \otimes (14) \otimes (14)$	-	fermion

**Table 4.2** Fundamental particles and colour singlet bound states in  $G_2$  compared to  $SU(3)$ .

## 4.1 The deconfinement transition in $G_2$ Yang-Mills

The smallest simple and simply connected Lie group with a trivial centre is the 14 dimensional exceptional Lie group  $G_2$ . This is one reason why  $G_2$  gauge theory has been investigated by the group in Bern in a series of papers [57, 58, 127]. Quarks and anti-quarks transform under the fundamental 7-dimensional representation. All representations of  $G_2$  are real, and therefore it cannot be distinguished between infinitely heavy test quarks or anti-quarks by their transformation behaviour under the gauge group. Both have the same colour charge. This is in contrast to  $SU(N_c)$  gauge theories where quarks and anti-quarks transform under the fundamental and anti-fundamental representation. For  $N_c > 2$  these representations are inequivalent, which has important consequences for the lattice formulation of QCD based on an arbitrary gauge group. This important difference between  $G_2$  and  $SU(3)$  gauge theories will be discussed later in chapter 7. Since the centre of  $G_2$  is *trivial*, these fundamental charges can be screened by at least three gluons in the adjoint 14-dimensional representation,

$$(7) \otimes (14) \otimes (14) \otimes (14) = (1) \oplus \dots \quad (4.6)$$

From the reduction of tensor products (2.14) into irreducible representations the colour singlet bound states that are the possibly dominant degrees of freedom in the confined phase can be taken. Tab. 4.2 compares fundamental particles and possible colour singlet bound states of  $G_2$  and  $SU(3)$  gauge theory. In both cases the spectrum should contain fermionic baryons, bosonic mesons and glueballs. Additionally,  $G_2$  gauge theory has *diquarks* and various bound states of gluons and quarks which are not present in  $SU(3)$ .

A very common argument for the order of a phase transition is the size of the broken subgroup of the underlying symmetry. According to Elitzur's theorem [128], a local symmetry cannot spontaneously be broken and therefore the size of the global symmetry group is important. For  $SU(2)$  gluodynamics with centre  $\mathbb{Z}(2)$  one finds a second-order phase transition, while  $SU(3)$  with centre  $\mathbb{Z}(3)$  possesses a first order deconfinement phase transition. Although there is no symmetry reason for a deconfinement phase transition in  $G_2$  gluodynamics, it has been conjectured that a first order deconfinement transition without order parameter exists [58, 129]. Arguments for a first order transition are the large mismatch of degrees of freedom between the confinement phase and the deconfinement phase. In this sense the size of the underlying Lie algebra matters. In the following the deconfinement phase transition is investigated on

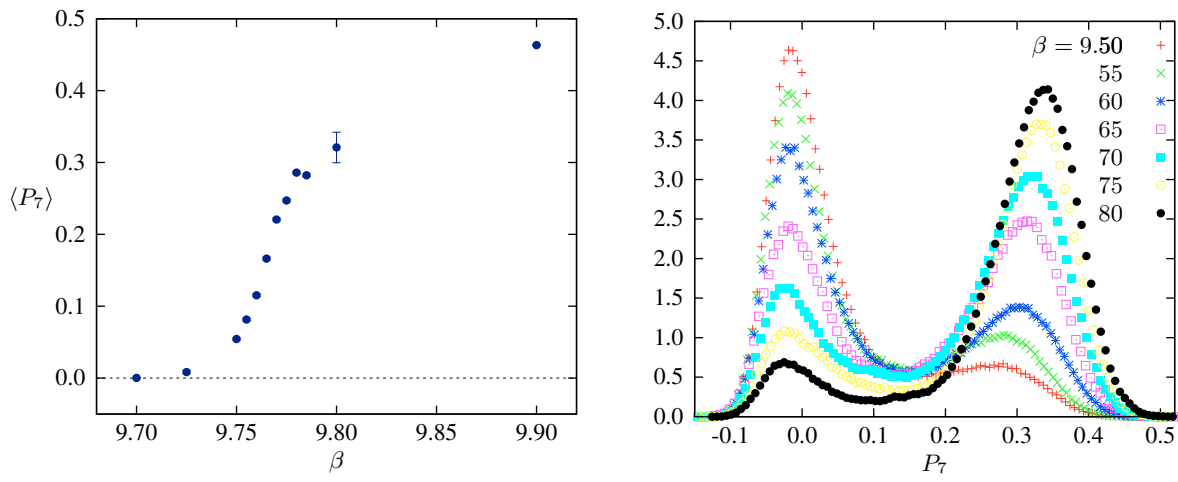


**Figure 4.1** *Left panel:* Polyakov loop expectation values at the finite temperature confinement-deconfinement transition on a  $16^3 \times 6$  lattice. *Right panel:* Histograms of the Polyakov loop in the vicinity of the phase transition point  $\beta_{\text{crit}} = 9.765$ , pointing to a first order deconfinement transition.

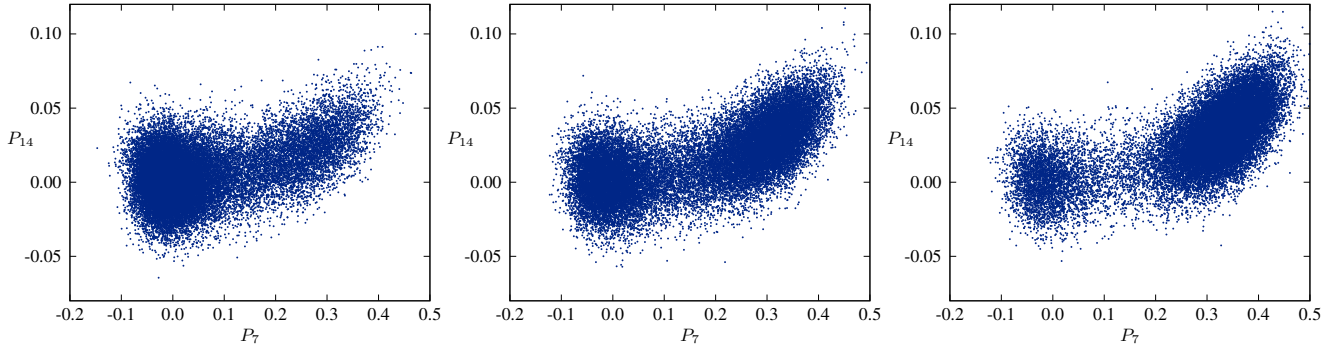


**Figure 4.2** Scatter plots of the Polyakov loop in the fundamental region of  $G_2$  at  $\beta = 9.750$ ,  $\beta = 9.765$  and  $\beta = 9.785$ .

the lattice.

The simulations have been performed with the described IHMC algorithm and the standard Wilson gauge action (3.35). The Polyakov loop serves as *approximate order parameter*, separating the confined from the unconfined phase with a rapid change at the transition or crossover. This rapid change is depicted in Fig. 4.1 (left panel), which shows the expectation value of  $P$  for  $G_2$  gluodynamics as a function of the inverse gauge coupling  $\beta = 7/g^2$ . Fig. 4.1 (right panel) shows histograms of the Polyakov loop in the vicinity of the critical coupling  $\beta_c$ . The double peak structure points to a first order transition, which is in agreement with earlier results in [58, 129]. In chapter 6 also a finite size scaling analysis is performed, which confirms the result. Fig. 4.2 shows the distribution of the Polyakov loop for three different temperatures in the fundamental region of  $G_2$ . For a temperature below the phase transition temperature, the Polyakov loop is almost distributed uniformly according to the Haar measure of  $G_2$  (left panel). At the phase transition temperature the double peak structure is clearly visible (centre panel) and above the phase transition the Polyakov loop tends towards the unit element of the gauge group (right panel).

group	$SU(2)$	$SU(3)$	$SU(4)$	$G_2$	$F_4$	$E_6$	$E_7$	$Sp(2)$	$Sp(3)$
Cartan name	$A(1)$	$A(2)$	$A(3)$	$G_2$	$F_4$	$E_6$	$E_7$	$C(2)$	$C(3)$
rank	1	2	3	2	4	6	7	2	3
dimension algebra	3	8	15	14	52	78	133	10	21
dimension def. rep.	2	3	4	7	26	27	56	4	6
centre	$\mathbb{Z}(2)$	$\mathbb{Z}(3)$	$\mathbb{Z}(4)$	$\mathbb{1}$	$\mathbb{1}$	$\mathbb{Z}(3)$	$\mathbb{Z}(2)$	$\mathbb{Z}(2)$	$\mathbb{Z}(2)$
order phase transition $3d$	2	2	?	?	1	1	?	2	1
order phase transition $4d$	2	1	1	1	1	1	1	1	1

**Table 4.3** The rank, dimension of the algebra, dimension of the defining representation, the centre group and the order of the deconfinement phase transition for different Lie groups are shown.

## 4.2 The deconfinement transition in three dimensions

Since in chapter 5 gluodynamics in three dimensions at zero temperature is studied, the finite temperature phase transition in three dimensions is also investigated and compared to various other gauge groups. Table 4.3 compares the rank, the dimension of the defining and adjoint representation as well as the centre of the gauge groups  $SU(2)$ ,  $SU(3)$ ,  $SU(4)$ ,  $G_2$ ,  $F_4$ ,  $E_6$ ,  $Sp(2)$  and  $Sp(3)$ . In the last two lines the order of the phase transition in three and four spacetime dimensions is shown, see also [127, 130]. While in four dimensions all gauge theories except  $SU(2)$  Yang-Mills possess a first order phase transition, the situation in three dimensions is quite different. The transition for  $SU(2)$ ,  $SU(3)$  and  $Sp(2)$  gauge theory is of second order. In the case of  $SU(4)$  the transition is of second order or a very weak first order phase transition while for larger groups the transition is first order. Although the centre of  $G_2$  is much smaller than the centre of  $SU(4)$ , the groups are of comparable size, i.e. dimension 14 for  $G_2$  and dimension 15 for  $SU(4)$ . If the phase transition for  $G_2$  would be first order, this may be a hint that the transition of  $SU(4)$  is also first order. In Fig. 4.3 (left panel) the plaquette density  $\langle \mathcal{O}_P \rangle$  for the gauge groups  $SU(2)$ ,  $SU(3)$ ,  $G_2$ ,  $SU(4)$ ,  $F_4$  and  $E_6$  on a  $24^2 \times 6$  lattice are compared as a function of  $\beta/\beta^*$ , where  $\beta^*$  is the critical coupling at the phase transition point. Although the plaquette density is not a renormalization group invariant quantity and therefore the values between different groups are not directly comparable, an ordering of the plaquette value with the size of the algebra at the phase transition point is seen. From the plaquette variable it is hard to distinguish between  $G_2$  and  $SU(4)$  gauge theory. In Fig. 4.3 (right panel) the Polyakov loop in the defining representation is shown as a function of  $\beta$  normalized with the critical coupling. For  $SU(2)$  and  $SU(3)$  the transition is second order. In the case of  $F_4$  and  $E_6$  gauge theory a jump of the Polyakov loop points to a first order phase transition. Again,  $G_2$  and  $SU(4)$  gauge theory are comparable. Finally, in Fig. 4.4 the Polyakov loop distribution in the vicinity of the phase transition point is shown for the gauge group  $G_2$ ,  $F_4$  and  $E_6$  in the fundamental region. In the case of  $F_4$  and  $E_6$  the coexistence of confined and deconfined phase clearly point to a first order phase transition. For  $E_6$  also the  $\mathbb{Z}(3)$  centre symmetry in the chosen projection into the fundamental region is visible. In the case of  $G_2$  the situation is less clear. In order to decide whether the transition is first or second order, simulations on larger lattices as well as a finite size scaling analysis have to be performed.

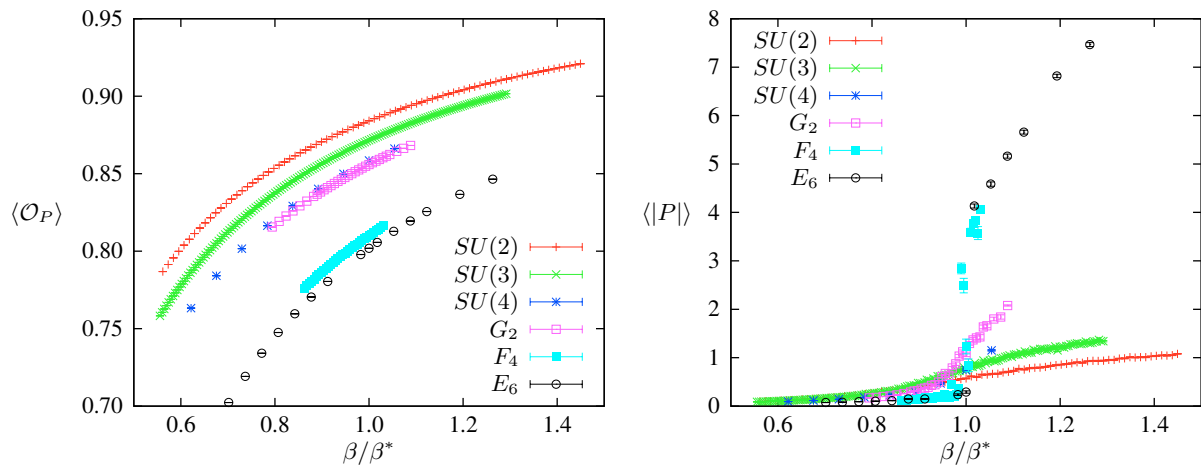


**Figure 4.3** Plaquette and Polyakov loop for different gauge groups in three dimensions on a  $24^2 \times 6$  lattice.

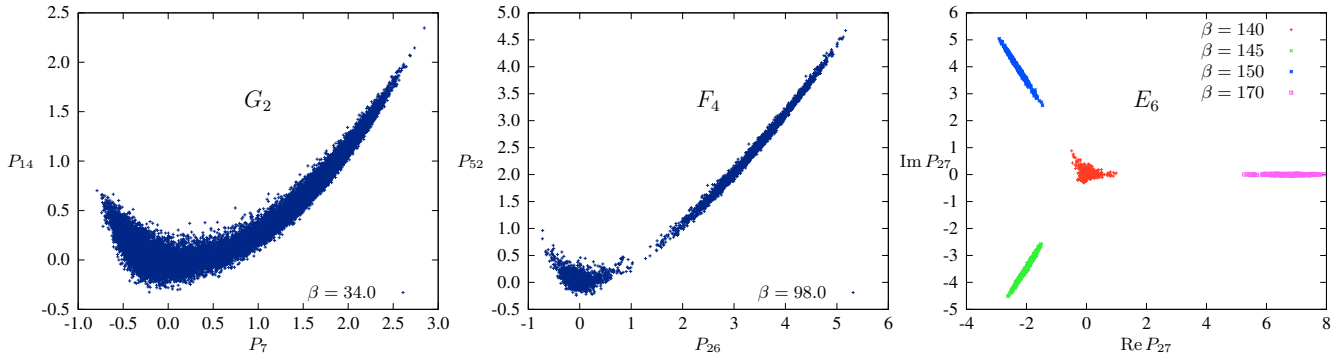


**Figure 4.4** Scatter plot of the Polyakov loop in the fundamental domain near the phase transition point.

## 4.3 Conclusions

In the present chapter the deconfinement phase transition of  $G_2$  Yang-Mills theory has been studied. In agreement with earlier results, a first order phase transition without order parameter from the low temperature confined to the high temperature deconfined phase has been found. Compared to  $SU(3)$  gauge theory, where the deconfinement phase transition coincides with the breaking of a global  $\mathbb{Z}(3)$  centre symmetry,  $G_2$  gauge theory possesses a *strong* first order phase transition, although there is no global symmetry that is broken. This suggests, that indeed not the size of the centre but the dimension of the algebra, and therefore the mismatch of degrees of freedom between both phases, is important for the order of the phase transition. This suggestion is also confirmed by results in three spacetime dimensions, where  $SU(3)$  gauge theory possesses clearly a second order phase transition, while the order of the phase transition for  $G_2$  is still unclear. This is very similar to the situation in  $SU(4)$  gauge theory with algebra dimension 15 (compared to 14 for  $G_2$ ), where there is still an ongoing dispute whether the transition is of first or second order [131, 132]. To answer this question, it may be helpful to further investigate  $G_2$  gauge theory in three dimensions and its relation to generalized continuous and discrete spin models [78, 133–135]. In the next chapter  $G_2$  Yang-Mills theory in three and four spacetime dimensions at zero temperature is explored, to confirm the picture of exceptional confinement given here.

# 5 Exceptional gluodynamics at zero temperature

As already pointed out, confinement in  $G_2$  gauge theory refers to a linearly rising inter-quark potential at intermediate scales and string breaking at larger asymptotic scales. In this chapter  $G_2$  gauge theory in three and four spacetime dimensions at zero temperature is investigated. First, Casimir scaling and string breaking in  $SU(N_c)$  gauge theories are reviewed as well as predictions from bosonic string theory. Then algorithmic details and the computation of the inter-quark potential on the lattice are explained. In three and four spacetime dimensions the inter-quark potential in different representations of the gauge group is computed, to confirm the assumptions made about exceptional confinement. Finally, the results are compared to analytical results, obtained from the dynamic of bosonic strings [136–139] as well as to calculations in three-dimensional Yang-Mills theory based on a Hamiltonian approach [140]. The results presented in this chapter have been published in [81].

In QCD quarks and anti-quarks can only be screened by particles with non-vanishing 3-ality, especially not by gluons. Thus, in zero-temperature *gluodynamics* the potential energy for two static colour charges is linearly rising up to arbitrary large separations of the charges. The potentials for charges in a representation  $\mathcal{R}$  can be extracted from the two-point correlator of Polyakov loops

$$\langle P_{\mathcal{R}}(0)P_{\mathcal{R}}(R) \rangle = e^{-\beta T V_{\mathcal{R}}(R)}, \quad (5.1)$$

or the expectation values of Wilson loops with temporal extent  $T$  according to

$$\langle W_{\mathcal{R}}(R, T) \rangle = e^{\kappa_{\mathcal{R}} - T V_{\mathcal{R}}(R)}. \quad (5.2)$$

With dynamical quarks the string should break at a characteristic length  $r_b$ , due to the spontaneous creation of quark anti-quark pairs from the energy stored in the flux tube connecting the static charges. However, for intermediate separations  $r < r_b$ , the string cannot break since there is not enough energy stored in the flux tube.

For *pure gauge theories* the following qualitative behaviour of the static potential is expected: At short distances perturbation theory applies and the interaction is dominated by gluon exchange, giving rise to a Coulomb-like potential  $V \sim -\alpha/r$ , with the strength  $\alpha$  being proportional to the value  $\mathcal{C}_{\mathcal{R}}$  of the quadratic Casimir operator in the given representation  $\mathcal{R}$  of the charges [141]. At intermediate distances, from the onset of confinement to the onset of colour screening at  $r_b$ , the potential is expected to be linearly rising, as  $V \sim \sigma r$ , and the corresponding string tension is again proportional to the quadratic Casimir [123]. At asymptotic distance scales (partial) screening sets in, such that the string tension typically decreases and only depends on the  $N$ -ality of the representation. In particular, for centre-blind colour charges or gauge groups without centre, the potential flattens. The characteristic length  $r_b$  where the intermediate confinement regime turns into the asymptotic screening regime is determined by the masses of the debris left after string breaking. The Casimir scaling hypothesis, according to which the

string tension at intermediate scales is proportional to the quadratic Casimir of the representation [142], is exact for two dimensional continuum and lattice gauge theories, and dimensional reduction arguments support that it also holds in higher dimensions. Within the Hamiltonian approach to Yang-Mills theories in  $2 + 1$  dimensions, the following prediction for the string tensions has been derived [143],

$$\sigma_{\mathcal{R}} = \frac{g^4}{4\pi} \frac{C_{14} C_{\mathcal{R}}}{12^2}, \quad (5.3)$$

with a recent refinement in [140].<sup>a</sup> These analytical results directly predict Casimir scaling in three dimensions. In four dimensions Casimir scaling can be explained via Gaussian field correlators [144]. For *pure*  $SU(2)$  and  $SU(3)$  gauge theories in three and four dimensions there is now conclusive numerical evidence for *Casimir scaling* from Monte-Carlo simulations, for  $SU(2)$  in three dimensions [142, 145] and in four dimensions [146–149] as well as for  $SU(3)$  in four dimensions at finite temperature [150] and zero temperature [151–154]. In particular, the simulations for  $SU(3)$  gluodynamics in [153] confirm Casimir scaling within 5% for separations up to 1 fm of static charges in representations with Casimirs (normalized by the Casimir of (3)) up to 7. *String breaking* for charges in the adjoint representation has been found in several simulations: In three dimensional  $SU(2)$  gluodynamics with improved action and different operators in [155, 156] and in four dimensional  $SU(2)$  gluodynamics in [157] with the help of a variational approach involving string and glueball operators. For a critical discussion of the various approaches see [158], where string breaking in a simple setting but with an improved version of the Lüscher-Weisz algorithm has been analyzed and compared with less sophisticated approaches. There is a number of works in which a violation of Casimir scaling on intermediate scales have been reported. For example, it has been claimed that in four dimensional  $SU(N_c)$  gluodynamics with larger  $N \in \{4, 6\}$ , the numerical data favor the sin-formula, as suggested by supersymmetry, in place of the Casimir scaling formula [159]. The differences between the Casimir scaling law and sin-formula are tiny, and it is very difficult to discriminate between the two predictions in numerical simulations. Indeed, in [160] agreement with Casimir scaling and sin-formula in four dimensions and disagreement in three dimensions has been claimed. In addition, the high precision simulations based on the Lüscher-Weisz algorithm in [158, 161] point to a violation of the Casimir scaling law in three dimensional  $SU(2)$  gluodynamics. In a very recent paper Pepe and Wiese [162] reanalyzed the static potential for  $SU(2)$  gluodynamics in three dimensions with the help of the Lüscher-Weisz algorithm and substantiated Casimir scaling violation at intermediate scales, while confirming 2-ality scaling at asymptotic scales.

For *gauge theories with matter* a similar qualitative behavior is expected: A Coulomb-like potential at short distances, Casimir scaling at intermediate distances and (partial) screening at asymptotic distances. The string tension at asymptotic scales depends both on the  $N$ -alities of the static colour charges and of the dynamical matter. In particular, if dynamical quarks or scalars can form centre blind composites with the static charges, then the potential is expected to flatten at large separations. To see any kind of screening between fundamental charges requires a full QCD simulation with sea quarks, which is demanding. Thus the earlier works dealt with gauge theories with scalars in the fundamental representation. For example, in [163] clear numerical evidence for string breaking in the three dimensional  $SU(2)$

---

<sup>a</sup>The factor  $1/12^2$  in the formula given here arises from a different normalization of the quadratic Casimir operator.

Yang-Mills-Higgs model via a mixing analysis of string and two-meson operators has been presented. Probably the first observation of hadronic string breaking in simulations of QCD<sub>3</sub> with two flavours of dynamical staggered fermions using only Wilson loops has been reported in [164, 165]. Despite extensive searches for colour screening in four dimensional gauge theories with dynamical fermions, the results are still preliminary at best. First indications for string breaking in two-flavour QCD, albeit only at temperatures close to or above the critical deconfinement temperature, have been reported in [166]. More recently Bali et al. used sophisticated methods (e.g. optimized smearing, improved action, stochastic estimator techniques, hopping parameter acceleration) to resolve string breaking in two-flavour QCD at a value of the lattice spacing  $a^{-1} \approx 2.37$  GeV and of the sea quark mass slightly below  $m_s$  [167]. By extrapolation they estimate that in real QCD with light quarks the string breaking should happen at  $r_b \approx 1.13$  fm.

To measure the static potential and study string breaking three approaches have been used: correlations of Polyakov loops at finite temperature, variational ansatz using two types of operators (for the string-like states and for the broken string state) and Wilson loops. Most results on Casimir scaling and string breaking have been obtained with the first two methods. This is attributed to the small overlap of the Wilson loops with the broken-string state. To measure Polyakov or Wilson loop correlators for charges in higher representations or to see screening at asymptotic scales, dealing with extremely small signals down to  $10^{-40}$  is required. In order to measure such small signals, existing algorithms have to be improved considerably or/and improved versions of the Lüscher-Weisz multistep algorithm are needed.

## 5.1 Exponential error reduction for Wilson loops

In the confining phase the rectangular Wilson loop scales as

$$W(L, T) \propto \exp(-\sigma L \cdot T). \quad (5.4)$$

In order to estimate the string tension  $\sigma$ , areas  $LT$  ranging from 0 up to 100 are probed and thus  $W$  will vary by approximately 40 orders of magnitude. A brute force approach, where statistical errors for the expectation value of Wilson or Polyakov loops decrease with the inverse square root of the number of statistically independent configurations by just increasing the number of generated configurations, will miserably fail. Nevertheless, convincing results on  $G_2$  Casimir scaling on intermediate scales for representations with relative Casimirs  $C'_R \leq 5$  have been obtained in [126] with a variant of the smearing procedure. When reproducing these results, it was found that the calculated string tensions depend sensitively on the smearing parameter [105]<sup>b</sup>. Thus, to obtain accurate and reliable numbers for the static potential and to detect string breaking, the multi-step Lüscher-Weisz algorithm with exponential error reduction for the time transporters of the Wilson loops was implemented [168]. With this method the absolute errors of Wilson lines decrease exponentially with the temporal extent  $T$  of the line. Since details of the implementation for different representations depend on the gauge group, the algorithm has to be reviewed in detail. The expectation value  $W_{\mathcal{R}}$  of a Wilson loop  $\mathcal{W}$  in a representation  $\mathcal{R}$  is the

---

<sup>b</sup>This is not the case for the ratios of string tensions.

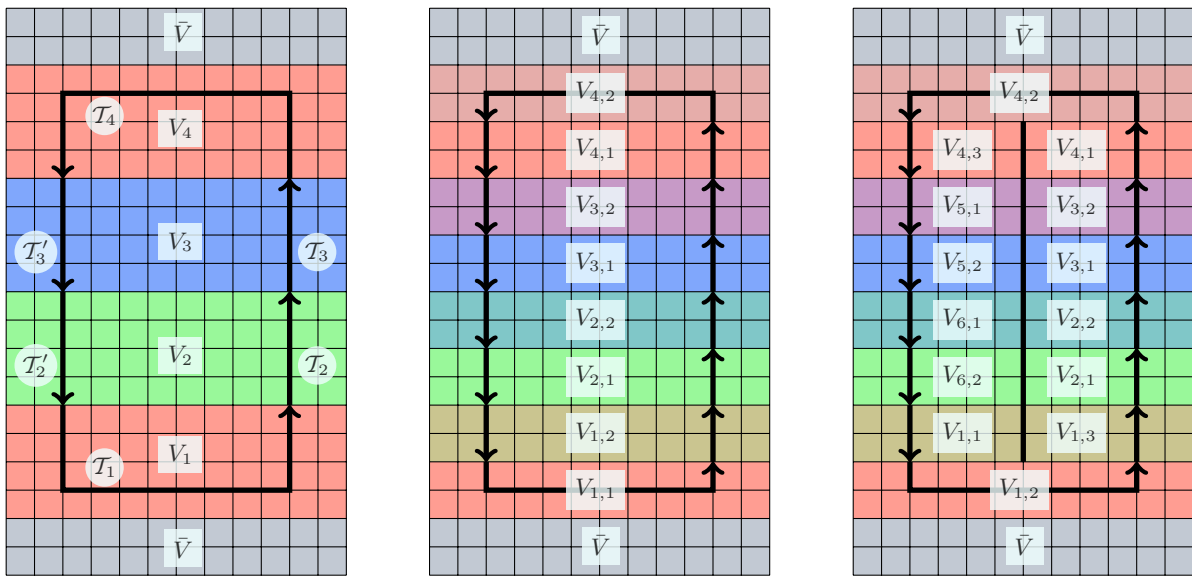


**Figure 5.1** Iterative slicing (from left to right) of lattice and Wilson loop during the multi-level algorithm.

trace of the expectation value of a product of parallel transporters  $\mathcal{T}_i$  in sublattices  $V_i$  in the appropriate representation,

$$W_{\mathcal{R}} = \text{tr} \langle \mathcal{W}_{\mathcal{R}} \rangle = \langle \text{tr}_{\mathcal{R}} \mathcal{W} \rangle = \langle \text{tr}_{\mathcal{R}} (\mathcal{T}_1 \mathcal{T}_2 \cdots \mathcal{T}_{n-1} \mathcal{T}_n) \rangle, \quad (5.5)$$

where  $\text{tr}_{\mathcal{R}}$  stands for the polynomial in the characters of the fundamental representations (2.15). This can also be written as a tensor product

$$W_{\mathcal{R}} = \langle \text{tr}_{\mathcal{R}} \mathcal{C}' (\mathcal{T}_1 \otimes \mathcal{T}_2 \otimes \cdots \otimes \mathcal{T}_{n-1} \otimes \mathcal{T}_n) \rangle = \langle \mathcal{C} (\mathcal{T}_1^{\mathcal{R}} \otimes \mathcal{T}_2^{\mathcal{R}} \otimes \cdots \otimes \mathcal{T}_{n-1}^{\mathcal{R}} \otimes \mathcal{T}_n^{\mathcal{R}}) \rangle, \quad (5.6)$$

where  $\mathcal{C}'$  and  $\mathcal{C}$  are the particular contractions of indices that lead to the Wilson loop  $\mathcal{W}_{\mathcal{R}}$  and  $\mathcal{T}^{\mathcal{R}}$  is the transporter in representation  $\mathcal{R}$ . With the definition of a sublattice expectation value

$$[\mathcal{T}_n]_n = \frac{1}{Z_n} \int_{\text{sublattice } n} \mathcal{D}\mathcal{U} \mathcal{T}_n e^{-S}, \quad (5.7)$$

where all link variables on the boundary of the sublattice are fixed, the Wilson loop can be written as

$$W_{\mathcal{R}} = \left\langle \mathcal{C} \left( [\mathcal{T}_{1,1}^{\mathcal{R}} \otimes \cdots \otimes \mathcal{T}_{1,m_1}^{\mathcal{R}}]_1 \otimes \cdots \otimes [\mathcal{T}_{n,1}^{\mathcal{R}} \otimes \cdots \otimes \mathcal{T}_{n,m_n}^{\mathcal{R}}]_n \right) \right\rangle_{\text{boundaries}}, \quad (5.8)$$

where in the outer expectation value only the link variables on the boundaries of the sublattices are updated. The indices  $m_n$  denote all  $\{m_n\}$  disconnected contributions in the  $n$ -th sublattice. This method of calculating a Wilson loop is possible, because in the Wilson action only links on a single plaquette interact with each other. Now a multi-level scheme can be defined by the recursion relation

$$[\mathcal{T}_n]_n = [\mathcal{C}_n ([\mathcal{T}_{n_1}]_{n_1} \otimes \cdots \otimes [\mathcal{T}_{n_m}]_{n_m})]_n, \quad (5.9)$$

where  $\mathcal{C}_n$  is again the contraction that leads to the transporter  $\mathcal{T}_n$ . An example of a two-level algorithm is given in Fig. 5.1. At the first level, the lattice is divided into  $n_t$  sublattices  $V_1, \dots, V_{n_t}$  (containing the Wilson loop) and separated by time slices plus the remaining sublattice, denoted by  $\bar{V}$ . The time extent

of each sublattice  $V_n$  is 4, such that  $n_t$  is the smallest natural number with  $4n_t \geq T + 2$ . In Fig. 5.1 (left panel)  $T = 14$  and the lattice is split into four sublattices  $V_1, V_2, V_3, V_4$ , containing the Wilson loop plus the complement  $\bar{V}$ . In this particular example, the Wilson loop is the product of parallel transporters

$$\mathcal{W} = \mathcal{T}'_2 \cdots \mathcal{T}'_{n_t-1} \mathcal{T}_{n_t} \mathcal{T}_{n_t-1} \cdots \mathcal{T}_2 \mathcal{T}_1 = \mathcal{T}'_2 \mathcal{T}'_3 \mathcal{T}'_4 \mathcal{T}'_3 \mathcal{T}'_2 \mathcal{T}_1. \quad (5.10)$$

If a sublattice  $V_n$  contains only one connected piece of the Wilson loop (as  $V_1$  and  $V_4$  do), then for the calculation only the sublattice expectation value  $[\mathcal{T}_n]_n$  is needed. If  $V_n$  contains two disconnected pieces (as  $V_2$  and  $V_3$ ) then the tensor product  $[\mathcal{T}_n \otimes \mathcal{T}'_n]_n$  has to be calculated in order to recover in the end the correct sum over configurations. The updates in each sublattice are done with fixed link variables on the time-slices bounding the sublattice. Calculating the expectation value of the full Wilson loop reduces to averaging over the links in the  $n_t + 1$  time slices,

$$W_{\mathcal{R}} = \left\langle \mathcal{C} \left( [\mathcal{T}'_1]_1 \left[ \mathcal{T}'_2 \otimes \mathcal{T}'_2 \right]_2 \cdots \left[ \mathcal{T}'_{n_t-1} \otimes \mathcal{T}'_{n_t-1} \right]_{n_t-1} [\mathcal{T}'_{n_t}]_{n_t} \right) \right\rangle_{\text{boundaries}}. \quad (5.11)$$

Here  $\mathcal{C}$  is that particular contraction of indices that leads to the trace of the product (5.10). In a two-level algorithm each sublattice  $V_n$  is further divided into two sublattices  $V_{n,1}$  and  $V_{n,2}$ , see Fig. 5.1 (middle panel), and the sublattice updates are done on the small sublattices  $V_{n,k}$  with fixed link variables on the time slices separating the sublattices  $V_{n,k}$ . In this way one finds two levels of nested averages. Iterating this procedure gives the *multi-level algorithm*. Since the dimensions  $d_{\mathcal{R}}$  grow rapidly with the Dynkin labels  $[p, q]$  – for example, in the following Casimir scaling for charges in the 189 dimensional representation  $[2, 1]$  is verified – it is difficult to store the many expectation values of tensor products of parallel transporters. Thus a slight modification of the Lüscher-Weisz algorithm was implemented, where the lattice is further split by spatially slicing along a hyperplane orthogonal to the plane defined by the Wilson loop, see Fig. 5.1 (right panel). The sublattice updates are done with fixed link variables on the same time slices as before and in addition on the newly introduced space slice. Instead of  $n_t$  sublattices containing the Wilson loop, there are now  $2n_t - 2$  sublattices. But now every sublattice contains only one connected part of the Wilson loop and (5.11) is replaced by

$$W_{\mathcal{R}} = \left\langle \text{tr} \prod_{n=1}^{2n_t-2} [\mathcal{T}'_n]_n \right\rangle_{\text{boundaries}}. \quad (5.12)$$

An iteration of this procedure by additional splittings of the time slices leads again to a multi-level algorithm. In the simulations two and three level algorithms with time-slicings  $(4 / 2)$ ,  $(8 / 4 / 2)$  and  $(12 / 4 / 2)$  are used, depending on the size of the Wilson loop and the size of the lattice. The expectation value for Wilson loops (and hence transporters  $\mathcal{T}_n$ ) of varying sizes and in different representations is calculated. In (5.6) it is possible to calculate the traced Wilson loop  $\text{tr}(\mathcal{W}_{\mathcal{R}})$  in an arbitrary representation  $\mathcal{R}$  as a polynomial in the fundamental characters  $\text{tr}(\mathcal{W}_7)$  and  $\text{tr}(\mathcal{W}_{14})$ . In (5.8) this is no longer possible, since the sublattice expectation value is not a group element anymore. Therefore it is necessary to compute the matrix representation  $\mathcal{R}$  for each sublattice transporter  $\mathcal{T}_n$ . The construction for the 8 lowest matrix representations for  $G_2$  is given in (2.19). To avoid the storage of tensor products of large representations, the modified algorithm as explained above was implemented. The Lüscher-Weisz

algorithm is also applied to calculate the correlators of two Polyakov loops  $\langle P_{\mathcal{R}}(0)P_{\mathcal{R}}(R) \rangle$  on larger lattices. In this case the complete lattice is divided into sublattices separated by time slices, hence there is no complement  $\bar{V}$ . Since the Polyakov loops are only used for lower-dimensional representations, the lattice has not to be split by a spatial slicing. Actually, for the calculations of Polyakov loop correlators mostly a three level Lüscher-Weisz algorithm is used,

$$\langle P_{\mathcal{R}}(0)P_{\mathcal{R}}(R) \rangle = \left\langle \mathcal{C} \prod_{n=1}^{\beta_T/4} \left[ [\mathcal{T}_{n_1}^{\mathcal{R}}(0) \otimes \mathcal{T}_{n_1}^{\mathcal{R}}(R)]_{n_1} [\mathcal{T}_{n_2}^{\mathcal{R}}(0) \otimes \mathcal{T}_{n_2}^{\mathcal{R}}(R)]_{n_2} \right]_n \right\rangle_{\text{boundaries}}. \quad (5.13)$$

Here  $\mathcal{C}$  is the contraction that leads to the product of traces and the size of the lowest level is two (each transporter  $\mathcal{T}$  is a product of two links in temporal direction). In their work Lüscher and Weisz showed that the statistical errors are exponentially suppressed with the temporal extent of the loop. Assuming that in each sublattice the transporters are statistically independent (which is a rather good assumption in the confined phase, but not in the deconfined phase), the number of *independent configurations* is roughly given by

$$n_{\text{total}} \approx n_0^{n_T}, \quad (5.14)$$

where  $n_T$  is the number of time slices on the lowest level and  $n_0$  the number of configurations in each sublattice expectation value on the lowest level. For  $n_T = T/2$  the statistical error  $\delta$  is then approximately given by

$$\delta \approx \omega n_{\text{total}}^{-\frac{1}{2}} \approx \omega n_0^{-\frac{T}{4}}. \quad (5.15)$$

The constant  $\omega$  depends, for instance, on the size of the boundary and the number of configurations on the other levels as well as on the autocorrelation time. The relative error of an exponentially decreasing correlation function  $C(T)$ ,

$$\frac{\delta}{C(T)} \approx \frac{\omega n_0^{-T/4}}{\exp(-\sigma RT)} = \omega \exp\left(T\left(\sigma R - \frac{\ln n_0}{4}\right)\right), \quad (5.16)$$

can then be tuned such that it is nearly constant. The advantage of Polyakov loops is that, on a fixed lattice size, more time slices are involved. Also the boundary is smaller than for Wilson loops, especially if in addition the spatial slicing for Wilson loops is used. In most simulations the number of configurations on each level is chosen such that it increases by a factor of ten on each level, for example  $n_2 = 10$ ,  $n_1 = 100$  and  $n_0 = 1000$ . In this case the statistical error arising from the fixed boundary is sufficiently small.

## 5.2 Casimir scaling and string breaking in $G_2$ gluodynamics

The static inter-quark potential is linearly rising on intermediate distances and the corresponding string tension will depend on the representation of the static charges. Similar to the known results for  $SU(N)$  gauge theories, it is expected to find *Casimir scaling* where the string tensions for different representations  $\mathcal{R}$  and  $\mathcal{R}'$  scale according to

$$\frac{\sigma_{\mathcal{R}}}{c_{\mathcal{R}}} = \frac{\sigma_{\mathcal{R}'}}{c_{\mathcal{R}'}} \quad (5.17)$$

with quadratic Casimir  $c_{\mathcal{R}}$ . Although all string tensions will vanish at asymptotic scales, it is still possible to check for Casimir scaling at intermediate scales where the linearity of the inter-quark potential is nearly fulfilled.

To extract the static quark anti-quark potential two different methods are available. The first makes use of the behavior of rectangular Wilson loops in representation  $\mathcal{R}$  for large  $T$ ,

$$\langle W_{\mathcal{R}}(R, T) \rangle = \exp(\kappa_{\mathcal{R}}(R) - V_{\mathcal{R}}(R)T). \quad (5.18)$$

Here  $V_{\mathcal{R}}(R)$  is the *Cornell* potential [169, 170]

$$V_{\mathcal{R}}(R) = \gamma_{\mathcal{R}} - \frac{\alpha_{\mathcal{R}}}{R} + \sigma_{\mathcal{R}}R, \quad (5.19)$$

with self energy contribution  $\gamma_{\mathcal{R}}$ , Coulomb interaction  $\alpha_{\mathcal{R}}$  and string tension  $\sigma_{\mathcal{R}}$ . If the confining string has already formed, the term  $\frac{\alpha}{R}$  shows a universal behaviour with  $\alpha = (d - 2)\pi/24$  for the lowest representation (Lüscher term). The potential can be extracted from the ratio of two Wilson loops with different time extent according to

$$V_{\mathcal{R}}(R) = \frac{1}{\tau} \ln \frac{\langle W_{\mathcal{R}}(R, T) \rangle}{\langle W_{\mathcal{R}}(R, T + \tau) \rangle}. \quad (5.20)$$

With the Lüscher-Weisz algorithm the expectation values of Wilson loops are calculated and fitted to the right hand side of (5.20) with the potential  $V_{\mathcal{R}}(R)$  in (5.19). The fitting has been done for external charges, separated by one lattice unit up to separations  $R$  with acceptable signal to noise ratios. From the fits the constants  $\gamma_{\mathcal{R}}$ ,  $\alpha_{\mathcal{R}}$  and  $\sigma_{\mathcal{R}}$ , entering the static potential, are extracted. For an easier comparison of the numerical results on lattices of different size and for different values of  $\beta$ , the constant contribution to the potentials is subtracted in the figures, according to

$$\tilde{V}_{\mathcal{R}}(R) = V_{\mathcal{R}}(R) - \gamma_{\mathcal{R}}. \quad (5.21)$$

The statistical errors are determined with the Jackknife method. In addition, the *local string tension*

$$\sigma_{\text{loc}, \mathcal{R}} \left( R + \frac{\rho}{2} \right) = \frac{V_{\mathcal{R}}(R + \rho) - V_{\mathcal{R}}(R)}{\rho}, \quad (5.22)$$

given by the Creutz ratio [171]

$$\sigma_{\text{loc}, \mathcal{R}} \left( R + \frac{\rho}{2} \right) = \frac{\alpha_{\mathcal{R}}}{R(R + \rho)} + \sigma_{\mathcal{R}} = \frac{1}{\tau\rho} \ln \frac{\langle W_{\mathcal{R}}(R + \rho, T) \rangle \langle W_{\mathcal{R}}(R, T + \tau) \rangle}{\langle W_{\mathcal{R}}(R + \rho, T + \tau) \rangle \langle W_{\mathcal{R}}(R, T) \rangle}, \quad (5.23)$$

is determined. The second method to calculate the string tensions uses correlators of two Polyakov loops,

$$V_{\mathcal{R}}(R) = -\frac{1}{\beta_T} \ln \langle P_{\mathcal{R}}(0) P_{\mathcal{R}}(R) \rangle. \quad (5.24)$$

The correlators are calculated with the three-level Lüscher-Weisz algorithm and are fitted with the static potential  $V_{\mathcal{R}}(R)$  with fit parameters  $\gamma_{\mathcal{R}}$ ,  $\alpha_{\mathcal{R}}$  and  $\sigma_{\mathcal{R}}$ . Now the local string tension takes the form

$$\sigma_{\text{loc}, \mathcal{R}} \left( R + \frac{\rho}{2} \right) = -\frac{1}{\beta_T \rho} \ln \frac{\langle P_{\mathcal{R}}(0) P_{\mathcal{R}}(R + \rho) \rangle}{\langle P_{\mathcal{R}}(0) P_{\mathcal{R}}(R) \rangle}. \quad (5.25)$$

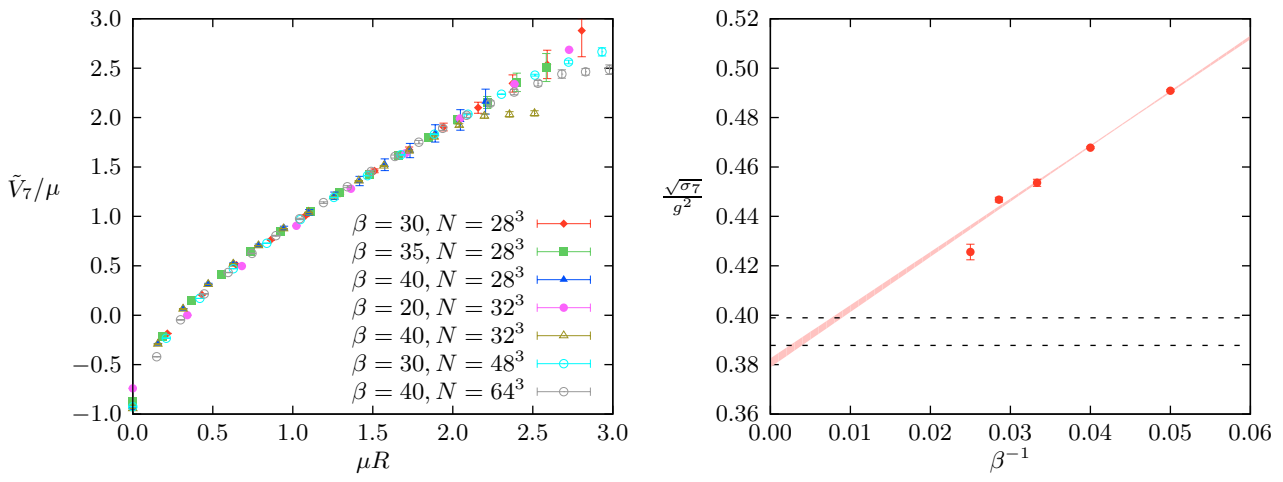


**Figure 5.2** *Left panel:* Continuum scaling of the fundamental potential. *Right panel:* Linear continuum extrapolation of the string tension. The shaded region indicates the corresponding error bound. The dotted lines are the theoretical predictions.

### 5.2.1 Continuum scaling

Most IHMC simulations are performed on a  $28^3$  lattice with Wilson loops of time extent  $T = 12$ . To extract the static potentials from the ratio of Wilson loops in (5.20),  $\tau = 2$  is chosen. The fits to the static potential (5.19) for charges in the *fundamental* (7) representation and for values  $\beta = 30, 35$  and  $40$  yield the lattice parameters  $\alpha, \gamma$  and  $\sigma$  given in Tab. C.1 in the appendix.

Since for  $G_2$  there exists no natural mass scale  $\mu$  from experiments, the string tension in the (7) representation is chosen as a reference scale,

$$\mu = \sqrt{\sigma_7}. \quad (5.26)$$

Nevertheless, using the Sommer scale [172]

$$R^2 \frac{\partial V_7(R)}{\partial R} \Big|_{R=R(c)} = R^2 \sigma_{\text{loc},7} \Big|_{R=R(c)} = c = 1.65, \quad r(c) = R(c) a \approx 0.5 \text{ fm}, \quad (5.27)$$

it is possible to assign a physical value to  $\mu$ . In these units the lattice spacing is ranging from 0.06 fm to 0.138 fm, corresponding to physical volumes of  $(3.84 \text{ fm})^3$  to  $(4.42 \text{ fm})^3$ , see Tab. C.2 (appendix). The mass scale is then given by

$$\mu = \sqrt{\sigma_7} \approx 490 \text{ MeV}. \quad (5.28)$$

To check for scaling, the potentials in ‘physical’ units,  $V/\mu$ , are plotted as a function of  $\mu R$  in Fig. 5.2. Now it is observed that the potentials for the three values of  $\beta$  are the same within error bars. In addition, they agree with the potential (in physical units) extracted from the Polyakov loop on much larger  $32^3, 48^3$  and  $64^3$  lattices. Formula (5.3) gives the string tension in the continuum as a function of the coupling  $\beta \propto 1/g^2$  [143]. To compare this continuum result with the obtained lattice data, the corresponding value  $g^{-2} \sqrt{\sigma_7}$  is extrapolated linearly in  $\beta^{-1} \propto a$  to the continuum limit by using the couplings and lattice sizes in Tab. C.2 (appendix). This procedure is motivated by the (in leading order) linear behavior

that has been found in a similar study for gauge groups  $SU(2)$  up to  $SU(5)$  [173]. For increasing  $\beta$  the scaling window with a linearly rising potential shrinks and it becomes more difficult to extract reliable values for the intermediate string tension. Thus a linear fit to all points in table C.2 (appendix) leads to  $g^{-2}\sqrt{\sigma_7} = 0.381(5)$  (see Fig. 5.2), with a rather large reduced  $\chi^2 = 8.56$ , whereas a linear fit to the reliable data points with the 3 smallest  $\beta$ -values yields  $g^{-2}\sqrt{\sigma_7} = 0.376(2)$ , with a small reduced  $\chi^2 = 0.51$ . Both fit-values are in good agreement with the prediction of Eq. (5.3),  $g^{-2}\sqrt{\sigma_7} = 0.39894$ . Corrections to this theoretical value have been derived in a systematic expansion in [140],

$$g^{-2}\sqrt{\sigma_7} = \sqrt{\frac{1}{2\pi}}(1 - 0.02799 + \dots) \approx 0.38778, \quad (5.29)$$

but they are still subject to ambiguities in defining a low momentum cutoff that may change this value by up to 3%. With keeping possible systematic uncertainties in the extrapolation procedure in mind, which are not reflected in the given statistical error, a complete agreement between analytical and numerical results is apparent.

## 5.2.2 Casimir scaling in three dimensions

Now higher representations are investigated to check for Casimir scaling. The fitted constants  $\alpha_{\mathcal{R}}, \gamma_{\mathcal{R}}$

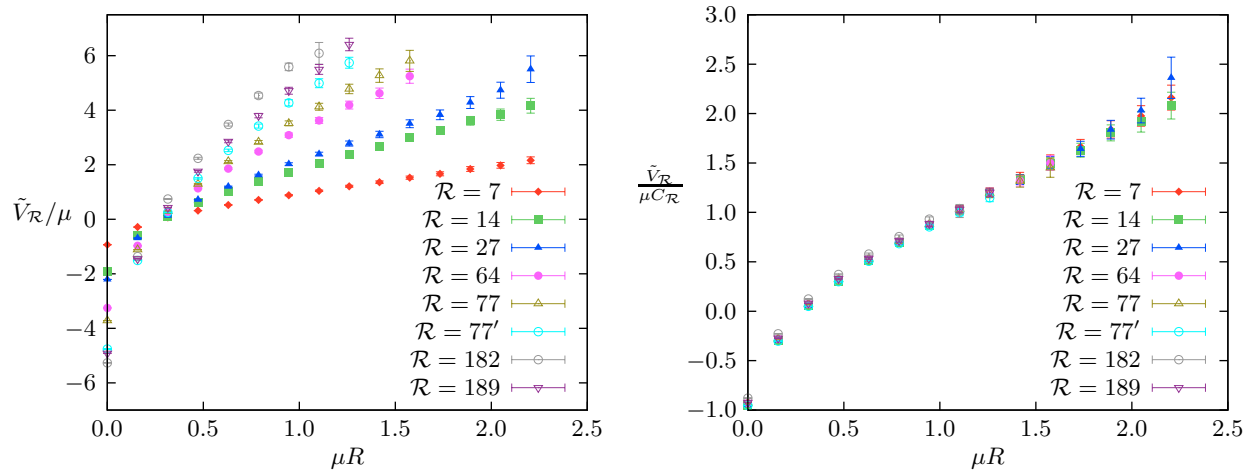


**Figure 5.3** Unscaled (left panel) and scaled (right panel) potential with  $\beta = 40$  on a  $28^3$  lattice.

and  $\sigma_{\mathcal{R}}$  of the potential (5.19) for the eight smallest representations are given in Tab. C.3 in the appendix. The Casimir scaling of coefficients becomes apparent when divided by the corresponding coefficients of the static potential in the (7) representation. The *local string tensions* extracted from the Creutz ratio can be determined much more accurately than the global string tensions extracted from fits to the static potentials. Tab. C.4 in the appendix contains the local string tensions for static charges in the eight smallest representations for  $\rho = 1$  and different  $R$  in (5.23), divided by the corresponding local string tensions in the 7 representation. The results are insensitive to the distance  $R$  in the Creutz ratio. They agree within 1 percent with the values for the Casimir ratios  $\mathcal{C}'_{\mathcal{R}} = \mathcal{C}_{\mathcal{R}}/\mathcal{C}_7$  given in the last row of that table. In Fig. 5.3 (left panel) the values for the eight potentials  $V_7, \dots, V_{189}$  (with statistical errors),

measured in ‘physical units’  $\mu$  defined in (5.26), are plotted. The distance of the charges is measured in the same system of units. The linear rise at intermediate scales is clearly visible, even for charges in the 189-dimensional representation. Fig. 5.3 (right panel) contains the same data points rescaled with the quadratic Casimirs of the corresponding representations. The eight rescaled potentials fall on top of each other within error bars. This implies that the *full potentials* for short and intermediate separations of the static charges show Casimir scaling. To further check for Casimir scaling, the *local string tensions*

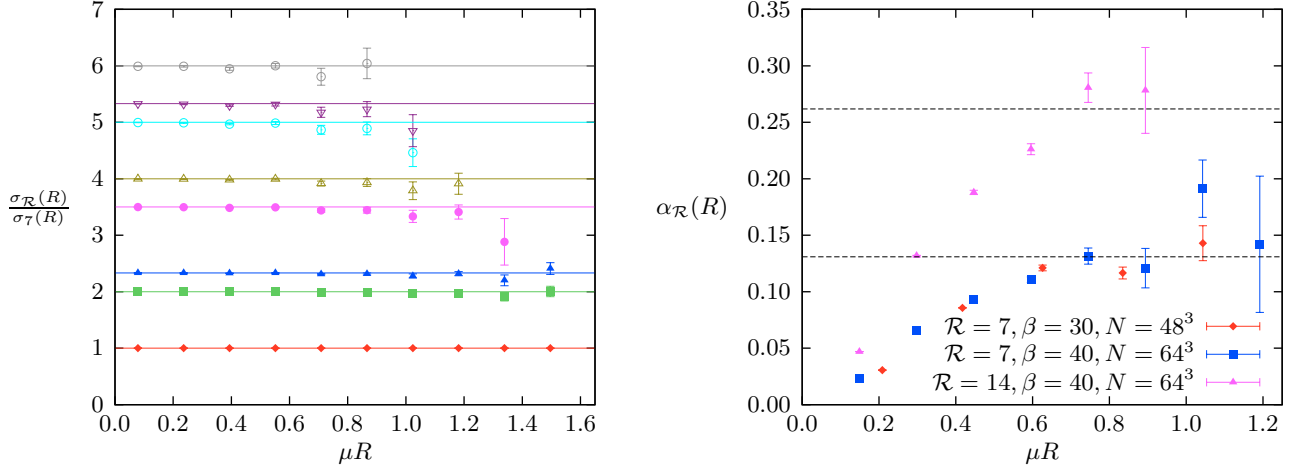


**Figure 5.4** *Left panel:* Ratio of the local string tension with  $\beta = 40$  scaled on a  $28^3$  lattice for the eight smallest representations. *Right panel:* Local Lüscher term at two different couplings and for two different representations.

with  $\rho = 1$  are calculated, this time for all  $R$  between 1 and 10 and not only for  $R = 0, 1, 2$  as in Tab. C.4 (appendix). The horizontal lines in Fig. 5.4 (left panel) are the values predicted by the Casimir scaling hypothesis. Clearly, there is no sign of Casimir scaling violation visible on a  $28^3$  lattice near the continuum at  $\beta = 40$ . Of course, for widely separated charges in higher dimensional representations the error bars are not negligible even for an algorithm with exponential error reduction.

### 5.2.3 Lüscher term

In Tab. C.3 in the appendix it can be seen that the dimensionless coefficient  $\alpha_{\mathcal{R}}$  in the static potential scales with the quadratic Casimir, similarly to the string tension. The corresponding term, if measured at distances where the flux tube is fully developed, is referred to as *Lüscher term*. Its value has been calculated by Lüscher for charges in the fundamental representation, in  $d$  dimensions  $\alpha = (d - 2)\pi/24$ , and it is believed to be universal [174]. The value  $\alpha = \pi/24$  in 3 dimensions is off the results in Tab. C.1 (appendix). However, since the coefficients in this table are fitted to the static potential from  $R = 1$  to values of  $R$  with acceptable signal to noise ratio, they contain contributions from the short range Coulombic tail. To calculate  $\alpha_{\mathcal{R}}$  at intermediate distances, it is better to use the (local) Lüscher term

$$\alpha_{\text{loc},\mathcal{R}}(R) = \frac{\alpha_{\mathcal{R}} R^2}{R^2 - \rho^2} = \frac{R^3}{2\beta_T \rho^2} \ln \frac{\langle P_{\mathcal{R}}(0) P_{\mathcal{R}}(R + \rho) \rangle \langle P_{\mathcal{R}}(0) P_{\mathcal{R}}(R - \rho) \rangle}{\langle P_{\mathcal{R}}(0) P_{\mathcal{R}}(R) \rangle \langle P_{\mathcal{R}}(0) P_{\mathcal{R}}(R) \rangle}, \quad (5.30)$$

with  $\rho = 1$ . In Fig. 5.4 (right panel) the local Lüscher term is plotted for charges in the (7) and (14) representation at couplings  $\beta \in \{30, 40\}$ . The data for the defining 7-dimensional representation at intermediate distances are in agreement with the theoretical prediction  $\alpha_7 = \pi/24 \approx 0.131$ . The local Lüscher term for the adjoint representation approaches a value close to  $\alpha_{14} \approx \pi/12$ . Although this exceeds the universal prediction of [174] by a factor 2, this behavior is in close analogy to the situation in 3 dimensional  $SU(5)$  Yang-Mills theory, where Casimir scaling of the local Lüscher term at short distances has been reported for the 10-dimensional representation [175]. Since the Lüscher term is expected to show up at asymptotic large distances, this term can only be extracted if the flux tube has fully developed before string breaking sets in. Whether this is the case for  $G_2$  gauge theory is not clear. The results suggest that this happens for charges in the 7-dimensional representation.

## 5.2.4 String breaking and glue-lumps in three dimensions

To observe the breaking of strings connecting static charges at intermediate scales, when further increasing the separation of the charges, high statistics IHMC simulations on a  $48^3$  lattice with  $\beta = 30$  have been performed. For charges in the two fundamental representations of  $G_2$ , expectation values of Wilson loops and products of Polyakov loops have been calculated. When a string breaks, each static charge in the representation  $\mathcal{R}$  at the end of the string is screened by  $N(\mathcal{R})$  gluons to form a colour blind glue-lump. It is expected, that the dominant decay channel for an over-stretched string is given by: string  $\rightarrow$  glue-lump + glue-lump. For a string to decay, the energy stored in the string must be sufficient to produce two glue-lumps. According to (2.14) it requires at least 3 gluons to screen a static charge in the (7) representation, one gluon to screen a charge in the (14) representation and two gluons to screen a charge in the (27) representation. The separations of the charges where string breaking sets in are calculated as well as the masses of the produced glue-lumps. The mass of such a quark-gluon bound state can be obtained from the correlation function according to

$$\exp(-m_{\mathcal{R}}T) \propto C_{\mathcal{R}}(T) = \left\langle \left( \bigotimes_{n=1}^{N(\mathcal{R})} F_{\mu\nu}(y) \right) \Big|_{\mathcal{R},a} \mathcal{R}(\mathcal{U}_{yx})_{ab} \left( \bigotimes_{n=1}^{N(\mathcal{R})} F_{\mu\nu}(x) \right) \Big|_{\mathcal{R},b} \right\rangle, \quad (5.31)$$

where  $\mathcal{R}(\mathcal{U}_{yx})$  is the temporal parallel transporter in the representation  $\mathcal{R}$  from  $x$  to  $y$  of length  $T$ . It represents the static sources in the representation  $\mathcal{R}$ .  $N(\mathcal{R})$  is the number of gluons necessary to screen the charge. The vertical line means projection of the tensor product onto that linear subspace on which the irreducible representation  $\mathcal{R}$  acts,

$$(14) \otimes (14) \otimes \cdots \otimes (14) = \mathcal{R} \oplus \cdots . \quad (5.32)$$

For example, for charges in the (14) representation the projection is simply

$$F_{\mu\nu}(x) \Big|_{14,a} = F_{\mu\nu}^a(x), \quad \text{where} \quad F_{\mu\nu}^a T^a = F_{\mu\nu}. \quad (5.33)$$

For charges in the (7) representation projection of the reducible representation  $(14) \otimes (14) \otimes (14)$  onto the irreducible representation (7) is necessary. Using the embedding of  $G_2$  into  $SO(7)$  representations,

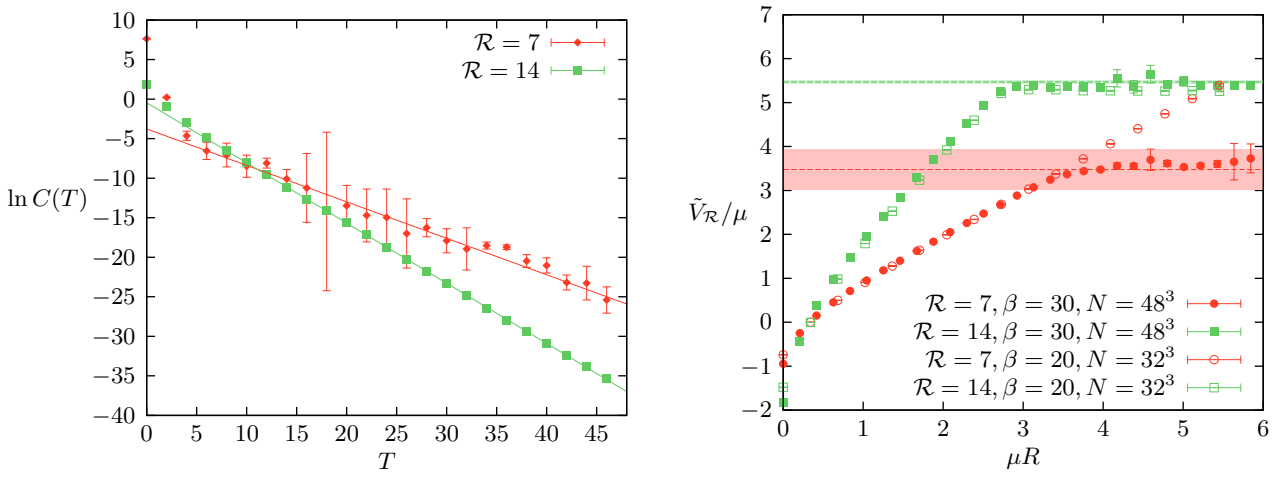


**Figure 5.5** *Left panel:* Glue-lump correlator (lattice size  $48^3$ ,  $\beta = 30$ ). *Right panel:* Potential for both fundamental representations at  $\beta \in \{20, 30\}$  and corresponding glue-lump mass for  $\beta = 30$ .

it can be shown that this projection can be done with the help of the totally antisymmetric  $\varepsilon$ -tensor with 7 indices,

$$F_{\mu\nu}(x) \otimes F_{\mu\nu}(x) \otimes F_{\mu\nu}(x) \Big|_{7,a} \propto F_{\mu\nu}^p(x) F_{\mu\nu}^q(x) F_{\mu\nu}^r(x) \varepsilon_{abcdefg} T_{bc}^p T_{de}^q T_{fg}^r. \quad (5.34)$$

Fig. 5.5 (left panel) shows the logarithm of the glue-lump correlator (5.31) as a function of the separation of the two lumps for static charges in the fundamental representations (7) and (14). The linear fits to the data yield the glue-lump masses  $m_7 a = 0.46(4)$ ,  $m_{14} a = 0.761(3)$ , corresponding to a physical mass of  $m_7 \approx 1066$  MeV and  $m_{14} \approx 1764$  MeV. Thus it is expected that the subtracted static potentials approach the asymptotic values  $\tilde{V}_{\mathcal{R}} \rightarrow 2m_{\mathcal{R}} - \gamma_{\mathcal{R}}$ . With the fit-values  $\gamma_7 a = 0.197(1)$  and  $\gamma_{14} a = 0.381(2)$  one finds

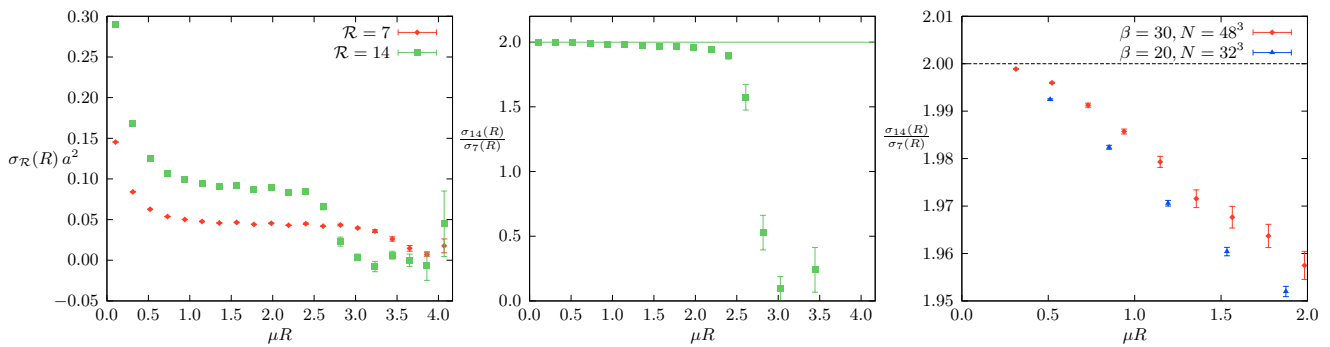
$$\tilde{V}_7/\mu \rightarrow 3.47 \quad , \quad \tilde{V}_{14}/\mu \rightarrow 5.47. \quad (5.35)$$

Fig. 5.5 (right panel) shows the rescaled potentials for charges in the fundamental representations together with the asymptotic values (5.35) extracted from the glue-lump correlators. At fixed coupling  $\beta = 30$  both potentials flatten exactly at separations of the charges where the energy stored in the flux tube is twice the glue-lump energy. However, the direct comparison of the potentials for two different couplings, i.e. different lattice spacings, reveals that the potential for adjoint charges is nearly free of lattice artifacts, while the string breaking distance for charges in the defining representation is strongly coupling dependent and the continuum limit is not reached yet. A good approximation for the string breaking distance is then given by  $V_{\mathcal{R}}(R^b) \approx 2m_{\mathcal{R}}$ . Assuming Casimir scaling for the coefficients  $\alpha_{\mathcal{R}}, \gamma_{\mathcal{R}}$  and  $\sigma_{\mathcal{R}}$  in the static potential one obtains

$$\mu R_{\mathcal{R}}^b = \left( \sqrt{\alpha_{\mathcal{R}} + \frac{1}{4} \left( \frac{\gamma_{\mathcal{R}}}{\mu} - M_{\mathcal{R}} \right)^2} - \frac{1}{2} \left( \frac{\gamma_{\mathcal{R}}}{\mu} - M_{\mathcal{R}} \right) \right), \quad M_{\mathcal{R}} = \frac{2m_{\mathcal{R}}}{\mu C'_{\mathcal{R}}}. \quad (5.36)$$

Inserting the result from the last row in Tab. C.1 in the appendix and the glue-lump masses one finds  $\mu R_7^b = 3.49$  and  $\mu R_{14}^b = 2.77$ . In dimensionful units, the string breaking distance is given by

$$R_7^b \approx 1.40 \text{ fm} \quad \text{and} \quad R_{14}^b \approx 1.11 \text{ fm}. \quad (5.37)$$



**Figure 5.6** *Left panel:* Local string tension ( $48^3$  lattice,  $\beta = 30$ ). *Centre panel:* Casimir scaling of local string tension ( $48^3$  lattice,  $\beta = 30$ ). *Right panel:* Deviations from Casimir scaling at two different couplings.

These values agree well with the separations  $\mu R$  in Fig. 5.5 (right panel), where the static potentials flatten such that string breaking sets in at scales predicted by formula (5.36). Fig. 5.6 (left panel) shows the local string tensions in the two fundamental representations and Fig. 5.6 (centre panel) their ratio. Especially the last plot makes clear, that the string connecting charges in the adjoint representation breaks earlier than the string connecting charges in the (7) representation. Just at the critical separation predicted by formula (5.36), the ratio of local string tensions  $\sigma_{14}(R)/\sigma_7(R)$  shows indeed a pronounced knee.

### 5.2.5 Signs of Casimir scaling violations

Although the coarse grained view onto the ratio of local string tensions up to the string breaking distance (Fig. 5.6, centre panel) shows an approximate Casimir scaling, a closer look uncovers deviations from the expected Casimir ratio of the adjoint and defining representation (see Fig. 5.6 right panel). The results for two different lattice spacings indicate, that for short distances, in the Coulombic part of the potential, Casimir scaling is fulfilled, in agreement with the predictions of perturbation theory, valid at short distances. For larger distances the measured ratio drops by about 2.5% near the string breaking distance. Similar deviations have already been reported in [158, 161] for three-dimensional  $SU(2)$  gauge theory. In either case the scale dependence identifies Casimir scaling violations as a purely non-perturbative long range effect. Of course, the given error bounds in Fig. 5.6 may be taken with care, as they include only statistical uncertainties. Lattice artifacts are still visible and further work will be necessary to confirm that this violation persists in the continuum limit.

### 5.2.6 Casimir scaling in four dimensions

In this last section results for the static potential in four dimensions are presented. The IHMC simulations have been performed on a small  $14^4$  and a larger  $20^4$  lattice for different values of  $\beta$ . The static potentials and local string tensions have been extracted from (5.20) and (5.23), where the expectation values have been calculated with a two-step Lüscher-Weisz algorithm. Tab. C.5 (appendix) contains the fits to the parameters in the potential for static charges in the (7) representation for these lattices and values for  $\beta$ .

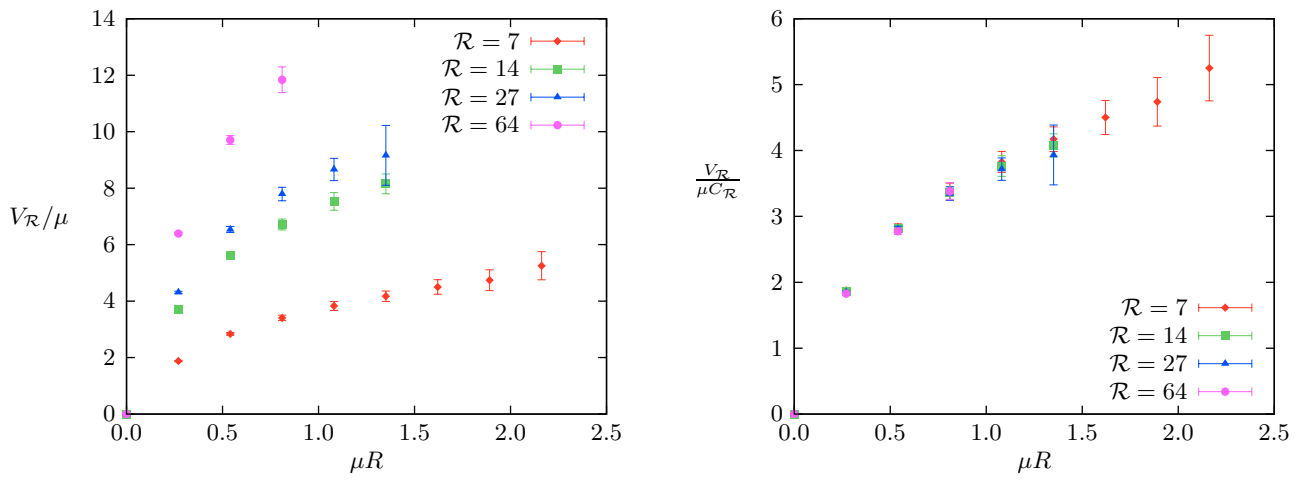


**Figure 5.7** Unscaled (left panel) and scaled (right panel) potential at  $\beta = 9.7$  on a  $14^4$  lattice.

Applying again the Sommer scale, the data yield a mass scale of approximately

$$\mu = \sqrt{\sigma_7} \approx 450 \text{ MeV}, \quad (5.38)$$

corresponding to  $a = 0.14$  fm on the larger  $20^4$  lattice and  $a(\beta = 9.7) = 0.12$  fm and  $a(\beta = 10) = 0.089$  fm on the smaller lattice. The physical volumes are then between  $(1.25 \text{ fm})^4$  and  $(2.80 \text{ fm})^4$ . Fig. 5.7 (left panel) shows the static potentials in ‘physical units’  $\mu = \sqrt{\sigma_7}$ , for charges in the 7, 14, 27 and 64 dimensional representations and coupling  $\beta = 9.7$ , as function of the distance between the charges (in physical units). The corresponding value for  $\sigma_7$  is taken from Tab. C.5 (appendix). The same coupling has been used in [126] on an asymmetric  $14^3 \times 28$  lattice. After normalizing the potentials with the quadratic Casimirs, they are identical within error bars, as can be seen in Fig. 5.7 (right panel). The findings are in complete agreement with the results in [126] on Casimir scaling in four-dimensional  $G_2$  gluodynamics at  $\beta = 9.7$  and with the accurate results on Casimir scaling on intermediate scales in three-dimensional  $G_2$  gluodynamics. Figs. 5.8 shows the corresponding results for a weaker coupling  $\beta = 10$  closer to the continuum limit. For this small coupling the potential can only be measured up to separations  $\mu R \approx 1.5$  of the charges. However, this can be done with high precision and for higher-dimensional representations. Similar as for  $\beta = 9.7$  the potentials normalized with the second order Casimirs fall on top of each other. This confirms Casimir scaling for  $G_2$  gluodynamics in four dimensions for charges in representations with dimensions 7, 14, 27, 64, 77, 77', 182 and 189. Finally, simulations on a much larger  $20^4$  lattice at  $\beta = 9.7$  are done in order to calculate the static potential for larger separations of the static quarks. Unfortunately, the distance  $\mu R \approx 3$  is still not sufficient to detect string breaking, see Fig. 5.9 (left panel). However, again the potentials normalized with the quadratic Casimirs shown in Fig. 5.9 (right panel) are equal within error bars. In Tab. C.6 in the appendix the fit-values for the parameters of the potentials on the larger  $20^4$  lattice are listed for static charges in the representations with dimensions 7, 14 and 27. For all representations Casimir scaling of all three parameters in the potential is found. Unfortunately, the fit-parameters cannot be determined reliably in the (64) representation with the present data. This is attributed to larger errors for the potentials at intermediate scales, see Fig. 5.9 (right panel). Therefore, the parameters can only be determined from

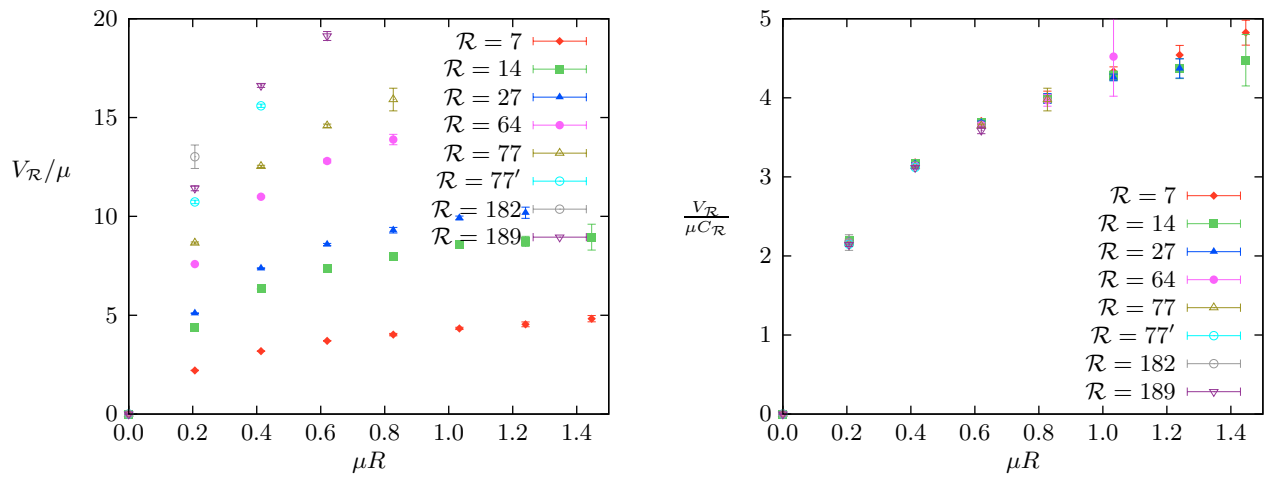


**Figure 5.8** Unscaled (left panel) and scaled (right panel) potential at  $\beta = 10$  on a  $14^4$  lattice.

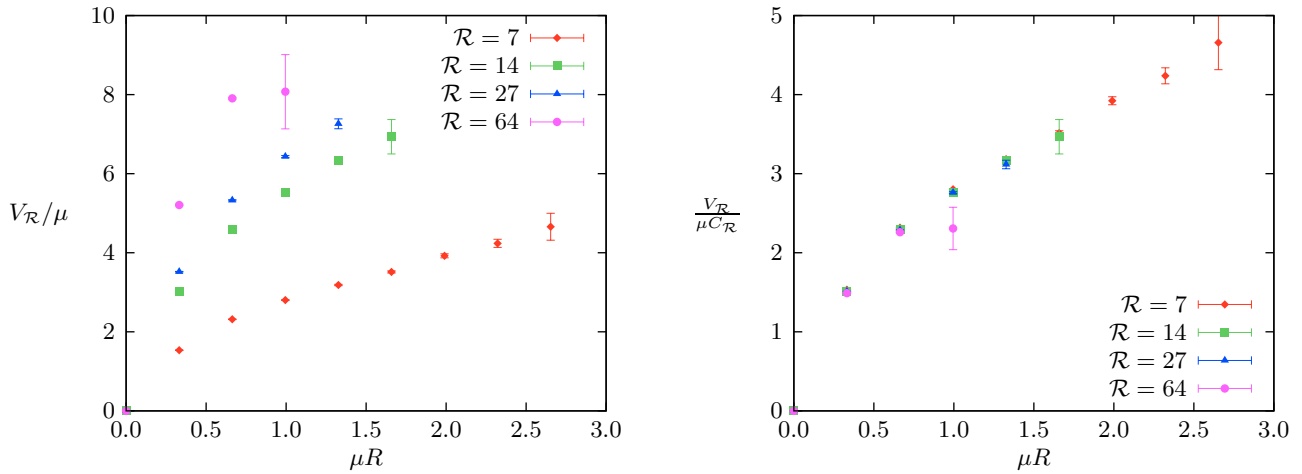


**Figure 5.9** Unscaled (left panel) and scaled (right panel) potential at  $\beta = 9.7$  on a  $20^4$  lattice.

the ultraviolet part of the potential for this representation ( $R < 3$ ), which is rather Coulomb-like than linearly rising. Much more conclusive are the local string tensions calculated on the larger lattice (now up to the (64) representation). Tab. C.7 (appendix) contains the local string tensions divided by the local string tensions in the (7) representation. These normalized values are constant up to separations of the charges where the statistical errors are under control. Compared to the corresponding numbers in three dimensions, see Tab. C.4 in the appendix, it is now possible to see a slight dependence of the local string tensions (from Eq. (5.22)) on the distance  $R$ . Despite the lower precision of the results in four dimensions compared to the corresponding results in three dimensions, again Casimir scaling is confirmed on short to intermediate scales within 5 percent. All simulation results for the local string tensions  $\sigma_{\mathcal{R}}(R)$ , normalized by  $\sigma_7(R)$  on a  $14^4$  lattice with  $\beta \in \{9.7, 10\}$  and on a  $20^4$  lattice with  $\beta = 9.7$  and for  $\mu R \leq 1.5$ , are collected in Fig. 5.10. The horizontal lines in this figure show the prediction of the Casimir scaling hypothesis. The normalized data points are compatible with each other and with the hypothesis.

## 5.3 Conclusions

A slightly modified Lüscher-Weisz multi-step algorithm with exponential error reduction has been implemented to measure the static potentials for charges in various  $G_2$  representations. The accurate results in three dimensions show, that all parameters of the fitted static potentials show Casimir scaling, see Tab. C.1 in the appendix. The global string tensions extracted from these fits show, that possible deviations from Casimir scaling must be less than 4 percent. Additionally, the local string tensions have been extracted from the Creutz ratios to obtain even more precise data. In this way, Casimir scaling at short distances  $\sqrt{\sigma_7}R < 1$  has been confirmed with 1 percent accuracy. Thus it can be concluded, that in three dimensional  $G_2$  gluodynamics the Casimir scaling violations of the string tensions are small for all charges in the representations with dimensions 7, 14, 27, 64, 77, 77', 182 and 189. For charges in the two fundamental representations IHMC simulations on larger lattices have been performed to detect string breaking at asymptotic scales.

In three dimensions it has been observed, that string breaking indeed sets in at the expected scale where the energy stored in the flux tube is sufficient to create two glue-lumps. To confirm this expectation, masses of glue-lumps associated with static charges in the fundamental representations have been calculated. Here, close to the string breaking distance, systematic Casimir scaling violations show up at the 2.5 percent level, and they have been identified as a non-perturbative effect arising only at large distances. Finally, the prediction for the numerical value of the string tension in three dimensions has been confirmed by a continuum extrapolation of the precise data.

In four-dimensional  $G_2$  gluodynamics, Casimir scaling has been found for charges in the representations (7), (14), (27) and (64), similar as in three dimensions, although the uncertainties are of course larger. But within error bars no violation of Casimir scaling has been seen, and this confirms the corresponding results in [126], obtained with a variant of the smearing procedure. To see the expected string breaking in four dimensions, larger lattices than those used in the present work are needed. The investigations on Casimir scaling and string breaking confirm the picture of exceptional confinement given in chapter 4. Although it is often believed that confinement is related to centre symmetry, it has been shown here that  $G_2$  gauge theory is a confining theory in the sense, that static charges are screened and an intermediate non-vanishing string tension exists. Therefore  $G_2$  Yang-Mills shares an interesting feature with QCD. In the next chapter it will indeed be shown that  $G_2$  gluodynamics coupled to fundamental scalars can be used as a *toy model* for QCD.

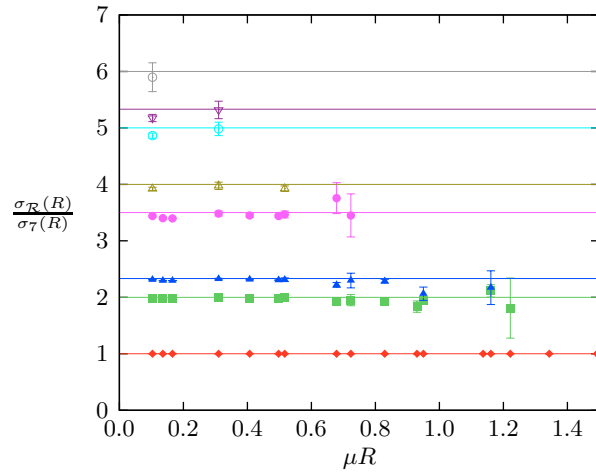


**Figure 5.10** Scaled local string Tension with  $\beta \in \{9.7, 10\}$  on  $14^4$  and  $20^4$  lattices.

# 6 The $G_2$ Yang-Mills Higgs model

In the present chapter  $G_2$ -Yang-Mills theory coupled to a fundamental scalar field is investigated. The obtained results have been published in [80]. It will be shown that this theory has interesting connections to QCD with fundamental quarks and can in some sense be seen as a *toy model* for QCD. The gauge group  $SU(3)$  of strong interaction is a subgroup of  $G_2$ , and this observation has interesting consequences, as pointed out in [57]. A Higgs field in the fundamental 7 dimensional representation can break the  $G_2$  gauge symmetry to the  $SU(3)$  symmetry via the Higgs mechanism. The corresponding continuum action is given by

$$S_{\text{YMH}}[A, \phi] = \int d^4x \left( \frac{1}{4g^2} \text{tr} F_{\mu\nu} F^{\mu\nu} + \frac{1}{2} (D_\mu \phi, D_\mu \phi) + V(\phi) \right). \quad (6.1)$$

where  $V(\phi) = \lambda(\phi^2 - \nu^2)^2$  is a quartic potential for the Higgs field. Taking the limit  $\lambda \rightarrow \infty$  and rescaling  $\phi \rightarrow \nu\phi$  fixes the length of the scalar field, i.e.  $\phi^2 = 1$ . In the limit  $g^{-1} \rightarrow \infty$  the gauge bosons decouple and the theory reduces to an  $O(7)$  invariant non-linear sigma model,

$$S_{\text{NLSM}}[\phi] = \kappa \int d^4x \partial_\mu \phi \partial^\mu \phi, \quad \phi^2 = 1, \quad \kappa = \frac{1}{2} \nu^2, \quad (6.2)$$

which is expected to have a second order (mean field) symmetry breaking transition down to  $O(6)$ . The mean field prediction for the critical coupling is  $\kappa_{c,\text{mf}} = \frac{n}{2d} = \frac{7}{8}$ , and this value bounds  $\kappa_c$  from below [176]. For finite values of the gauge coupling  $g$ ,

$$S_{\text{YMH}}[A, \phi] = \int d^4x \left( \frac{1}{4g^2} \text{tr} F_{\mu\nu} F^{\mu\nu} + \kappa (D_\mu \phi, D_\mu \phi) \right), \quad (6.3)$$

the gauge bosons take part in the dynamics. The global  $SO(7)$  symmetry is broken to a local  $G_2$  gauge symmetry. Making use of the coset space relation [85]

$$G_2/SU(3) \sim SO(7)/SO(6) \sim S^6, \quad (6.4)$$

a sketch of the expected phase diagram is obtained. For small values of  $\kappa$  the theory is expected to stay in the Higgs symmetric phase (vanishing vacuum expectation value of the Higgs field), and qualitatively the theory behaves similar to pure  $G_2$  gluodynamics. With respect to the  $SU(3)$  subgroup of  $G_2$ , the fundamental representations (7) and (14) branch into the following irreducible  $SU(3)$ -representations:

$$(7) \longrightarrow (3) \oplus (\bar{3}) \oplus (1) \quad , \quad (14) \longrightarrow (8) \oplus (3) \oplus (\bar{3}). \quad (6.5)$$

The Higgs field branches into a fundamental and an anti-fundamental scalar and into a colour singlet with respect to  $SU(3)$ . Similarly, a  $G_2$ -gluon branches into a massless  $SU(3)$ -gluon and additional gauge bosons with respect to  $SU(3)$ . If the Higgs field picks up a vacuum expectation value  $\nu$ , the 6 gauge bosons belonging to the coset space (6.4) eat up the non-singlet scalar fields and acquire a mass proportional to  $\nu$ . The other 8 gluons belonging to  $SU(3)$  remain massless, such that the spectrum in the broken phase consists of 8 massless gluons (confined in glueballs), 6 massive gauge bosons and one

massive Higgs particle. In the limit of  $\nu \rightarrow \infty$  the 6 massive gauge bosons become infinitely heavy and are removed from the spectrum. In this limit the  $G_2$  Higgs model reduces to  $SU(3)$  Yang-Mills theory. The  $\mathbb{Z}(3)$  centre symmetry of  $SU(3)$  gluodynamics will be restored, the Polyakov loop is an order parameter for confinement and string breaking in the fundamental representation will not occur. Even more interesting, for intermediate and large values of  $\nu$ , the  $G_2$  Yang-Mills-Higgs theory mimics  $SU(3)$  gauge theory with dynamical *vector quarks*. Similar as dynamical quarks and anti-quarks, they transform in the representations (3) and  $(\bar{3})$  of  $SU(3)$  and thus explicitly break the  $\mathbb{Z}(3)$  centre symmetry. As in QCD they are expected to weaken the deconfinement phase transition. Thus it has been conjectured in [58] that there may exist a critical endpoint where the first order transition disappears. The masses of these *quarks* and the length scale at which string breaking occurs increase with increasing  $\nu$ . The known transitions in the limiting cases  $\nu \rightarrow 0$ ,  $\nu \rightarrow \infty$  or  $\beta \rightarrow \infty$  are depicted in Fig. 6.1. In the limit  $\nu = 0$ ,  $G_2$  gluodynamics with a first order deconfinement phase transition is recovered, in agreement with the findings in [129]. In the other extreme case  $\nu \rightarrow \infty$  one ends up with  $SU(3)$  gluodynamics with a weak first order deconfinement transition. For large values of  $\beta$  a second order phase transition is expected, with increasing vacuum expectation value  $\nu$  of the Higgs field. Here the natural question arises, whether the first order deconfinement transition connects  $G_2$  and  $SU(3)$  gluodynamics. Then a single tri-critical point may exist, where the first order transition line meets the second order transition line. In this point, all three phases, the confinement phase and the symmetric and broken deconfinement phases, meet. In another possible scenario the first order transition line ends and turns into a crossover, such that the confinement phase is analytically connected to both deconfinement phases.

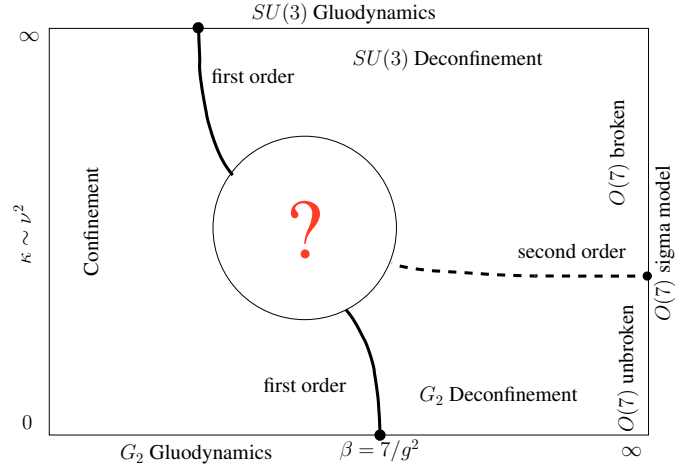


**Figure 6.1** Expected phase diagram in the parameter space  $(7/g^2, \kappa)$ .

In the limit  $\nu = 0$ ,  $G_2$  gluodynamics with a first order deconfinement phase transition is recovered, in agreement with the findings in [129]. In the other extreme case  $\nu \rightarrow \infty$  one ends up with  $SU(3)$  gluodynamics with a weak first order deconfinement transition. For large values of  $\beta$  a second order phase transition is expected, with increasing vacuum expectation value  $\nu$  of the Higgs field. Here the natural question arises, whether the first order deconfinement transition connects  $G_2$  and  $SU(3)$  gluodynamics. Then a single tri-critical point may exist, where the first order transition line meets the second order transition line. In this point, all three phases, the confinement phase and the symmetric and broken deconfinement phases, meet. In another possible scenario the first order transition line ends and turns into a crossover, such that the confinement phase is analytically connected to both deconfinement phases.

## 6.1 The phase diagram of the $G_2$ Higgs model: overview

To investigate this model on the lattice, the IHMC algorithm described in chapter 3 is used. The corresponding lattice action to (6.3) for the  $G_2$  valued link variables and a normalized Higgs field with 7 real components reads as

$$S_{\text{YMH}}[\mathcal{U}, \Phi] = \beta \sum_{\square} \left( 1 - \frac{1}{7} \text{tr Re } \mathcal{U}_{\square} \right) - \kappa \sum_{x, \mu} \Phi_{x+\hat{\mu}} \mathcal{U}_{x, \mu} \Phi_x, \quad \Phi_x \cdot \Phi_x = 1. \quad (6.6)$$

It depends on the inverse gauge coupling  $\beta$  and the hopping parameter  $\kappa \sim \nu^2$ . In the following the phases and transition lines of Fig. 6.1 are localized and analysed with high statistics simulations of the

Polyakov loop distribution and susceptibility, plaquette and Higgs action susceptibilities, and finally with derivatives of the mean action with respect to the hopping parameter  $\kappa$ . Besides the transition lines indicated in Fig. 6.1, it is expected that there exists another line of monopole driven bulk transitions. This line emanates from the bulk crossover in pure  $G_2$  gluodynamics at  $\beta = 9.45$  [129]. This bulk crossover does not scale with the volume and temperature. On small lattices it interferes with the deconfinement phase transition, but for lattices with temporal extent  $N_t \geq 6$  the transitions in pure  $G_2$  gluodynamics are well separated. This bulk crossover is also investigated at finite  $\nu$  to ensure that it stays far below the deconfinement transition for all values of  $\nu$ . With the help of the local HMC algorithm sketched previously, several relevant observables are calculated to probe the phases and phase transition lines in the  $(\beta, \kappa)$  plane.

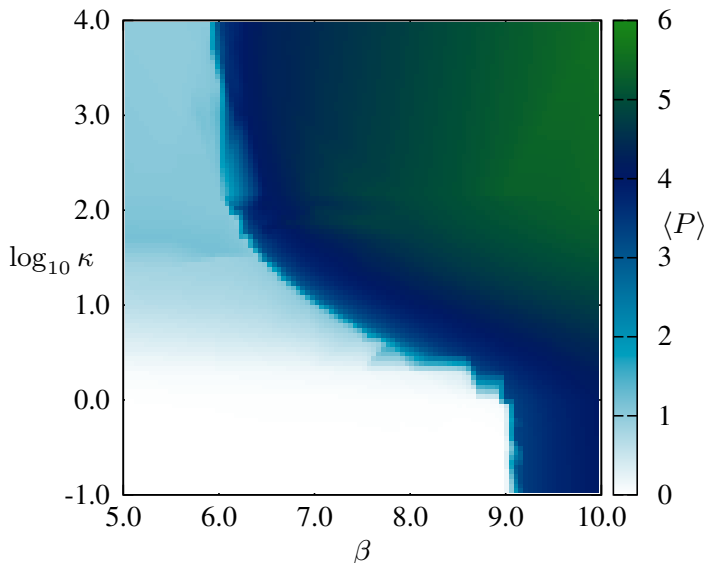


**Figure 6.2** Expectation values of  $P$  in the coupling constant plane and on a small  $12^3 \times 2$  lattice

First, the phase diagram obtained on small lattices is presented. For vanishing  $\kappa$ ,  $G_2$  gluodynamics is recovered, which shows a first order finite temperature deconfinement phase transition. The transition is discontinuous since there is a large mismatch of degrees of freedom in the confined and unconfined phases. At the other extreme value  $\kappa = \infty$ , six of the fourteen gauge bosons decouple from the dynamics and  $SU(3)$  gluodynamics is recovered, which shows a first order deconfinement phase transition as well. The question arises, whether the first order transitions in  $G_2$  and  $SU(3)$  gluodynamics are connected by an unbroken line of first order transitions or whether there are two critical endpoints. In the latter case the confined

and unconfined phases could be connected continuously. On the other hand, for arbitrary  $\kappa$  but  $\beta \rightarrow \infty$ , the gauge degrees of freedom decouple from the dynamics and a non-linear  $O(7)$  sigma model remains. It is expected that the  $O(7)$  symmetry is spontaneously broken to  $O(6)$  for sufficiently large values of the hopping parameter and that this transition is of second order.

In order to localize the confinement-deconfinement transition line(s), first the Polyakov loop expectation value is measured as (approximate) order parameter for confinement on a small  $12^3 \times 2$  lattice in a large region of parameter space ( $\beta = 5 \dots 10$ ,  $\kappa = 0 \dots 10^4$ ). For  $\kappa \gg 1$  the Polyakov loop takes its values in the reducible representation  $(3) \oplus (\bar{3}) \oplus (1)$  of  $SU(3)$  and approximately satisfies

$$\langle P \rangle \approx 1 + \langle P + \bar{P} \rangle_{SU(3)}. \quad (6.7)$$

Thus, for large  $\kappa$ ,  $\langle P \rangle \approx 1$  in the confining phase and  $\langle P \rangle \approx 7$  or  $\langle P \rangle \approx -2$  in the unconfined phase, where  $P$  is near one of the three centre elements of  $SU(3)$ , should be found. This ambiguity of assigning a value to the Polyakov loop in the unconfined phase is eliminated by mapping values with  $\langle P \rangle < 1$  to

$3 - 2\langle P \rangle$ . The result for  $\langle P \rangle$  is depicted in Fig. 6.2. It is observed, that in the confining phase the expectation value varies from 0 to 1 when the hopping parameter increases. For large values of  $\beta$  in the unconfined phase, the Polyakov loop is near the identity or (for large  $\kappa$ ) near one of the three centre elements of  $SU(3)$ . On the small lattice the Polyakov loop jumps along a continuous curve connecting the confinement-deconfinement transitions of pure  $G_2$  and pure  $SU(3)$  gluodynamics. This suggests that there exists a connected first order transition curve all the way from  $\kappa = 0$  to  $\kappa = \infty$ . To see whether this is indeed the case, high-precision simulations on larger lattices are performed. A careful analysis of histograms and susceptibilities for Polyakov loops and the Higgs action shows, that the first order lines starting at  $\kappa = 0$  and at  $\kappa = \infty$  do not meet. This happens in a rather small region in parameter space in a way that the two first order lines almost meet. They may be connected by a line of continuous transitions or in-between there may exist a window connecting the confined and unconfined phases smoothly.

For  $\beta \rightarrow \infty$  one is left with a non-linear  $O(7)$  sigma model with action

$$S_\sigma = -\kappa \sum_{x,\mu} \Phi_{x+\hat{\mu}} \Phi_x, \quad (6.8)$$

and this model shows a second order transition at a critical coupling  $\kappa_c$  from a  $O(7)$  symmetric to a  $O(6)$  symmetric phase. To see how this transition continues to finite values of  $\beta$ , the expectation values  $\langle \mathcal{O}_P \rangle$  and  $\langle \mathcal{O}_H \rangle$  of the (averaged) plaquette variable and Higgs action

$$\mathcal{O}_P = \frac{1}{7 \cdot 6 \cdot V} \sum_{\square} \text{Re tr } \mathcal{U}_{\square} \quad \text{and} \quad \mathcal{O}_H = \frac{1}{V} \sum_{x\mu} \Phi_{x+\hat{\mu}} \mathcal{U}_{x,\mu} \Phi_x. \quad (6.9)$$

are measured together with the corresponding susceptibilities

$$\chi(\mathcal{O}) = V (\langle \mathcal{O}^2 \rangle - \langle \mathcal{O} \rangle^2). \quad (6.10)$$

The finite size scaling theory predicts, that near the transition point the maximum of the susceptibilities scales with the volume to the power of the corresponding critical exponent  $\gamma$

$$\chi(\mathcal{O}) \sim aL^{\gamma/\nu} + b, \quad (6.11)$$

where  $\nu$  is the critical exponent related to the divergence of the correlation length. For a first order phase transition it is expected, that the susceptibility peak scales linearly with the spatial volume (since  $N_t$  is fixed). More precisely, for a first order transition  $\gamma = 1$  and  $\nu = 1/3$  are expected, while for a second order transition  $\gamma \neq 1$  is valid [177].

The expectation values and logarithms of susceptibilities on a small  $6^3 \times 2$ -lattice are depicted in Fig. 6.3. The expectation value of a plaquette variable jumps at the deconfinement transition line and the corresponding susceptibility is peaked. This is in full agreement with the jump of the Polyakov loop across this transition line. The expectation value of the Higgs action and the corresponding susceptibility both spot the deconfinement transition well. However, they also discriminate between the  $O(7)$  unbroken and broken phases. The data on the small lattice point to a second order Higgs transition line in the YMH model for all  $\beta > \beta_{\text{deconf}}(\kappa)$ . This could imply that the second order line ends at the first order

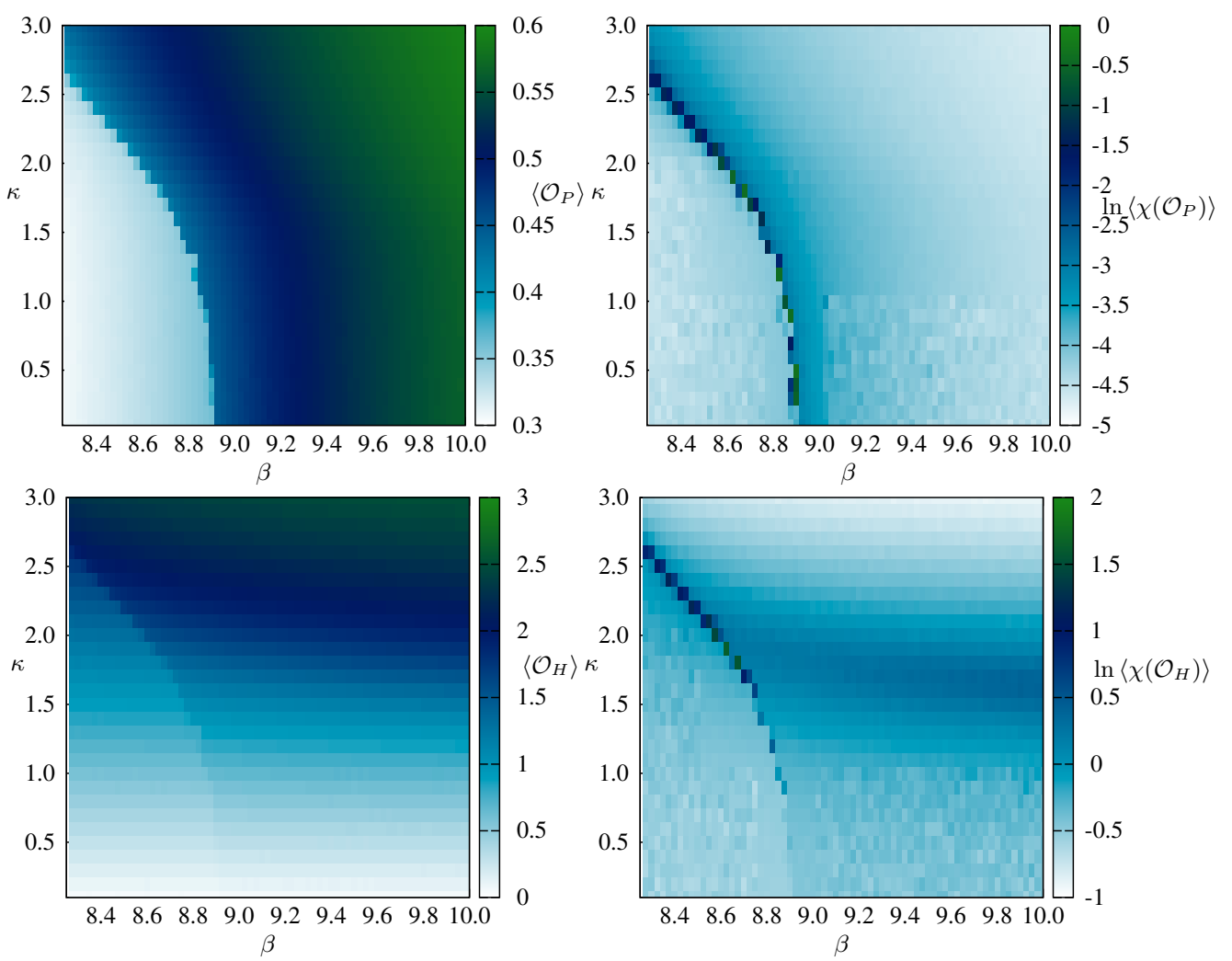


**Figure 6.3** Average plaquette, Higgs action, and susceptibilities near the critical point on  $6^3 \times 2$  lattice.

deconfinement transition line. To determine the order of the Higgs transition line, the finite size scaling of

$$\chi(\mathcal{O}_H) = \frac{\partial}{\partial \kappa} \langle \mathcal{O}_H \rangle \quad \text{and} \quad \chi^{(2)}(\mathcal{O}_H) = \frac{\partial^2}{\partial^2 \kappa} \langle \mathcal{O}_H \rangle \quad (6.12)$$

is considered for lattices up to  $20^3 \times 6$ . The results presented below show that the Higgs transitions are second order transitions. Unfortunately it cannot be excluded, that the second order line turns into a crossover near the deconfinement transition line.

The results for the complete phase diagram in the  $(\beta, \kappa)$  plane, as calculated on a larger  $16^3 \times 6$  lattice, are summarized in Fig. 6.4. Histograms and susceptibilities near the marked points on the transition lines in this figure are calculated. If the triple point exists, an extrapolation to the point where the confined phase meets both unconfined phases leads to the couplings  $\beta_{\text{trip}} = 9.62(1)$  and  $\kappa_{\text{trip}} = 1.455(5)$ . Near this point the deconfinement transition is very weak, continuous, or absent and thus high-statistics simulations on larger lattices have been performed to investigate this region in parameter space more carefully. Some of the results are presented in the following sections. Up to a rather small region surrounding  $(\beta_{\text{trip}}, \kappa_{\text{trip}})$  it turned out, that the deconfinement transition is first order and the Higgs transition is second order. However, in this small region around the *would-be* triple point, the deconfinement transition is

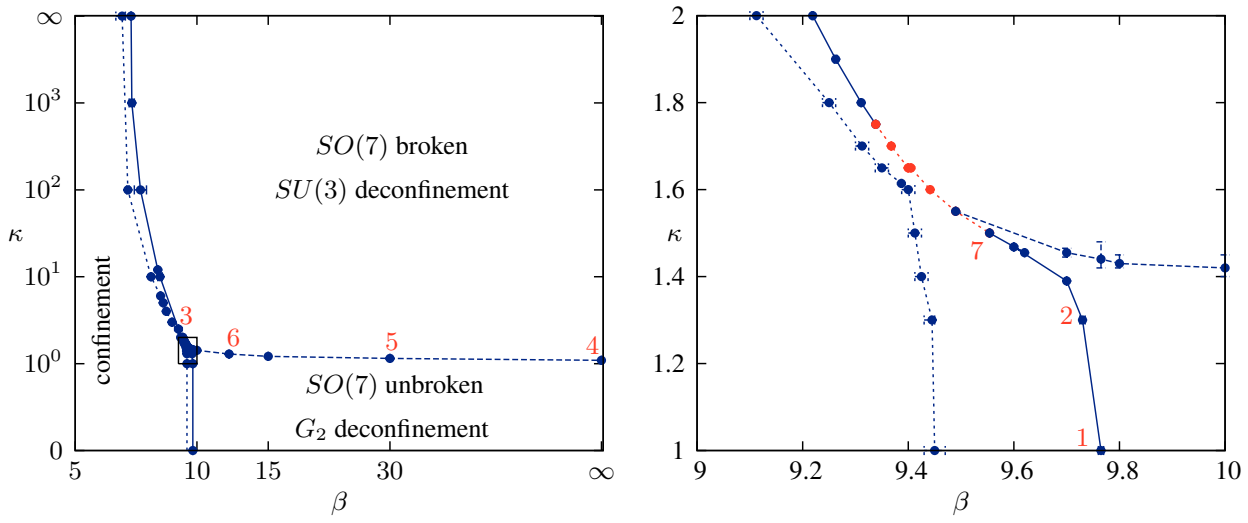


**Figure 6.4** Phase transition lines on a  $16^3 \times 6$  lattice. The solid line corresponds to the first order deconfinement transitions, the dashed line to the second order Higgs transitions and the dotted line to the left of the first order line to the bulk transitions. The plot on the right panel shows the details inside the small box in the plot on the left panel, where the transition lines almost meet. The dotted line between the first order lines corresponds to a window, where the transition is a crossover or a continuous one. The points 1-7 are discussed in the text and the points 2, 3 and 7 have been investigated previously by Pepe and Wiese [58].

either second order or absent. For a comparison with the results of Pepe and Wiese, their work [58] is included at points 2 ( $\kappa = 1.3$ ), 7 ( $\kappa = 1.5$ ) and 3 ( $\kappa = 4$ ). A qualitative agreement between the results, obtained in this work and their results is found, although they performed simulations on different lattices.

### 6.1.1 The bulk transition

The existence of a bulk transition in lattice gauge theories at zero temperature can influence its finite temperature behaviour. Such transitions are almost independent of the size of the lattice and are driven by lattice artifacts [178]. Bulk transitions between the unphysical strong coupling and the physical weak coupling regimes in lattice gauge theories are the rule rather than the exception. The strong coupling bulk phase contains vortices and monopoles, which disorder Wilson loops down to the ultraviolet length scale given by  $a^2\sigma \sim \mathcal{O}(1)$  [179, 180]. In the weak coupling phase the short distance physics is determined by asymptotic freedom and  $a^2\sigma \ll 1$ . Both  $SU(2)$  and  $SU(3)$  lattice theories exhibit a rapid crossover between the two phases, which becomes more pronounced for  $SU(4)$  [179]. For  $SU(N)$  with  $N \geq 5$  the bulk transition is first order [179].  $SU(3)$  lattice gauge theory with mixed fundamental ( $f$ ) and adjoint ( $a$ ) actions shows a first order bulk transition for large  $\beta_a$  and small  $\beta_f$ . For decreasing  $\beta_a$  the transition line terminates at a critical point and turns into a crossover touching the line  $\beta_a = 0$ . On lattices with  $N_t = 2$  the deconfinement transition line joins the bulk transition line smoothly from below and for  $N_t \geq 4$  from above [181, 182]. More relevant is the finding in [129], that the bulk transition in pure  $G_2$  gauge theory at  $\beta = 9.45$  is a crossover [129].

The values for the plaquette variables and Polyakov loops from the strong to the weak coupling regime

are scanned, to find a bulk transition that might interfere with the finite temperature deconfinement transition. For various values between  $\kappa = 0$  and  $\kappa = \infty$  on a  $12^3 \times 6$  and  $16^3 \times 6$  lattice the position and nature of the bulk transitions is determined. In full agreement with [129] a crossover at  $(\beta, \kappa) \approx (9.44, 0)$  is seen, which is visible as a broad peak in the plaquette susceptibility depicted in the right panel of Fig. 6.5. The Polyakov loop does not detect this crossover. Note that for small  $\kappa$  the position of the bulk

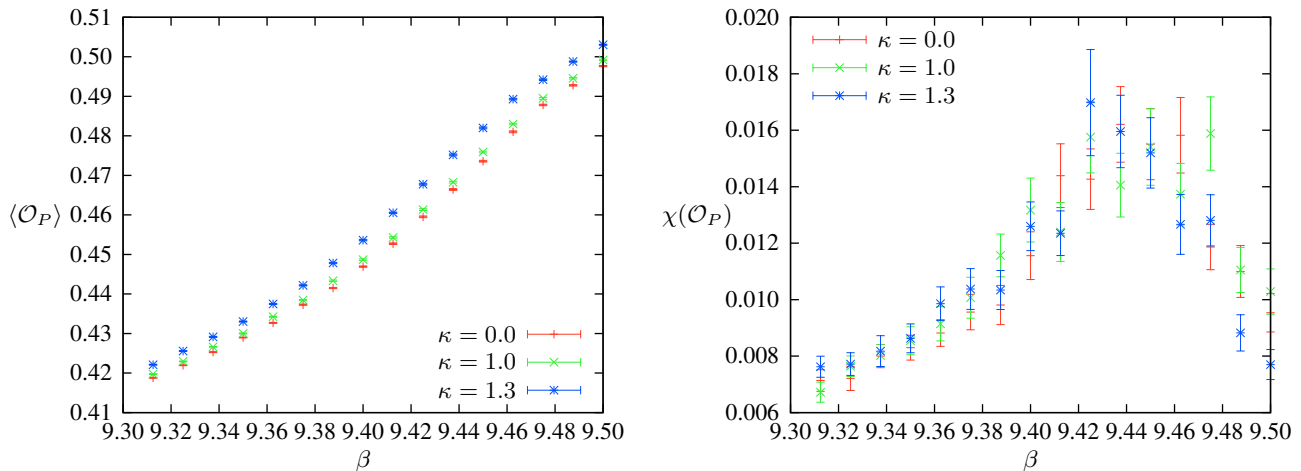


**Figure 6.5** Plaquette (left panel) and susceptibility (right panel) for small values of  $\kappa$  near the bulk transition on a  $12^3 \times 6$  lattice.

transition does not depend on the hopping parameter, which means that the bulk transition line hits the line  $\kappa = 0$  vertically. Despite the broad peak in the susceptibility of the plaquette density, the bulk and deconfinement transition are clearly separated, and this agrees with the results in [183]. In the region  $1.3 \leq \kappa \leq 1.6$  the critical coupling  $\beta_c$  decreases with increasing  $\kappa_c$ , but the nature of the transition does not change much, as can be seen in Fig. 6.6 (top row). The plaquette density seems to be a continuous function of  $\beta$  and  $\kappa$ , and we conclude that the transition is still a crossover.

Between  $\kappa = 1.6$  and  $\kappa = 1.65$  the peak in the bulk transition  $\kappa$  becomes pronounced. In this region the distance between the bulk and deconfinement transitions becomes very small. Nevertheless, it is expected that the extremely localized bulk transition still does not interfere with the weak deconfinement transition. For values of  $\kappa$  between 1.65 and approximately 2.5 the position of the bulk transition gets more sensitive to the hopping parameter, and the distance to the deconfinement transition line increases again. The nature of the transition changes at the same time. A large gap in the action density separates the strong coupling from the weak coupling region. This is depicted in Fig. 6.6 (bottom row). The many data points taken at  $\kappa = 1.8$  show, that the size of the gap does not depend on the volume, and this points to a first order transition. For  $\kappa \gtrsim 2.5$  the situation changes again. The gap in the plaquette density closes and the position of the bulk transition tends to that of the bulk transition in  $SU(3)$  gluodynamics, which again is a crossover. There is ample evidence that bulk transitions are driven by monopoles on the lattice [178]. Consequently, the density of monopoles [181] as a function of  $\beta$  for  $\kappa = 0$  and  $\kappa = 1.8$  is calculated. The density  $M$  together with the plaquette variable are plotted in Fig. 6.7. For  $\kappa = 0$  they vary smoothly with  $\beta$ , as expected for a crossover, but for  $\kappa = 1.8$  they jump at the same  $\beta \approx 9.25$ . The

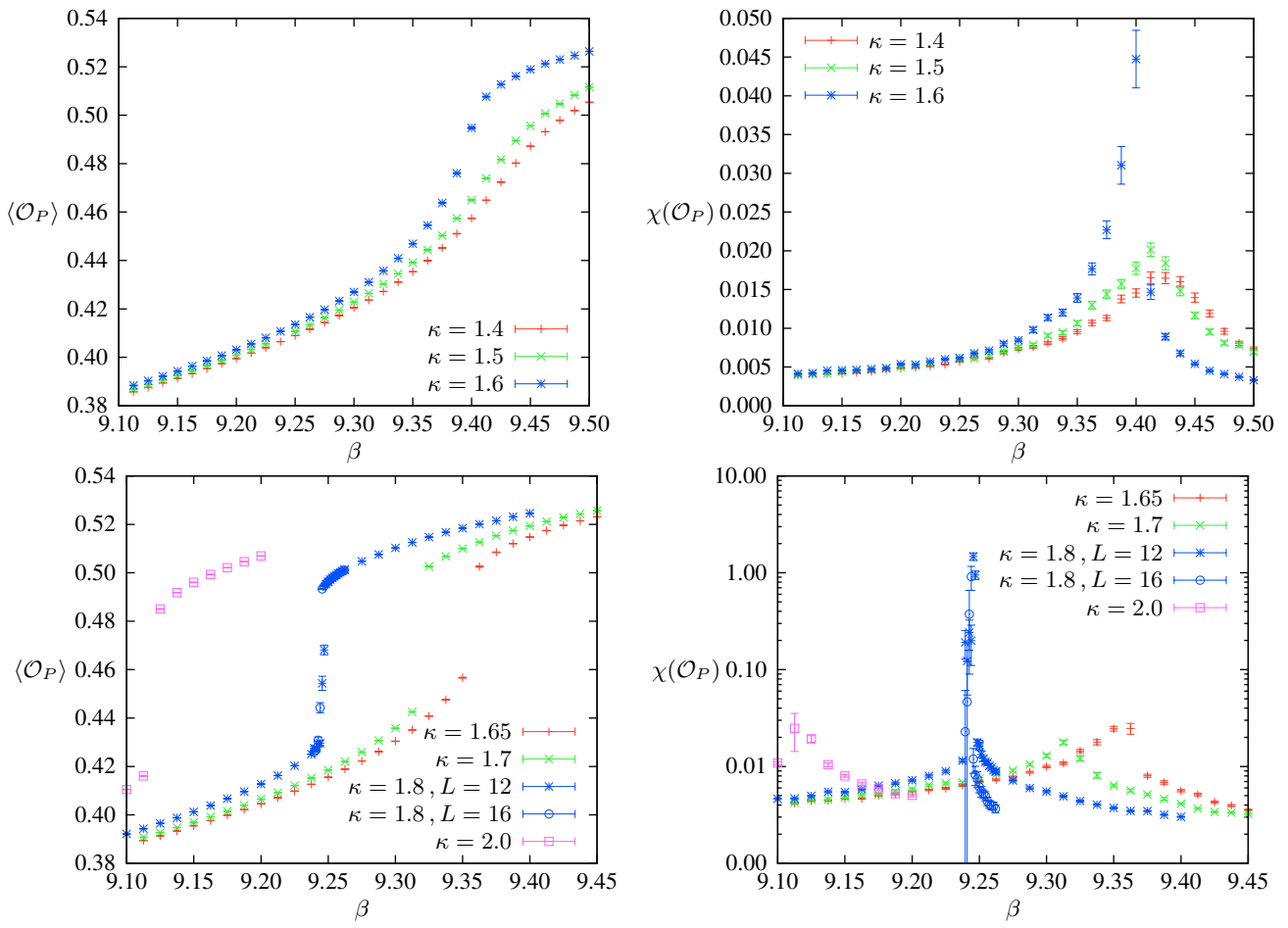


**Figure 6.6** Plaquette (left panel) and susceptibility (right panel) for intermediate values of  $\kappa$  near the bulk transition on a  $12^3 \times 6$  lattice.

height of the jump does not depend on the lattice size, see Fig. 6.7 (right panel). Thus one finds strong evidence that the bulk transition is intimately related to the condensation of monopoles in the strong coupling  $G_2$  Higgs model.

Finally, it is necessary to comment on the behaviour near  $\kappa = 1.6$ . Here the  $G_2$  Higgs model behaves similar to  $SU(3)$  gluodynamics with mixed fundamental and adjoint actions. The latter shows a first order bulk transition which turns into a crossover for small  $\beta_a$ . It seems that for  $\kappa \gtrsim 1.6$  the massive  $G_2$  gluons are heavy enough, such that the approximate centre symmetry of the unbroken  $SU(3)$  is at work. This may explain why a first order transition for  $\kappa \gtrsim 1.6$  is found.

## 6.2 The transition lines away from the triple point

In this section again the confinement-deconfinement transition is investigated. Sufficiently far away from the suspected triple point at  $\beta_{\text{trip}} = 9.62(1)$  and  $\kappa_{\text{trip}} = 1.455(5)$ , the signals for first and second order phase transitions are unambiguous and are presented in this section. The measurements taken near the would-be triple point are less conclusive and will be presented and analysed in the following section.

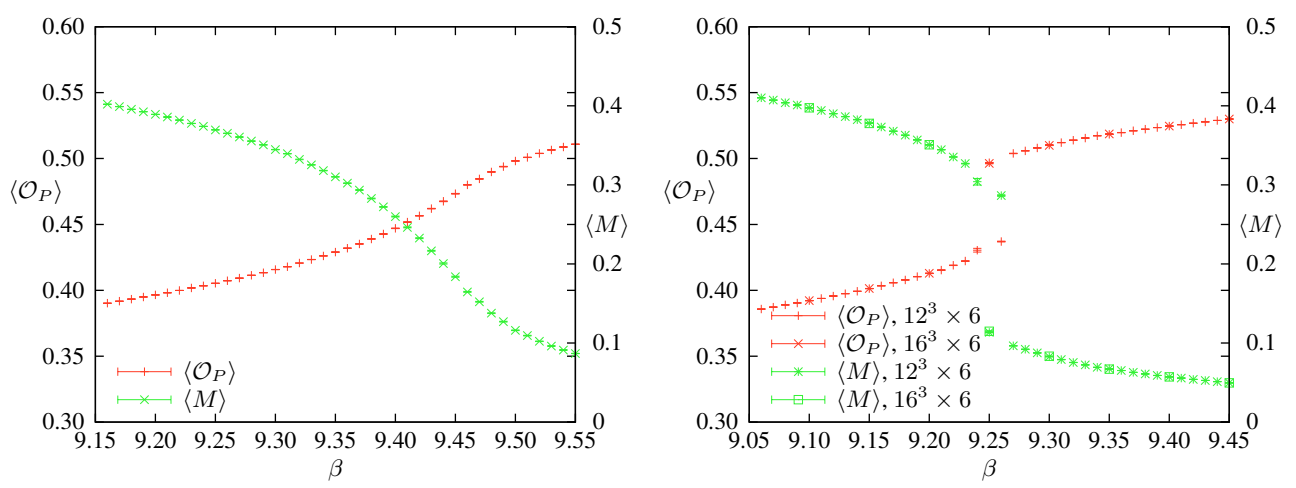


**Figure 6.7** Plaquette and monopole density for  $\kappa = 0$  and  $\kappa = 1.8$  on a  $12^3 \times 6$  and  $16^3 \times 6$  lattice.

## 6.2.1 The confinement-deconfinement transition line

Already the histograms for the Polyakov loop show, that the deconfinement transition is first order for values of the hopping parameter  $\kappa$  in the intervals  $[0, 1.4]$  and  $[1.7, \infty]$ . Two typical distributions for

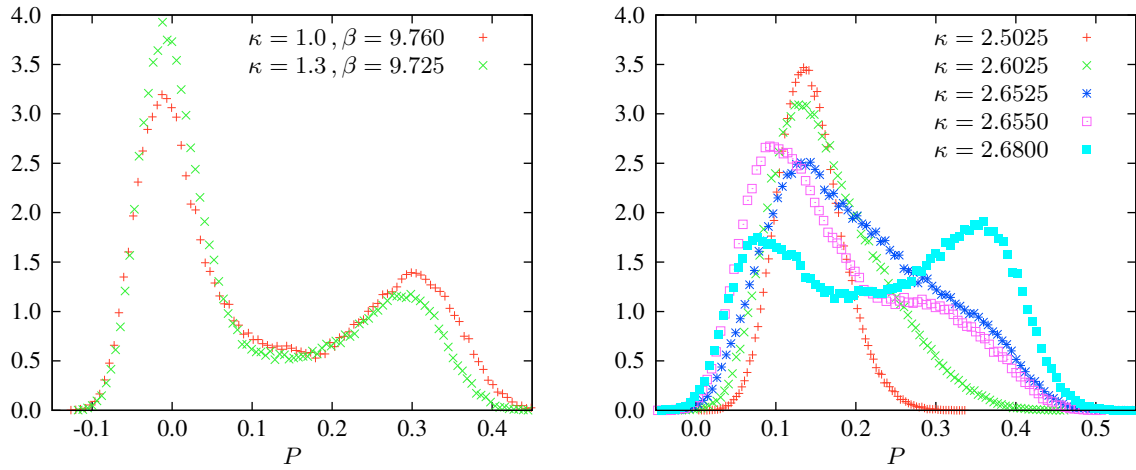


**Figure 6.8** Distributions of the Polyakov loop on a  $16^3 \times 6$  lattice. Left panel:  $(\beta, \kappa) = (9.76, 1)$  and  $(9.725, 1.3)$ ; Right panel:  $\beta = 9$  and various values of the hopping parameter.

$\kappa = 1.0$  and  $\kappa = 1.3$ , corresponding to the points 1 and 2 in the phase diagram in Fig. 6.4, are depicted in Fig. 6.8 (left panel). These and other histograms with  $\kappa \lesssim 1.4$  show a clear double peak structure near the transition line and are almost identical to the histogram for  $\kappa = 0$ . Similar results are obtained for larger hopping parameters  $\kappa \gtrsim 1.7$ .

In Fig. 6.8 (right panel), histograms of the Polyakov loops for  $\beta = 9$  and hopping parameters in the vicinity of  $\kappa \approx 2.6$  are plotted, corresponding to point 3 in Fig. 6.4. The histograms with  $\kappa \leq 2.6525$  show peaks at almost the same positions. The systems with these small values of  $\kappa$  are in the confined phase. For larger  $\kappa$  values the peak moves towards the ‘would-be’ centre elements of the subgroup  $SU(3)$  and a second peak appears. Again the double-peak structure of the distribution points to a first

order transition. The spatial sizes of the lattices are varied and no finite size effects in the distributions for  $N_s \geq 16$  are observed.

## 6.2.2 The Higgs transition line

For  $\beta \rightarrow \infty$  the gauge degrees of freedom are frozen and a non-linear  $O(7)$  sigma model is recovered, which shows a second order transition from an  $O(7)$  symmetric massive phase to an  $O(6)$  symmetric massless phase. With the help of a cluster algorithm [106] the constrained scalar field is updated and the susceptibility of

$$\mathcal{O}_\sigma = \frac{1}{V} \sum_{x,\mu} \Phi_{x+\hat{\mu}} \Phi_x, \quad \chi(\mathcal{O}_\sigma) = -\frac{1}{\kappa V} \partial_\kappa \langle S_\sigma \rangle, \quad (6.13)$$

is calculated, which is proportional to the sigma model action  $S_\sigma$  in (6.8). The results of the simulations on lattices with varying spatial sizes are depicted in Fig. 6.9. The susceptibility of the action becomes

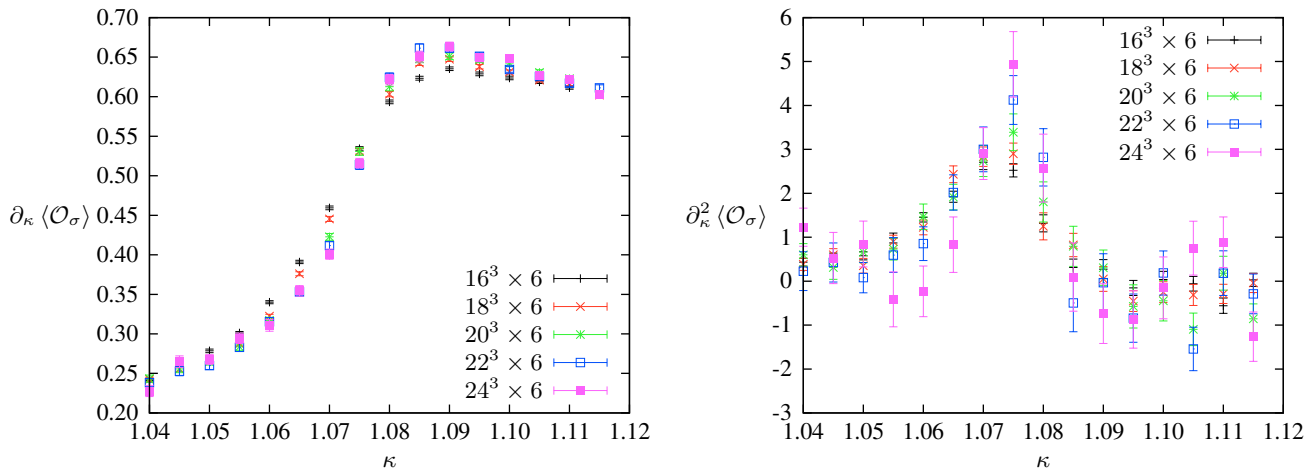


**Figure 6.9** The first and second derivative of the average sigma model action for different spatial lattice sizes.

steeper as the spatial volume increases, while the peak of the (normalized) second derivative also increases. This means that the system undergoes a second order transition at  $\kappa_c = 1.075(5)$  (corresponding to point 4 in Fig. 6.4) from a massive  $O(7)$  symmetric phase with vanishing vacuum expectation value to a massless  $O(6)$  symmetric phase with non-vanishing expectation value. Actually, the mean field theory for  $O(n)$  models in  $d$  dimensions predicts a second order transition at the critical coupling  $\kappa_{c,\text{mf}} = n/2d$ . For the model in 4 dimensions the mean-field prediction is  $\kappa_{c,\text{mf}} = 7/8 \approx 0.875$ , which is not far from the numerical value.

For smaller values of  $\beta$  the gauge degrees of freedom participate in the dynamics and  $\partial_\kappa \langle S \rangle$  is now proportional to the susceptibility of  $\mathcal{O}_H$  in (6.9). The plots in Figs. 6.10 and 6.11 show a similar behavior of the first and second derivatives of the average Higgs action for  $\beta = 30$  and 12, corresponding to the points 5 and 6 in the phase diagram in Fig. 6.4. Even for the smaller value  $\beta = 12$ , it can be seen that the susceptibility becomes steeper with increasing lattice size, while the second derivative of the average

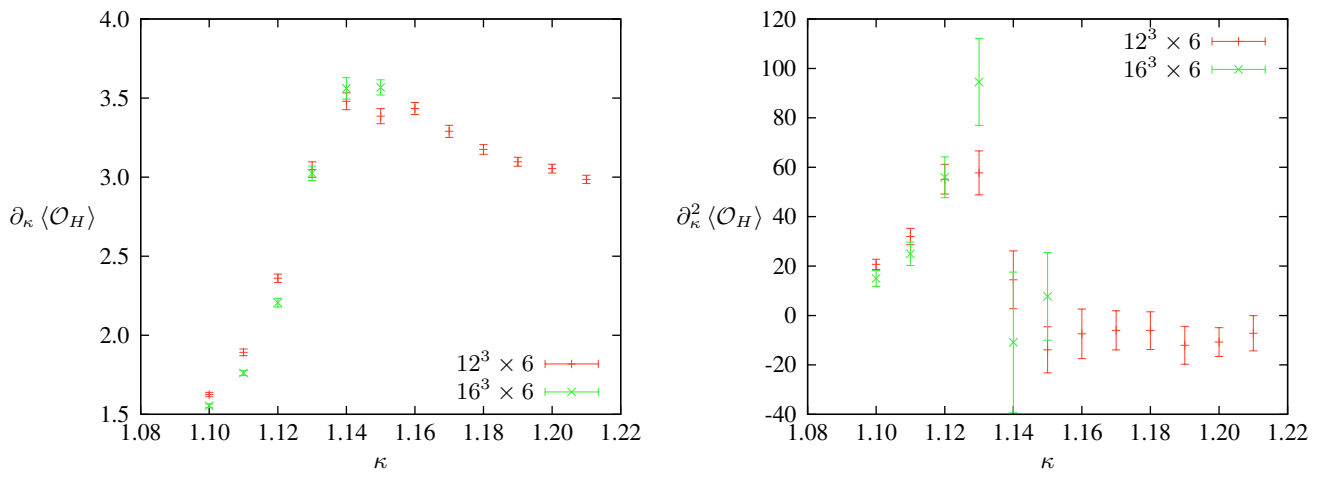


**Figure 6.10** First and second derivative of the average action with respect to the hopping parameter for different spatial lattice sizes at  $\beta = 30$ .

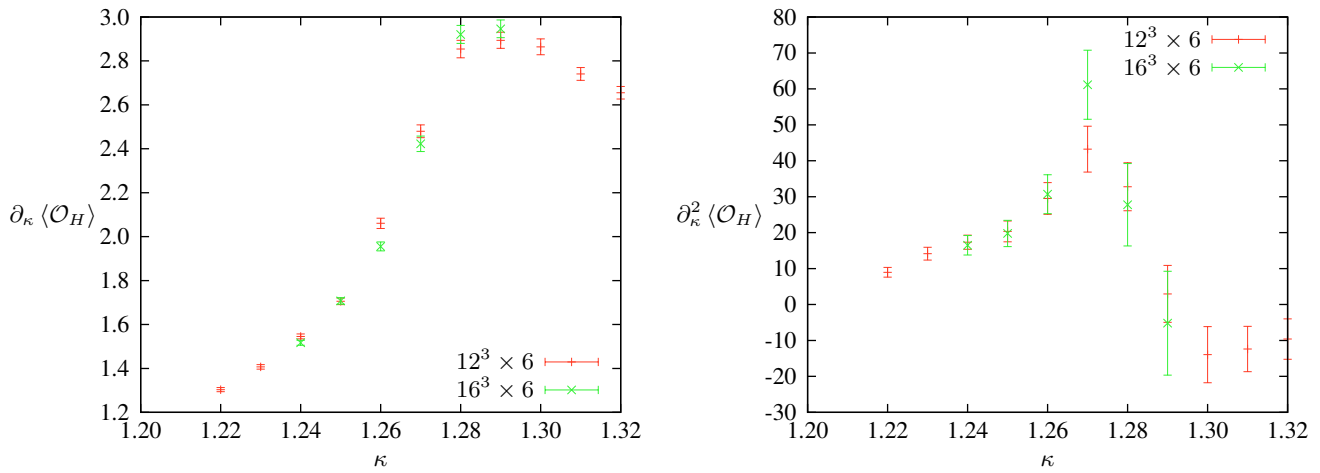


**Figure 6.11** First and second derivative of the average action with respect to the hopping parameter for different spatial lattice sizes at  $\beta = 12$ .

action increases. This already demonstrates that the second order transition at the asymptotic region  $\beta \rightarrow \infty$  extends to smaller values of  $\beta$ .

### 6.3 The transition lines near the triple point

When the first order transition gets weaker, it becomes increasingly difficult to distinguish it from a second order transition or a crossover. For example, the four histograms in Fig. 6.12 (left panel) show distributions of the Polyakov loop at point 7 in the phase diagram depicted in Fig. 6.4, corresponding to  $\kappa = 1.5$  and  $\beta$  varying between 9.5525 and 9.5550. All histograms are computed from 400 000 configurations on a medium size  $16^3 \times 6$  lattice. The histogram on top left shows a pronounced peak at  $P \approx 0.1$ , corresponding to the value in the confined phase. With increasing  $\beta$  a second peak builds up at  $P \approx 0.25$ , corresponding to a value in the unconfined phase. A lot more histograms have been

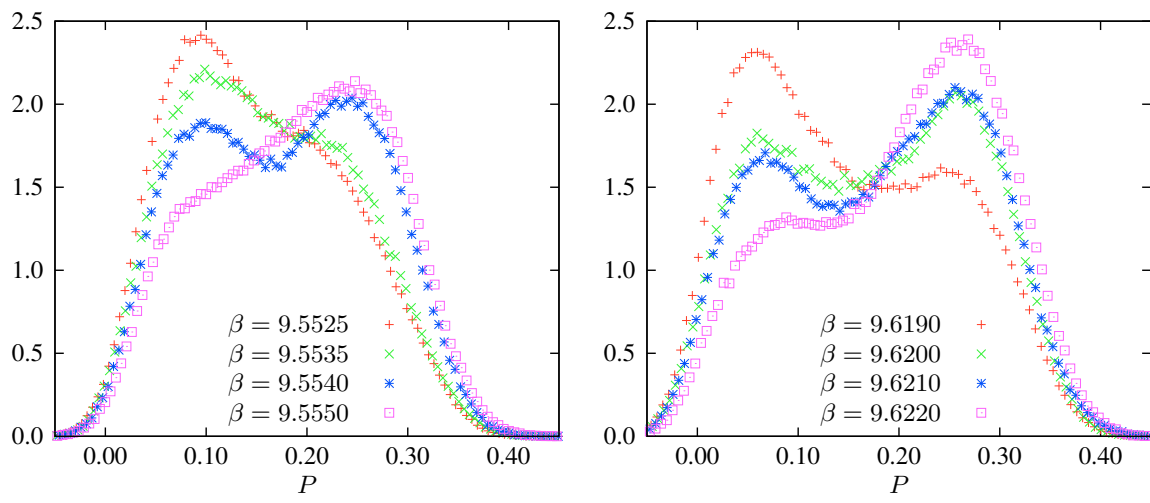


**Figure 6.12** *Left panel:* Distributions of the Polyakov loop at  $\kappa = 1.5$ , where the transition is weakly first order on a  $16^3 \times 6$  lattice with 400 000 configurations for each histogram. *Right panel:* Distribution of the Polyakov loop at  $(\beta, \kappa) = (9.6190, 1.455) - (9.6220, 1.455)$  near the supposed triple point; 400 000 configurations on  $16^3 \times 6$  lattice.

calculated and will allow to conclude that the well separated peaks in the distribution are of equal heights for  $\beta_c \approx 9.5535$ . At this point the Polyakov loop jumps from the smaller to the larger value. For even larger values of  $\beta$  the second peak at larger  $P$  takes over and the system is in the unconfined phase.

Although the histograms point to a weakly first order transition, at this point it is not possible to rule out that the transition at  $\kappa = 1.5$  and  $\beta \approx 9.5535$  is of second order. Later it is found to be a first order transition. When slightly decreasing the value of  $\kappa$ , the signal for a first order transition is more pronounced. This is illustrated in the Polyakov loop histograms depicted in Fig. 6.12 (right panel). If further increasing the value from  $\kappa = 1.5$  to  $\kappa = 1.55$ , the peak of the Polyakov loop does not jump at the transition point at  $\beta \approx 9.4885$ . Instead, it increases smoothly from  $P \approx 0.12$  in the confinement phase to  $P \approx 0.24$  in the deconfinement phase, as seen in Fig. 6.13. Therefore it can be conjectured, that in this region of parameter space the first order transition turns into a continuous transition or a crossover, which is later confirmed by an even more careful analysis. Next, the size-dependence of the average Polyakov loop, plaquette variable, and Higgs action per lattice site are studied together with their susceptibilities. The following results are obtained on lattices with  $N_t = 6$  and spatial extents  $N_s \in \{12, 16, 20, 24\}$  and for  $\beta = 9.5535$ . This corresponds to points in the neighborhood of point 7 in the phase diagram in Fig. 6.4. Fig. 6.14 shows the  $\kappa$ -dependence of the Polyakov loop and its susceptibility for the four different lattices. The measurements have been taken at 20 different values of the hopping parameter in the vicinity of  $\kappa = 1.5$ . In this way the phase transition line is crossed almost vertically in the  $\kappa$ -direction at the transition point 7 in the phase diagram in Fig. 6.4. The  $\kappa$ -dependence has been calculated with the reweighting method. Later it turned out that the peak of the susceptibility at  $\kappa_c \approx 1.501$  scales linearly with the volume. This linear dependence is characteristic for a first order transition. The plots in Fig. 6.15 show the  $\kappa$  dependence of the average plaquette variable and the corresponding susceptibility for the four lattices. Again it is observed that the susceptibility peak at  $\kappa_c \approx 1.501$  increases linearly

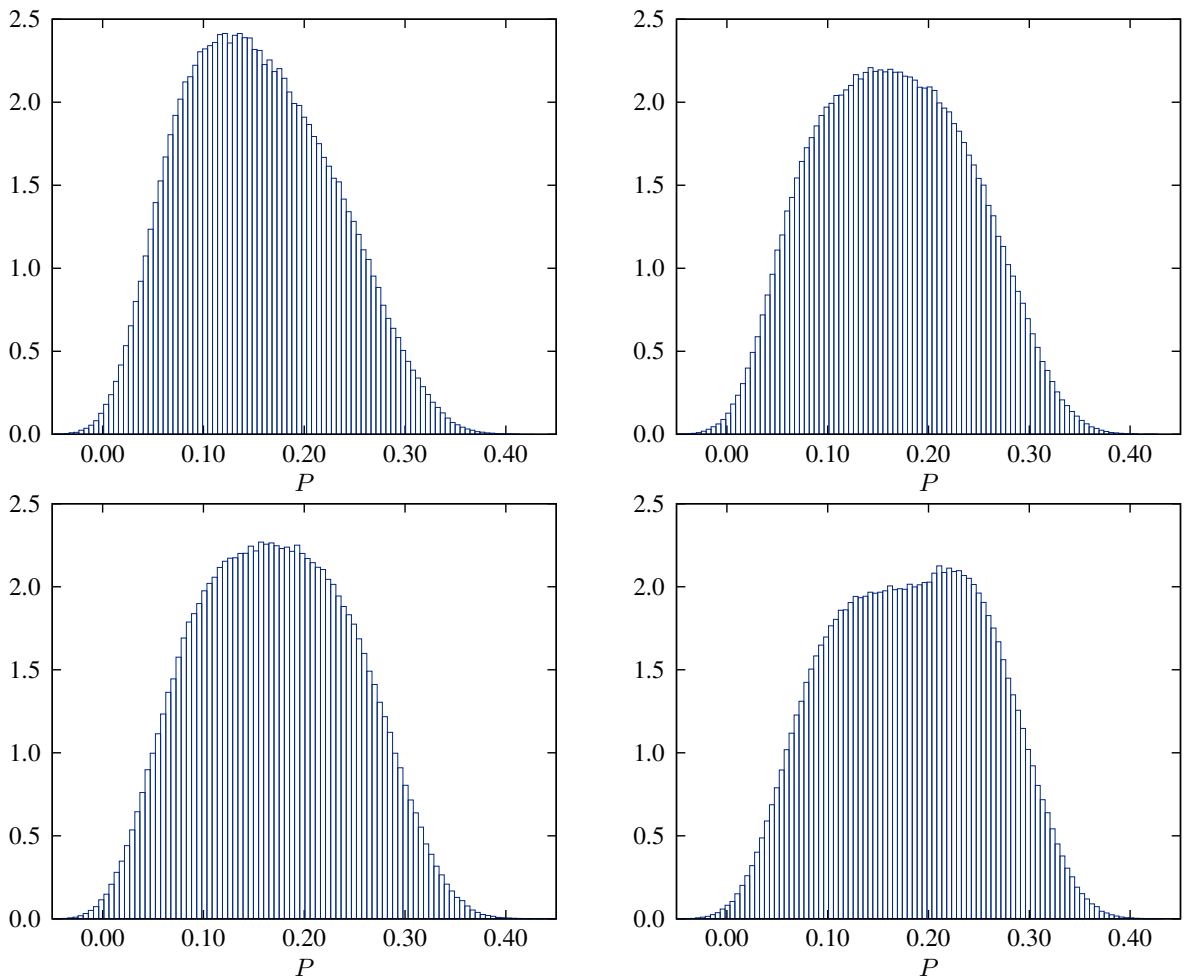


**Figure 6.13** Distributions of the Polyakov loop at  $\kappa = 1.55$  where the transition is probably not first order on a  $16^3 \times 6$  lattice with 800 000 configurations for each histogram. Top left  $\beta = 9.4875$ , top right  $\beta = 9.4885$ , bottom left  $\beta = 9.4895$  and bottom right  $\beta = 9.4905$  ( $\beta_c \approx 9.4885$ ).

with the volume of the lattice. Also note that on the small  $12^3 \times 6$  lattice the peak in the susceptibility can hardly be seen. The two plots in Fig. 6.16 show the  $\kappa$  dependence of the average Higgs action per lattice point and corresponding susceptibility. Similarly as for the Polyakov loop and the plaquette, a peak of the susceptibility is observed at the same value  $\kappa_c \approx 1.501$ . To check for finite size scaling, the susceptibilities, corresponding to the Polyakov loop, plaquette variable, and Higgs action per site as a function of the volume are investigated. The results are plotted in Fig. 6.17 (left panel). For an easier comparison, the data points are normalized by the peak value for the largest lattice with lattice size  $N_s = 24$ . The linear dependence of the peak of the susceptibilities on the volume is clearly visible for the larger three lattices, and this linear dependence is predicted by a first order transition [177]. In recent studies of the lattice  $SU(2)$  Higgs model in [183] it turned out, that for  $N_s = N_t \lesssim 18$  the maxima of the susceptibilities are well described by a function of the form  $aL^4 + b$ , so that they seem to scale linearly with the volume, as expected for a first order transition at zero temperature. Simulations on larger lattices revealed however, that the susceptibility peaks all saturate at larger values of  $L$  and no singularities seems to develop in the thermodynamic limit. For the lattice  $G_2$  Higgs model considered

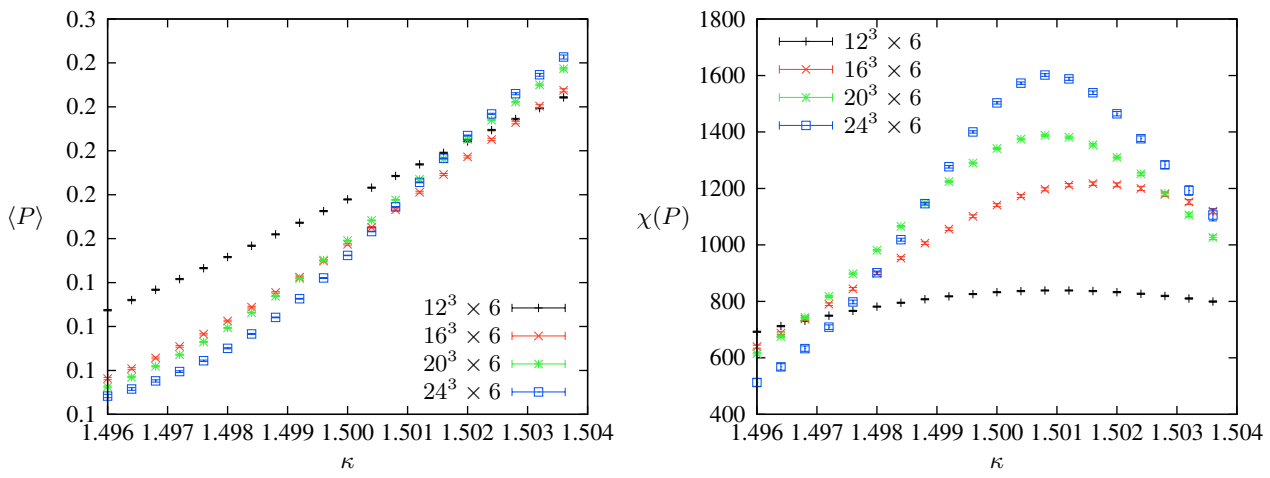


**Figure 6.14** Finite size scaling of Polyakov loop and Polyakov loop susceptibility at  $\beta = 9.5535$ .

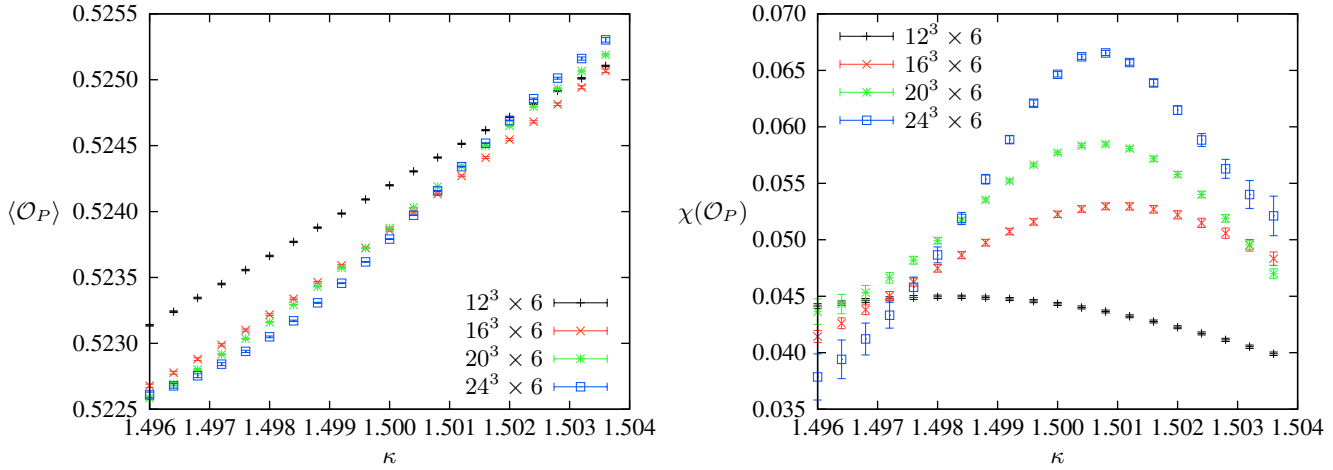


**Figure 6.15** Finite size scaling of the plaquette variable and its susceptibility for  $\beta = 9.5535$ .

in the present work, no flattening of the peaks is seen for larger lattices with  $N_s$  up to 24, and this is interpreted as a signal for a true first order transition. The table in the right panel of Fig. 6.17 shows the extrapolation of the critical hopping parameter to infinite volumes. Finally, for each lattice size the value  $\kappa_c(V)$  is calculated at which the Polyakov loop, plaquette, and Higgs action susceptibilities take their maxima. Note, that on the larger lattices with  $N_s = 20$  and 24, the three critical hopping parameters are the same within statistical errors and the resolution of the reweighting grid ( $\Delta\kappa = 0.0004$ ). The infinite volume extrapolation yields the critical value  $\kappa_c = 1.5008$ .

### 6.3.1 The first order lines do not meet

The previous results on the  $16^3 \times 6$  lattice leave a small region in parameter space near  $(\beta, \kappa) \approx (9.4, 1.6)$ , where the transition may be continuous or where it is possible to cross smoothly between the confined and unconfined phases. Since a jump of the Polyakov loop expectation values in the infinite volume limit

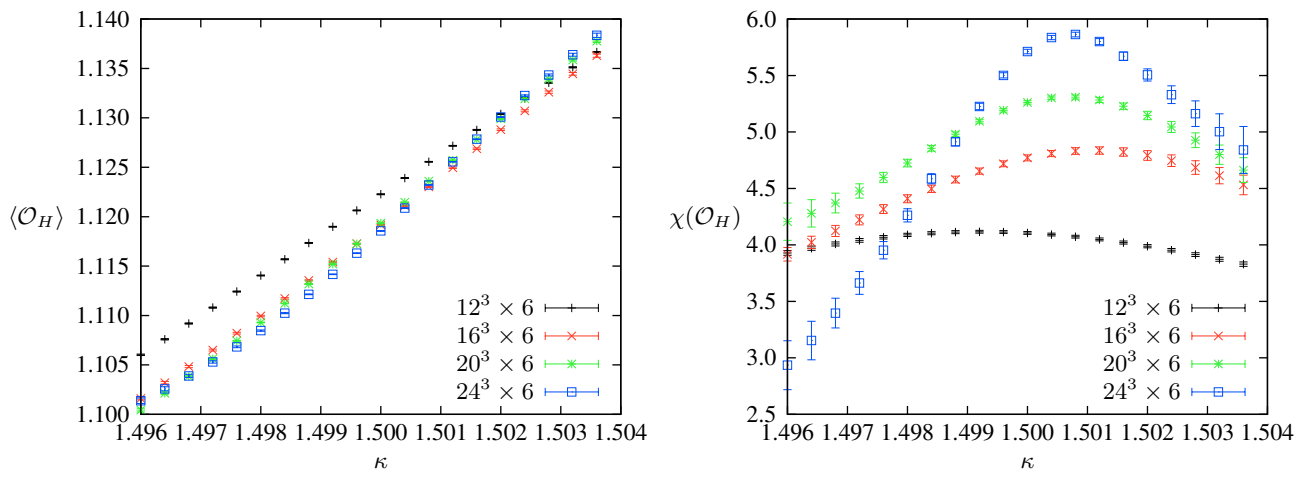
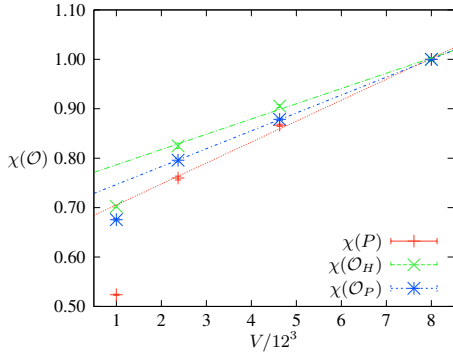


**Figure 6.16** Finite size scaling of Higgs action and its susceptibility for  $\beta = 9.5535$ .



Volume	$12^3$	$16^3$	$20^3$	$24^3$
$\chi(P)$	1.5012	1.5016	1.5008	1.5008
$\chi(\mathcal{O}_H)$	1.4992	1.5012	1.5008	1.5008
$\chi(\mathcal{O}_P)$	1.4980	1.5008	1.5008	1.5008

**Figure 6.17** *Left panel:* Finite size scaling of the three susceptibilities at the transition point with  $\beta = 9.5535$ . The lines are fits to the peak values,  $\chi_{\max}(V) = aV + b$ . *Right panel:* Critical coupling  $\kappa_c$  obtained from the maximum of the susceptibility peaks of Polyakov loop, plaquette and Higgs action for different spatial volumes at  $\beta = 9.5535$ . The errors are given by the density of the reweighting grid ( $\Delta\kappa = 0.0004$ ).

points to a first order transition, the quantity

$$\Delta P = \langle P \rangle_{\text{deconfined}} - \langle P \rangle_{\text{confined}} \quad (6.14)$$

is investigated more carefully. In the small parameter region the critical curve  $(\beta_c, \kappa_c)$  is localized with the histogram method. At the critical point the height of the confinement peak is equal to the height of the deconfinement peak. For fixed  $\kappa_c$  the transition line is crossed when increasing the inverse gauge coupling. Then the maximal jump is measured as a function of the step size  $\Delta\beta$  for one step size below and one above  $\beta_c$ . For a first order transition the jump should not depend much on  $\Delta\beta$ , whereas for a continuous transition or a crossover  $\Delta P$  should decrease with decreasing  $\Delta\beta$ . The results on a  $16^3 \times 6$  lattice are depicted in Fig. 6.18. For  $9.35 \lesssim \beta_c \lesssim 9.52$  corresponding to  $1.52 \lesssim \kappa_c \lesssim 1.72$ , it is observed, that the jump approaches zero with shrinking step size, and this clearly points to second order confinement-deconfinement transitions or crossovers in these small parameter regions. Simulations on a larger  $20^3 \times 6$  lattice confirm these results. Fig. 6.19 shows histograms of the Polyakov loop for  $\kappa$  values between 1.5 and 1.7. At  $\kappa = 1.5$  a weak first order transition is still observed, which turns into

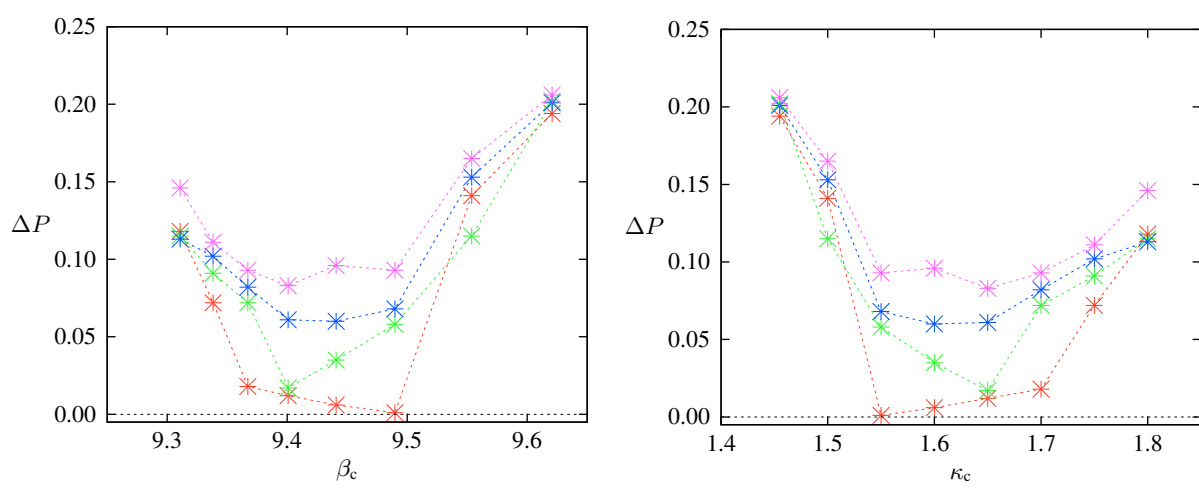


**Figure 6.18** Difference of Polyakov loop in confined and unconfined phase at the phase transition point for various critical couplings  $\beta_c, \kappa_c$  and various intervals around the critical coupling  $\beta_c$ , red:  $\Delta\beta = 0.0005$ , green:  $\Delta\beta = 0.0015$ , blue:  $\Delta\beta = 0.0025$ , pink:  $\Delta\beta = 0.0035$ ,  $\kappa$  is fixed ( $\Delta\kappa = 0$ ). The region in which  $\Delta P \rightarrow 0$  indicates a crossover or continuous transition.

a continuous transition or crossover for  $1.5 < \kappa \leq 1.7$ . Within the given resolution in parameter space, the window is the same as on the  $16^3 \times 6$  lattice. Since the critical couplings for spatial volumes beyond  $20^3$  do not change, it is concluded that the gap will not close in the infinite volume limit. This shows that the two first order lines emanating from  $\kappa = 0$  and  $\kappa = \infty$  do not meet. Here the question arises, whether such a gap in the first order line between the confined and unconfined phases is expected. The celebrated Fradkin-Shenker-Osterwalder-Seiler theorem [184, 185], originally proven for the  $SU(N)$  Higgs model with scalars in the fundamental representation, says, that there is no complete separation between the Higgs and the confinement regions. Any point deep in the confinement regime and any point deep in the Higgs regime are related by a path, such that Green's functions of local, gauge invariant operators vary analytically along the path. Thus, there is no abrupt change from a colourless to a colour-charged spectrum. This is consistent with the fact that there are only colour singlet asymptotic states in both 'phases'. The proof of the theorem relies crucially on using a completely fixed unitary gauge. A complete gauge fixing is not possible with scalars in the adjoint representation of  $SU(N)$ , since these scalars are centre blind. Thus, the theorem does not hold for adjoint scalars. Indeed, with adjoint scalars there exists a phase boundary separating the Higgs and confined phases. It is not completely obvious whether these results are relevant for the phase diagram of the  $G_2$  Higgs model. The centre of  $G_2$  is trivial and the 14 dimensional adjoint representation is just one of the two fundamental representations. Since there is no need to break the centre one may conclude, that the confinement-like regime and the Higgs-like regimes are analytically connected. In addition, for large values of the hopping parameter the centre of the corresponding  $SU(3)$  gauge theory is explicitly broken by the scalar fields, similar as for the  $SU(3)$  Higgs model with scalars in the fundamental representation. These arguments suggest that there exists a smooth crossover between the confining and Higgs phases. However, one important assumption of the Fradkin-Shenker theorem is not fulfilled for the  $G_2$  Higgs model. The theorem assumes that there exists no transition for large  $\kappa$ . Consequently, at large  $\kappa$  it is possible to move from large to small  $\beta$

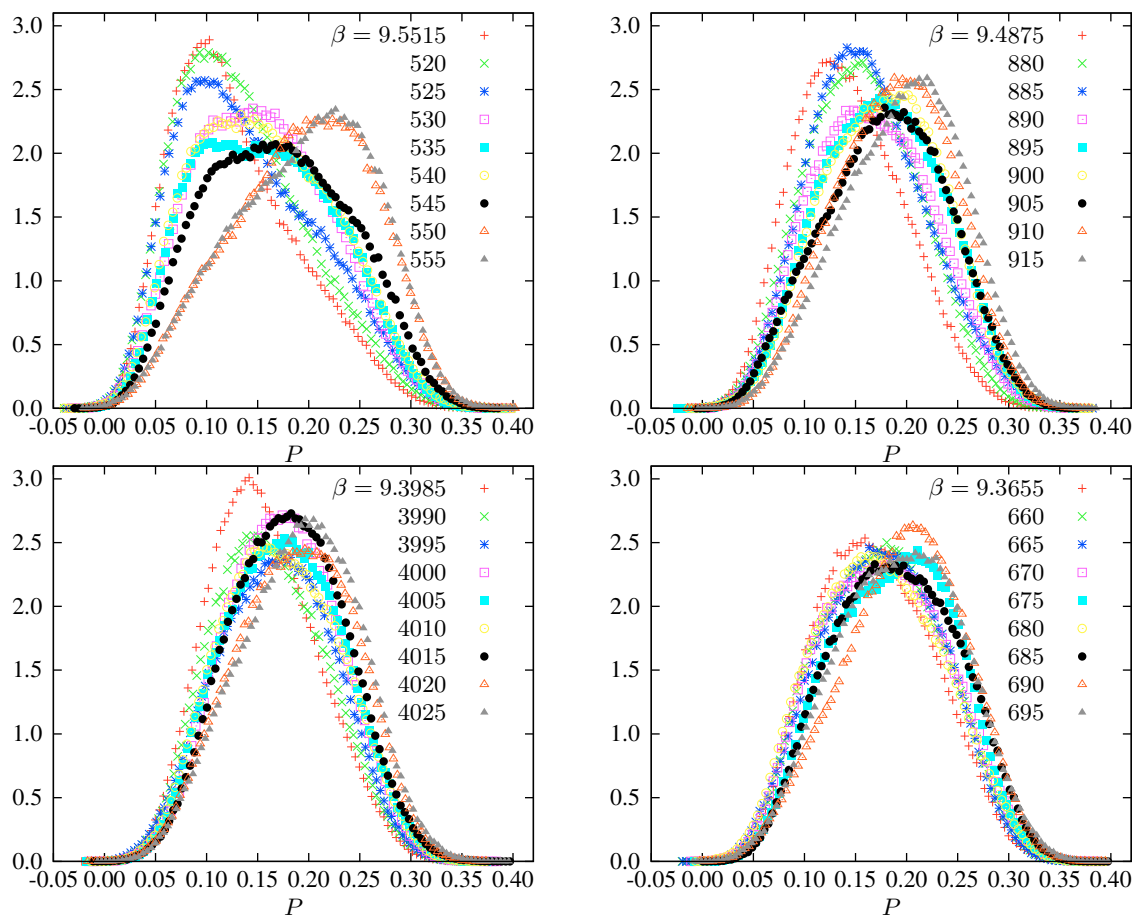


**Figure 6.19** Distribution of the Polyakov loop near the phase transition point for  $\kappa = 1.5$  (top left),  $\kappa = 1.55$  (top right),  $\kappa = 1.65$  (bottom left) and  $\kappa = 1.7$  (bottom right) on a  $20^3 \times 6$  lattice.

and then at small  $\beta$  further on to small values of  $\kappa$  without hitting a phase transition. Clearly this is not possible for the  $G_2$  Higgs model, which means, that not all assumption of the theorem hold true.

## 6.4 Conclusions

In this chapter, the proposed and earlier seen [58, 129] first order transition for pure  $G_2$  gluodynamics has been confirmed, which corresponds to the line  $\kappa = 0$  in the phase diagram of the Higgs model. A first analysis on smaller lattices indicates, that this first order transition is connected to the first order deconfinement transition in  $SU(3)$  gluodynamics, corresponding to the limit  $\kappa \rightarrow \infty$ , by a smooth curve of first order transitions. The same analysis spots another curve of second order transitions emanating from  $\beta \rightarrow \infty$  and meeting the first order line at a triple point.

For this first analysis histograms for the Polyakov loop, Higgs action, and plaquette action have been calculated. To identify the second order transition line, the finite size scaling of various susceptibilities and of the second derivative of the action with respect to the hopping parameter have been studied. The final result of the performed analysis on a  $16^3 \times 6$  lattice is depicted in Fig. 6.20.

Note that the tiny region in the vicinity of the would-be triple point is very much enlarged in this figure.

In this tiny region in the  $(\beta, \kappa)$  plane, where the order of the transition can not be decided, the slope of  $\langle P \rangle$  in the vicinity of the suspected transition has been studied. The simulations show, that the two first order curves emanating from the lines with  $\kappa = 0$  and  $\kappa = \infty$  end before they meet. The two curves may be connected by a line of second order transitions or they may end at two (critical) endpoints, in which case the confined and unconfined phases are smoothly connected. If indeed there exists a crossover in the  $G_2$  Higgs model at a finite value of the hopping parameter, then the gauge model behaves very similar to QCD with massive quarks.

To finally answer the question about the behavior of the  $G_2$  Higgs model theory in the vicinity of the ‘would-be triple point’ at  $(\beta, \kappa) \approx (9.4, 1.6)$ , further simulations with an even higher statistics and a more sophisticated analysis of the action susceptibilities may be necessary. However, this will not be an easy task, since already an efficient (and parallelized) IHMC algorithm and much CPU time has been used to arrive at the results presented in the work. Earlier studies of the susceptibility peaks in the simpler  $SU(2)$  Higgs model on smaller lattices pointed to a first order transition at  $\beta \lesssim 2.5$ . Recent simulations on larger lattices in [183] showed, that the susceptibility peaks do not scale with the volume, which means, that there is actually no first order transition for these small values of  $\beta$ . No flattening of the peaks with increasing volumes for  $N_s \leq 24$  has been seen and it has been concluded, that the solid line in Fig. 6.20 is a first order line. However, of course, it cannot be excluded, that the correlation length is larger than expected and that

simulations on even larger lattices are necessary, to finally settle the question about the position and size of the window connecting the confined with the unconfined phase. However, this will be difficult, and therefore it would be very helpful to actually prove (if possible and under weaker assumptions), whether the confining and Higgs phases of  $G_2$  can be connected analytically, perhaps with similar arguments as applied to  $SU(N)$  Higgs models with matter in the fundamental representations [184, 185].

Concluding, it has been shown that fundamental matter is able to weaken the deconfinement phase transition. This is very similar to QCD, where for light quarks in the fundamental representation a crossover from the confined to the deconfined phase has been found. However so far, only scalar matter fields have been considered in the present work. In the next chapter, the influence of dynamical quarks in the 7-dimensional fundamental representation of  $G_2$  is studied. It is expected that these fundamental matter fields are also able to weaken the deconfinement phase transition and may provide an interesting opportunity to gain new insights into the QCD phase diagram.

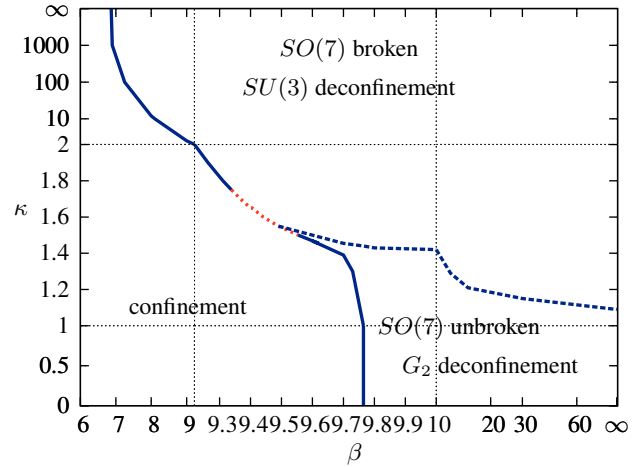


**Figure 6.20** Complete phase diagram in the  $(\beta, \kappa)$ -plane on a  $16^3 \times 6$  lattice. The neighbourhood of the ‘would-be triple point’ is very much enlarged and the variable scale in the diagram is responsible for the cusps in the transition lines. The solid line indicates a first order transition, the dashed line (blue) a second order transition, and the dotted line (red) a second order transition or a crossover.

# 7 A QCD-like theory with fermionic baryons

As it was already pointed out in the introduction, one of the main challenges of QCD is to gain new insight into its phase diagram. Due to the fermion sign problem of QCD at real quark chemical potential, Monte-Carlo techniques are not directly applicable to investigate the QCD phase diagram, especially at low temperatures and high densities [186, 187]. Understanding the theory in this region of the QCD parameter space is, for instance, very important for dense quark systems and the formation of compact stellar objects as well as heavy-ion collision experiments.

Currently, the only reliable information is obtained from continuum methods and model calculations [45, 188–190]. These methods usually require approximations and therefore their validity in all regions of the QCD parameter space is still unclear. Nevertheless, Fig. 7.1 shows a sketch of the QCD phase diagram, inspired by the different approaches.

For vanishing baryon chemical potential  $\mu_B$  and physical values of the quark masses, the low temperature confinement phase is separated by a crossover from the high temperature deconfined quark gluon plasma in the early universe [28, 188, 191]. At small values of the chemical potential, results can be obtained from reweighting techniques [192–194] or Taylor expansion around vanishing chemical potential [195–200]. With these methods it was possible to investigate the QCD phase diagram for small densities and high temperatures, i.e.  $\mu_B/T \lesssim 1$ . Nevertheless, the existence of a critical point as deduced from model calculations, where the crossover from a confined to a deconfined phase at zero and small values of baryon chemical potential (net baryon density) turns into a real phase transition, is still unclear [193, 199, 201]. Another possibility is to simulate QCD at imaginary chemical potential, where the sign problem is absent. The obtained results can then be continued analytically to real values of the quark chemical potential [202–206]. At small temperatures and large values of the quark chemical potential, so far all lattice techniques miserably fail due to the severeness of the sign problem. The obtained results are based on model calculations [38, 188], which mostly agree on a first order phase transition between nuclear matter and quark matter. At asymptotic high net baryon densities colour superconductivity is expected. In between and at finite temperature more exotic phases, as for instance a quarkionic phase, i.e. deconfined but chirally broken matter or crystalline phases, are proposed [39–41].

A theory that is accessible to Monte-Carlo techniques is two-flavour QCD with isospin chemical

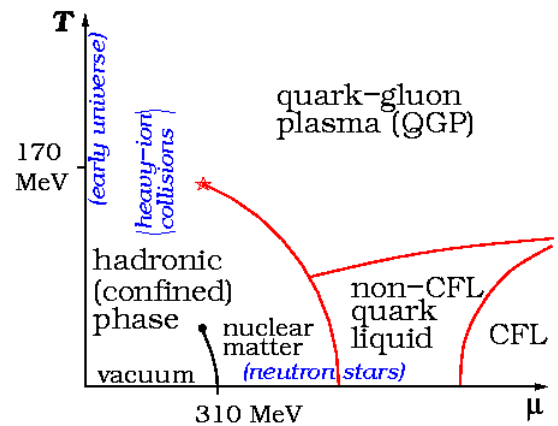


**Figure 7.1** Schematic phase diagram of QCD, taken from Wikipedia

potential  $\mu_1$ . Phenomenological arguments suggest, that two-flavour QCD at zero temperature remains in the vacuum state until the chemical potential reaches the energy of the lowest hadronic bound state, i.e. the pion mass [207]. Consequently, all observables should not depend on  $\mu_1$  for  $\mu_1 < m_\pi/2$ . However, on the other hand the grand canonical potential, i.e. the logarithm of the partition function, naively depends on  $\mu_1$ . This obstacle is known as the isospin *silver blaze problem*. It was solved in [208], showing that the complex phase factor exactly cancels the dependence on  $\mu_1$  for  $\mu_1 < m_\pi/2$ . In the case of baryon chemical potential  $\mu_B$  the situation is much more complicated. It is believed that the system remains in the vacuum, until  $\mu_B$  reaches the energy of the lightest state carrying non-vanishing baryon number [209, 210].

Another approach to the QCD phase diagram is to investigate QCD-like theories having as many features as possible in common with QCD. One example of those theories is two-colour QCD. Its phase diagram was explored very recently and with much effort in a series of papers [51–56, 211–213]. Although the results reveal many interesting aspects, the main drawback of two-colour QCD is the absence of fermionic degrees of freedom in the hadron spectrum. The baryons are bosons instead of fermions and this leads to profound differences to QCD, such as Bose-Einstein condensation with a BEC-BCS crossover at high densities instead of the usual liquid-gas transition of nuclear matter. However, at high densities the fermionic nature of baryons is expected to become important. Another example for a QCD-like theory is adjoint QCD, where matter transforms under the adjoint (real) representation of the gauge group [51, 52, 214].

Here, a QCD-like theory based on the exceptional gauge group  $G_2$  is proposed. It has already been shown that  $G_2$ -Yang-Mills theory undergoes a first order phase transition from the low-temperature confined phase to the high-temperature deconfined phase [58, 129] and therefore behaves very similar to  $SU(3)$ . Additionally, in chapter 6 it has been shown that already *scalar quarks* can weaken the deconfinement phase transition until it becomes a crossover. Now fundamental fermions are coupled to  $G_2$ -Yang-Mills in order to study the phase diagram of  $G_2$ -QCD at finite density. The quenched theory has already been explored in [215], showing that chiral symmetry is broken at low temperatures and restored at high temperatures.

In this work, it will be shown that even at finite quark chemical potential  $\mu$  the fermion determinant is non-negative. This, in principle, allows to investigate the phase diagram at zero temperature and finite chemical potential. Moreover, the spectrum contains fermionic baryons and the theory is expected to behave in many aspects very similar to QCD. Below, the continuum formulation of  $G_2$ -QCD is developed, simulations on different lattices are performed and the obtained phase diagram is presented. The results will be published in a series of forthcoming papers [216, 217]. First results on smaller lattices have already been published in [82].

## 7.1 Continuum formulation of $G_2$ -QCD

To understand QCD with gauge group  $G_2$ , it is important to work out the symmetries of the continuum theory. In principle, this has been done for an arbitrary gauge group (and in more detail for  $SU(2)$ ) in [51]. In the following the details for  $G_2$  are explained. The action of  $N_f$  flavour QCD with arbitrary

gauge group  $\mathcal{G}$  in Minkowski spacetime is given by

$$S = \int d^4x \operatorname{tr} \left\{ -\frac{1}{4} F_{\mu\nu} F^{\mu\nu} + \sum_{n=1}^{N_f} \bar{\Psi}_n (i \gamma^\mu (\partial_\mu - g A_\mu) - m) \Psi_n \right\}, \quad (7.1)$$

Under charge conjugation the matter part of the Lagrange density transforms up to boundary terms, as

$$\begin{aligned} \mathcal{L}[\Psi^C, A, m] &= \bar{\Psi}^C (i \gamma^\mu (\partial_\mu - g A_\mu) - m) \Psi^C \\ &= \bar{\Psi} (i \gamma^\mu (\partial_\mu + g A_\mu^\top) - m) \Psi = \mathcal{L}[\Psi, -A^\top, m], \end{aligned} \quad (7.2)$$

with  $\Psi = (\Psi_1, \dots, \Psi_{N_f})$ . Therefore, the charge conjugated spinor  $\Psi^C$  fulfills the same equation of motions if the gauge field obeys the condition

$$A_\mu^\top = -A_\mu = -A_\mu^a T_a. \quad (7.3)$$

Since every representation of  $G_2$  is real, the generators  $T_a$  of the algebra  $\mathfrak{g}_2$  can be chosen as anti-symmetric real-valued  $7 \times 7$  matrices and equation (7.3) holds. Then it is possible to write the matter part of the action (7.1) as a sum over  $2N_f$  Majorana spinors  $\lambda_n$

$$S[\Psi, A] = \int d^4x \bar{\Psi} (i \gamma^\mu (\partial_\mu - g A_\mu) - m) \Psi = \int d^4x \bar{\lambda} (i \gamma^\mu (\partial_\mu - g A_\mu) - m) \lambda \quad (7.4)$$

with  $\lambda = (\chi, \eta) = (\lambda_1, \dots, \lambda_{2N_f})$ . Here  $\lambda$  obeys the Majorana condition  $\lambda^C = C \bar{\lambda}^\top = \lambda$ ,  $\bar{\lambda}^C = -\lambda^\top C^{-1} = \bar{\lambda}$  and is related to the Dirac spinor as

$$\Psi = \chi + i \eta, \quad \bar{\Psi} = \bar{\chi} - i \bar{\eta}, \quad \Psi^C = \chi - i \eta, \quad \bar{\Psi}^C = \bar{\chi} + i \bar{\eta}. \quad (7.5)$$

Now the (baryon) chemical potential  $\mu$  enters the partition function as a Lagrange multiplier, similar to temperature. It violates the Majorana decomposition, because in the microscopic Lagrangian it enters as an off-diagonal term in flavour space,

$$\mathcal{L} = \bar{\Psi} (i \not{D} - m + i \gamma_0 \mu) \Psi = \begin{pmatrix} \bar{\chi} \\ \bar{\eta} \end{pmatrix} \begin{pmatrix} i \not{D} - m & i \gamma_0 \mu \\ -i \gamma_0 \mu & i \not{D} - m \end{pmatrix} \begin{pmatrix} \chi \\ \eta \end{pmatrix}. \quad (7.6)$$

In the following the spectrum and the chiral properties of (7.6) are investigated.

### 7.1.1 The spectrum of the Dirac operator

For Monte-Carlo methods to be applicable, the determinant of the Euclidean Dirac operator has to be non-negative. The Euclidean gamma matrices are Hermitian. The continuum Dirac operator is then given by

$$D[A, m, \mu] = \gamma_E^\mu (\partial_\mu - g A_\mu) - m + \gamma_{E0} \mu. \quad (7.7)$$

According to [51, 52], if a unitary operator  $T$  exists such that the Dirac operator obeys the relation

$$D^* T = T D, \quad (7.8)$$

with  $T^* T = -\mathbb{1}$  and  $T^\dagger = T^{-1}$ , the eigenvalues of the Dirac operator come in complex conjugate pairs and all real eigenvalues are doubly degenerate.

**Proof** Let  $\lambda$  be an eigenvalue of  $D$  with eigenvector  $\psi$ ,  $T$  a unitary operator with  $D^*T = TD$  and  $\chi = T^{-1}\psi^*$ , then it follows

$$D\chi = DT^{-1}\psi^* = T^{-1}TDT^{-1}\psi^* = T^{-1}D^*\psi^* = T^{-1}\lambda^*\psi^* = \lambda^*\chi, \quad (7.9)$$

and  $\lambda^*$  is also an eigenvalue of  $D$ . Suppose now  $T^*T = -\mathbb{1}$ , then

$$\psi^\dagger\chi = (\chi^\dagger\psi)^* = (\psi^\dagger T^{-1}\psi)^* = (\psi^\dagger T\psi)^* = \psi^\dagger T^*\psi^* = -\psi^\dagger (T^{-1}\psi^*) = -\psi^\dagger\chi, \quad (7.10)$$

concluding that  $\psi^\dagger\chi = 0$ . Every real eigenvalue is therefore doubly degenerate and together with (7.9) this shows that the determinant of  $D$  is non-negative. In order to prove this feature for  $G_2$ -QCD,  $T$  is applied to the Dirac operator,

$$TD T^\dagger = T\gamma_{\mathbb{E}}^\mu T^\dagger \partial_\mu - gT\gamma_{\mathbb{E}}^\mu A_\mu T^\dagger - m + T\gamma_{\mathbb{E}0} T^\dagger \mu, \quad (7.11)$$

and with the decomposition of  $T$  into a spinor ( $\Gamma$ ) and colour ( $F$ ) part ( $T = \Gamma \otimes F$ ),

$$TD T^\dagger = \Gamma\gamma_{\mathbb{E}}^\mu \Gamma^\dagger \partial_\mu - g\Gamma\gamma_{\mathbb{E}}^\mu \Gamma^\dagger F A_\mu F^\dagger - m + \Gamma\gamma_{\mathbb{E}0} \Gamma^\dagger \mu \quad (7.12)$$

is obtained. To fulfill (7.8),  $\Gamma$  and  $F$  have to satisfy the following relations

$$\Gamma\gamma_{\mathbb{E}\mu} \Gamma^\dagger = \gamma_{\mathbb{E}\mu}^*, \quad \Gamma\gamma_{\mathbb{E}0} \Gamma^\dagger \mu = \gamma_{\mathbb{E}0}^* \mu^* \quad \text{and} \quad F A_\mu F^\dagger = A_\mu^*. \quad (7.13)$$

For real chemical potential and Hermitian gamma matrices, the first two equations are satisfied by  $\Gamma = C\gamma_5$ . Since all representations of  $G_2$  are real ( $A_\mu = A_\mu^*$ ),  $F$  is the identity and therefore

$$T = C\gamma_5 \otimes \mathbb{1} \quad (7.14)$$

is obtained. Indeed, this choice satisfies  $T^{-1} = T^\dagger$  and  $T^*T = -\mathbb{1}$ , and therefore the fermion determinant is real and non-negative for any gauge field configuration and any real value of quark chemical potential,

$$\det D[A, m, \mu] \geq 0. \quad (7.15)$$

This feature of the fermion determinant makes Markov chain Monte-Carlo techniques applicable, because the path integral measure  $\mathcal{D}A_\mu \det D[A, m, \mu] e^{-S_B}$  is real and non-negative and can be interpreted as a probability distribution to generate a Markov chain.

## 7.1.2 Chiral symmetry

Because of the Majorana constraint, the chiral symmetry in  $G_2$ -QCD will be different from that of  $SU(3)$ -QCD. First of all the chiral transformation associated to the vector current  $j_\mu = \bar{q}\gamma_\mu q$ ,

$$\lambda \mapsto e^{\beta \otimes \mathbb{1}} \lambda. \quad (7.16)$$

is investigated. Here,  $\beta$  is a  $2N_f \times 2N_f$  matrix in flavour space. The Majorana constraint then requires  $\beta = \beta^*$  or  $\beta = i\pi \text{diag}(n_1, \dots, n_{2N_f})$ . The conjugated spinor transforms as

$$\bar{\lambda} = -\lambda^\dagger C^{-1} \mapsto -(e^{\beta \otimes \mathbb{1}} \lambda)^\dagger C^{-1} = \bar{\lambda} e^{\beta^\dagger \otimes \mathbb{1}}. \quad (7.17)$$

The action (7.4) is invariant if  $\beta$  fulfills the equation  $\beta + \beta^T = i 2 \pi m$  and altogether

$$\beta \in \mathfrak{so}(2N_f) \quad \text{or} \quad \frac{\beta}{i\pi} \in \{0, 1\}^{2N_f} \quad (7.18)$$

is obtained.

The second symmetry under investigation is the axial vector chiral symmetry with classically conserved current  $j_\mu^5 = \bar{q} \gamma_\mu \gamma_5 q$ ,

$$\lambda \mapsto e^{i\alpha \otimes \gamma_5} \lambda, \quad \bar{\lambda} = -\lambda^T C^{-1} \mapsto \bar{\lambda} e^{i\alpha^T \otimes \gamma_5}. \quad (7.19)$$

Here the Majorana constraint requires  $\alpha = \alpha^*$ . The action is invariant if  $\alpha = \alpha^T$ . Therefore,  $i\alpha$  corresponds to a complex embedding of symmetric and anti-Hermitian matrices in  $\mathfrak{so}(2N_f)$  and each of the diagonal parts to a  $U(1)$  factor,

$$\alpha \in \mathfrak{so}(2N_f) \quad \text{or} \quad \alpha = \theta \in \mathfrak{u}(1)^{2N_f}. \quad (7.20)$$

To find the combined symmetry group it has to be taken into account that left- and right-handed spinors can, due to

$$\lambda_{L/R} = P_{L/R} \lambda = P_{L/R} \lambda^C = P_{L/R} C \gamma_0^T \lambda^* = C P_{L/R}^* \gamma_0^T \lambda^* = C \gamma_0^T P_{R/L}^* \lambda^* = C \gamma_0^T \lambda_{R/L}^*, \quad (7.21)$$

not be rotated independently. For instance, in a Majorana representation with  $C = -\gamma_0$  the left-handed spinor is the complex conjugate of the right-handed one,  $\lambda_{L/R} = \lambda_{R/L}^*$ . Moreover, the axial  $\mathfrak{so}(2N_f)$  and the vector  $\mathfrak{so}(2N_f)$  do not commute and the corresponding symmetry group does not factorize. To find the most general chiral transformation, it is possible to write the matrices  $\alpha$ ,  $\beta$  and  $\theta$  in terms of the  $N(2N - 1)$   $\mathfrak{su}(2N)$  ladder operators  $E_{ij}$ ,

$$E_{ij} = |i\rangle \langle j| \quad \text{for} \quad 1 \leq i < j \leq 2N, \quad (7.22)$$

and algebra generators ( $h_i$  are the generators of the Cartan subalgebra)

$$T_{ij}^R = \frac{1}{2} (E_{ij} + E_{ij}^T), \quad T_{ij}^I = \frac{1}{2i} (E_{ij} - E_{ij}^T), \quad T_i^C = h_i, \quad (7.23)$$

where the superscripts R and I stand for the real and imaginary embedding of  $\mathfrak{so}(2N)$  generators and C denotes the Cartan subalgebra. Then

$$\alpha = \alpha^a T_a^R, \quad \beta = i \beta^a T_a^I \quad \text{and} \quad \theta_{\text{traceless}} = \theta^a T_a^C, \quad (7.24)$$

and the trace-part of  $\theta$  corresponds to an additional  $U(1)$  factor. With these definitions, a general chiral transformation can be written as

$$U(\alpha, \beta, \theta) = \exp \left\{ i \left( \alpha^a T_a^R + \theta^a T_a^C + \text{tr} \theta \right) \otimes \gamma_5 + i \beta^a T_a^I \otimes \mathbb{1} \right\}. \quad (7.25)$$

In terms of left- and right-handed projection operators, the chiral symmetry transformation is given by

$$\begin{aligned} U(\alpha, \beta, \theta) &= \exp \left\{ i \left( \alpha^a T_a^R + \theta^a T_a^C + \text{tr} \theta \right) \otimes (P_R - P_L) + i \beta^a T_a^I \otimes (P_R + P_L) \right\} \\ &= \exp \left\{ i \left( \alpha^a T_a^R + \beta^a T_a^I + \theta^a T_a^C + \text{tr} \theta \right) \right\} \otimes P_R \\ &\quad + \exp \left\{ -i \left( \alpha^a T_a^R - \beta^a T_a^I + \theta^a T_a^C + \text{tr} \theta \right) \right\} \otimes P_L \\ &= U_R(\alpha, \beta, \theta) \otimes P_R + U_L(\alpha, \beta, \theta) \otimes P_L, \end{aligned} \quad (7.26)$$

where  $\alpha^a T_a^R + \beta^a T_a^I + \theta^a T_a^C = t_a T^a$  is a general element of  $SU(2N)$ . Indeed,  $U_L = U_R^* = U_{L=R^*}$  is a unitary matrix with  $N_\alpha + N_\beta + N_\theta = N_f(2N_f - 1) + N_f(2N_f - 1) + 2N_f = 4N_f^2$  degrees of freedom and therefore a general element of  $U(2N_f)$ . The discrete part of the vector symmetry is already contained in the  $U(2N_f)$ , and thus the chiral symmetry of  $G_2$ -QCD reads

$$U(2N_f)_{L=R^*} = SU(2N_f)_{L=R^*} \otimes U(1)_A / \mathbb{Z}(2N_f), \quad (7.27)$$

in agreement with the results in [57]. Together with the local gauge symmetry, this is the symmetry group of the classical action. As in QCD it is expected that the axial  $U(1)$  is broken by the axial anomaly. The change in the Lagrangian due to the anomaly is given by [218],

$$\Delta\mathcal{L} = 2i \operatorname{tr}(\alpha \otimes \gamma_5 \gamma_\mu \gamma_\nu \gamma_\rho \gamma_\sigma \otimes F^{\mu\nu} F^{\rho\sigma}) = 2i \operatorname{tr}(\alpha) \operatorname{tr}\left(F^{\mu\nu} \tilde{F}_{\mu\nu}\right). \quad (7.28)$$

Therefore the  $U(1)$  is broken to the discrete subgroup  $\mathbb{Z}(2)$ , being part of the vector transformations. Indeed, it is the trivial part of the  $U(1)_B$  associated to baryon number conservation. Thus, the chiral symmetry of the quantum theory is

$$SU(2N_f)_{L=R^*} \otimes \mathbb{Z}(2)_B. \quad (7.29)$$

In the following, explicit or spontaneous chiral symmetry breaking triggered by a Dirac mass term or a non-vanishing chiral condensate is investigated.

### 7.1.3 Chiral symmetry breaking, Goldstone bosons and baryon charge

In the presence of a non-vanishing Dirac mass term or a non-vanishing chiral condensate, the theory is no longer invariant under the axial  $SO(2N_f)_A$  transformations. Therefore the chiral symmetry is expected to be broken partially (explicit or spontaneous) to its maximal vector subgroup,

$$SU(2N_f)_{L=R^*} \otimes \mathbb{Z}(2)_B \mapsto SO(2N_f)_V \otimes \mathbb{Z}(2)_B, \quad (7.30)$$

leading to  $4N_f^2 - 1 - N_f(2N_f - 1) = N_f(2N_f + 1) - 1$  (would-be) Goldstone bosons in the symmetry broken phase. Contrary, in the presence of a non-vanishing chemical potential, the Dirac operator is no longer diagonal w.r.t. the decomposition into Majorana flavours. In this case and for vanishing Dirac mass  $m = 0$ , the chiral symmetry is the same as in QCD,

$$SU(2N_f)_{L=R^*} \otimes \mathbb{Z}(2)_B \mapsto U(N_f)_A \otimes U(N_f)_V = SU(N_f)_A \otimes SU(N_f)_V \otimes U(1)_B / \mathbb{Z}(N_f). \quad (7.31)$$

Then for  $m \neq 0$ , chiral symmetry is broken as

$$SU(N_f)_A \otimes SU(N_f)_V \otimes U(1)_B / \mathbb{Z}(N_f) \mapsto SU(N_f)_V \otimes U(1)_B / \mathbb{Z}(N_f). \quad (7.32)$$

Now it is only necessary to show that  $m \neq 0$ , and after that switching on chemical potential leads to the same group as the other way around. Since the part of the Lagrangian belonging to the chemical potential is not diagonal in the Majorana decomposition, it is not possible to transform the Majorana components of a Dirac spinor independently. Therefore, the vector group  $SO(2N_f)_V$  is broken down to

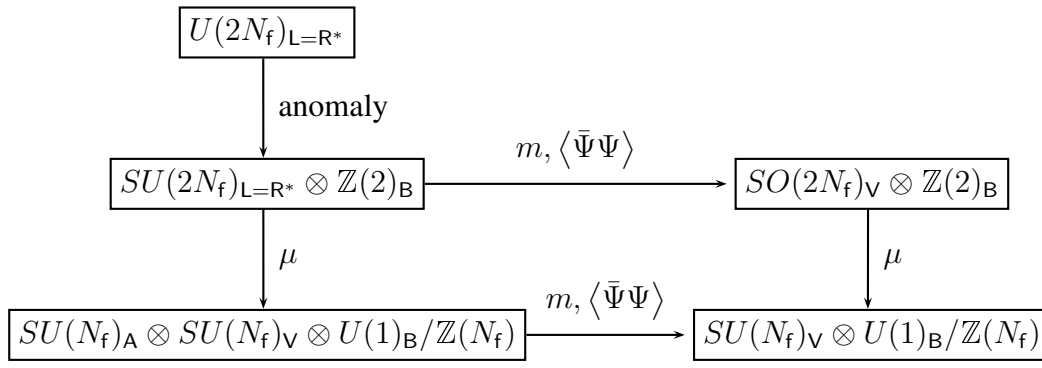


**Figure 7.2** Chiral symmetry breaking in  $G_2$ -QCD

transformations that do not interchange the Majorana spinors building a single Dirac flavour. But then also complex transformations are allowed, leading to the residual  $SU(N_f)_V$  symmetry group. Altogether the chiral symmetry breaking of  $G_2$ -QCD is shown in Fig. 7.2. Finally, the conserved charges, i.e. physical particles, corresponding to the conserved axial and vector currents,

$$j_A^{\mu a} = \bar{\lambda} \gamma^\mu \gamma_5 \otimes T_{R/C}^a \lambda \quad \text{and} \quad j_V^{\mu a} = \bar{\lambda} \gamma^\mu \otimes T_1^a \lambda \quad (7.33)$$

have to be identified. The content of the axial chiral multiplet consists of  $(N_f + 1)(2N_f - 1)$  operators

$$\begin{aligned} \frac{1}{2} (\bar{\lambda}_i \gamma_5 \lambda_j + \bar{\lambda}_j \gamma_5 \lambda_i) &= \bar{\lambda}_i \gamma_5 \lambda_j & \text{for } 1 \leq i < j \leq 2N & \text{ and} \\ \frac{1}{2} (\bar{\lambda}_i \gamma_5 \lambda_i - \bar{\lambda}_{i+1} \gamma_5 \lambda_{i+1}) & & \text{for } 1 \leq i < 2N_f. & \end{aligned} \quad (7.34)$$

The vector charge vanishes identically and the operators associated to the trace part of the axial symmetry (broken by the anomaly) and to the trace part of the vector symmetry ( $U(1)_B$  associated to baryon number conservation) are given by

$$\bar{\lambda}_i \gamma_5 \lambda_i \quad \text{and} \quad \bar{\lambda}_i \lambda_i. \quad (7.35)$$

If chiral symmetry is spontaneously broken, the axial chiral multiplet becomes massless, according to the Goldstone theorem. In analogy to QCD, the associated particles are called pions ( $\pi$ ). The ones corresponding to the trace part of the anomaly and the trace part of the vector symmetry are called  $\eta'$  and  $f'$ , respectively.

Similar to QCD, mesons consist of a quark and an anti-quark. With respect to the  $U(1)_B$  subgroup of the chiral vector symmetry they are invariant, i.e. they do not carry baryon charge. Baryons are fermionic bound states, for instance three quarks or a single quark and three gluons, that are not invariant under the  $U(1)_B$  subgroup. Consequently, they carry baryon number. Additionally, also baryonic *diquarks* (bound states of two quarks) exist, for instance the pion is a diquark with baryon charge two. This is in contrast to QCD, where diquarks cannot exist and the pions are pseudoscalar mesons instead.

#### 7.1.4 Towards QCD at finite chemical potential

Again, with a Higgs field in the fundamental representation of the gauge group, the gauge symmetry can be broken down to the  $SU(3)$  subgroup of  $G_2$ . In the limit of an infinitely heavy scalar field, the matter

part of the microscopic Lagrangian (7.6) in the colour decomposition is given by (here for simplicity the complex representation of  $G_2$  is used)

$$\mathcal{L} = \begin{pmatrix} \bar{\Psi}_3 \\ \bar{\Psi}_{\bar{3}} \\ \bar{\Psi}_1 \end{pmatrix} \begin{pmatrix} i \not{D}_3 - m + i \gamma_0 \mu & 0 & 0 \\ 0 & i \not{D}_{\bar{3}} - m + i \gamma_0 \mu & 0 \\ 0 & 0 & i \not{D}_1 - m + i \gamma_0 \mu \end{pmatrix} \begin{pmatrix} \Psi_3 \\ \Psi_{\bar{3}} \\ \Psi_1 \end{pmatrix}, \quad (7.36)$$

where  $\not{D}_3$ ,  $\not{D}_{\bar{3}}$  and  $\not{D}_1$  are the gauge covariant derivatives in the fundamental (3), anti-fundamental ( $\bar{3}$ ) and colour-singlet (1) representation of  $SU(3)$ , respectively. Using the relation

$$\int d^4x \bar{\Psi}_{\bar{3}} (i \not{D}_{\bar{3}} - m + i \gamma_0 \mu) \Psi_{\bar{3}} = \int d^4x \bar{\Psi}_{\bar{3}}^C (i \not{D}_3 - m - i \gamma_0 \mu) \Psi_{\bar{3}}^C, \quad (7.37)$$

and the change in the integration variables

$$\begin{aligned} (\Psi_3, \Psi_{\bar{3}}, \Psi_1) &\mapsto (\Psi_3, \Psi_{\bar{3}}^C, \Psi_1) = (\Psi_u, \Psi_d, \Psi_1), \\ (\bar{\Psi}_3, \bar{\Psi}_{\bar{3}}, \bar{\Psi}_1) &\mapsto (\bar{\Psi}_3, \bar{\Psi}_{\bar{3}}^C, \bar{\Psi}_1) = (\bar{\Psi}_u, \bar{\Psi}_d, \bar{\Psi}_1), \end{aligned} \quad (7.38)$$

the Lagrangian in the limit of an infinitely heavy scalar field is equivalent to the Lagrangian of two-flavour QCD with isospin chemical potential and equal mass for the up- and down-quarks,

$$\mathcal{L} = \bar{\Psi}_u (i \not{D} - m + i \gamma_0 \mu) \Psi_u + \bar{\Psi}_d (i \not{D} - m - i \gamma_0 \mu) \Psi_d + \bar{\Psi}_1 (i \not{D} - m + i \gamma_0 \mu) \Psi_1, \quad (7.39)$$

where  $\not{D}$  is now the covariant derivative with respect to the gauge group  $SU(3)$ . Additionally, a colour-singlet quark is present. In this decomposition the absence of the sign problem is evident. In order to recover QCD with baryon chemical potential, a more involved breaking mechanism, employing also Yukawa-type interactions for the scalar field and the quarks, is necessary. Maybe it would be possible to gradually switch on the sign problem, allowing for an extrapolation to QCD.

### 7.1.5 One-flavour $G_2$ -QCD

In contrast to QCD, already in the case of a single Dirac flavour a non-trivial chiral symmetry is present, and chiral symmetry breaking can be observed. This is the reason why in the following only  $G_2$ -QCD with a single Dirac flavour  $N_f = 1$  is investigated. The chiral symmetry is then given by

$$SU(2)_{L=R^*} \otimes \mathbb{Z}(2)_B. \quad (7.40)$$

The Dirac spinor can be decomposed into two Majorana spinors,  $\Psi = \chi + i \eta$ . The axial and vector chiral transformations can explicitly be worked out. They read

$$\begin{aligned} O_A(\alpha) \begin{pmatrix} \chi \\ \eta \end{pmatrix} &= \cos(\alpha) \begin{pmatrix} \chi \\ \eta \end{pmatrix} + i \sin(\alpha) \gamma_5 \begin{pmatrix} \eta \\ \chi \end{pmatrix} \\ O_V(\beta) \begin{pmatrix} \chi \\ \eta \end{pmatrix} &= \cos(\beta) \begin{pmatrix} \chi \\ \eta \end{pmatrix} + \sin(\beta) \begin{pmatrix} -\eta \\ \chi \end{pmatrix} \\ U_A(\theta) \begin{pmatrix} \chi \\ \eta \end{pmatrix} &= \begin{pmatrix} \cos(\theta_1) \chi \\ \cos(\theta_2) \eta \end{pmatrix} + i \gamma_5 \begin{pmatrix} \sin(\theta_1) \chi \\ \sin(\theta_2) \eta \end{pmatrix} \quad \text{and} \quad Z_B(z) \begin{pmatrix} \chi \\ \eta \end{pmatrix} = \begin{pmatrix} z_1 \chi \\ z_2 \eta \end{pmatrix}, \end{aligned} \quad (7.41)$$

with  $\alpha, \beta$  and  $\theta \in \mathbb{R}$  and  $z \in \{-1, 1\}$ . In the case  $m = 0$  and  $\mu = 0$  and with the identity  $-C^{-1}\gamma_\mu\gamma_5 = \gamma_5^\top C^{-1}\gamma_\mu$ , it is evident that (7.6) is indeed invariant. A Dirac mass term breaks the axial symmetry but is invariant under  $SO(2)_V = U(1)_B$  and  $\mathbb{Z}(2)_B$ . If the symmetry is spontaneously broken by a non-vanishing chiral condensate, 2 massless Goldstone bosons occur, which become massive in the case of an explicit Dirac mass term. The corresponding creation operators are given by

$$\pi_+ = \pi_- = \pi_\pm = \bar{\chi}\gamma_5\eta \quad \text{and} \quad \pi_0 = \frac{1}{\sqrt{2}}(\bar{\chi}\gamma_5\chi - \bar{\eta}\gamma_5\eta). \quad (7.42)$$

The operators corresponding to the anomaly and baryon number conservation are given by  $\bar{\chi}\gamma_5\chi$ ,  $\bar{\eta}\gamma_5\eta$ ,  $\bar{\chi}\chi$  and  $\bar{\eta}\eta$ . Linear combinations lead to

$$\eta' = \frac{1}{\sqrt{2}}(\bar{\chi}\gamma_5\chi + \bar{\eta}\gamma_5\eta) \quad \text{and} \quad f' = \frac{1}{\sqrt{2}}(\bar{\chi}\chi + \bar{\eta}\eta). \quad (7.43)$$

The chiral symmetry can also be expressed in terms of the Dirac spinor. The vector symmetry reads  $\Psi \mapsto e^{i\alpha}\Psi$  and is identified as  $U(1)_B$  associated to baryon number conservation. Written in terms of the Dirac spinor, the pions and the  $\eta'$  and  $f'$  are given by

$$\pi_\pm = \bar{\Psi}^C\gamma_5\Psi - \bar{\Psi}\gamma_5\Psi^C, \quad \pi_0 = \bar{\Psi}^C\gamma_5\Psi + \bar{\Psi}\gamma_5\Psi^C, \quad \eta' = \bar{\Psi}\gamma_5\Psi \quad \text{and} \quad f' = \bar{\Psi}\Psi, \quad (7.44)$$

indeed showing that the pions are diquarks instead of mesons. The corresponding correlation functions, used in the lattice simulations to extract the mass, read

$$\begin{aligned} C_\pi(x, y) &= \langle \pi_0(x) \pi_0^\dagger(y) \rangle = \langle \pi_\pm(x) \pi_\pm^\dagger(y) \rangle = \left\langle \overbrace{\bar{\chi}(x)\gamma_5\chi(x) \bar{\chi}(y)\gamma_5\chi(y)} \right\rangle, \\ C_{\eta'}(x, y) &= \langle \eta'(x) \eta'^\dagger(y) \rangle = 2 \left\langle \overbrace{\bar{\chi}(x)\gamma_5\chi(x) \bar{\chi}(y)\gamma_5\chi(y)} \right\rangle + \left\langle \overbrace{\bar{\chi}(x)\gamma_5\chi(x) \bar{\chi}(y)\gamma_5\chi(y)} \right\rangle, \\ C_{f'}(x, y) &= \langle f'(x) f'^\dagger(y) \rangle = 2 \left\langle \overbrace{\bar{\chi}(x)\chi(x) \bar{\chi}(y)\chi(y)} \right\rangle + \left\langle \overbrace{\bar{\chi}(x)\chi(x) \bar{\chi}(y)\chi(y)} \right\rangle, \end{aligned} \quad (7.45)$$

showing that the pion masses are degenerate and its correlation functions contain only connected contributions. The difference between the  $\eta'$  and the pion correlation function is only the disconnected contribution. Additionally, the mass of the  $\sigma$ -meson is obtained from the connected part of the  $f'$  correlation function,

$$C_\sigma(x, y) = \langle \sigma(x) \sigma^\dagger(y) \rangle = \left\langle \overbrace{\bar{\chi}(x)\chi(x) \bar{\chi}(y)\chi(y)} \right\rangle. \quad (7.46)$$

In the following the lattice formulation and observables are discussed and results of one-flavour lattice simulations are presented.

## 7.2 Lattice formulation and thermodynamic observables

The lattice action for  $G_2$ -QCD (4.1) reads

$$S_{\text{QCD}}[\mathcal{U}, \Psi] = S_{\text{Sym}}[\mathcal{U}, \beta] - \sum_{xy} \bar{\Psi}_x D_{xy}[\mathcal{U}, m, \mu] \Psi_y, \quad (7.47)$$

where  $S_{\text{Sym}}$  is the Symanzik-improved gauge action and  $D[\mathcal{U}, m, \mu]$  the Wilson-Dirac operator at bare fermion mass  $m$  and real baryon chemical potential  $\mu$ ,

$$D_{xy} = (m + 4)\delta_{xy} - \frac{1}{2} \sum_{\nu=1}^4 (\gamma_\nu - 1) e^{\mu\delta_{\nu,0}} \mathcal{U}_{x,\nu} \delta_{x,y-\nu} + (\gamma_\nu + 1) e^{-\mu\delta_{\nu,0}} \mathcal{U}_{x-\nu,\nu}^\dagger \delta_{x,y+\nu}. \quad (7.48)$$

In the following, also the hopping parameter  $\kappa = (2m + 8)^{-1}$  is used. The simulations are carried out with the described rHMC algorithm for Dirac fermions. In these first simulations, only a single Dirac flavour  $N_f = 1$  is considered, since this is the simplest case and, in difference to QCD, already a continuous non-trivial chiral symmetry and possible pseudo-Goldstone bosons exist. In addition to the Polyakov loop, the plaquette variable and its susceptibilities, the following thermodynamic observables are considered to investigate the phase diagram: The chiral condensate  $\Sigma(T, \mu, m)$  is given by

$$\Sigma(T, \mu, m) = \frac{1}{V} \frac{\partial \ln Z}{\partial m} = \frac{1}{V} \sum_x \langle \bar{\Psi} \Psi \rangle = \frac{1}{V} \langle \text{tr} Q^{-1} \rangle_{\text{eff}}. \quad (7.49)$$

If data are available, its value is renormalized with the chiral condensate at zero temperature and vanishing chemical potential,  $\Sigma_{\text{ren}}(T, \mu, m) = \Sigma(T, \mu, m) / \Sigma(0, 0, m)$ . Its derivative with respect to the bare quark mass  $m$  defines the chiral susceptibility (here only the disconnected part is taken into account)

$$\begin{aligned} \chi(\Sigma) &= \left( \frac{\partial \Sigma}{\partial m} \right)_{\text{disc}} = V \left( \left\langle \frac{1}{V^2} \sum_{x,y} \bar{\Psi}(x) \Psi(x) \bar{\Psi}(y) \Psi(y) \right\rangle - \left\langle \frac{1}{V} \sum_x \bar{\Psi}(x) \Psi(x) \right\rangle^2 \right)_{\text{disc}} \\ &= \frac{1}{V} \left( \left\langle (\text{tr} Q^{-1})^2 \right\rangle_{\text{eff}} - \langle \text{tr} Q^{-1} \rangle_{\text{eff}}^2 \right). \end{aligned} \quad (7.50)$$

The quark number density is the derivative of the partition function with respect to the chemical potential  $\mu$  and therefore a monotonically increasing function in  $\mu$ ,

$$\begin{aligned} n_q(T, \mu, m) &= \frac{1}{V} \frac{\partial \ln Z}{\partial \mu} = -\frac{1}{2V} \sum_{xy} \left\langle \bar{\Psi}_x \frac{\partial D_{xy}}{\partial \mu} \Psi_y \right\rangle = -\frac{1}{V} \left\langle \text{tr} Q^{-1} \frac{\partial Q}{\partial \mu} \right\rangle_{\text{eff}} \\ &= -\frac{1}{2V} \sum_x \left\langle \bar{\Psi}_x (\gamma_0 - 1) e^\mu \mathcal{U}_{x,0} \Psi_{x+0} - \bar{\Psi}_x (\gamma_0 + 1) e^{-\mu} \mathcal{U}_{x-0,0}^\dagger \Psi_{x-0} \right\rangle. \end{aligned} \quad (7.51)$$

The second derivative,  $\chi(n_q) = \frac{1}{V} \frac{\partial^2 \ln Z}{\partial \mu^2}$ , defines the quark number susceptibility. And finally the quark energy density is given by

$$e_q(T, \mu, m) = -\frac{1}{2V} \sum_x \left\langle \bar{\Psi}_x (\gamma_0 - 1) e^\mu \mathcal{U}_{x,0} \Psi_{x+\hat{0}} + \bar{\Psi}_x (\gamma_0 + 1) e^{-\mu} \mathcal{U}_{x-\hat{0},0}^\dagger \Psi_{x-\hat{0}} \right\rangle. \quad (7.52)$$

The quark energy density and the plaquette density are renormalized by their values at zero temperature and vanishing chemical potential according to

$$\begin{aligned} e_{q,\text{ren}}(T, \mu, m) &= e_q(T, \mu, m) - e_q(0, 0, m), \\ \langle \mathcal{O}_P \rangle_{\text{ren}}(T, \mu, m) &= \langle \mathcal{O}_P \rangle(T, \mu, m) - \langle \mathcal{O}_P \rangle(0, 0, m). \end{aligned} \quad (7.53)$$

The simulations are performed with the described rHMC algorithm and Monte-Carlo statistics between 1000 configurations for the larger  $16^3 \times 6$  to  $16^4$  lattices and up to 10000 configurations for the smaller  $8^3 \times 2$  to  $8^3 \times 16$  lattices.

## 7.3 The phase diagram of $G_2$ -QCD

In the present section one-flavour  $G_2$ -QCD is investigated on small lattices with a spatial volume of  $8^3$  lattice points and different temporal extents of the lattice. First, the finite temperature phase transition at zero chemical potential is compared to the phase transition in pure (quenched) gauge theory. The results for the Polyakov loop and its susceptibility on a  $8^3 \times 2$  lattice are shown in Fig. 7.3. For  $\kappa = 0$  the

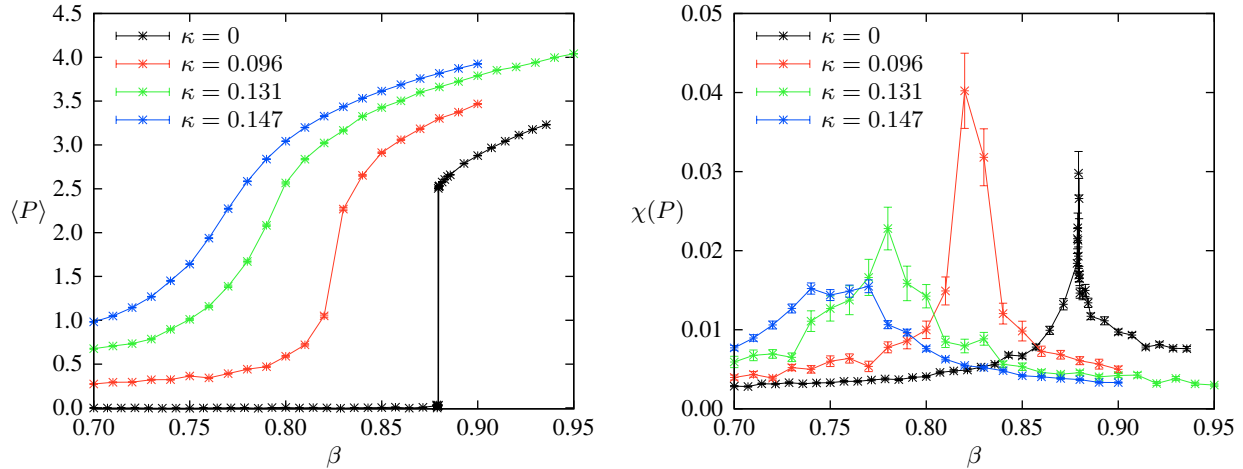


**Figure 7.3** *Left panel:* Polyakov loop at finite temperature and zero chemical potential for  $\kappa = 0, 0.096, 0.131$  and  $0.147$ . *Right panel:* Susceptibility of the Polyakov loop.

first order transition of the quenched theory is clearly visible. When increasing the hopping parameter from  $\kappa = 0$  to  $\kappa = 0.147$ , the transition shifts to smaller values of  $\beta$  and becomes weaker. This is also expected from QCD, where at the line  $m_d = m_u = m_s$  the phase transition changes from a first order transition for large up and down quark masses to a crossover in the vicinity of the physical point [219]. The second interesting observable at finite temperature and zero chemical potential is the chiral condensate. In Fig. 7.4 it is shown together with its susceptibility. Although chiral symmetry is explicitly broken by the Wilson mass, a transition is seen in the chiral condensate, roughly at the same position as for the Polyakov loop. With smaller quark masses the peak in the susceptibility becomes broader, also pointing to a crossover at finite temperature and zero chemical potential. This is similar to QCD and in difference to adjoint QCD (which also does not suffer from a fermion sign problem), where the chiral and deconfinement phase transition are clearly separated [51]. To set a physical scale, the pion mass  $m_\pi$  (would-be Goldstone boson) is calculated in lattice units as a function of  $\beta$ , and the result is shown in Fig. 7.5 (left panel). For  $\beta = 0.6$  to  $\beta \approx 0.9$  the pion mass is nearly constant, while for  $\beta \gtrsim 0.9$  it decreases with increasing  $\beta$ , as expected in the continuum limit (scaling window). The mass of the sigma meson, the connected part of the  $f'$ , is for small values of  $\beta$  larger than the pion mass, but for larger values of  $\beta$  both masses coincide. In Fig. 7.5 (right panel) the masses of the first excited states of the pion and sigma meson are also shown. Now it is possible to set a physical scale for the temperature  $T$  (using the dependence of the lattice pion ground state mass on the inverse lattice gauge coupling  $\beta$ ,

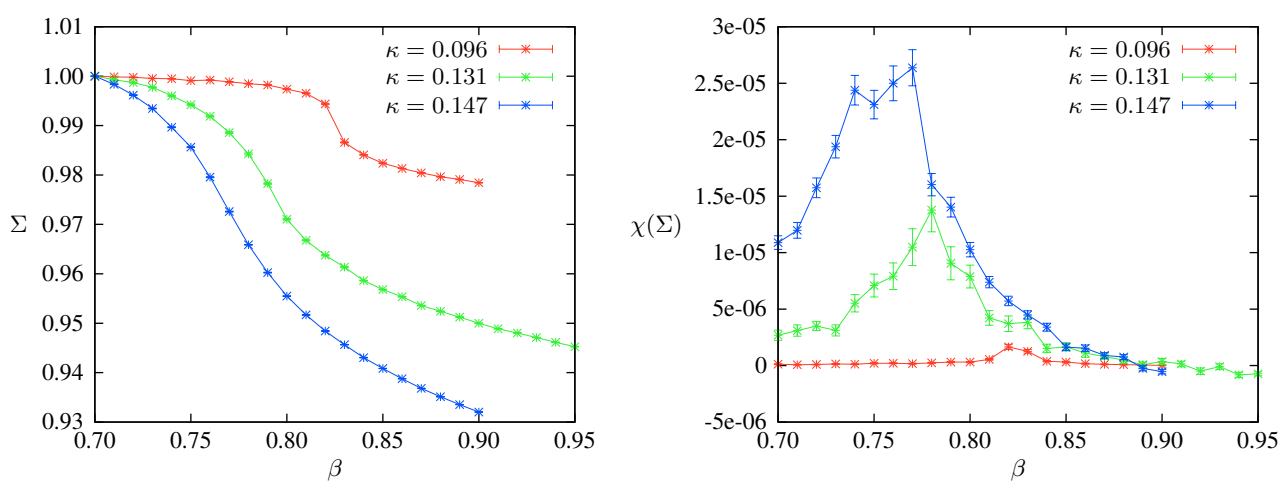


**Figure 7.4** *Left panel:* Chiral condensate (rescaled) at finite temperature and zero chemical potential for  $\kappa = 0.096, 0.131$  and  $0.147$ . *Right panel:* Susceptibility of the chiral condensate.

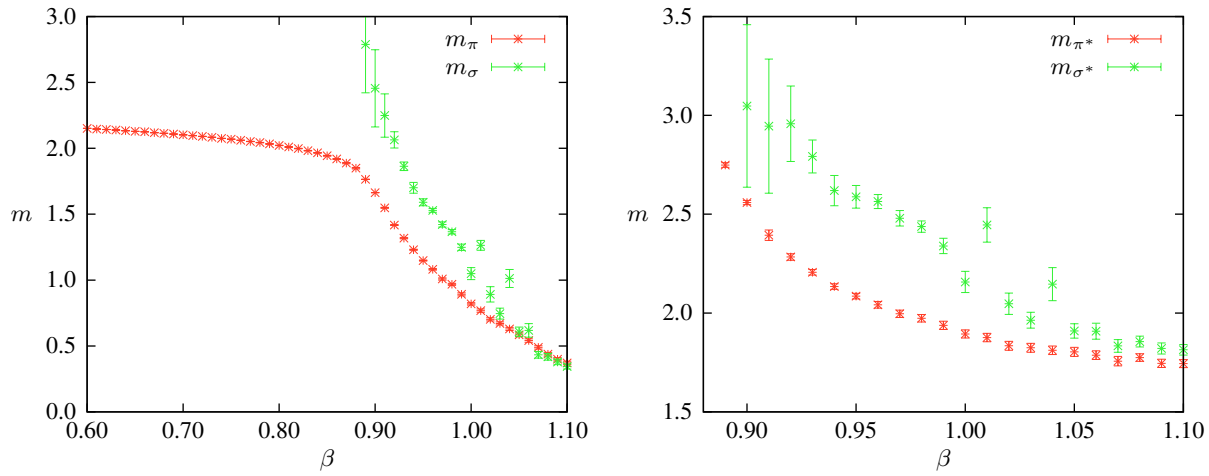


**Figure 7.5** *Left panel:* Pion and Sigma ground state masses on a  $8^3 \times 16$  lattice. *Right panel:* Masses of excited Pion and Sigma.

i.e. the lattice spacing  $a$ ) according to

$$\tilde{a} \equiv m_\pi(\beta) = m_{\pi,\text{phys}} a(\beta) \quad \text{and} \quad T(\beta) = \frac{1}{N_t a(\beta)} = \frac{m_{\pi,\text{phys.}}}{N_t m_\pi(\beta)}. \quad (7.54)$$

In the following the phase diagram is calculated as a function of the dimensionless parameters

$$\tilde{T} = \frac{T}{m_{\pi,\text{phys}}} = \frac{1}{N_t m_\pi(\beta)} \quad \text{and} \quad \tilde{\mu} = \frac{\mu}{m_\pi} = \frac{\mu_{\text{phys}}}{m_{\pi,\text{phys}}} \quad \text{or} \quad \tilde{\mu}/\tilde{T} = \mu N_t. \quad (7.55)$$

By fixing the scale in this way for  $\beta = 0.6$  up to  $\beta \approx 0.9$ , the temperature is almost constant. This is clearly a lattice artifact and coincides with the condensation of monopoles in the bulk phase, investigated below. Fig. 7.6 shows the finite temperature phase transition in physical units on a  $8^3 \times 2$  lattice compared to a  $8^3 \times 4$  lattice. Assuming  $T_c \approx 160$  MeV as the physical phase transition temperature yields a pion mass of  $m_{\pi,\text{phys}} \approx 662$  MeV for the smaller lattice and  $m_{\pi,\text{phys}} \approx 1024$  MeV for the larger lattice,

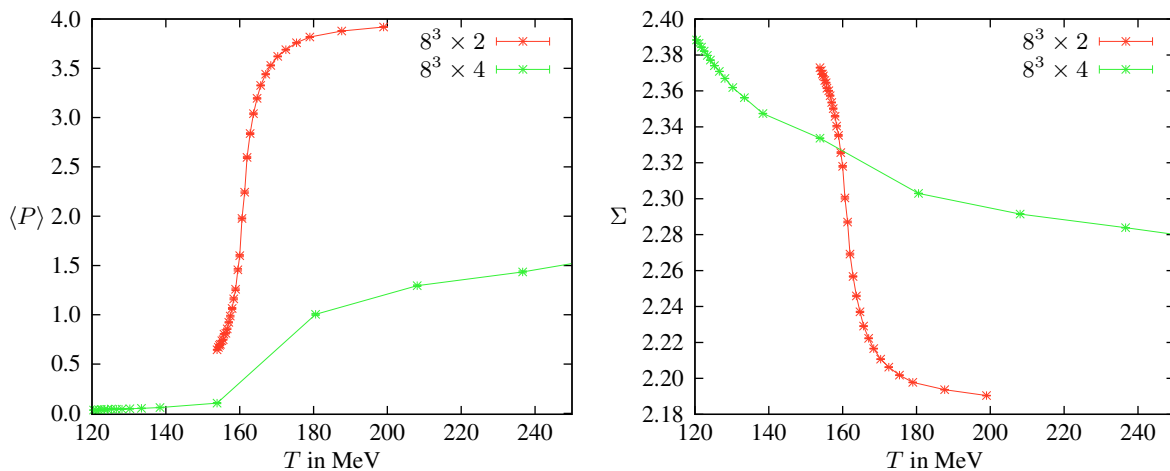


**Figure 7.6** Polyakov loop (left panel) and chiral condensate (right panel) as a function of temperature for the  $8^3 \times 2$  and  $8^3 \times 4$  lattice at  $\kappa = 0.147$ .

indicating strong discretization and finite size errors. The lattice spacing is then ranging from  $a(N_t = 2, \beta = 0.6) \approx 0.64$  fm to  $a(N_t = 2, \beta = 1.1) \approx 0.11$  fm on the smaller lattice and  $a(N_t = 4, \beta = 0.6) \approx 0.41$  fm to  $a(N_t = 4, \beta = 1.1) \approx 0.07$  fm on the larger lattice, corresponding to physical volumes between  $V \approx (5.12 \text{ fm})^3$  and  $V \approx (0.56 \text{ fm})^3$ .

### 7.3.1 The bulk transition

In chapter 6 it was shown, that on these small lattices (without quarks and with the Wilson gauge action) the finite temperature deconfinement transition happens in an unphysical bulk phase. This bulk phase is also present in  $G_2$ -QCD, where the Wilson gauge action is replaced by the Symanzik-improved gauge action. The monopole density  $\langle M \rangle$  and the plaquette variable  $\langle \mathcal{O}_P \rangle$  at finite temperature and zero chemical potential (on a  $8^3 \times 2$  lattice for different values of  $\kappa$ ) are shown in Fig. 7.7. The transition, visible

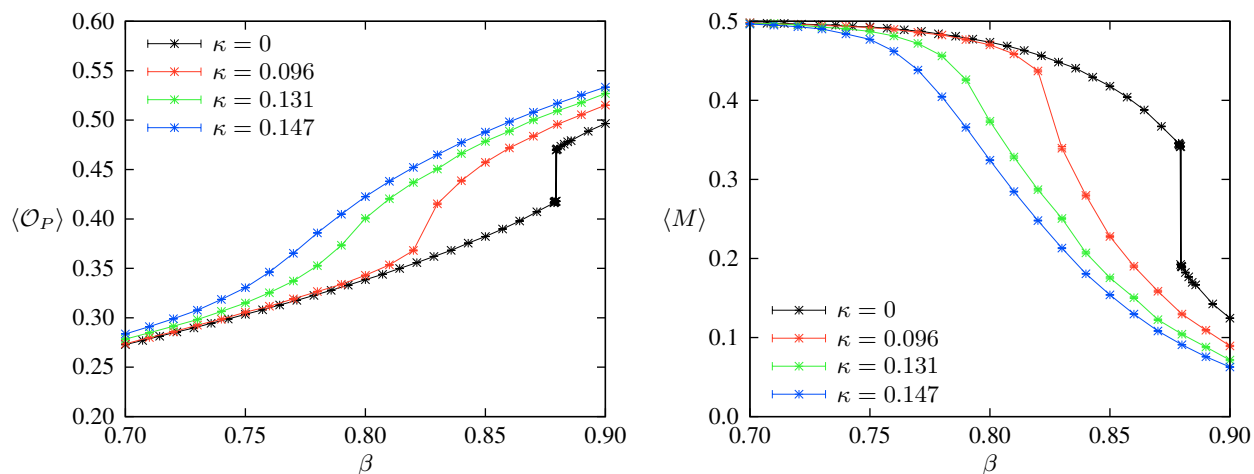


**Figure 7.7** Plaquette (left panel) and monopole density (right panel) at finite temperature and zero chemical potential for  $\kappa = 0, 0.096, 0.131, 0.147$  on a  $8^3 \times 2$  lattice.

in the plaquette variable, coincides with the condensation of monopoles and therefore is not a physical transition. As expected, the bulk transition shifts also to smaller values of  $\beta$  with increasing hopping parameter, but for all values of  $\kappa$  it overshadows the physical deconfinement transition. In the following, a bare quark mass of  $m = -0.6$  is chosen, corresponding to  $\kappa = 0.147$ . At this value of  $\kappa$  the transition is already substantially weaker than the transition in the quenched ensemble. The corresponding critical gauge coupling on the  $N_t = 2$  lattice is given by  $\beta_c \approx 0.75(2)$ . In Fig. 7.8 the plaquette and monopole density for  $\kappa = 0.147$  are shown for different temporal extents of the lattice. For  $N_t = 2$ , the bulk

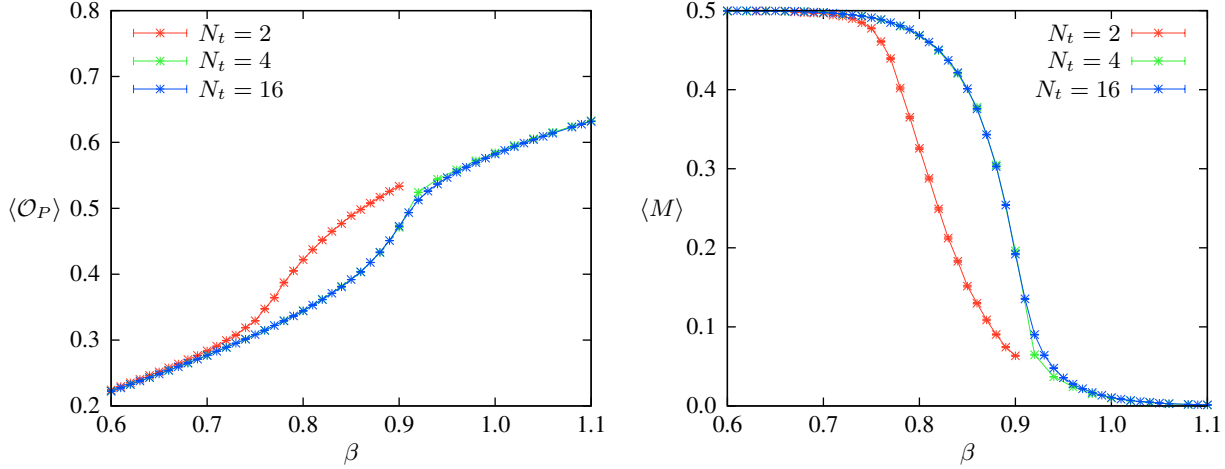


**Figure 7.8** Plaquette (left panel) and monopole density (right panel) at zero chemical potential for  $\kappa = 0.147$  and various temporal extents of the lattice, i.e.  $N_t = 2$ ,  $N_t = 4$  and  $N_t = 16$ .

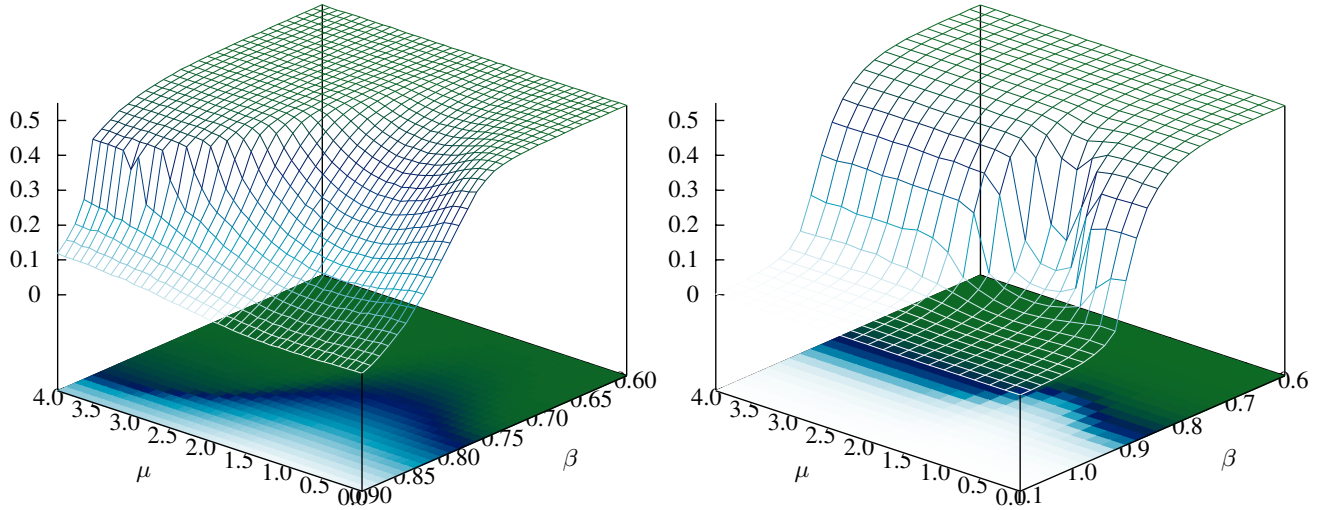


**Figure 7.9** Left panel: Monopole density on a  $8^3 \times 2$  lattice. Right panel: Monopole density on a  $8^3 \times 4$  lattice.

transition occurs at smaller values of  $\beta$  than for  $N_t = 4$  and  $N_t = 16$ . In the pure gauge theory the bulk transition does not depend on the spatial or temporal extent of the lattice. It depends only on the mass of the scalar field, as studied previously, or on the quark mass, as it is in the present case. The

mismatch, observed in Fig. 7.8, indicates an effectively higher mass (due to strong finite size effects or discretization errors) for the smallest lattice with temporal extent of two lattice points. Finally, the bulk transition in the  $(\beta, \mu)$  plane is investigated, and the results for  $N_t = 2$  and  $N_t = 4$  are shown in Fig. 7.9. At intermediate values of the chemical potential the bulk transition shifts to smaller values of  $\beta$ , while for larger values of the chemical potential it occurs at the  $\beta$  value for the quenched theory. The obtained results for the monopole density show, that at finite temperature the continuum physics is overshadowed by an unphysical bulk phase. Nevertheless, it is interesting to study these small lattices, since, as already seen in the previous chapter, some observables, e.g. the Polyakov loop, are insensible to the condensation of monopoles and therefore may provide relevant information. But of course the obtained results have to be verified on larger lattices. At zero temperature it is possible to choose  $\beta$  such that the monopole density is already small enough, and therefore the results should be reliable.

### 7.3.2 The phase diagram at zero temperature: overview

At zero temperature  $G_2$ -QCD is investigated on a  $8^3 \times 16$  lattice in the parameter region  $\beta = 0.90 \dots 1.10$  and  $\mu = 0 \dots 2$ . The monopole density is already sufficiently small, such that the system is outside the bulk phase for all values of  $\beta$  and  $\mu$ . The phase diagram at zero temperature is plotted as a function of the chemical potential and the dimensionless lattice spacing  $\tilde{a}$ , in order to identify finite size effects and lattice artifacts. The scale is again set by the ground state pion mass  $m_\pi$ . In Fig. 7.10 (left panel) the quark number density is shown. It is observed, that for small values of the chemical potential the

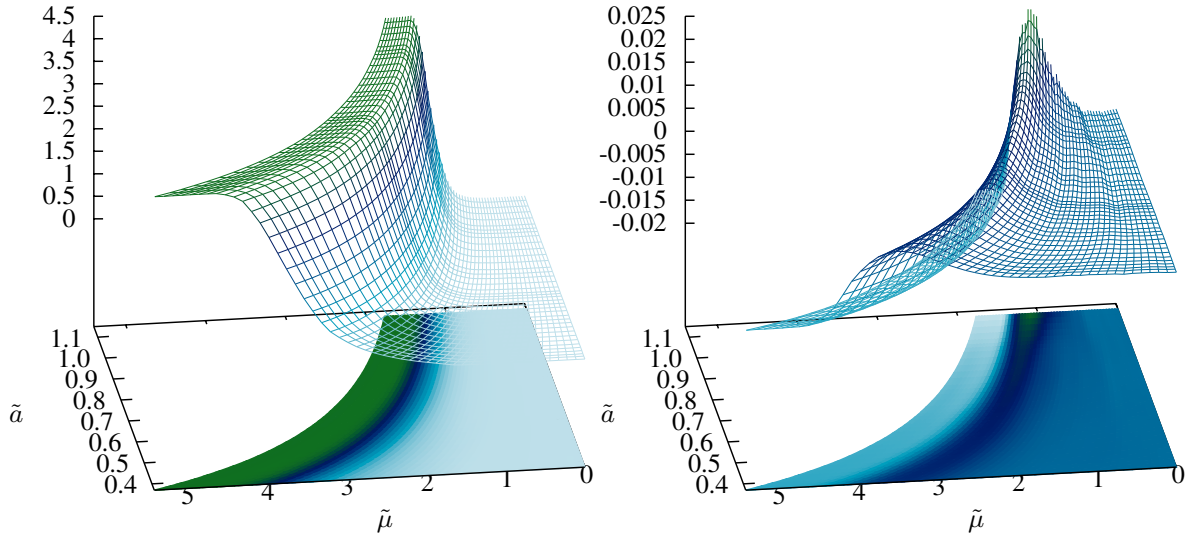


**Figure 7.10** Quark number density (left panel) and renormalized plaquette (right panel) on a  $8^3 \times 16$  lattice.

system remains in the vacuum, i.e. the quark number density vanishes, which is expected due to the *silver blaze property* of QCD. While increasing the chemical potential the quark number density is rising, indicating that baryonic matter is present and the system is no longer in the vacuum state. At even larger  $\tilde{\mu} > \tilde{\mu}_{\text{sat}}(\tilde{a})$  the quark number density saturates. A possible explanation is that each lattice site is occupied by bound states carrying non-vanishing baryon number. The saturation threshold  $\tilde{\mu}_{\text{sat}}(\tilde{a})$

depends on the lattice spacing and shifts to larger values of the chemical potential  $\tilde{\mu}$  with decreasing  $\tilde{a}$ , indicating that the saturation is only a lattice artifact that might vanish in the continuum limit. The value of the saturation,  $n_{q,\text{sat}} = 4.12(1)$ , does not depend on the lattice spacing and stays far below its maximum value of  $n_{q,\text{max}} = 2N_c = 14$ . So far it is still an open question why the quark number density takes this particular value at the saturation density. One possibility is a filling of the lattice with a mixture of two and three quark bound states, i.e. diquarks and protons (neutrons), but also a filling with quark-gluon hybrids or heavier bound states is supposable. Whether a complete filling of  $n_q = 14$  is achieved in the continuum limit (due to saturation at larger values of the chemical potential) remains an open question for future investigations. In the right panel of Fig. 7.10 the renormalized plaquette variable is shown. For smaller values of the lattice spacing, only a very weak signal at the deconfinement transition is observed. At larger values of the chemical potential the plaquette takes its value as in the quenched ensemble. Fig. 7.11 shows the Polyakov loop and the renormalized chiral condensate. For small values of the chemical potential the system stays in a confined and chirally broken phase, as

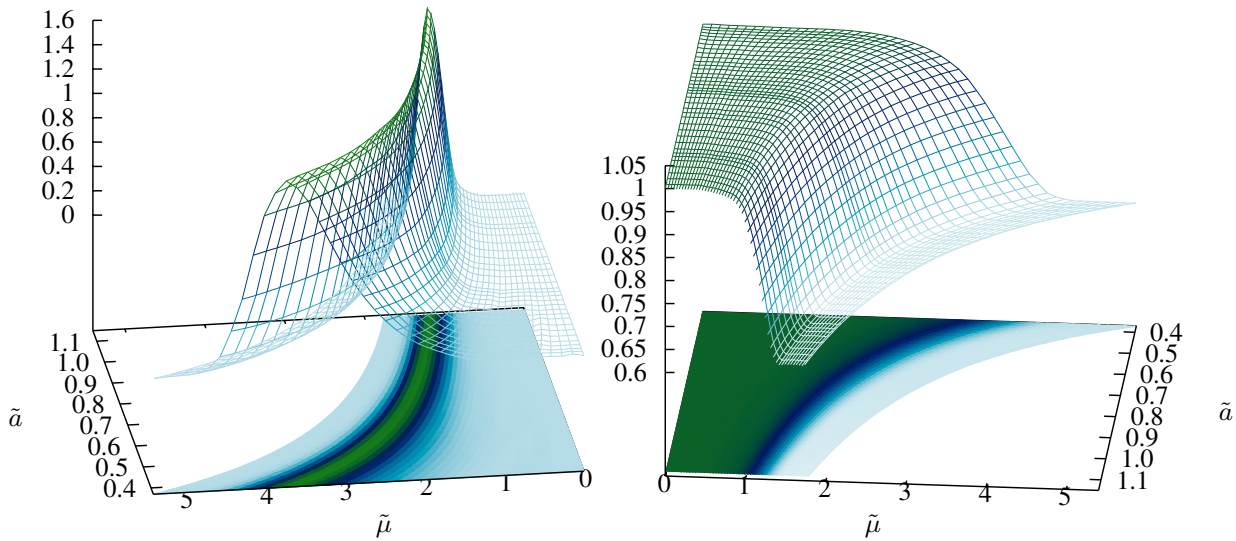


**Figure 7.11** Polyakov loop (left panel) and renormalized chiral condensate (right panel) on a  $8^3 \times 16$  lattice.

expected. When increasing the chemical potential, the theory undergoes a deconfining phase transition. Nearly at the same point the chiral condensate drops down, indicating chiral restoration. With decreasing lattice spacing  $\tilde{a}$ , the transition shifts to larger values of  $\tilde{\mu}$ . Thus, for these large values of  $\tilde{\mu}$  and on this rather small lattice, the system is far away from the continuum limit. For  $\tilde{\mu} > \tilde{\mu}_{\text{sat}}$  the theory confines again<sup>a</sup>. A possible reason is that due to the saturation the theory behaves similar as pure Yang-Mills theory.

In conclusion, if the quark number density is saturated, then many observables, e.g. the Polyakov loop and the plaquette, behave as in the quenched ensemble at vanishing chemical potential. This has also been observed in 2-colour QCD in [53]. Although at this point the saturation is only a lattice artifact, a

<sup>a</sup>Although the Polyakov loop is not an order parameter for confinement, it is expected that a small Polyakov loop coincides with a confinement phase.

similar saturation effect is expected in the continuum limit due to the Pauli blocking, but at a much larger value of the chemical potential as observed here.

### 7.3.3 The phase diagram at zero temperature: the onset transition to nuclear matter

The onset transition from the vacuum to nuclear matter is studied in Fig. 7.12. At  $\tilde{\mu}_0 \approx 0.5$ , a transition

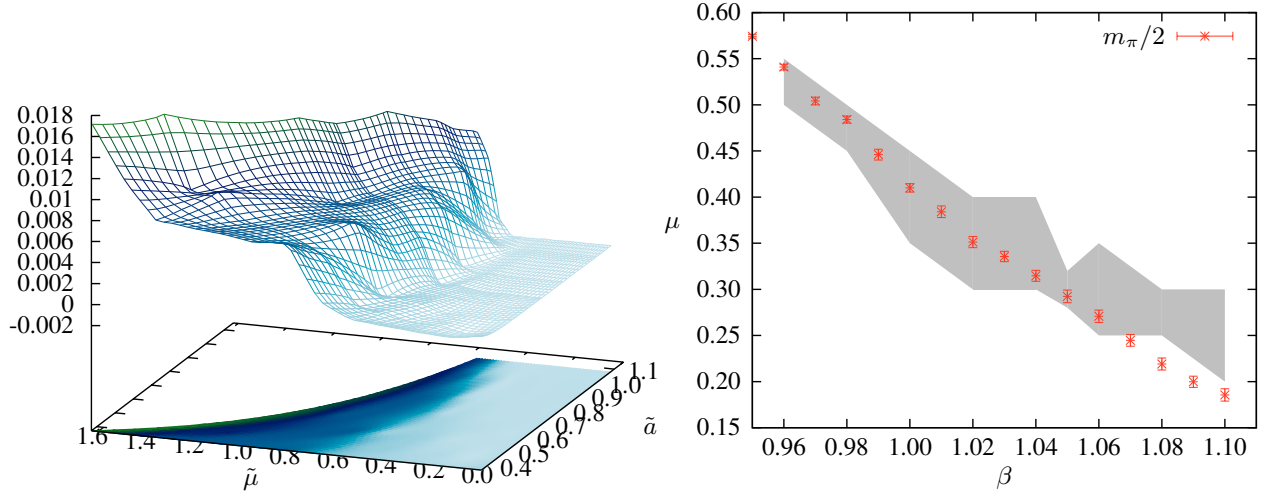


**Figure 7.12** Quark number density (left panel) and onset transition to nuclear matter (shaded region), compared to half of the pion mass (right panel).

in the quark number density (left panel) is observed. The value of the onset does almost not depend on the lattice spacing, indicating that at smaller values of  $\tilde{\mu}$  finite size effects are less important than for larger values of the chemical potential. In the right panel, the transition (shaded region) is compared to half of the pion mass, and a clear coincidence is visible. This indeed verifies that  $G_2$ -QCD possesses the *silver blaze property* for baryon chemical potential, i.e. half of the mass of the lightest bound state carrying baryon number is a lower bound for the onset transition to nuclear matter. With decreasing lattice spacing  $\tilde{a}$ , a plateau develops for  $\tilde{\mu}_0(\tilde{a}) < \tilde{\mu} < \tilde{\mu}_1(\tilde{a})$ , where the quark number density is almost constant. For  $\tilde{\mu} > \tilde{\mu}_1(\tilde{a})$  it starts again to increase until it saturates at  $\tilde{\mu}_{\text{sat}}$ . In the left panel of Fig. 7.13, the renormalized quark energy density is plotted. It shows qualitatively the same behaviour as the quark number density, i.e. for  $\tilde{\mu} < \tilde{\mu}_0$  it does not depend on the chemical potential, verifying again the *silver blaze property*. In the right panel, the energy per quark  $e_{q,\text{ren}}/n_q$  is shown for  $\tilde{\mu} > \tilde{\mu}_0$ . At intermediate values of the chemical potential, a minimum at  $\tilde{\mu} \approx 1.1 \sim 1126$  MeV is observed, while the ratio approaches its saturation value from below for large values of  $\tilde{\mu}$ . This observable is of great interest in the formation of neutron or quark stars, as pointed out in [220]. The minimum would correspond to the bulk of a neutron or quark star, depending on whether it is located in the confined or deconfined phase. In the present simulations it is located in the confined phase but, due to saturation and finite volume effects and a strong dependence on the quark mass, this might change on larger lattices.

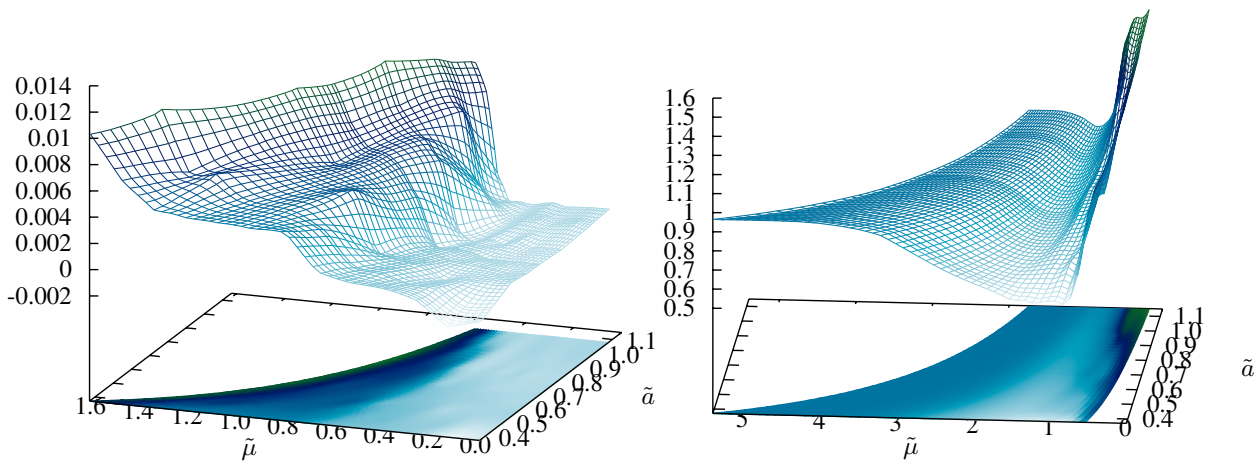


**Figure 7.13** Left panel: Renormalized quark energy density. Right panel: Energy per quark  $e_{q,\text{ren}}/n_q$ .

### 7.3.4 The phase diagram at zero temperature: separation of scales

As observed above, different transitions show up in the quark number density. For  $\beta = 1.05$  simulations with a higher resolution in  $\mu$ -direction and an improved statistics have been performed. In Fig. 7.14 the Polyakov loop, the chiral condensate and the quark number density are shown. Although the lattices

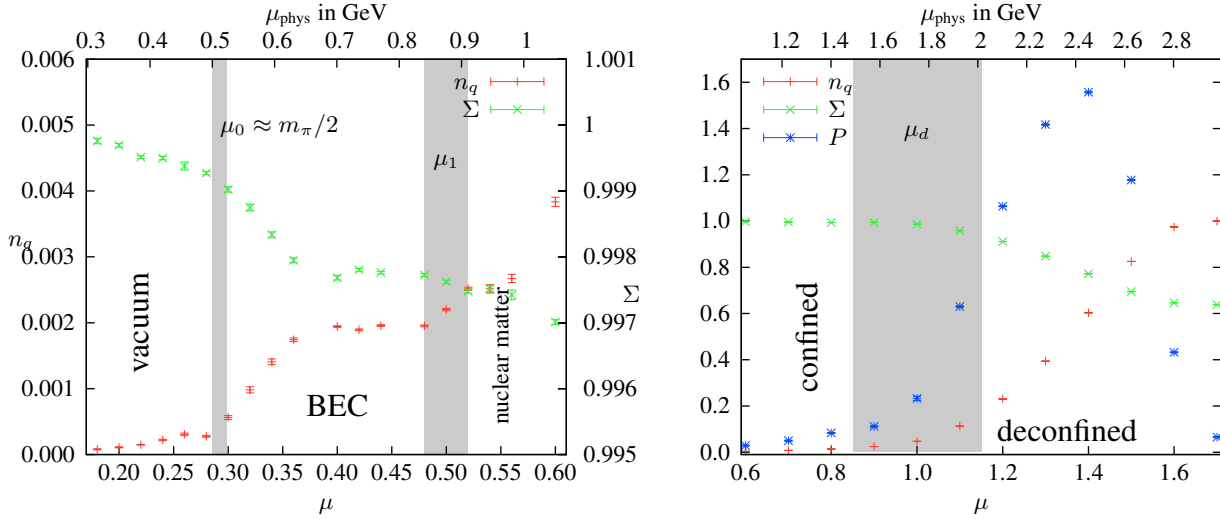


**Figure 7.14** Normalized quark number density  $n_q/n_{q,\text{sat}}$ , renormalized chiral condensate  $\Sigma$  and Polyakov loop  $P$  on a  $8^3 \times 16$  lattice at  $\beta = 1.05$ .

are very small and finite size and volume effects may change the picture, in the following a possible explanation is given. For  $\mu < \mu_0$  the system remains in the vacuum state. As observed, the scale of  $\mu_0$  is related to the diquark mass, i.e.  $\mu_0 \approx m_\pi/2 \sim 512 \text{ MeV}$ . For  $\mu > \mu_0$  the diquarks condense, forming a Bose-Einstein condensate (BEC), in the same way as observed in two-color QCD [220]. Therefore, the chiral condensate should be rotated into a diquark condensate. So far the diquark condensate has not been calculated but a drop in the chiral condensate is observed.

The next onset at  $\mu = \mu_1 \sim 870 \text{ MeV}$  may correspond to a transition from the BEC phase to ‘ordinary’

fermionic nuclear matter, in contrast to QCD where the transition is expected to be from the vacuum to fermionic nuclear matter. The scale for  $\mu_1$  is then set by the lightest fermionic baryon, e.g. the quark-gluon hybrid or the neutron (proton).

The third scale corresponds to the onset of deconfinement at  $\mu = \mu_2 = \mu_d \sim 1.5$  to  $2.0$  GeV. The Polyakov loop is not an order parameter for confinement and therefore is not absolutely clear where the transition in the bare chemical potential is located. Also saturation effects set in and the Monte-Carlo statistics is not sufficient to compute the Polyakov loop susceptibility which might give a better value of  $\mu_d$  than the very rough estimate here. In the deconfined phase the quark number density and quark energy density are roughly given by the Stefan-Boltzmann expressions for a degenerate system of weakly-interacting massless quarks, populating a Fermi sphere up to some maximum momentum  $k_F = \mu$ ,

$$n_q^{\text{SB}} = \frac{N_f N_c}{3\pi^2} \mu^3 \quad \text{and} \quad e_q^{\text{SB}} = \frac{N_f N_c}{3\pi^2} \mu^4. \quad (7.56)$$

Therefore, in Fig. 7.15 the quark number density and the quark energy density are plotted normalized to their Stefan-Boltzmann expressions. In order to decide whether indeed a confined phase with ‘ordinary’

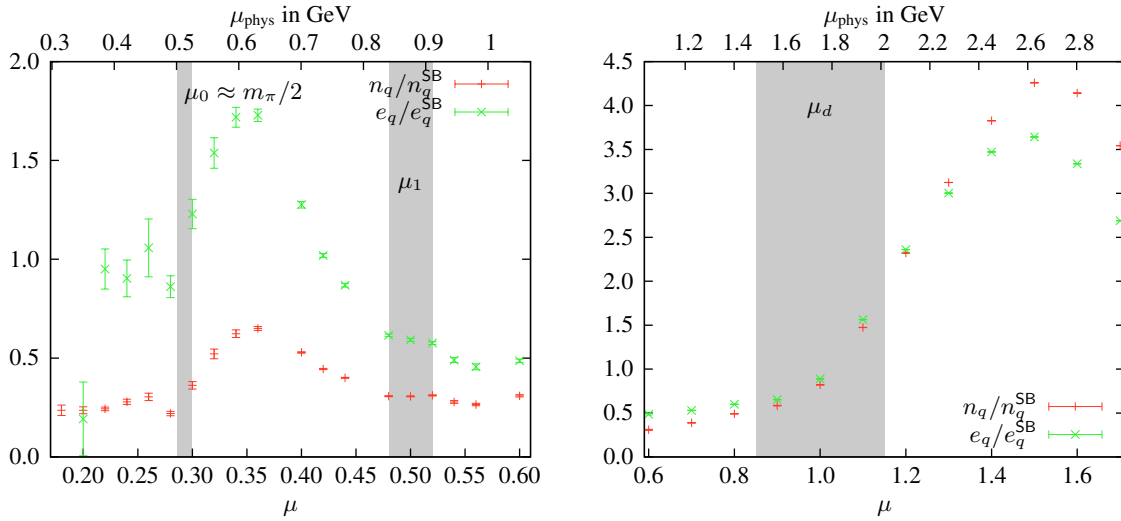


**Figure 7.15** Quark number density and renormalized quark energy density normalized to their Stefan-Boltzmann expressions.

fermionic nuclear matter exist, further simulations and a more precise determination of the deconfinement phase transition at zero temperature are necessary. In the next section, the phase diagram at finite temperature is investigated.

### 7.3.5 The phase diagram at finite temperature

At finite temperature the phase diagram is investigated on a  $8^3 \times 2$  and on a  $8^3 \times 4$  lattice in the parameter region  $\beta = 0.6 \dots 1.1$  and  $\mu = 0 \dots 4$ . In physical units  $(\tilde{T}, \tilde{\mu})$ , the bulk phase is nearly shrunk to a single point due to the almost constant pion mass. Therefore the ratio  $\tilde{\mu}/\tilde{T}$  is chosen, which is proportional to the lattice chemical potential for a fixed temporal extent of the lattice. Fig. 7.16 (left panel)

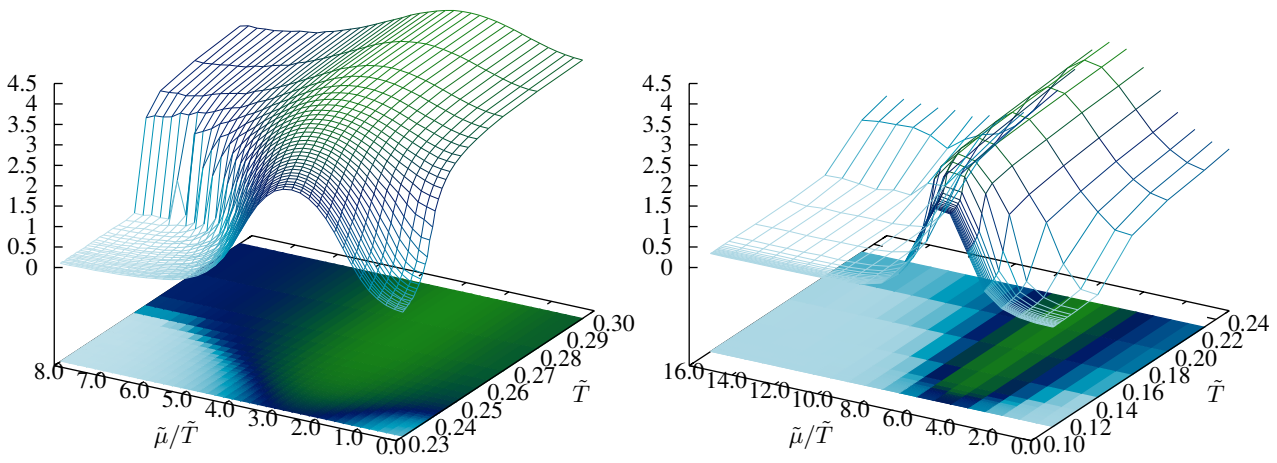


**Figure 7.16** Polyakov loop on a  $8^3 \times 2$  lattice (left panel) and on a  $8^3 \times 4$  lattice (right panel).

shows the Polyakov loop on the small  $8^3 \times 2$  lattice. At vanishing chemical potential the deconfinement transition is seen. For very large values of the chemical potential  $\tilde{\mu}/\tilde{T} > 8$ , the phase transition in the quenched theory is recovered. Below the phase transition temperature  $\tilde{T}_c(\mu = 0) \approx 0.24$ , the Polyakov loop shows (in  $\mu$ -direction) qualitatively the same behaviour as in the case of vanishing temperature, but the peak becomes broader. Above the phase transition, also a peak in the Polyakov loop is seen at finite  $\tilde{\mu}/\tilde{T} \approx 3.0$ . On the larger  $N_t = 4$  lattice, the Polyakov loops shows almost the same behaviour. The quark number density for both lattices is shown in Fig. 7.17. As in the case of zero temperature

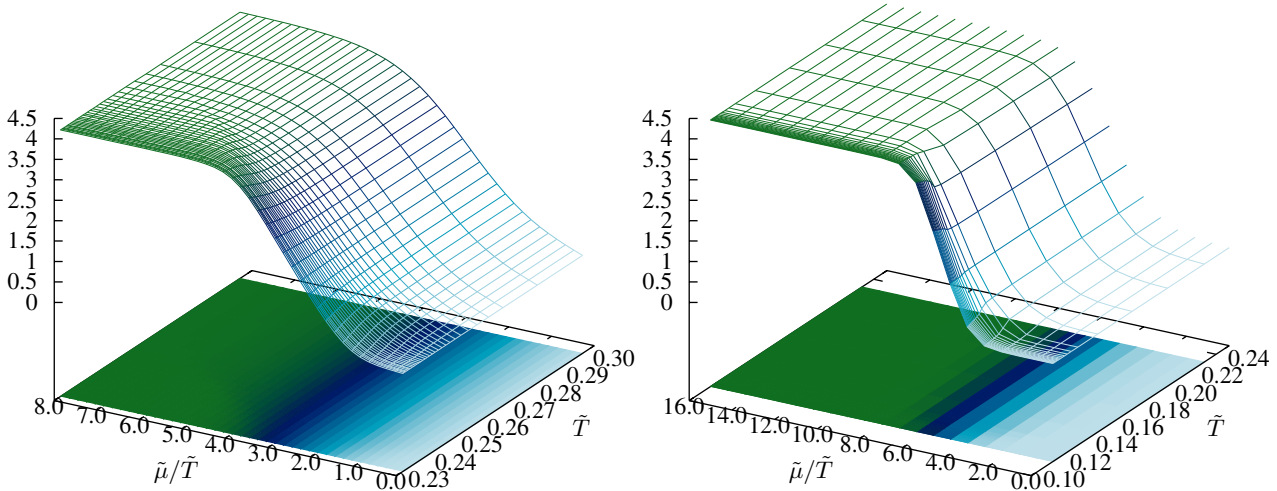


**Figure 7.17** Quark number density on a  $8^3 \times 2$  lattice (left panel) and on a  $8^3 \times 4$  lattice (right panel).

a saturation is observed. The saturation value is the same as for zero temperature,  $n_{q,\text{sat}} \approx 4.12$ , i.e. it does not depend on the temperature. For the smaller lattice the system saturates at approximately  $\tilde{\mu}/\tilde{T}(N_t = 2) \approx 4.0$ , compared to  $\tilde{\mu}/\tilde{T}(N_t = 4) \approx 8.0$  for the larger lattice. In the bare lattice parameter  $\mu$ , the saturation takes place at  $\mu \approx 2$  for both lattices. Moreover, in Fig. 7.18 the chiral condensate is shown. The chiral transition almost coincides with the transition observed in the Polyakov loop, at finite temperature as well as at finite chemical potential. In contrast to the Polyakov loop, no saturation artifact

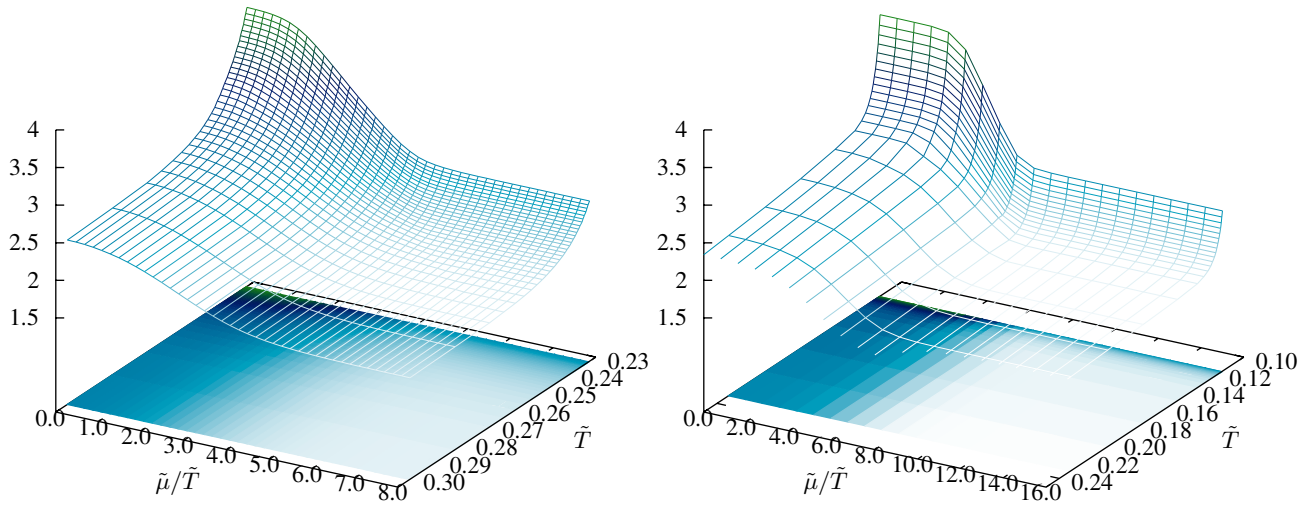


**Figure 7.18** Chiral condensate on a  $8^3 \times 2$  lattice (left panel) and on a  $8^3 \times 4$  lattice (right panel).

in the chiral condensate for large values of  $\mu$  is observed, i.e. there is no transition back to the chirally broken phase. Finally, the data obtained on the  $8^3 \times 4$  and the zero temperature results at  $\beta = 0.90$  are merged into a single phase diagram. Here a linear interpolation between the finite temperature and the zero temperature regime is used. The plots for the quark number density, the Polyakov loop, the chiral condensate and the plaquette variable are shown in Fig. 7.19. The only reliable information can be obtained from values of  $\mu$  much smaller than the saturation threshold, best seen in the quark number density (the green region corresponds to *unphysical* lattice artifacts). As observed before, in this *physical* regime the obtained results depend, in physical units, only slightly on the lattice spacing. At small temperatures, the onset of the deconfinement transition meets the zero temperature axes almost vertically and roughly coincides with the chiral restoration. With increasing temperature the deconfinement transition shifts to lower values of the chemical potential and finally meets the finite temperature axes almost vertically. The reflection point is roughly given by  $(\tilde{T}, \tilde{\mu})_{\text{refl}} \approx (0.14, 0.34)$ , corresponding to physical values of

$$(T, \mu)_{\text{refl}} \approx (142 \text{ MeV}, 348 \text{ MeV}). \quad (7.57)$$

Compared to the results for the critical point in QCD in [193, 199], this reflection point is not far off. The chiral transition seems to be much stronger for temperatures below the reflection point than for temperatures above the reflection point. The renormalized plaquette variable is shown in the lower right panel of Fig. 7.19. Mainly two peaks in the plaquette variable are observed. One at zero temperature, coinciding with the chiral and deconfinement phase transition, and one in the vicinity of the reflection point. The peak at finite temperature might be a lattice artifact due to the bulk transition. In contrast to the Polyakov loop, the quark number density and the chiral condensate, the plaquette variable is very sensitive to the condensation of monopoles. Unfortunately, at these small lattices and due to the bulk phase, the shown phase diagram might change dramatically on larger and finer lattices. Also, the pion mass and therefore the quark mass, is quite heavy compared to the QCD physical values. Consequently, in the next section a larger lattice with a lower pion mass is investigated. The raw data for the investigated small lattices are shown in the appendix D.

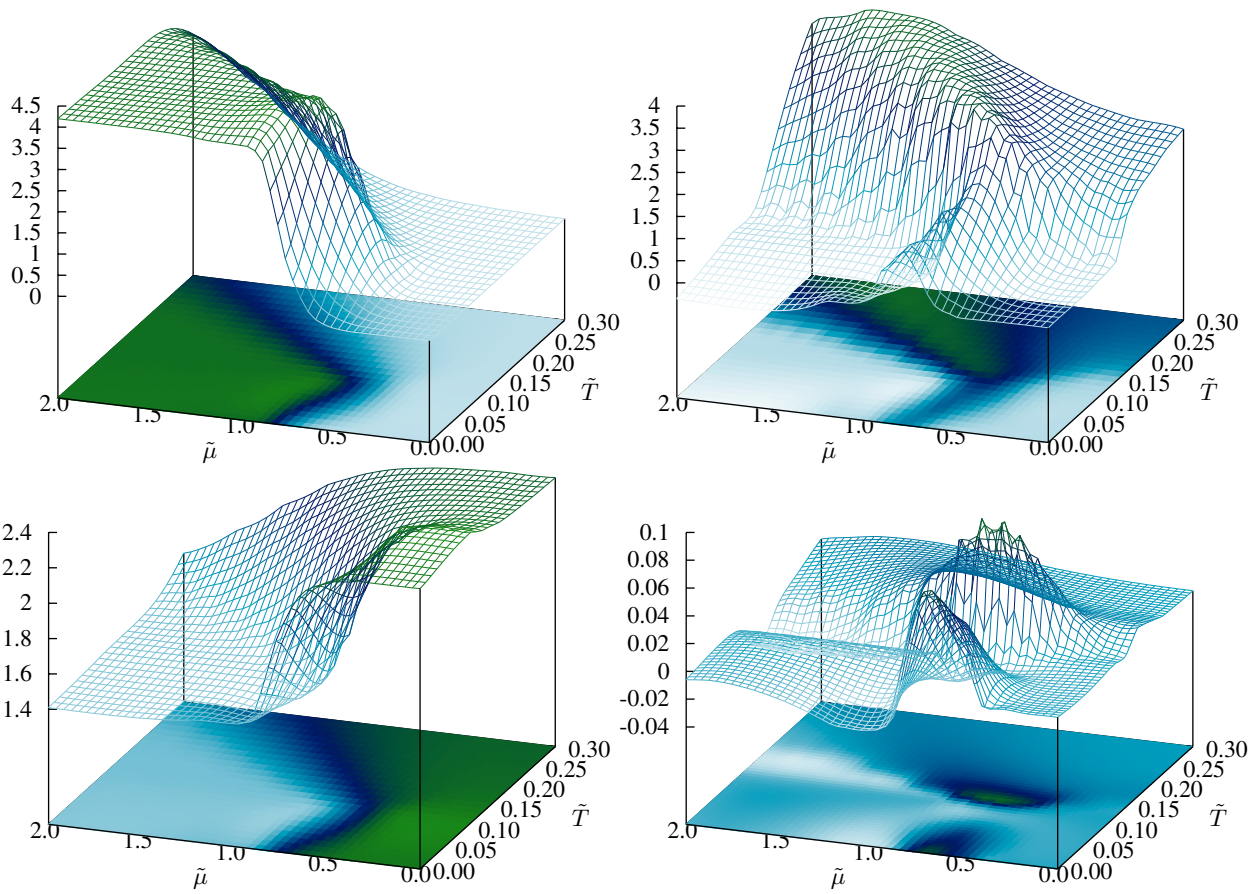


**Figure 7.19** The phase diagram of  $G_2$ -QCD as obtained on small lattices  $8^3 \times 4$  and  $8^3 \times 16$ . Shown are the quark number density (upper left panel), the Polyakov loop (upper right panel), the chiral condensate (lower left panel) and the (renormalized) plaquette variable (lower right panel).

### 7.3.6 The phase diagram on a larger lattice

To verify the results obtained on the small lattices, simulations on larger  $16^3 \times 6$ ,  $16^3 \times 8$  and  $16^4$  lattices at  $\beta = 0.85 \dots 1.1$  and  $\mu = 0 \dots 2$  are performed. As for the small lattice, the finite temperature phase transition for different hopping parameters  $\kappa$  is compared to the phase transition in the quenched ensemble, as seen in Fig. 7.20. With increasing  $\kappa$  the phase transition shifts again to smaller values of  $\beta$ , indicated by the Polyakov loop (left panel). For the chiral condensate (centre panel) and the plaquette (right panel) almost no transition can be observed for  $\kappa = 0.147$  and  $\kappa = 0.156$ , as expected for a crossover. Probably the quark masses are very heavy or the residual Wilson mass is quite large, due to a very coarse lattice far away from the continuum limit and scaling window. In this case it would be hard to observe spontaneous chiral symmetry breaking. In Fig. 7.21 (left panel) the mass of the pion ground state and first excited state are shown as a function of the inverse gauge coupling  $\beta$  for three different values of  $\kappa$ . With increasing  $\kappa$  the pion becomes lighter. The smallest pion mass at  $\kappa = 0.156$  and  $\beta = 1.00$  is (in lattice units) given by  $m_\pi = 0.33(1)$ . For  $\kappa = 0.156$  the point at which the pion becomes massless (and therefore chiral symmetry can be restored exactly in the continuum limit) is between  $\beta = 1.00$  and  $\beta = 1.05$ . In Fig. 7.21 (right panel) the mass of the  $\sigma$ -meson is shown. Similar as on the

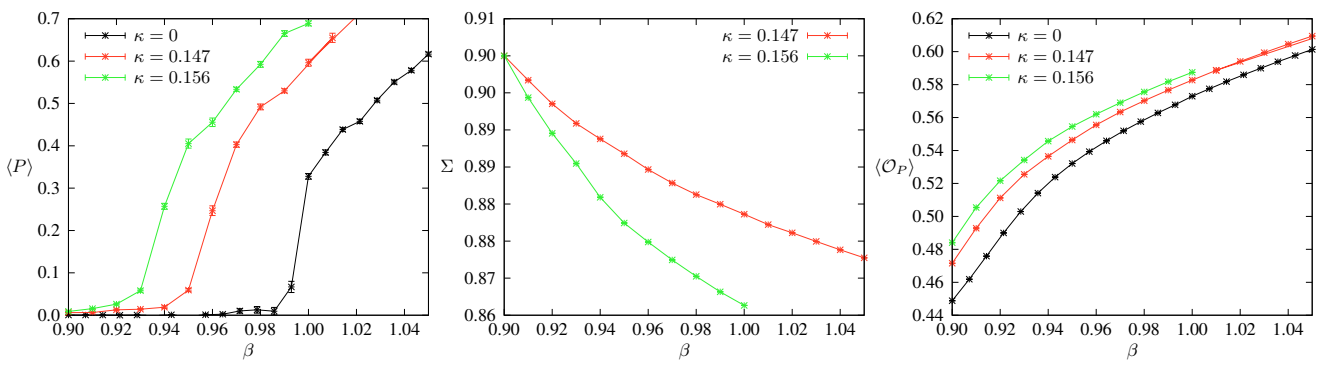


**Figure 7.20** Polyakov loop (left panel), (rescaled) chiral condensate (centre panel) and plaquette (right panel) at finite temperature and zero chemical potential for  $\kappa = 0, 0.147, 0.156$ .

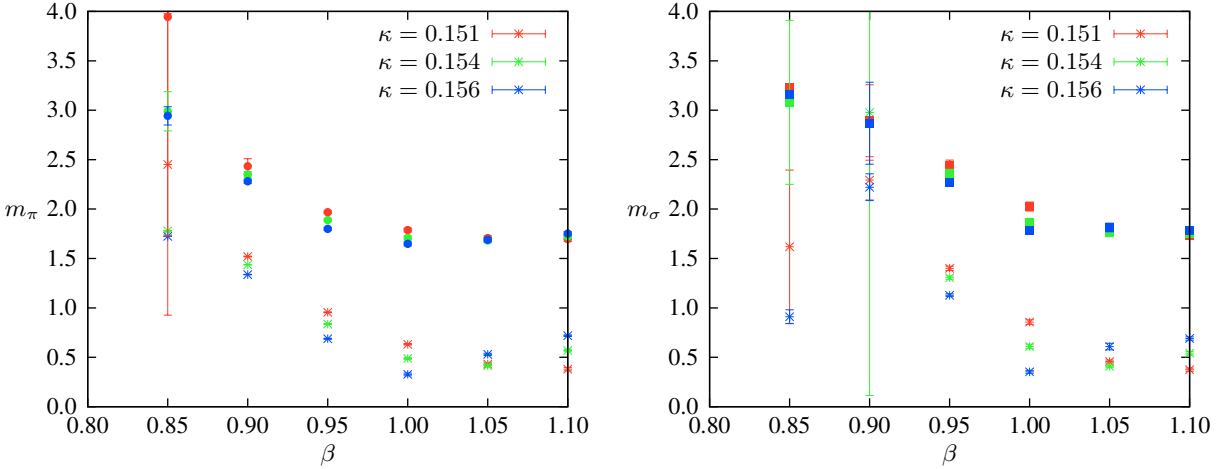


**Figure 7.21** *Left panel:* Ground state and first excited mass of the pion on a  $16^4$  lattice for different values of  $\kappa$ . *Right panel:* Ground state and first excited mass of the sigma meson.

smaller lattice, for  $\kappa = 0.156$  and  $\beta = 1.00$ , the sigma meson is approximately as heavy as the pion,  $m_\sigma = 0.35(2)$ . In the following simulations,  $\kappa = 0.156$  and  $\beta = 1.00$  at zero temperature and  $\beta = 0.90$  at finite temperature for slices in  $\mu$  direction are chosen. A phase transition temperature  $T_c = 160$  MeV at  $\beta_c = 0.94$  corresponds to a pion mass of  $m_{\pi,\text{phys}} \approx 785$  MeV. The lattice spacing is then ranging from  $a(\beta = 0.90) \approx 0.33$  fm to  $a(\beta = 1.00) \approx 0.082$  fm, leading to a box size between  $V \approx (1.32 \text{ fm})^3$  for the simulations at zero temperature and  $V \approx (5.28 \text{ fm})^3$  in the finite temperature simulations. The temperature on the smaller  $N_t = 6$  lattice is then given by  $T \approx 98$  MeV, and on the (colder)  $N_t = 8$  lattice by  $T \approx 73$  MeV. In the following only the raw data are presented, and in the end a combined phase diagram in physical units is given. In Fig. 7.22 (left panel), the Polyakov loop at zero temperature and finite temperature is shown as a function of the bare chemical potential. With increasing temperature the peak in the Polyakov loop becomes broader and the onset of the deconfinement transition shifts to smaller values of the chemical potential. For larger values of the chemical potential the Polyakov loop drops to zero again. In the centre panel of Fig. 7.22, the renormalized chiral condensate is plotted. The transition roughly coincides with the deconfinement transition. In the right panel the quark number

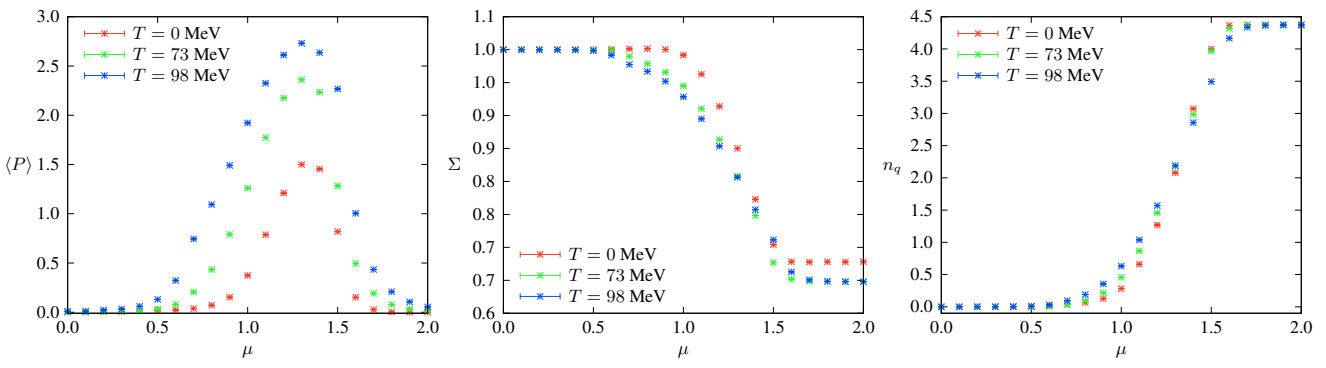


**Figure 7.22** Polyakov loop (left panel), renormalized chiral condensate (centre panel) and quark number density (right panel) at zero temperature and at finite temperature as a function of the bare chemical potential.

density is shown. With decreasing temperature the onset shifts to larger values of the chemical potential. The saturation value of  $n_{q,\text{sat}} = 4.37(1)$  does again not depend on the temperature. It is only slightly larger than on the smaller lattices used before. In Fig. 7.23 (left panel) the quark number density is shown as a function of  $\tilde{\mu}$ . At finite temperature the onset of the transition happens below  $\tilde{\mu} = 0.5$ .

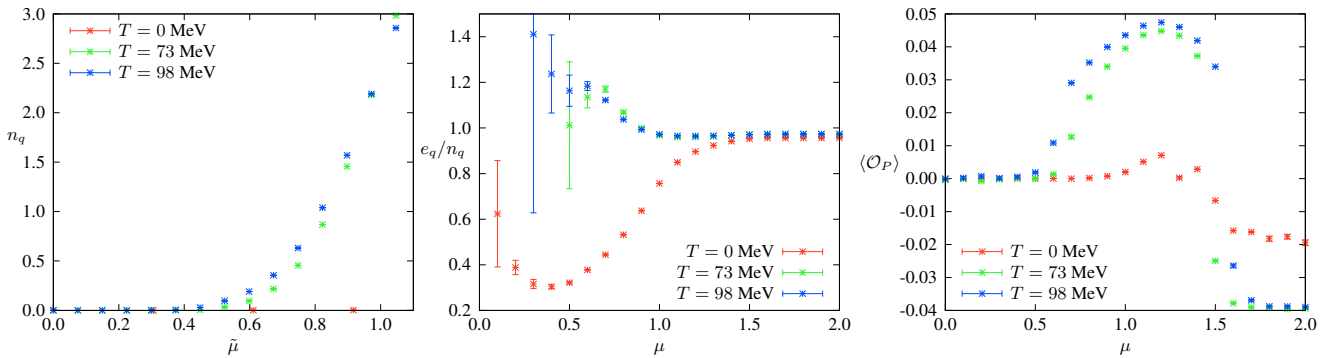


**Figure 7.23** Quark number density as a function of physical chemical potential  $\tilde{\mu}$  (left panel) and  $e_{q,\text{ren}}/n_q$  (centre panel) and the plaquette variable (right panel) as a function of the bare chemical potential  $\mu$ .

Unfortunately, the *silver blaze property* at zero temperature can not be verified at this point due to the (in lattice units) very small pion mass, and simulations with higher statistics and at different values of  $\beta$  are necessary. In the centre panel of Fig. 7.23, the renormalized energy per quark  $e_{q,\text{ren}}/n_q$  is shown. Here, the behaviour at zero temperature and finite temperature is different. At zero temperature it approaches the saturation from below and a minimum is observed at  $\mu \approx 0.4$ . Finally, the right panel shows the renormalized plaquette variable. Again, as on the small lattices, it indicates the transition at zero and finite temperature nicely, in contrast to the finite temperature transition in Fig. 7.20 (right panel). This may indicate that at these rather small temperatures a real phase transition from the confined to the deconfined phase happens, while the transition is only a crossover at vanishing chemical potential. But so far the results are not conclusive and have to be verified by further simulations.

## 7.4 Conclusions

In the present chapter  $G_2$ -QCD has been investigated in the continuum and on the lattice. It has been shown that the fermion determinant is non-negative for real baryon chemical potential due to the reality of the gauge group. Furthermore, it turned out that already one-flavour  $G_2$ -QCD possesses a non-trivial chiral symmetry, that can be seen as a flavour symmetry for the two Majorana flavours composing a Dirac spinor. First simulations on different lattices have been performed and the obtained results are summarized in a sketch of the  $G_2$ -QCD phase diagram in Fig. 7.24.

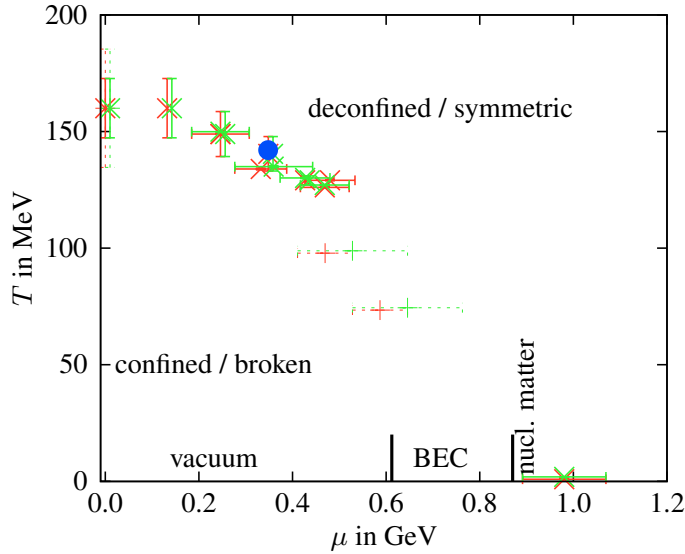


**Figure 7.24** Sketch of the  $G_2$ -QCD phase diagram as obtained from the  $8^3 \times 16$ ,  $8^3 \times 4$  (solid) and  $16^4$ ,  $16^3 \times 8$  and  $16^3 \times 6$  (dotted) lattice. The red points correspond to a transition in the Polyakov loop and the green points to a transition in the chiral condensate. The blue point denotes the reflection point of the transition line.

degrees of freedom are fermionic baryons), and at even larger values of  $\mu$  the theory deconfines and chiral symmetry is restored. For large values of the chemical potential, saturation in the quark number density and again confinement has been observed and has been identified as a lattice artifact. The obtained results at zero temperature, and especially the saturation at larger values of the chemical potential, are indeed very similar to the result for the Polyakov loop and quark number density in two-colour QCD. With increasing temperature, the deconfinement and chiral restoration transition shift to lower values of the chemical potential and finally meet the finite temperature axis. Qualitatively, the results on the smaller lattices have been verified at some points in the phase diagram on a larger lattice. So far, the order of the deconfining and chiral phase transition and the question whether they coincide at zero and finite temperature still remains an open problem and has to be addressed in further simulations and on larger lattices. An outlook to future simulations is given in the summary.

At finite temperature the bulk transition known from pure  $G_2$  Yang Mills theory has been monitored as a function of chemical potential. On the small lattices with  $N_t = 2$  and  $N_t = 4$  it overshadows the deconfinement transition, while the monopole density is almost zero for  $N_t \geq 6$  at the deconfinement transition. Simulations on rather small lattices at zero temperature indicate, that  $G_2$ -QCD shares an important feature with QCD, namely the *silver blaze property*. It has been shown that the onset transition from the vacuum to nuclear matter happens at half of the mass of the lightest bound state carrying baryon number, i.e. the diquark. Above the onset transition the diquarks form a Bose-Einstein condensate. At larger values of the chemical potential, a transition to the ‘ordinary’ nuclear matter phase of QCD is expected (the dominant

# 8 Supersymmetric lattice gauge theories

In the present chapter, supersymmetric Yang-Mills (SYM) theories in different spacetime dimensions are investigated. For the  $\mathcal{N} = 1$  supersymmetric Yang-Mills theory in four dimensions, the low energy effective actions are reviewed. Then a dimensional reduction to three and one spacetime dimension is performed. To investigate these theories on the lattice, the Wilson formulation is used, where a fine-tuning of the bare gluino mass is necessary in order to restore supersymmetry in the continuum limit on the lattice. First simulation results for these theories with an emphasis on restoration of supersymmetry on the lattice are presented.

## 8.1 $\mathcal{N} = 1$ supersymmetric Yang-Mills theory in 4 dimensions

The on-shell action in four spacetime dimensions is given by [66, 68]

$$S_{\text{SYM}} = \int d^4x \operatorname{tr} \left\{ -\frac{1}{4} F_{\mu\nu} F^{\mu\nu} + \frac{i}{2} \bar{\lambda} \gamma_\mu D^\mu \lambda + m \bar{\lambda} \lambda \right\}, \quad (8.1)$$

where  $F_{\mu\nu} = \partial_\mu A_\nu - \partial_\nu A_\mu - ig [A_\mu, A_\nu]$  is the usual field strength tensor with dimensionless gauge coupling constant  $g$ . The gauge field  $A_\mu$  transforms under the adjoint action of the gauge group and  $\lambda$  is a single Majorana spinor. In a supersymmetric theory the number of bosonic degrees of freedom has to match the number of fermionic ones. The gauge bosons (gluons) transform under the adjoint representation, and therefore the fermions (gluinos) have to transform under the adjoint representation, too. The covariant derivative, acting on a Majorana spinor  $\lambda$ , is then given by

$$D_\mu \lambda = \partial_\mu \lambda - ig [A_\mu, \lambda]. \quad (8.2)$$

The action (8.1) is invariant under local gauge transformations and in the massless case  $m = 0$  under the supersymmetry transformations

$$\delta A_\mu = i \bar{\epsilon} \gamma_\mu \lambda \quad , \quad \delta \lambda = i \Sigma_{\mu\nu} F^{\mu\nu} \epsilon \quad \text{and} \quad \delta \bar{\lambda} = -i \bar{\epsilon} \Sigma_{\mu\nu} F^{\mu\nu}, \quad (8.3)$$

where  $\epsilon$  is an arbitrary constant Majorana spinor. The gluino mass term  $m$  introduces a soft breaking of supersymmetry. In the following, only  $SU(2)$  gauge theory is studied as the simplest non-abelian supersymmetric gauge theory. The action (8.1) is invariant under local gauge transformations as well as under the chiral  $U(1)_A$  transformation

$$\lambda \mapsto e^{i\alpha\gamma_5} \lambda \quad \text{and} \quad \bar{\lambda} \mapsto \bar{\lambda} e^{i\alpha\gamma_5}. \quad (8.4)$$

This axial symmetry is equivalent to the R-symmetry in supersymmetric models. It is broken by the chiral anomaly to the discrete subgroup  $\mathbb{Z}(2N_c) = \mathbb{Z}(4)$ . A non-vanishing gluino condensate  $\langle \bar{\lambda} \lambda \rangle \neq 0$  breaks the discrete symmetry down to a  $\mathbb{Z}(2)$  symmetry, leaving  $N_c$  inequivalent ground states of the

theory related by transformations in the quotient group  $\mathbb{Z}(2N_c)/\mathbb{Z}(2)$ . For  $N_c = 2$ , two degenerate ground states exist, that can be distinguished by the sign of the gluino condensate. A gluino mass term  $m$  then lifts this degeneracy such that

$$\langle \bar{\lambda}\lambda \rangle > 0 \quad \text{for } m > 0 \quad \text{and} \quad \langle \bar{\lambda}\lambda \rangle < 0 \quad \text{for } m < 0. \quad (8.5)$$

Considering the bare gluino mass as a free parameter, it is expected that the theory possesses a first order phase transition at vanishing renormalized gluino mass, if the chiral symmetry is spontaneously broken [221]. The chiral condensate serves as an order parameter, changing its sign at the phase transition point. In [68], Veneziano and Yankielowicz argued, that the only supersymmetry breaking operator is a non-vanishing gluino mass. Thus, beside the failure of the Leibniz rule, supersymmetry is broken on the lattice if chiral symmetry is explicitly broken. In order to restore supersymmetry on the lattice, it is therefore sufficient to fine-tune the theory to a massless gluino in the continuum limit. Due to confinement, the gluino is not part of the physical spectrum, and it is not possible to measure its mass directly. But chiral perturbation theory and the OZI rule (known from QCD) relate the renormalized gluino mass to the pion mass [71],

$$m_g \propto m_\pi^2, \quad (8.6)$$

suggesting that the limit of a vanishing gluino mass is equivalent to the limit of a vanishing pion mass. Very recently,  $\mathcal{N} = 1$  SYM theory in four dimensions has been investigated with much effort on the lattice. Mainly two formulations are in use: The Wilson approach with adjoint fermions, introduced by Curci and Veneziano in [70] and further employed in [71, 75, 222–228], and domain-wall fermions in [73, 74, 229, 230]. But so far the obtained results for the mass spectrum are not conclusive. Here, the Wilson approach is employed together with a fine-tuning of the gluino mass.

### 8.1.1 Low-energy effective actions

As in Yang-Mills theories, it is believed that in SYM theories only colourless asymptotic states exist and a mass gap is dynamically generated. The gluons and gluinos must disappear from the spectrum and the theory has to be described by new effective degrees of freedom. The classical action (8.1) is invariant under chiral, scale and supersymmetry transformations. In the quantum theory these symmetries are broken by the chiral and scale anomalies respectively. The composite operators that appear in the anomalies can be thought of as component fields of a general chiral superfield. This colourless component fields are the relevant degrees of freedom at low energies. Veneziano and Yankielowicz (VY) [68] proposed an effective Lagrangian (with the correct anomalies and symmetries), that leads to the particle spectrum shown in Table 8.1. According to the QCD notation, the pseudoscalar boson is called  $a - \eta'$ , where  $a$  stands for adjoint. The scalar boson is called  $a - f_0$ . Additionally, the multiplet contains a fermionic gluino-gluon bound state. If supersymmetry is unbroken, they all have the same mass and form a supermultiplet. In the effective action of Veneziano and Yankielowicz colourless operators  $\propto F^{\mu\nu} F_{\mu\nu}$  and  $\propto F^{\mu\nu} \epsilon_{\mu\nu}^{\sigma\rho} F_{\sigma\rho}$  are integrated out, so there are no gluon-gluon bound states. But these bound states, glueballs for example, are not necessarily heavier than the bound states in the VY-multiplet. Similar as in QCD the  $0^+$  glueball could be the lightest bound state of the theory. Also glueballs can couple to the  $a - \eta'$  and  $a - f_0$  bound

multiplet	particle	operator	spin	mass	SYM-name	QCD-name
VY	1 pseudoscalar boson	$\bar{\lambda}\gamma_5\lambda$	0	$m_{g\bar{g}}^{0-}$	$a - \eta'$	$\eta'$
	1 scalar boson	$\bar{\lambda}\lambda$	0	$m_{g\bar{g}}^{0+}$	$a - f_0$	$f_0$
	1 Majorana fermion	$F_{\mu\nu}\Sigma^{\mu\nu}\lambda$	$\frac{1}{2}$	$m_{g\bar{g}}$	gluino-gluonball	-
FGS	1 scalar boson	$F^{\mu\nu}F_{\mu\nu}$	0	$m_{gg}^{0+}$	$0^+$ - gluonball	$0^+$ - gluonball
	1 pseudoscalar boson	$F^{\mu\nu}\epsilon_{\mu\nu}^{\sigma\rho}F_{\sigma\rho}$	0	$m_{gg}^{0-}$	$0^-$ - gluonball	$0^-$ - gluonball
	1 Majorana fermion	$F_{\mu\nu}\Sigma^{\mu\nu}\lambda$	$\frac{1}{2}$	$m_{g\bar{g}}$	gluino - gluonball	-

**Table 8.1** Particles of the Veneziano-Yankielowicz (VY) and Farrar-Gabadadze-Schwetz (FGS) multiplet.

states, leading to dynamical mass mixing between the gluonball and the VY-multiplet. Therefore, Farrar, Gabadadze and Schwetz (FGS) introduced a second chiral super multiplet with a different mass [231], which has a particle content shown in Table 8.1. It also contains a scalar boson, the  $0^+$  - gluonball, a pseudoscalar boson, the  $0^-$  - gluonball, as well as a fermionic bound state, a gluino - gluonball. Again, if supersymmetry is unbroken, the masses inside one multiplet are degenerate. Because of mass mixing the masses of the two multiplets are different. It is believed that the FGS-multiplet is lighter than the VY-multiplet, but, depending on the couplings in the effective action, different solutions are possible. If supersymmetry is broken by a gluino mass term, the masses inside one multiplet are no longer degenerate and the  $0^+$  gluonball should be the lightest particle.

### 8.1.2 Dimensional reduction

In the following dimensional reduced versions in three and one spacetime dimensions are investigated. Therefore,  $n$  spatial dimensions are compactified using Kaluza-Klein reduction. In the dimensional reduced action the fields no longer depend on the compactified dimensions and the derivative  $\partial_\alpha f = 0$  vanishes for any field. Here  $\alpha = 1 \dots n$  labels the compactified dimensions. This implies the dimensional reduction rules

$$\begin{aligned}
D_\mu\lambda &= \partial_\mu\lambda - ig[A_\mu, \lambda] \rightarrow D_I\lambda = \partial_I\lambda - ig[A_I, \lambda] \quad \text{and} \quad D_\alpha\lambda = -ig[\phi_\alpha, \lambda], \\
F_{\mu\nu} &= \partial_\mu A_\nu - \partial_\nu A_\mu - ig[A_\mu, A_\nu] \rightarrow \begin{cases} F_{IJ} = \partial_I A_J - \partial_J A_I - ig[A_I, A_J] \\ F_{I\alpha} = D_I\phi_\alpha, \quad F_{\alpha\beta} = -ig[\phi_\alpha, \phi_\beta] \end{cases}, \quad (8.7)
\end{aligned}$$

where the scalar field  $\phi_\alpha$  is the appropriate component of the gauge vector field in four dimensions. With a rescaling of the fields as  $A_\mu \rightarrow g^{-1}A_\mu$ ,  $\phi_\alpha \rightarrow g^{-1}\phi_\alpha$  and  $\lambda \rightarrow g^{-1}\lambda$  and Wick-rotation to Euclidean time by  $\gamma_0 \rightarrow i\gamma_0$  and  $A_0 \rightarrow iA_0$ , the Euclidean action corresponding to (8.1) is given by

$$S^E = \frac{\alpha}{2} \int d^D x \operatorname{tr} \left\{ \frac{1}{2} F_{IJ} F_{IJ} + \bar{\lambda} \gamma_I^E D_I \lambda + D_I \phi_\alpha D_I \phi_\alpha - \bar{\lambda} \gamma_\alpha^E [\phi_\alpha, \lambda] - \frac{1}{2} [\phi_\alpha, \phi_\beta] [\phi_\alpha, \phi_\beta] \right\} \quad (8.8)$$

with  $D = 4 - n$  and dimensionful coupling  $\alpha = \frac{V_2}{g^2}$ . In the following, this theory is discussed in one and three spacetime dimensions with an emphasis on the restoration of supersymmetry on the lattice. The simulations are performed with the rHMC algorithm and a Monte-Carlo statistics of up to 500000 configurations for  $d = 1$  and approximately 10000 configurations for  $d = 3$ .

## 8.2 Supersymmetric quantum mechanics

The Euclidean action of supersymmetric quantum mechanics, i.e. one time dimension, is given by

$$S^E = \alpha \int dt \operatorname{tr} \left\{ \frac{1}{2} \bar{\lambda} \gamma_0^E D_0 \lambda + \frac{1}{2} D_0 \phi_\alpha D_0 \phi_\alpha - \frac{1}{2} \bar{\lambda} \gamma_\alpha^E [\phi_\alpha, \lambda] - \frac{1}{4} [\phi_\alpha, \phi_\beta] [\phi_\alpha, \phi_\beta] \right\}. \quad (8.9)$$

It has already been studied in [232, 233] with an emphasis on the large  $N_c$  limit and the AdS/CFT conjecture. Here, the dependence of the spectrum of the Dirac operator on fermion boundary conditions and the supersymmetric continuum limit is investigated. Generalized boundary conditions for the fermionic field  $\lambda$  are introduced by (only  $\varphi = 0$  and  $\varphi = 1$  are compatible with the Majorana constraint on  $\lambda$ )

$$\lambda(N_t) = e^{i\pi\varphi} \lambda(0), \quad (8.10)$$

such that  $\varphi = 0$  corresponds to periodic (supersymmetric) and  $\varphi = 1$  to antiperiodic (thermal) boundary conditions. For antiperiodic boundary conditions, the path integral is the usual thermal partition function with temperature  $T = 1/(aN_t)$ , while for periodic boundary conditions the path integral gives the Witten index. For periodic boundary conditions, fermionic modes can be constant in time and hence  $N_c^2 - 1$  fermionic zero modes exist. The distribution of the lowest eigenvalues of the fermion operator is shown in Fig. 8.1, where the fermionic zero modes for  $\varphi = 0$  are clearly visible. For generalized boundary

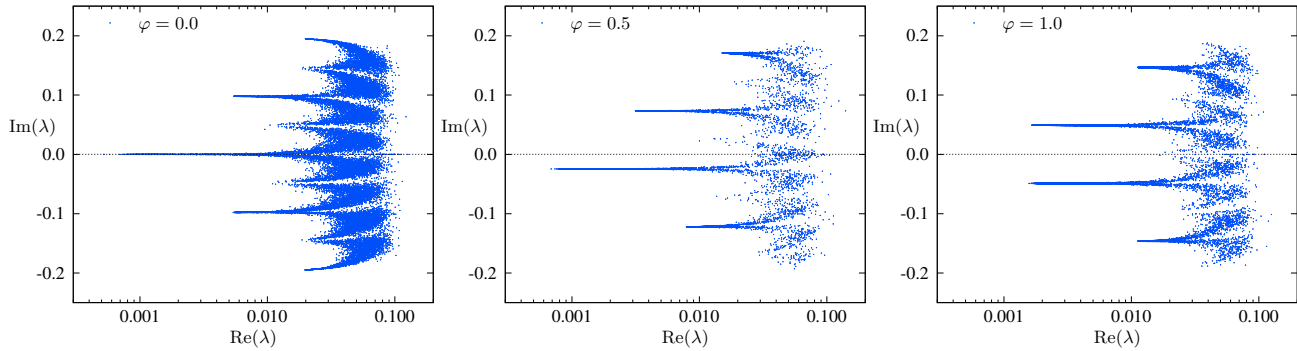


**Figure 8.1** Distribution of the lowest eigenvalues  $\lambda$  of the Dirac operator in the complex plane for different fermion boundary conditions on a  $N_t = 64$  lattice and  $\alpha = 12.0$ .

conditions, the zero mode is lifted for  $0 < \varphi < 2$ . In the case of periodic and antiperiodic boundary conditions, the spectrum is symmetric w.r.t. the real axis. All eigenvalues are at least doubly degenerate and therefore the Pfaffian is always positive [232]. In the case of thermal boundary conditions, supersymmetry is broken due to finite temperature. In Fig. 8.2 (left panel) the distribution of  $\ln \phi^2$  is shown for different boundary conditions. For  $\varphi = 0$  the fluctuations of the scalar field into the flat directions of the classical potential of (8.9) are suppressed due to the fermionic zero mode<sup>a</sup>. With increasing  $\varphi$ , the scalar field distribution develops long tails towards larger values of the scalar field. In order to investigate the restoration of supersymmetry on the lattice, the *bosonic Ward identity* (density of the bosonic action)

$$\langle s_B \rangle = ((N_c^2 - 1)N_s - (N_c^2 - 1)) / 2 = 9/2 = 4.5 \quad (8.11)$$

<sup>a</sup>Due to cancelations in the effective potential between fermionic and bosonic contributions for intact supersymmetry [232].

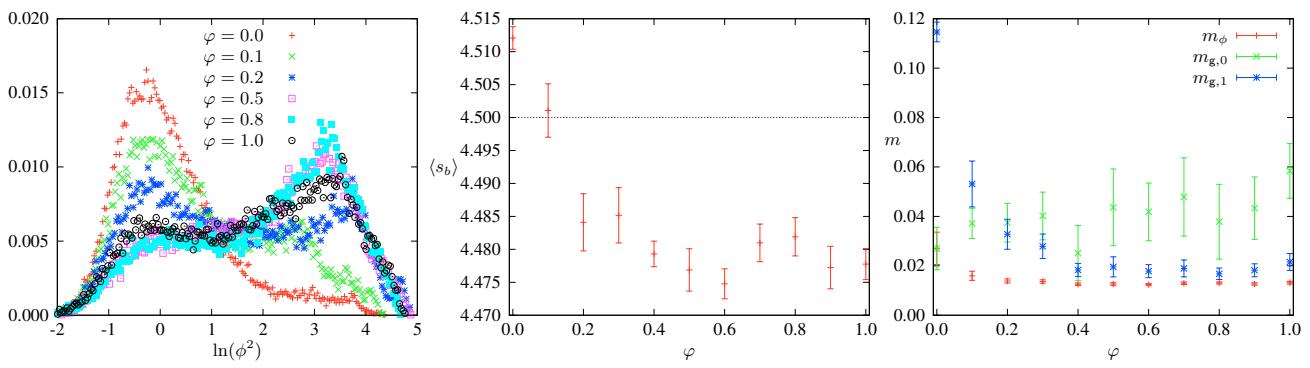


**Figure 8.2** *Left panel:* Distribution of  $\ln \phi^2$  for different fermionic boundary conditions. *Centre panel:* Bosonic Ward identity as a function of the boundary phase  $\varphi$ . *Right panel:* Scalar and gluino mass.

is studied together with the scalar field mass  $m_\phi$  and the gluino mass  $m_{g,0}$  and  $m_{g,1}$  obtained from the Lorentz structure of the gluino correlation function,  $C_{gg}(t) = \langle \lambda(0) \mathcal{U}_{0 \rightarrow t} \lambda(t) \rangle = C_0(t) \mathbb{1} + C_1(t) \gamma_0^E$ , where  $\mathcal{U}_{0 \rightarrow t}$  denotes the parallel transport necessary to obtain a gauge invariant correlator. In Fig. 8.2 (centre panel), the bosonic Ward identity is compared to its continuum value. It is very sensitive to the boundary condition for  $\varphi \approx 0$ , while it is almost constant for  $0.4 < \varphi \leq 1$ . In the right panel the scalar and gluino mass are shown. For periodic boundary conditions,  $m_\phi$  and  $m_{g,0}$  almost coincide, while for antiperiodic boundary conditions this is the case for  $m_\phi$  and  $m_{g,1}$ . Finally, the continuum limit is investigated. A ‘naive’ continuum limit (vanishing physical temporal extent), i.e.  $\alpha \rightarrow \infty$  and therefore  $a \rightarrow 0$ , is given in Fig. 8.3 (left panel). For periodic boundary conditions the Ward identity

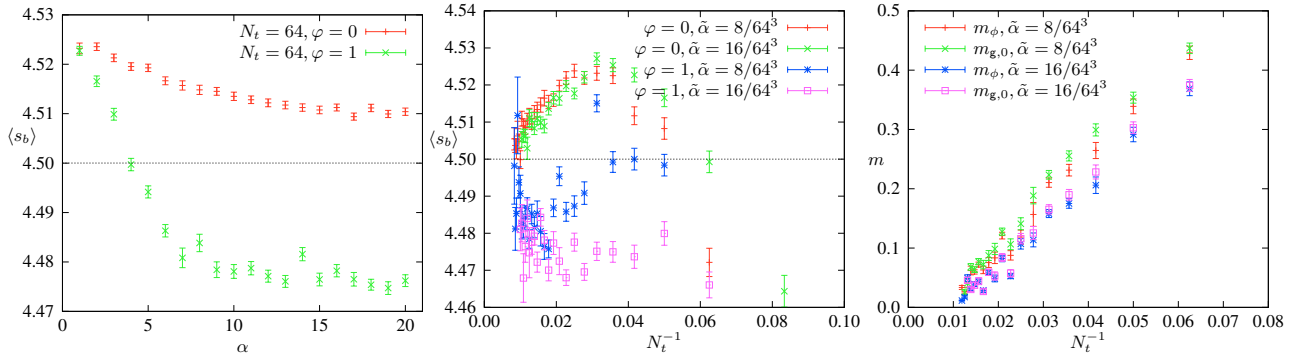


**Figure 8.3** Bosonic Ward identity as a function of  $\alpha$  (left panel) and Bosonic Ward identity (centre panel) and scalar and gluino mass (right panel) for two different values of  $\tilde{\alpha} = \alpha/N_t^3$ .

decreases towards its continuum value, while for antiperiodic boundary conditions also the temperature increases with increasing  $\alpha$ , leading to a violation of supersymmetry in this ‘naive’ continuum limit. An ‘improved’ continuum limit is obtained by  $N_t \rightarrow \infty$  and fixed dimensionless coupling constant  $\tilde{\alpha} = \alpha/N_t^3$ . In Fig. 8.3 the bosonic Ward identity (centre panel) and the gluino and scalar mass (right panel) are shown as a function of  $N_t^{-1}$  for two different values of  $\tilde{\alpha}$ . In this improved continuum limit the bosonic action density is compatible with the supersymmetric continuum results of  $9/2$ , and the scalar and gluino mass vanish, indicating that supersymmetry is indeed restored in the continuum limit.

### 8.3 $\mathcal{N} = 2$ supersymmetric Yang-Mills theory in 3 dimensions

The action for  $\mathcal{N} = 2$  supersymmetric Yang-Mills theory in three dimensions is given by

$$S^E = \alpha \int d^3x \operatorname{tr} \left\{ \frac{1}{4} F_{IJ} F_{IJ} + \frac{1}{2} \bar{\lambda} \gamma_I^E D_I \lambda + \frac{1}{2} D_I \phi D_I \phi - \frac{1}{2} \bar{\lambda} \gamma_3^E [\phi, \lambda] + m \bar{\lambda} \lambda \right\}. \quad (8.12)$$

In the following, the theory is investigated on a  $16^2 \times 32$  lattice in the Wilson formulation. For different values of the overall gauge coupling  $\alpha$ , the critical coupling  $\kappa_{c,\text{OZI}}(\alpha)$  is determined such that the gluino becomes massless. Therefore in Fig. 8.4 (left and center panel) the square of the pion mass (which is proportional to the renormalized gluino mass) is shown for  $\alpha = 2.2$  and  $\alpha = 2.6$ . A linear fit to the

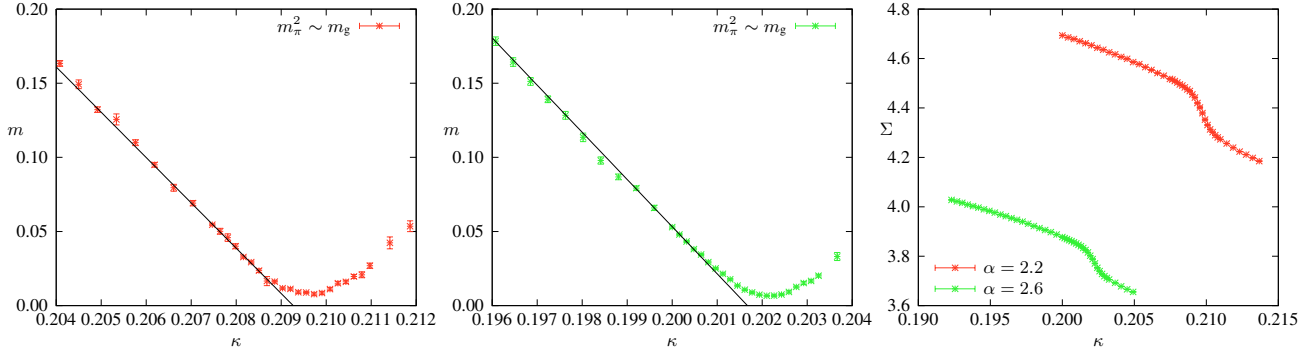


**Figure 8.4** Gluino mass (square of the pion mass) on a  $16^2 \times 32$  lattice for  $\alpha = 2.2$  (left panel) and  $\alpha = 2.6$  (centre panel). The black lines represent a linear fit to the limit of a vanishing gluino mass. The chiral condensate is shown in the right panel.

gluino mass yields

$$\kappa_{c,\text{OZI}}(2.2) = 0.2092(1) \quad \text{and} \quad \kappa_{c,\text{OZI}}(2.6) = 0.20167(2). \quad (8.13)$$

In the right panel of Fig. 8.4 the chiral condensate  $\Sigma(\alpha, \kappa)$  is shown and a transition is observed in the vicinity of the critical coupling obtained from the vanishing pion mass. Due to the residual Wilson mass at a finite lattice spacing, the chiral condensate is also renormalized additively,

$$\Sigma_{\text{ren}}(\alpha, \kappa) = Z_1 (\Sigma(\alpha, \kappa) - m_{\text{res}}) = Z_1 \Sigma(\alpha, \kappa) - Z_2 \kappa - Z_3, \quad (8.14)$$

where it is assumed that the residual Wilson mass is a linear function in  $\kappa$  (as it is the gluino mass). The renormalization constants  $Z_1$ ,  $Z_2$  and  $Z_3$  are fixed such that  $\Sigma_{\text{ren}}(\alpha, \kappa \ll \kappa_c) = 1 = -\Sigma_{\text{ren}}(\alpha, \kappa \gg \kappa_c)$ . The critical point obtained from the vanishing of the pion mass can be compared to the critical point obtained from the transition in the chiral condensate. Therefore in the left and center panel of Fig. 8.5 the chiral condensate and its susceptibility are shown as a function of  $\kappa$ , normalized to the critical  $\kappa_{c,\text{OZI}}(\alpha)$  obtained before. For both  $\alpha = 2.2$  and  $\alpha = 2.6$ , the deviations in the critical couplings are less than 0.5 percent, i.e.

$$\kappa_c(2.2) = 0.2097(4) \quad \text{and} \quad \kappa_c(2.6) = 0.2023(2). \quad (8.15)$$

Therefore, both methods are applicable in order to perform a supersymmetric continuum limit. In the right panel of Fig. 8.5 the bosonic action is plotted. Both curves for  $\alpha = 2.2$  and  $\alpha = 2.6$  intersect each

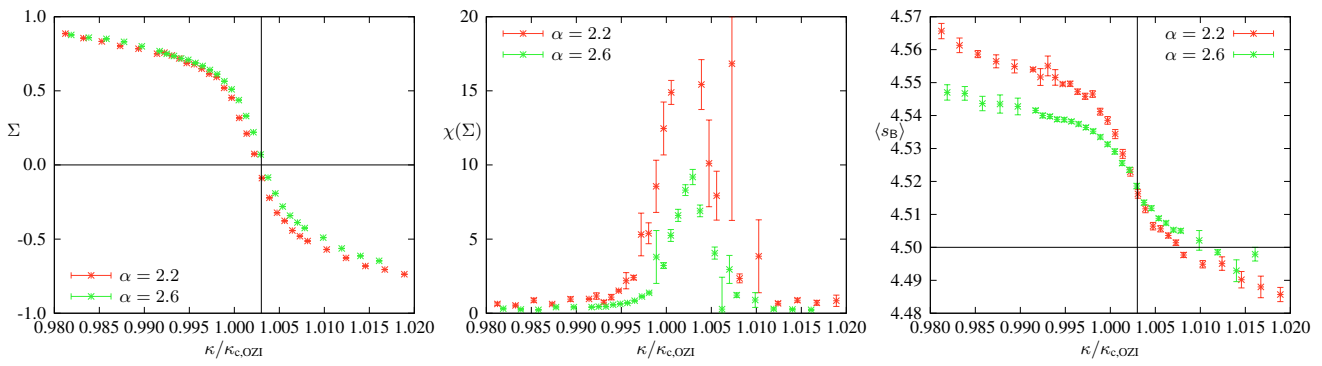


**Figure 8.5** Renormalized chiral condensate (left panel), chiral susceptibility (center panel) and bosonic action (right panel) for  $\alpha = 2.2$  and  $\alpha = 2.6$ .

other almost exactly at the critical coupling obtained from the chiral condensate. The deviation from the theoretical value for restoration of supersymmetry at the intersection point is also about 0.5 percent, indicating that a restoration of supersymmetry on the lattice for this model is possible. As pointed out before, the chiral condensate as a function of  $\kappa$  should undergo a first order phase transition at the point where the gluino mass vanishes. Therefore, in Fig. 8.6 histograms of the chiral condensate for  $\alpha = 2.6$  are shown in the vicinity of the critical coupling. The double peak structure observed at  $\alpha = 2.2$  and

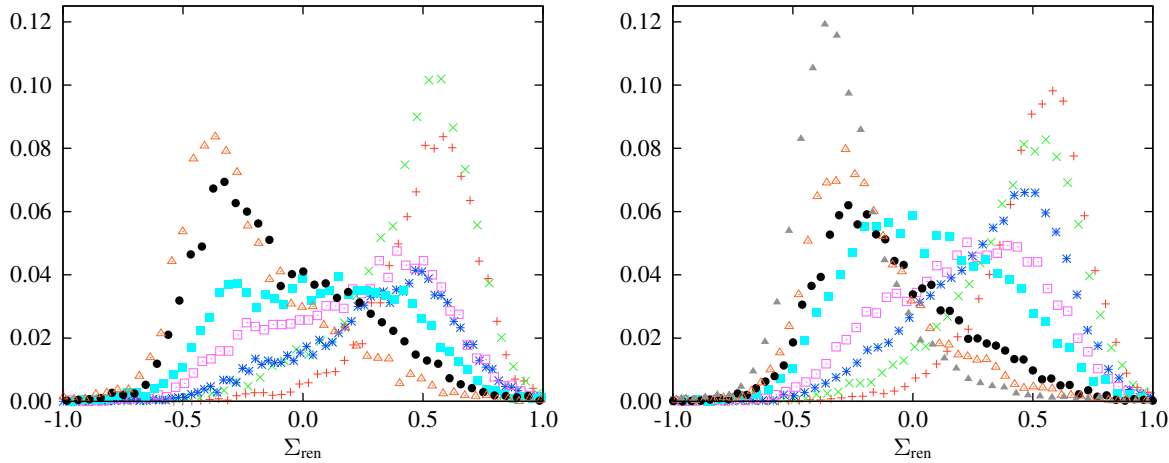


**Figure 8.6** Histograms of the renormalized chiral condensate for  $\alpha = 2.2$  (left panel) and  $\alpha = 2.6$  (right panel) and different values of  $\kappa$  in the vicinity of the critical point.

$\alpha = 2.6$  and the coexistence of both phases at the critical coupling clearly point to a first order phase transition. This indicates that chiral symmetry is spontaneously broken in the theory and supersymmetry can be restored in the continuum limit, i.e. the soft breaking of supersymmetry due to the Wilson mass can be removed by fine-tuning the bare gluino mass. In order to determine the critical line in the  $(\alpha, \kappa)$ -plane, the above sketched analysis is performed for different values of the gauge coupling and on different lattices. The results for two different lattices  $8^3 \times 16$  and  $16^3 \times 32$  are shown in Fig. 8.7 (left panel). On this rather coarse grid in parameter space, the critical couplings for both lattices coincide.

The mass spectrum in three dimensions can be obtained by dimensional reduction of the particle

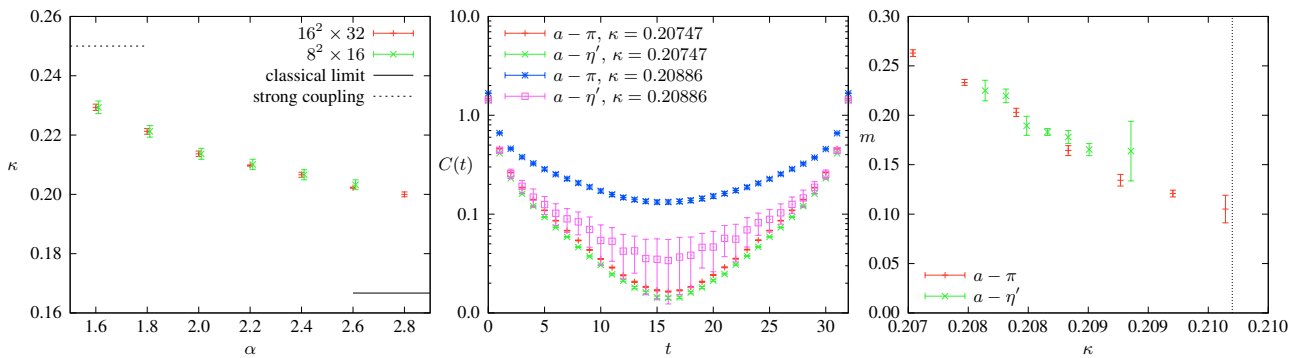


**Figure 8.7** Critical line in the  $(\alpha, \kappa)$ -plane (left panel), pion and  $a - \eta'$  correlation functions for two different values of  $\kappa$  (center panel) and  $\alpha = 2.2$ , and pion and  $a - \eta'$  mass for  $\alpha = 2.2$  as a function of  $\kappa$  (the dotted line denotes the supersymmetric limit).

content of the multiplets, suggested from the low-energy effective action in four dimensions. Additional particles are bound states between the gluino and the scalar field as well as between the gluon and the scalar field. So far it was not possible to determine these masses (due to strongly fluctuating bosonic fields), except for the  $a - \eta'$  meson. In Fig. 8.7 (center panel) the correlation function of the  $a - \eta'$  meson is compared to the pion correlation function for two different values of  $\kappa$ . The difference between the pion and  $\eta'$ -correlation function is only the disconnected contribution. Indeed, for larger values of  $\kappa$  the  $a - \eta'$  receives its mass from the disconnected contribution, while for smaller  $\kappa$  both correlation functions coincide. In the right panel of Fig. 8.7 both masses are shown as a function of  $\kappa$ . The results may indicate that the  $\eta'$  meson remains massive in the supersymmetric limit. But so far the results are very preliminary and have to be verified in further simulations.

## 8.4 Conclusions

In the present chapter supersymmetric gauge theories in one and three spacetime dimensions have been studied on the lattice. The models have been obtained from dimensional reduction of  $\mathcal{N} = 1$  supersymmetric Yang-Mills theory in four spacetime dimensions. In one dimension the spectrum of the Dirac operator has been investigated for different boundary conditions, and the lowest fermion and boson masses have been calculated. It has been shown that a supersymmetric continuum limit without fine-tuning is possible. In three dimensions the phase diagram as a function of the gauge coupling  $\alpha$  and the hopping parameter  $\kappa$  has been investigated, showing that a supersymmetric limit is possible if the bare gluino mass is fine-tuned, such that the renormalized gluino mass vanishes. Additionally, it has been shown that the supersymmetric limit coincides with a line of first order phase transition observed in the chiral condensate. In future simulations the mass spectrum of this strongly coupled supersymmetric lattice gauge theory will be calculated, to verify the proposed low energy effective actions and to improve existing methods, in order to investigate the mass spectrum and chiral properties of  $\mathcal{N} = 1$  SYM theory in four dimensions.

# 9 Summary and outlook

In this work different strongly-coupled gauge theories with and without fundamental matter have been studied on the lattice with an emphasis on the confinement problem and the QCD phase diagram at non-vanishing net baryon density as well as on possible supersymmetric extensions of the standard model of particle physics.

In gauge theories with a non-trivial centre symmetry, as for instance  $SU(3)$ -Yang-Mills theory, confinement is intimately related to the centre of the gauge group, and the Polyakov loop serves as an order parameter for confinement. In QCD, this centre symmetry is explicitly broken by quarks in the fundamental representation of the gauge group. But still quarks and gluons are confined in mesons, baryons and glueballs at low temperatures and small densities, suggesting that centre symmetry is not responsible for the phenomenon of confinement. Therefore it is interesting to study pure gauge theories without centre symmetry.

In this work this has been done by replacing the gauge group  $SU(3)$  of the strong interaction with the exceptional Lie group  $G_2$ , that has a trivial centre. To investigate  $G_2$  gauge theory on the lattice, a new and highly efficient update algorithm has been developed, based on a local HMC algorithm. Employing this algorithm, the proposed and already investigated first order phase transition from a confined to a deconfined phase has been confirmed, showing that indeed a first order phase transition without symmetry breaking or an order parameter is possible. In this context, also the deconfinement phase transition of the exceptional Lie groups  $F_4$  and  $E_6$  in three spacetime dimensions has been studied. It has been shown that both theories also possess a first order phase transition.

To understand confinement with exceptional Lie groups, for the gauge group  $G_2$  the dynamics of the confining string, connecting a charge and an anti-charge, has been studied at zero temperature with a slightly modified variant of the Lüscher-Weisz algorithm for exponential error reduction. Here Casimir scaling has been verified to a high precision for the 8 lowest-dimensional representations of the gauge group in three and four spacetime dimensions. The obtained results for a continuum extrapolation of the string tension are compared to a Hamiltonian approach to Yang-Mills theories, showing quite good agreement. Additionally, for the first time string breaking in the fundamental and adjoint representation of  $G_2$  gauge theory has been observed, and the string breaking scale has been compared to the mass of the glue-lumps, necessary to screen the colour charge in the corresponding representation. It has been found that the string breaking scale coincides exactly with the mass of the glue-lumps, as expected. With these investigations it has been shown that  $G_2$  gauge theory indeed behaves very similar to QCD, where the centre symmetry is explicitly broken.

With a scalar field in the fundamental representation of  $G_2$ , the gauge symmetry can be broken down to  $SU(3)$  gauge theory through the Higgs mechanism. The phase diagram of this  $G_2$  gauge Higgs model has been studied with Monte-Carlo simulations in four spacetime dimensions. With high-statistics simulations it has been shown, that the former first order phase transition in pure  $G_2$  gluodynamics turns into a crossover, once the scalar field mass is fine-tuned to a very small window in parameter space.

Therefore, the confinement phase is analytically connected to the Higgs symmetric and Higgs broken deconfinement phases. This exhibits an interesting analogy to QCD, where the first order phase transition of the quenched theory turns into a crossover for physical quark masses. By increasing the mass of the scalar field it has been verified, that pure  $SU(3)$  gauge theory is recovered in the limit of an infinitely heavy scalar field.

Inspired by the obtained results, a QCD-like theory based on the exceptional Lie group  $G_2$  has been proposed and investigated. It turns out that even at finite baryon chemical potential the fermion determinant is non-negative, making Monte-Carlo simulations feasible. Moreover, the theory contains fermionic baryons and behaves in many aspects very similar to QCD. The chiral symmetry of the theory has been examined and, compared to QCD, an enlarged symmetry group has been found. Even for a single Dirac flavour, spontaneous chiral symmetry breaking of a continuous symmetry is possible. In contrast to QCD, the corresponding Goldstone bosons are *diquarks* instead of mesons. With the help of a highly parallelized rHMC algorithm, the phase diagram of this gauge theory with fermionic baryons and quarks in the fundamental representation of the gauge group has been investigated with Monte-Carlo simulations for the first time. At vanishing temperature, the phase diagram as a function of chemical potential has been calculated on different lattices. It has been shown that the theory possesses the *silver blaze property*, i.e. the partition function does not depend on the chemical potential until it reaches the energy of half of the mass of the lightest bound state carrying baryon number. Therefore the mass of the pseudo-Goldstone boson of the chiral symmetry breaking, i.e. the *diquark* mass, has been calculated. Perfect agreement with the onset transition, separating the vacuum from nuclear matter, has been found. For intermediate values of the chemical potential a deconfining phase transition at zero temperature has been observed, and for even larger values of the chemical potential the system saturates and a similar behaviour to the quenched theory has been found. On a rather small lattice finite size effects have been investigated, indicating that the saturation threshold is a lattice artifact. For small values of the lattice spacing, plateaus in the quark number density and the Polyakov loop show up, that are almost independent of the lattice spacing. This has been interpreted as a separation of scales due to different bound states, i.e. diquarks, protons, etc. contributing to the total baryon number.

At finite temperature the phase diagram as a function of temperature and chemical potential has been calculated on different lattices. For small lattices the bulk transition, known from pure  $G_2$  gauge theory, has been investigated and it has been shown that it coincides with the condensation of monopoles. Unfortunately it completely overshadows the finite temperature deconfinement transition. On larger lattices the bulk transition is absent and the calculations reveal reliable information about the phase diagram. At low temperatures and densities, the system stays in a confined and chirally broken phase. For larger densities the system deconfines at a certain value of chemical potential. Here it is still unclear whether the deconfinement transition coincides with a restoration of chiral symmetry. For even larger values of the chemical potential the system saturates and the finite temperature phase transition of the quenched theory is recovered. Finally, a preliminary sketch of the  $G_2$ -QCD phase diagram has been presented.

These first investigations of  $G_2$ -QCD are a proof of principle that Monte-Carlo simulations at finite baryon density are feasible and that the obtained results may provide relevant input on the QCD phase diagram. Indeed, the performed simulations have been shown that the phase diagram of  $G_2$ -QCD is

an interesting playground for future investigations. A few topics that should be addressed are: At zero temperature the *silver blaze property* should be investigated at larger and finer lattices for different quark masses, to determine the order of the onset transition. A related question is whether more plateaus in the quark number density develop at finer and larger lattices. This also leads to the question whether the observed saturation value will reach its maximum value of 14 in the continuum limit. Furthermore, the masses of three-quark bound states and quark gluon hybrids have to be calculated and related to the onset transitions observed in the quark number density. Another interesting question at zero temperature is the order of the deconfinement transition and whether it coincides with chiral restoration. Here it will be interesting to investigate also two-flavour  $G_2$ -QCD, where the chiral symmetry group is  $SU(4)$  instead of  $SU(2)$ . At finite temperature the existence of a critical point has to be examined. Related questions regard possible exotic phases, as for instance the existence of a quarkionic or crystalline phase or colour superconductivity at asymptotic large values of net baryon density. Furthermore, the existence of a connection to QCD should be investigated. In this work it has been shown that a naive coupling to a fundamental scalar field leads to QCD with isospin chemical potential. Maybe a more involved breaking mechanism can gradually switch on the sign problem, leading to  $SU(3)$ -QCD with baryon chemical potential. In this case the deformation of the theory may provide relevant information to tackle the QCD sign problem.

In the last chapter of this work strongly-coupled supersymmetric gauge theories, based on dimensional reduction of four dimensional  $\mathcal{N} = 1$  supersymmetric Yang-Mills theory, have been studied on the lattice. For the supersymmetric quantum mechanics the spectrum of the Dirac operator has been investigated, in dependence of arbitrary fermion boundary conditions. A periodic structure has been obtained, corresponding to a fermionic zero mode for periodic boundary conditions. The mass of the gluino and the scalar supersymmetric partner particle have been determined in the continuum limit, showing that supersymmetry can be restored. In addition it has been shown, that the bosonic Ward identity for periodic and antiperiodic boundary conditions approaches its continuum value, also indicating that a supersymmetric continuum limit is possible. In first investigations in three spacetime dimensions the critical value of the gluino mass has been determined, such that in the continuum limit supersymmetry can be restored. This fine-tuning was done for different lattices and different values of the gauge coupling. Furthermore, it has been shown that the theory possesses a first order phase transition as a function of the renormalized gluino mass. The phase transition point coincides with a vanishing gluino mass, and therefore chiral symmetry is spontaneously broken in the supersymmetric continuum limit. In future simulations the mass spectrum of this supersymmetric theory will be investigated and compared to predictions from low-energy effective actions.

Concluding, the phase diagrams of different strongly-coupled gauge theories have been studied, employing lattice Monte-Carlo methods. The obtained results shine light on confinement in exceptional gauge theories as well as on the phase diagram of a QCD-like theory with fundamental quarks and fermionic baryons. Future investigations, especially on the  $G_2$ -QCD phase diagram, are on the way and may provide relevant information about the phase diagram of ‘ordinary’ QCD and the phenomena of the strong interaction, as observed in nature.

# Appendix A

## Conventions

The metric in Minkowski space time is given by

$$\eta_{\mu\nu} = (1, -1, -1, -1) = \frac{1}{2} \{ \gamma_\mu, \gamma_\nu \}, \quad (\text{A.1})$$

with Hermitian temporal gamma matrix  $\gamma_0 = \gamma_0^\dagger$  and anti-Hermitian spatial gamma matrices  $\gamma_i = -\gamma_i^\dagger$ . Additionally, a fifth Hermitian gamma matrix is defined as  $\gamma_5 = -i\gamma_0\gamma_1\gamma_2\gamma_3 = \gamma_5^\dagger$  with the property  $\gamma_5^2 = 1$ . The charge conjugation matrix  $C$  is defined by the relations

$$C\gamma_\mu^T C^{-1} = \eta\gamma_\mu = -\gamma_\mu, \quad C^{-1} = C^\dagger, \quad \text{and} \quad C^T = -C. \quad (\text{A.2})$$

On a Dirac spinor, it acts as charge conjugation

$$\Psi^C = C\bar{\Psi}^T = C\gamma_0^T\Psi^* \quad \text{and} \quad \bar{\Psi}^C = -\Psi^T C^{-1}. \quad (\text{A.3})$$

A definition that is independent of the basis for the gamma matrices is given by

$$C = i\gamma_2\gamma_0. \quad (\text{A.4})$$

Left- and right-handed projection operators are defined by

$$P_R = \frac{1}{2}(1 + \gamma_5), \quad P_L = \frac{1}{2}(1 - \gamma_5). \quad (\text{A.5})$$

Additionally, some useful relations are given

$$\begin{aligned} \gamma_5^T = \gamma_5^* = C^{-1}\gamma_5 C, \quad P_{R/L}^T = P_{R/L}^* = C^{-1}P_{R/L}C, \\ \bar{\Psi}^C\chi^C = \bar{\chi}\Psi \quad \text{and} \quad \bar{\Psi}^C\gamma_\mu\chi^C = -\bar{\chi}\gamma_\mu\Psi. \end{aligned} \quad (\text{A.6})$$

The Euclidean gamma matrices are obtained by

$$\gamma_0^E = \gamma_0 \quad \text{and} \quad \gamma_i^E = i\gamma_i. \quad (\text{A.7})$$

They are Hermitian matrices, satisfying  $\gamma_\mu^E = \gamma_\mu^{E\dagger}$ . The sigma matrices  $\Sigma_{\mu\nu}$  are defined as

$$\Sigma_{\mu\nu} = \frac{i}{4} [\gamma_\mu, \gamma_\nu]. \quad (\text{A.8})$$

# Appendix B

## Additional information about Lie groups

### B.1 The exceptional Lie group $G_2$

In the following, additional information on the explicit construction of the Lie group  $G_2$  are provided. Two different representations for the generators, a complex and a real one, are given. The real and complex representations for  $G_2$  are unitary equivalent to each other.

#### B.1.1 Complex representation

The 14 generators of a complex base for  $G_2$  are given [57] by

$$T_i = \frac{1}{\sqrt{2}} \begin{pmatrix} \lambda_i & 0 & 0 \\ 0 & -\lambda_i^* & 0 \\ 0 & 0 & 0 \end{pmatrix} \quad \text{for } i = 1 \dots 8, \quad (\text{B.1})$$

where  $\lambda_i$  are the usual Gell-Mann matrices, building a 7-dimensional reducible representation for the  $\mathfrak{su}(3)$  subgroup of  $\mathfrak{g}_2$ , and

$$T_{8+i} = \frac{1}{\sqrt{6}} \begin{pmatrix} 0 & \mathfrak{d}_i & \mathfrak{t}_i \\ -\mathfrak{d}_i^* & 0 & \mathfrak{t}_i^* \\ \mathfrak{t}_i^\dagger & \mathfrak{t}_i^T & 0 \end{pmatrix} \quad \text{for } i = 1 \dots 6, \quad (\text{B.2})$$

with

$$\begin{aligned} \mathfrak{d}_1 &= \begin{pmatrix} 0 & -1 & 0 \\ 1 & 0 & 0 \\ 0 & 0 & 0 \end{pmatrix} & \mathfrak{d}_2 &= \begin{pmatrix} 0 & i & 0 \\ -i & 0 & 0 \\ 0 & 0 & 0 \end{pmatrix} & \mathfrak{d}_3 &= \begin{pmatrix} 0 & 0 & 1 \\ 0 & 0 & 0 \\ -1 & 0 & 0 \end{pmatrix} \\ \mathfrak{d}_4 &= \begin{pmatrix} 0 & 0 & i \\ 0 & 0 & 0 \\ -i & 0 & 0 \end{pmatrix} & \mathfrak{d}_5 &= \begin{pmatrix} 0 & 0 & 0 \\ 0 & 0 & -1 \\ 0 & 1 & 0 \end{pmatrix} & \mathfrak{d}_6 &= \begin{pmatrix} 0 & 0 & 0 \\ 0 & 0 & i \\ 0 & -i & 0 \end{pmatrix} \end{aligned}$$

and

$$\begin{aligned} \mathfrak{t}_1 &= \sqrt{2} \begin{pmatrix} 0 \\ 0 \\ -1 \end{pmatrix} & \mathfrak{t}_2 &= \sqrt{2} \begin{pmatrix} 0 \\ 0 \\ -i \end{pmatrix} & \mathfrak{t}_3 &= \sqrt{2} \begin{pmatrix} 0 \\ -1 \\ 0 \end{pmatrix} \\ \mathfrak{t}_4 &= \sqrt{2} \begin{pmatrix} 0 \\ i \\ 0 \end{pmatrix} & \mathfrak{t}_5 &= \sqrt{2} \begin{pmatrix} -1 \\ 0 \\ 0 \end{pmatrix} & \mathfrak{t}_6 &= \sqrt{2} \begin{pmatrix} -i \\ 0 \\ 0 \end{pmatrix} \end{aligned}$$

They are normalized according to  $\text{tr}(T_a T_b) = 2\delta_{ab}$ .

## B.1.2 Real representation

In a real representation, the 14 generators of the Lie group  $G_2$  are given by [87]

$$T_1 = \frac{1}{2\sqrt{2}} \begin{pmatrix} 0 & 0 & 0 & 0 & 0 & 0 & 0 \\ 0 & 0 & 0 & 0 & 0 & 0 & 0 \\ 0 & 0 & 0 & 0 & 0 & 0 & 0 \\ 0 & 0 & 0 & 0 & 0 & 0 & -1 \\ 0 & 0 & 0 & 0 & 0 & -1 & 0 \\ 0 & 0 & 0 & 0 & 1 & 0 & 0 \\ 0 & 0 & 0 & 1 & 0 & 0 & 0 \end{pmatrix} \quad T_2 = \frac{1}{2\sqrt{2}} \begin{pmatrix} 0 & 0 & 0 & 0 & 0 & 0 & 0 \\ 0 & 0 & 0 & 0 & 0 & 0 & 0 \\ 0 & 0 & 0 & 0 & 0 & 0 & 0 \\ 0 & 0 & 0 & 0 & 0 & 1 & 0 \\ 0 & 0 & 0 & 0 & 0 & 0 & -1 \\ 0 & 0 & 0 & -1 & 0 & 0 & 0 \\ 0 & 0 & 0 & 0 & 1 & 0 & 0 \end{pmatrix}$$

$$T_3 = \frac{1}{2\sqrt{2}} \begin{pmatrix} 0 & 0 & 0 & 0 & 0 & 0 & 0 \\ 0 & 0 & 0 & 0 & 0 & 0 & 0 \\ 0 & 0 & 0 & 0 & 0 & 0 & 0 \\ 0 & 0 & 0 & 0 & -1 & 0 & 0 \\ 0 & 0 & 0 & 1 & 0 & 0 & 0 \\ 0 & 0 & 0 & 0 & 0 & 0 & -1 \\ 0 & 0 & 0 & 0 & 0 & 1 & 0 \end{pmatrix} \quad T_4 = \frac{1}{2\sqrt{2}} \begin{pmatrix} 0 & 0 & 0 & 0 & 0 & 0 & 0 \\ 0 & 0 & 0 & 0 & 0 & 0 & 1 \\ 0 & 0 & 0 & 0 & 0 & 1 & 0 \\ 0 & 0 & 0 & 0 & 0 & 0 & 0 \\ 0 & 0 & 0 & 0 & 0 & 0 & 0 \\ 0 & 0 & -1 & 0 & 0 & 0 & 0 \\ 0 & -1 & 0 & 0 & 0 & 0 & 0 \end{pmatrix}$$

$$T_5 = \frac{1}{2\sqrt{2}} \begin{pmatrix} 0 & 0 & 0 & 0 & 0 & 0 & 0 \\ 0 & 0 & 0 & 0 & 0 & -1 & 0 \\ 0 & 0 & 0 & 0 & 0 & 0 & 1 \\ 0 & 0 & 0 & 0 & 0 & 0 & 0 \\ 0 & 0 & 0 & 0 & 0 & 0 & 0 \\ 0 & 1 & 0 & 0 & 0 & 0 & 0 \\ 0 & 0 & -1 & 0 & 0 & 0 & 0 \end{pmatrix} \quad T_6 = \frac{1}{2\sqrt{2}} \begin{pmatrix} 0 & 0 & 0 & 0 & 0 & 0 & 0 \\ 0 & 0 & 0 & 0 & 1 & 0 & 0 \\ 0 & 0 & 0 & -1 & 0 & 0 & 0 \\ 0 & 0 & 1 & 0 & 0 & 0 & 0 \\ 0 & -1 & 0 & 0 & 0 & 0 & 0 \\ 0 & 0 & 0 & 0 & 0 & 0 & 0 \\ 0 & 0 & 0 & 0 & 0 & 0 & 0 \end{pmatrix}$$

$$T_7 = \frac{1}{2\sqrt{2}} \begin{pmatrix} 0 & 0 & 0 & 0 & 0 & 0 & 0 \\ 0 & 0 & 0 & -1 & 0 & 0 & 0 \\ 0 & 0 & 0 & 0 & -1 & 0 & 0 \\ 0 & 1 & 0 & 0 & 0 & 0 & 0 \\ 0 & 0 & 1 & 0 & 0 & 0 & 0 \\ 0 & 0 & 0 & 0 & 0 & 0 & 0 \\ 0 & 0 & 0 & 0 & 0 & 0 & 0 \end{pmatrix} \quad T_8 = \frac{1}{2\sqrt{6}} \begin{pmatrix} 0 & 0 & 0 & 0 & 0 & 0 & 0 \\ 0 & 0 & -2 & 0 & 0 & 0 & 0 \\ 0 & 2 & 0 & 0 & 0 & 0 & 0 \\ 0 & 0 & 0 & 0 & 1 & 0 & 0 \\ 0 & 0 & 0 & -1 & 0 & 0 & 0 \\ 0 & 0 & 0 & 0 & 0 & 0 & -1 \\ 0 & 0 & 0 & 0 & 0 & 1 & 0 \end{pmatrix}$$

$$\begin{aligned}
T_9 &= \frac{1}{2\sqrt{6}} \begin{pmatrix} 0 & -2 & 0 & 0 & 0 & 0 & 0 \\ 2 & 0 & 0 & 0 & 0 & 0 & 0 \\ 0 & 0 & 0 & 0 & 0 & 0 & 0 \\ 0 & 0 & 0 & 0 & 0 & 0 & 1 \\ 0 & 0 & 0 & 0 & 0 & -1 & 0 \\ 0 & 0 & 0 & 0 & 1 & 0 & 0 \\ 0 & 0 & 0 & -1 & 0 & 0 & 0 \end{pmatrix} & T_{10} &= \frac{1}{2\sqrt{6}} \begin{pmatrix} 0 & 0 & -2 & 0 & 0 & 0 & 0 \\ 0 & 0 & 0 & 0 & 0 & 0 & 0 \\ 2 & 0 & 0 & 0 & 0 & 0 & 0 \\ 0 & 0 & 0 & 0 & 0 & -1 & 0 \\ 0 & 0 & 0 & 0 & 0 & 0 & -1 \\ 0 & 0 & 0 & 1 & 0 & 0 & 0 \\ 0 & 0 & 0 & 0 & 1 & 0 & 0 \end{pmatrix} \\
T_{11} &= \frac{1}{2\sqrt{6}} \begin{pmatrix} 0 & 0 & 0 & -2 & 0 & 0 & 0 \\ 0 & 0 & 0 & 0 & 0 & 0 & -1 \\ 0 & 0 & 0 & 0 & 0 & 1 & 0 \\ 2 & 0 & 0 & 0 & 0 & 0 & 0 \\ 0 & 0 & 0 & 0 & 0 & 0 & 0 \\ 0 & 0 & -1 & 0 & 0 & 0 & 0 \\ 0 & 1 & 0 & 0 & 0 & 0 & 0 \end{pmatrix} & T_{12} &= \frac{1}{2\sqrt{6}} \begin{pmatrix} 0 & 0 & 0 & 0 & -2 & 0 & 0 \\ 0 & 0 & 0 & 0 & 0 & 1 & 0 \\ 0 & 0 & 0 & 0 & 0 & 0 & 1 \\ 0 & 0 & 0 & 0 & 0 & 0 & 0 \\ 2 & 0 & 0 & 0 & 0 & 0 & 0 \\ 0 & -1 & 0 & 0 & 0 & 0 & 0 \\ 0 & 0 & -1 & 0 & 0 & 0 & 0 \end{pmatrix} \\
T_{13} &= \frac{1}{2\sqrt{6}} \begin{pmatrix} 0 & 0 & 0 & 0 & 0 & -2 & 0 \\ 0 & 0 & 0 & 0 & -1 & 0 & 0 \\ 0 & 0 & 0 & -1 & 0 & 0 & 0 \\ 0 & 0 & 1 & 0 & 0 & 0 & 0 \\ 0 & 1 & 0 & 0 & 0 & 0 & 0 \\ 2 & 0 & 0 & 0 & 0 & 0 & 0 \\ 0 & 0 & 0 & 0 & 0 & 0 & 0 \end{pmatrix} & T_{14} &= \frac{1}{2\sqrt{6}} \begin{pmatrix} 0 & 0 & 0 & 0 & 0 & 0 & -2 \\ 0 & 0 & 0 & 1 & 0 & 0 & 0 \\ 0 & 0 & 0 & 0 & -1 & 0 & 0 \\ 0 & -1 & 0 & 0 & 0 & 0 & 0 \\ 0 & 0 & 1 & 0 & 0 & 0 & 0 \\ 0 & 0 & 0 & 0 & 0 & 0 & 0 \\ 2 & 0 & 0 & 0 & 0 & 0 & 0 \end{pmatrix} \tag{B.3}
\end{aligned}$$

They are normalized according to  $\text{tr}(T_a T_b) = -\frac{1}{2}\delta_{ab}$ .

## B.2 The exceptional Lie groups $F_4$ and $E_6$

The exceptional Lie group  $F_4$  is the automorphism group of the exceptional Jordan algebra, whose elements are  $3 \times 3$  matrices with octonionic entries. All representations are real and it has a trivial centre. The dimension of the corresponding algebra is 52 and the defining representation is 26-dimensional. It is a maximal subgroup of the exceptional Lie group  $E_6$  with algebra dimension 78 and 27-dimensional defining representation. The centre of  $E_6$  is  $\mathbb{Z}(3)$ . Details, regarding further properties and an explicit construction, can be found in [234, 235].

Both groups are not orthogonal / unitary and therefore in the Monte-Carlo simulations, the inverse of the gauge links has to be computed instead of the transpose / Hermitian conjugate.

# Appendix C

## $G_2$ Yang-Mills at zero temperature: tables

The tables provide additional data to the simulations of  $G_2$  gluodynamics at zero temperature in chap. 5.

$\beta, N$	30, 28 <sup>3</sup>	35, 28 <sup>3</sup>	40, 28 <sup>3</sup>	30, 48 <sup>3</sup>	40, 64 <sup>3</sup>	20, 32 <sup>3</sup>
$\gamma a$	0.185(8)	0.160(4)	0.147(5)	0.197(1)	0.164(1)	0.252(1)
$\alpha$	0.0881(7)	0.0752(3)	0.071(4)	0.098(1)	0.0887(1)	0.117(1)
$\sigma a^2$	0.046(1)	0.0340(8)	0.024(1)	0.0435(3)	0.0221(3)	0.1161(2)

**Table C.1** Potential for charges in the (7) representation.

$\beta$	$N$	$\sigma_7 a^2$	$g^{-2} \sqrt{\sigma_7}$	$R(c = 1.65)$	$a$	$\mu$
20	32 <sup>3</sup>	0.11807(19)	0.4908(4)	3.62	0.138 fm	490 MeV
25	40 <sup>3</sup>	0.06863(12)	0.4678(4)	4.76	0.105 fm	491 MeV
30	48 <sup>3</sup>	0.04481(28)	0.4536(14)	5.90	0.085 fm	490 MeV
35	56 <sup>3</sup>	0.03193(14)	0.4467(10)	7.00	0.071 fm	495 MeV
40	64 <sup>3</sup>	0.02219(33)	0.4256(32)	8.39	0.060 fm	489 MeV

**Table C.2** String tension for the (7) representation on lattice sizes and couplings that are used for the continuum extrapolation.

$\mathcal{R}$	7	14	27	64	77	77'	182	189
$\gamma_{\mathcal{R}} a$	0.147(5)	0.29(1)	0.34(1)	0.51(1)	0.58(1)	0.74(2)	0.83(1)	0.77(2)
$\gamma_{\mathcal{R}} a / \mathcal{C}'_{\mathcal{R}}$	0.147	0.145	0.146	0.146	0.145	0.148	0.138	0.144
$\gamma_{\mathcal{R}} / \gamma_7$	1	1.97	2.31	3.46	3.94	5.03	5.64	5.23
$\alpha_{\mathcal{R}}$	0.071(4)	0.145(8)	0.16(1)	0.24(1)	0.27(1)	0.36(1)	0.37(1)	0.36(1)
$\alpha_{\mathcal{R}} / \mathcal{C}'_{\mathcal{R}}$	0.071	0.0725	0.069	0.069	0.068	0.072	0.062	0.068
$\alpha_{\mathcal{R}} / \alpha_7$	1	2.04	2.25	3.38	3.80	5.07	5.21	5.07
$\sigma_{\mathcal{R}} a^2$	0.024(1)	0.048(2)	0.057(3)	0.086(4)	0.099(5)	0.120(6)	0.157(6)	0.132(6)
$\sigma_{\mathcal{R}} a^2 / \mathcal{C}'_{\mathcal{R}}$	0.024	0.024	0.024	0.025	0.025	0.024	0.026	0.025
$\sigma_{\mathcal{R}} / \sigma_7$	1	2.00	2.37	3.58	4.12	5.00	6.54	5.50

**Table C.3** Fit-parameters of static potentials.

$\mathcal{R}$	7	14	27	64	77	77'	182	189
$\sigma_{\mathcal{R}}(1/2)/\sigma_7(1/2)$	1	1.9996(3)	2.3327(5)	3.498(1)	3.997(2)	4.996(3)	5.991(5)	5.328(4)
$\sigma_{\mathcal{R}}(3/2)/\sigma_7(3/2)$	1	1.9989(7)	2.331(1)	3.495(5)	3.994(4)	4.989(7)	5.99(1)	5.321(9)
$\sigma_{\mathcal{R}}(5/2)/\sigma_7(5/2)$	1	1.996(1)	2.327(1)	3.484(5)	3.980(7)	4.96(1)	5.94(2)	5.29(1)
$\mathcal{C}'_{\mathcal{R}}$	1	2.0000	2.3333	3.5000	4.0000	5.0000	6.0000	5.3333

**Table C.4** Scaled local string tension.

	$\beta = 9.7, N = 14^4$	$\beta = 10, N = 14^4$	$\beta = 9.7, N = 20^4$
$\gamma_7 a$	0.83(8)	0.74(4)	0.68(9)
$\alpha_7$	0.40(7)	0.33(3)	0.28(8)
$\sigma_7 a^2$	0.07(2)	0.042(9)	0.11(1)
$R(c = 1.65)$	4.23	5.61	3.53
$a$	0.12 fm	0.089 fm	0.14 fm
$\mu$	434 MeV	453 MeV	466 MeV

**Table C.5** Parameters of the quark anti-quark potential in 4 dimensions for  $\mathcal{R} = 7$ .

$\mathcal{R}$	7	14	27
$\gamma_{\mathcal{R}} a$	0.68(9)	1.39(4)	1.61(3)
$\gamma_{\mathcal{R}} a / \mathcal{C}'_{\mathcal{R}}$	0.68	0.695	0.690
$\alpha_{\mathcal{R}}$	0.28(8)	0.60(2)	0.69(2)
$\alpha_{\mathcal{R}} / \mathcal{C}'_{\mathcal{R}}$	0.28	0.30	0.295
$\sigma_{\mathcal{R}} a^2$	0.11(1)	0.21(1)	0.251(9)
$\sigma_{\mathcal{R}} a^2 / \mathcal{C}'_{\mathcal{R}}$	0.11	0.105	0.107

**Table C.6** Fit-parameters of static potentials ( $20^4$  lattice,  $\beta = 9.7$ ).

$\mathcal{R}$	7	14	27	64
$\sigma_{\mathcal{R}}(1/2)/\sigma_7(1/2)$	1	1.973(1)	2.294(1)	3.396(8)
$\sigma_{\mathcal{R}}(3/2)/\sigma_7(3/2)$	1	1.987(3)	2.303(4)	3.44(2)
$\sigma_{\mathcal{R}}(5/2)/\sigma_7(5/2)$	1	1.92(1)	2.28(3)	—
$\mathcal{C}'_{\mathcal{R}}$	1	2.0000	2.3333	3.5000

**Table C.7** Scaled local string tension ( $20^4$  lattice,  $\beta = 9.7$ ).

# Appendix D

## Lattice results for $G_2$ -QCD: raw data

Here the raw data (without interpolation and scale setting) are shown as a function of the lattice gauge coupling  $\beta$  and the bare chemical potential  $\mu$  for the small lattices  $8^3 \times 16$ ,  $8^3 \times 4$  and  $8^3 \times 2$ .

### D.1 Zero temperature

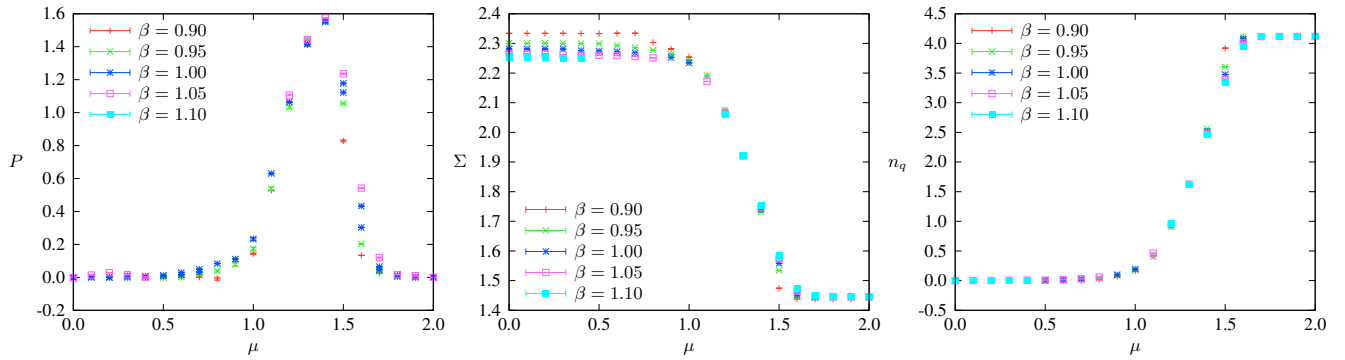


**Figure D.1** Polyakov loop (left panel), chiral condensate (centre panel) and quark number density (right panel) on a  $8^3 \times 16$  lattice.

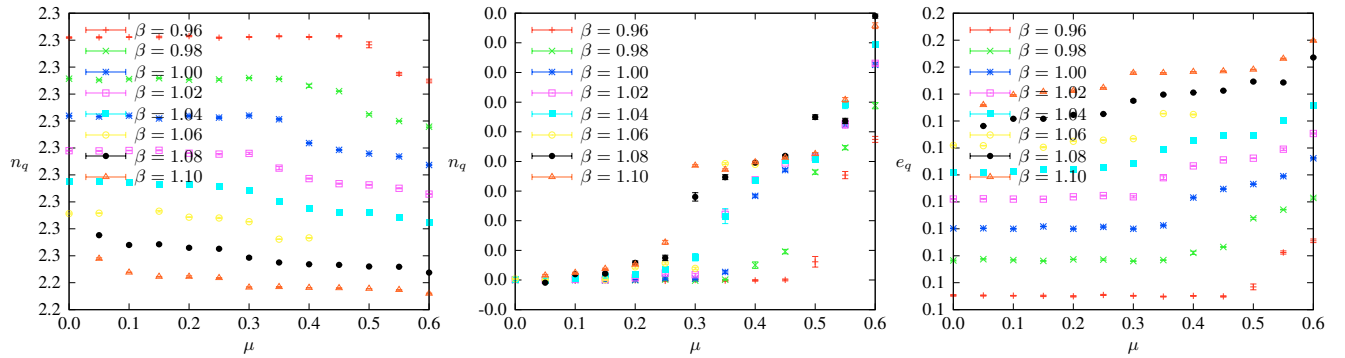


**Figure D.2** Chiral condensate (left panel), quark number density (centre panel) and quark energy density (right panel) on a  $8^3 \times 16$  lattice.

## D.2 Finite temperature

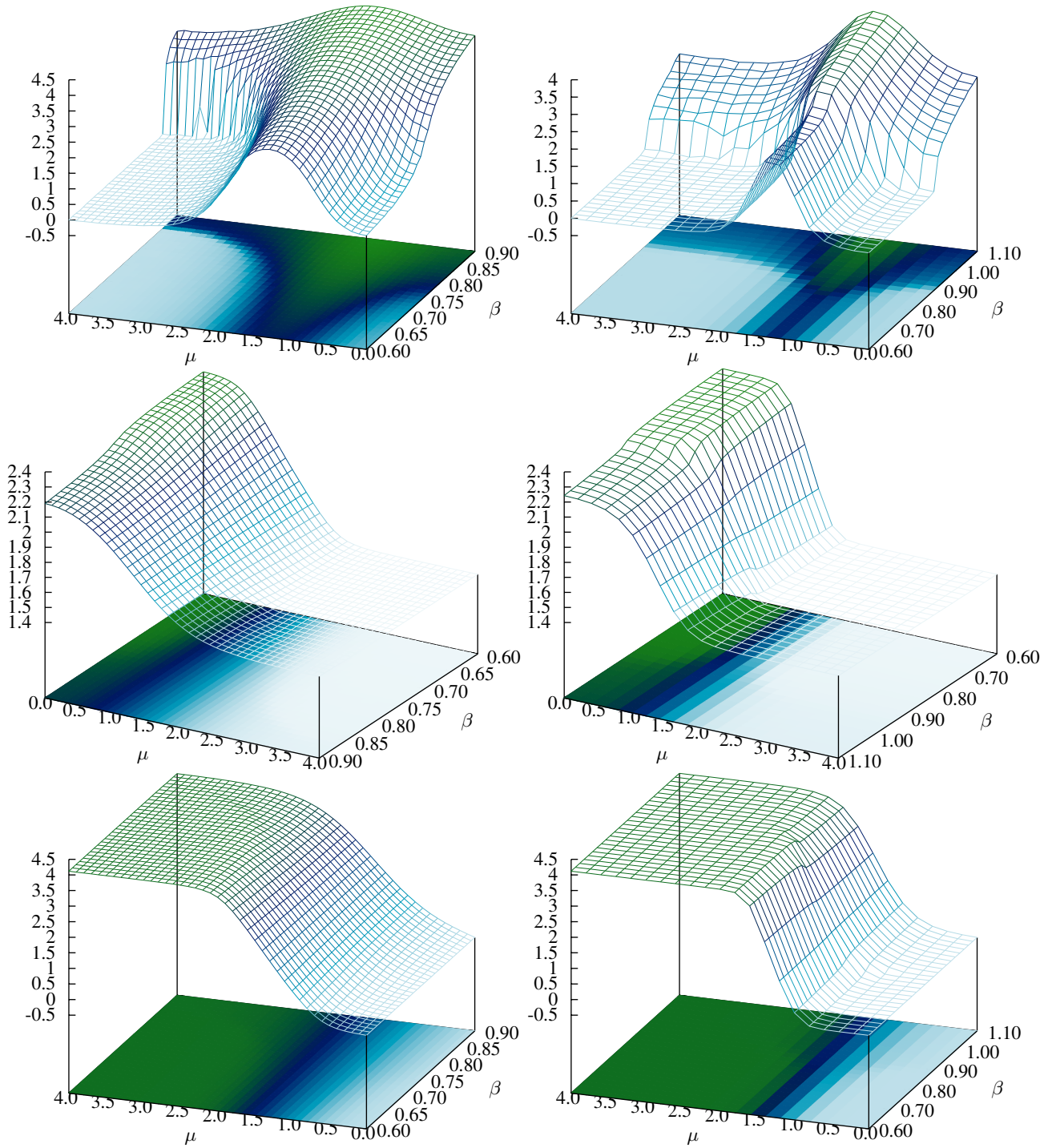


**Figure D.3** Polyakov loop (top row), chiral condensate (middle row) and quark number density (bottom row) on a  $8^3 \times 2$  lattice (left panel) and on a  $8^3 \times 4$  lattice (right panel).

# Appendix E

## Supersymmetric Yang-Mills theories on the lattice

### E.1 $\mathcal{N} = 2$ SYM in three dimensions in the continuum

The action of  $\mathcal{N} = 2$  SYM in three dimensions in Minkowski spacetime is given by

$$S = L_4 \int d^3x \left\{ -\frac{1}{4} \text{tr} F_{IJ} F^{IJ} + \frac{i}{2} \text{tr} \bar{\lambda} \gamma_I D^I \lambda - \frac{1}{2} \text{tr} D_I \phi D^I \phi + \frac{1}{2} g \text{tr} \bar{\lambda} \gamma_3 [\phi, \lambda] \right\}, \quad (\text{E.1})$$

where  $L_4$  is the size of the compactified fourth dimension. The supersymmetry transformations read

$$\begin{aligned} \delta A_I &= i\bar{\epsilon} \gamma_I \lambda \\ \delta \lambda &= (F^{IJ} \Sigma_{IJ} + 2D^I \phi \Sigma_{I3}) i\epsilon \\ \delta \bar{\lambda} &= -i\bar{\epsilon} (F^{IJ} \Sigma_{IJ} + 2D^I \phi \Sigma_{I3}) \\ \delta \phi &= i\bar{\epsilon} \gamma_3 \lambda \end{aligned} \quad (\text{E.2})$$

with arbitrary spinor  $\epsilon$ . After rescaling the fields as

$$\begin{aligned} A_\mu &\rightarrow g^{-1} A_\mu \\ \phi &\rightarrow g^{-1} \phi \\ \lambda &\rightarrow g^{-1} \lambda \end{aligned} \quad (\text{E.3})$$

and

$$\begin{aligned} F_{\mu\nu} &\rightarrow g^{-1} F_{\mu\nu} = g^{-1} (\partial_\mu A_\nu - \partial_\nu A_\mu - i[A_\mu, A_\nu]) \\ ig[A_\mu, \cdot] &\rightarrow i[A_\mu, \cdot] \end{aligned} \quad (\text{E.4})$$

the action takes the following form

$$\begin{aligned} S &= L_4 \int d^3x \left\{ -\frac{1}{4g^2} \text{tr} F_{IJ} F^{IJ} + \frac{i}{2g^2} \text{tr} \bar{\lambda} \gamma_I D^I \lambda - \frac{1}{2g^2} \text{tr} D_I \phi D^I \phi + \frac{1}{2g^2} \text{tr} \bar{\lambda} \gamma_3 [\phi, \lambda] \right\} \\ &= \alpha \int d^3x \text{tr} \left\{ -\frac{1}{4} F_{IJ} F^{IJ} + \frac{i}{2} \bar{\lambda} \gamma_I D^I \lambda - \frac{1}{2} D_I \phi D^I \phi + \frac{1}{2} \bar{\lambda} \gamma_3 [\phi, \lambda] \right\}, \end{aligned} \quad (\text{E.5})$$

with dimensionfull coupling constant  $\alpha = \frac{L_4}{g^2}$ . The Wick rotation is achieved by the following rules

$$\gamma_0 \rightarrow i\gamma_0 \quad , \quad A_0 \rightarrow iA_0, \quad (\text{E.6})$$

and then the Euclidean action reads

$$S^E = \alpha \int d^3x \text{tr} \left\{ \frac{1}{4} F_{IJ} F_{IJ} + \frac{1}{2} \bar{\lambda} \gamma_I^E D_I \lambda + \frac{1}{2} D_I \phi D_I \phi - \frac{1}{2} \bar{\lambda} \gamma_3^E [\phi, \lambda] \right\}. \quad (\text{E.7})$$

In 3 dimensions  $\gamma_I$  is a reducible representation and therefore it is possible to decompose it into a irreducible representation of the Clifford algebra according to

$$\gamma_I = \begin{pmatrix} \Gamma_I & 0 \\ 0 & -\Gamma_I \end{pmatrix} \quad \text{and} \quad \gamma_3 = i \begin{pmatrix} 0 & -\mathbb{1} \\ \mathbb{1} & 0 \end{pmatrix} \quad (\text{E.8})$$

where  $\Gamma_I$  forms a 2-dimensional representation of the clifford algebra in 3 dimensions,  $[\Gamma_I, \Gamma_J] = 2\eta_{IJ}$ . The Majorana spinor  $\lambda$  decomposes into two Majorana spinors in 3 dimensions,

$$\lambda = \begin{pmatrix} \eta_1 \\ \eta_2 \end{pmatrix} \quad \text{and} \quad \bar{\lambda} = \begin{pmatrix} \bar{\eta}_1 & -\bar{\eta}_2 \end{pmatrix}. \quad (\text{E.9})$$

Under this decomposition, different terms of the action transform as

$$\begin{aligned} \bar{\lambda} D \lambda &= \bar{\eta}_1 D \eta_1 - \bar{\eta}_2 D \eta_2, \\ \bar{\lambda} \gamma_3 D \lambda &= -i (\bar{\eta}_1 D \eta_2 + \bar{\eta}_2 D \eta_1), \\ \bar{\lambda} \gamma_I D \lambda &= \bar{\eta}_1 \Gamma_I D \eta_1 + \bar{\eta}_2 \Gamma_I D \eta_2, \end{aligned} \quad (\text{E.10})$$

where the operator  $D$  acts trivial in spinor space. Then the Minkowski action is equivalent to the following expression

$$\begin{aligned} S = L_4 \int d^3x \left\{ -\frac{1}{4} \text{tr} F_{IJ} F^{IJ} + \frac{i}{2} \text{tr} \bar{\eta}_1 \Gamma_I D^I \eta_1 + \frac{i}{2} \text{tr} \bar{\eta}_2 \Gamma_I D^I \eta_2 - \frac{1}{2} \text{tr} D_I \phi D^I \phi \right. \\ \left. - \frac{i}{2} g \text{tr} (\bar{\eta}_1 [\phi, \eta_2] + \bar{\eta}_2 [\phi, \eta_1]) \right\}. \end{aligned} \quad (\text{E.11})$$

## E.2 $\mathcal{N} = 2$ SYM in three dimensions on the lattice

For a Monte-Carlo simulation, the action with 4 dimensional spinor representation has the advantage that it is possible to construct a Hermitian Dirac operator due to the existence of a  $\gamma_5$  matrix. On the lattice also a SUSY-breaking mass term is added to fine-tune the theory into a SUSY invariant continuum limit,

$$S^E = \alpha \int d^3x \left( \text{tr} \left\{ \frac{1}{4} F_{IJ} F_{IJ} + \frac{1}{2} D_I \phi D_I \phi \right\} + \frac{1}{2} \bar{\lambda}_a \{ \gamma_I^E D_I^{ab} + m \delta^{ab} + \gamma_3^E f^{abc} \phi_c \} \lambda^b \right). \quad (\text{E.12})$$

The scalar part of the lattice action is given by

$$S_{\text{scalar}} = \sum_{x,I} \text{tr} (\phi_x^2 - \phi_{x+I} \mathcal{U}_{x,I}^A \phi_x), \quad (\text{E.13})$$

where  $\mathcal{U}^A$  are link variables in the adjoint representation. The fermionic part of the action is given by  $S_f = \frac{1}{2} \bar{\lambda} D \lambda$  with

$$D_{xy} = \left( m + dr + \gamma_3 \hat{\phi} \right) \delta_{x,y} - \frac{1}{2} \sum_I \left\{ (r - \gamma_I) \mathcal{U}_{x,I}^A \delta_{x+I,y} + (r + \gamma_I) \mathcal{U}_{x-I,I}^A \delta_{x-I,y} \right\}, \quad (\text{E.14})$$

where  $\hat{\phi}_{ab} = f_{abc} \phi^c$ . The lattice operator  $D$  can also be written in even-odd block form

$$D = \begin{pmatrix} M_{\text{ee}} & D_{\text{eo}} \\ D_{\text{oe}} & M_{\text{oo}} \end{pmatrix}. \quad (\text{E.15})$$

The operator  $D$  is  $\gamma_5$ -Hermitian, this means

$$\gamma_5 D \gamma_5 = D^\dagger \longrightarrow \gamma_5 D = (\gamma_5 D)^\dagger \quad (\text{E.16})$$

and implies the following relations

$$\begin{aligned} \gamma_5 M_{\text{ee}} \gamma_5 &= M_{\text{ee}}^\dagger, \\ \gamma_5 M_{\text{oo}} \gamma_5 &= M_{\text{oo}}^\dagger, \\ \gamma_5 D_{\text{eo}} \gamma_5 &= D_{\text{oe}}^\dagger, \\ \gamma_5 D_{\text{oe}} \gamma_5 &= D_{\text{eo}}^\dagger. \end{aligned} \quad (\text{E.17})$$

After integrating out the fermions one has to compute the determinant of  $D$ . This can be done in the following way

$$\det \gamma_5 D = \det \gamma_5 M_{\text{ee}} \det (\gamma_5 M_{\text{oo}} - \gamma_5 D_{\text{oe}} M_{\text{ee}}^{-1} D_{\text{eo}}). \quad (\text{E.18})$$

With the definitions

$$\begin{aligned} \tilde{D} &= \begin{pmatrix} M_{\text{ee}} & 0 \\ 0 & M_{\text{oo}} - D_{\text{oe}} M_{\text{ee}}^{-1} D_{\text{eo}} \end{pmatrix}, \quad L = \begin{pmatrix} \mathbb{1} & 0 \\ D_{\text{oe}} M_{\text{ee}}^{-1} & \mathbb{1} \end{pmatrix}, \quad U = \begin{pmatrix} \mathbb{1} & M_{\text{ee}}^{-1} D_{\text{eo}} \\ 0 & \mathbb{1} \end{pmatrix} \\ L^{-1} &= \begin{pmatrix} \mathbb{1} & 0 \\ -D_{\text{oe}} M_{\text{ee}}^{-1} & \mathbb{1} \end{pmatrix}, \quad U^{-1} = \begin{pmatrix} \mathbb{1} & -M_{\text{ee}}^{-1} D_{\text{eo}} \\ 0 & \mathbb{1} \end{pmatrix}, \end{aligned} \quad (\text{E.19})$$

the  $LU$  decomposition of  $D$  can be written as

$$D = L \tilde{D} U, \quad D^{-1} = U^{-1} \tilde{D}^{-1} L^{-1}. \quad (\text{E.20})$$

The inverse of the Matrix  $M$  can be computed exactly ( $\hat{m} = m + dr$ )

$$\begin{aligned} M &= \hat{m} \mathbb{1} \otimes \mathbb{1} + \gamma_3 \otimes \hat{\phi}, \\ M^{-1} &= \frac{1}{\hat{m} (\hat{m}^2 + \phi^2)} \left( \mathbb{1} \otimes (\hat{m}^2 \mathbb{1} + \phi \phi^\text{T}) - \hat{m} \gamma_3 \otimes \hat{\phi} \right), \\ M^\dagger M &= (\hat{m}^2 + \phi^2) \mathbb{1} \otimes \mathbb{1} - \mathbb{1} \otimes \phi \phi^\text{T}. \end{aligned} \quad (\text{E.21})$$

In the HMC ‘force’ the derivative with respect to  $\phi$ ,

$$\delta_{\phi_c} M_{ab} = \gamma_3 f_{abc} \delta \phi^c \quad (\text{E.22})$$

is needed. The determinant of the Hermitian square of  $M$  is given by

$$\det M^\dagger M = \hat{m}^8 (\hat{m}^2 + \phi^2)^8. \quad (\text{E.23})$$

These analytical expressions are used to speed up the simulations for  $\mathcal{N} = 2$  SYM theory on the lattice in three dimensions.

# Bibliography

- [1] W. Heisenberg. Über quantentheoretische Umdeutung kinematischer und mechanischer Beziehungen. *Zeitschrift für Physik*, 33(1):879–893, 1925.
- [2] M. Born, P. Jordan. Zur Quantenmechanik. *Zeitschrift für Physik*, 34:858, 1925.
- [3] E. Schrödinger. Quantisierung als Eigenwertproblem. *Annalen der Physik*, 385(13):437–490, 1926.
- [4] P.A.M. Dirac. The Quantum Theory of the Electron. *Proc. Roy. Soc. London*, A117:610–624, 1928.
- [5] Sin-Itiro Tomonaga and J. R. Oppenheimer. On infinite field reactions in quantum field theory. *Phys. Rev.*, 74(2):224–225, Jul 1948.
- [6] Julian Schwinger. On quantum-electrodynamics and the magnetic moment of the electron. *Phys. Rev.*, 73(4):416–417, Feb 1948.
- [7] R. P. Feynman. Space-time approach to non-relativistic quantum mechanics. *Rev. Mod. Phys.*, 20(2):367–387, Apr 1948.
- [8] C. N. Yang and R. L. Mills. Conservation of isotopic spin and isotopic gauge invariance. *Phys. Rev.*, 96:191–195, Oct 1954.
- [9] S. L. Glashow. Partial symmetries of weak interactions. *Nucl. Phys.*, 22:579–588, 1961.
- [10] Steven Weinberg. A model of leptons. *Phys. Rev. Lett.*, 19:1264–1266, Nov 1967.
- [11] H. Fritzsch, Murray Gell-Mann, and H. Leutwyler. Advantages of the Color Octet Gluon Picture. *Phys. Lett.*, B47:365–368, 1973.
- [12] K. Kodama, N. Ushida, C. Andreopoulos, N. Saoulidou, G. Tzanakos, P. Yager, B. Baller, D. Boehnlein, W. Freeman, B. Lundberg, J. Morfin, R. Rameika, J.C. Yun, J.S. Song, C.S. Yoon, S.H. Chung, P. Berghaus, M. Kubantsev, N.W. Reay, R. Sidwell, N. Stanton, S. Yoshida, S. Aoki, T. Hara, J.T. Rhee, D. Ciampa, C. Erickson, M. Graham, K. Heller, R. Rusack, R. Schwienhorst, J. Sielaff, J. Trammell, J. Wilcox, K. Hoshino, H. Jiko, M. Miyanishi, M. Komatsu, M. Nakamura, T. Nakano, K. Niwa, N. Nonaka, K. Okada, O. Sato, T. Akdogan, V. Paolone, C. Rosenfeld, A. Kulik, T. Kafka, W. Oliver, T. Patzak, and J. Schneps. Observation of tau neutrino interactions. *Physics Letters B*, 504(3):218 – 224, 2001.
- [13] A. Salam and J. C. Ward. Electromagnetic and weak interactions. *Phys. Lett.*, 13:168–171, 1964.
- [14] Kenneth G. Wilson. Confinement of quarks. *Phys. Rev. D*, 10:2445–2459, Oct 1974.

- [15] J. Greensite. *An introduction to the confinement problem*. Lecture Notes in Physics. Springer, 2011.
- [16] Peter W. Higgs. Spontaneous Symmetry Breakdown without Massless Bosons. *Phys.Rev.*, 145:1156–1163, 1966.
- [17] Ugo Amaldi, Wim de Boer, and Hermann Frstenau. Comparison of grand unified theories with electroweak and strong coupling constants measured at lep. *Physics Letters B*, 260(34):447 – 455, 1991.
- [18] Curtis G. Callan. Broken scale invariance in scalar field theory. *Phys. Rev. D*, 2:1541–1547, Oct 1970.
- [19] K. Symanzik. Small distance behaviour in field theory and power counting. *Communications in Mathematical Physics*, 18(3):227–246, 1970. 10.1007/BF01649434.
- [20] A. Petermann and E. C. G. Stueckelberg. Restriction of possible interactions in quantum electrodynamics. *Phys. Rev.*, 82:548–549, May 1951.
- [21] Kenneth G. Wilson. The renormalization group: Critical phenomena and the kondo problem. *Rev. Mod. Phys.*, 47:773–840, Oct 1975.
- [22] M. Gell-Mann and F. E. Low. Quantum electrodynamics at small distances. *Phys. Rev.*, 95:1300–1312, Sep 1954.
- [23] David J. Gross and Frank Wilczek. Ultraviolet behavior of non-abelian gauge theories. *Phys. Rev. Lett.*, 30:1343–1346, Jun 1973.
- [24] David J. Gross and Frank Wilczek. Asymptotically free gauge theories. i. *Phys. Rev. D*, 8:3633–3652, Nov 1973.
- [25] H. David Politzer. Asymptotic freedom: An approach to strong interactions. *Physics Reports*, 14(4):129 – 180, 1974.
- [26] H. David Politzer. Reliable perturbative results for strong interactions? *Phys. Rev. Lett.*, 30:1346–1349, Jun 1973.
- [27] M. Creutz. *Quarks, gluons, and lattices*. Cambridge monographs on mathematical physics. Cambridge University Press, 1985.
- [28] Aoki Y., Endrodi G., Fodor Z., Katz S. D., and Szabo K. K. The order of the quantum chromodynamics transition predicted by the standard model of particle physics. *Nature*, 443(7112):675–678, oct 2006. 10.1038/nature05120.

- [29] Frithjof Karsch. Lattice QCD at high temperature and density. *Lect.Notes Phys.*, 583:209–249, 2002, hep-lat/0106019. Lectures given at 40th Internationale Universitätswochen fuer Theoretische Physik: Dense Matter (IUKT 40), Schladming, Styria, Austria, 3-10 Mar 2001; corrected some typos Report-no: BI-TP 2001/10.
- [30] M. Cheng, N.H. Christ, S. Datta, J. van der Heide, C. Jung, et al. The Transition temperature in QCD. *Phys.Rev.*, D74:054507, 2006, hep-lat/0608013.
- [31] Y. Aoki, Z. Fodor, S.D. Katz, and K.K. Szabo. The QCD transition temperature: Results with physical masses in the continuum limit. *Phys.Lett.*, B643:46–54, 2006, hep-lat/0609068.
- [32] V.G. Bornyakov, M.N. Chernodub, Y. Mori, S.M. Morozov, Y. Nakamura, et al. Critical temperature in QCD with two flavors of dynamical quarks. *PoS*, LAT2005:157, 2006, hep-lat/0509122.
- [33] Y. Aoki, Szabolcs Borsanyi, Stephan Durr, Zoltan Fodor, Sandor D. Katz, et al. The QCD transition temperature: results with physical masses in the continuum limit II. *JHEP*, 0906:088, 2009, 0903.4155.
- [34] A. Bazavov, T. Bhattacharya, M. Cheng, N.H. Christ, C. DeTar, et al. Equation of state and QCD transition at finite temperature. *Phys.Rev.*, D80:014504, 2009, 0903.4379. 31 pages, 24 EPS-figures.
- [35] A. Bazavov, T. Bhattacharya, M. Cheng, C. DeTar, H.T. Ding, et al. The chiral and deconfinement aspects of the QCD transition. *Phys.Rev.*, D85:054503, 2012, 1111.1710.
- [36] P. Braun-Munzinger, J. Stachel, and Christof Wetterich. Chemical freeze-out and the qcd phase transition temperature. *Physics Letters B*, 596(12):61 – 69, 2004.
- [37] A. Andronic, P. Braun-Munzinger, and J. Stachel. Thermal hadron production in relativistic nuclear collisions: The hadron mass spectrum, the horn, and the qcd phase transition. *Physics Letters B*, 673(2):142 – 145, 2009.
- [38] Adam Miklos Halasz, A.D. Jackson, R.E. Shrock, Misha A. Stephanov, and J.J.M. Verbaarschot. On the phase diagram of QCD. *Phys.Rev.*, D58:096007, 1998, hep-ph/9804290.
- [39] Edward Witten. Cosmic separation of phases. *Phys. Rev. D*, 30:272–285, Jul 1984.
- [40] Ariel R Zhitnitsky. ‘nonbaryonic’ dark matter as baryonic colour superconductor. *Journal of Cosmology and Astroparticle Physics*, 2003(10):010, 2003.
- [41] Robert D. Pisarski. Phenomenology of the chiral phase transition. *Physics Letters B*, 110(2):155 – 158, 1982.
- [42] Sourendu Gupta. Lattice qcd with chemical potential: Evading the fermion-sign problem. *Pramana*, 63(6):1211–1224, 2004. 10.1007/BF02704891.

- [43] T.H.R. Skyrme. A Unified Field Theory of Mesons and Baryons. *Nucl.Phys.*, 31:556–569, 1962.
- [44] Claudia Ratti, Michael A. Thaler, and Wolfram Weise. Phase diagram and thermodynamics of the PNJL model. 2006, nucl-th/0604025. To appear in GSI Scientific Report on Compressed Baryonic matter.
- [45] Jens Braun, Bertram Klein, and Bernd-Jochen Schaefer. On the Phase Structure of QCD in a Finite Volume. 2011, 1110.0849.
- [46] Giorgio Parisi. On complex probabilities. *Physics Letters B*, 131(46):393 – 395, 1983.
- [47] Gert Aarts. Can stochastic quantization evade the sign problem? the relativistic bose gas at finite chemical potential. *Phys. Rev. Lett.*, 102:131601, Apr 2009.
- [48] Nikolay Prokof'ev and Boris Svistunov. Worm Algorithms for Classical Statistical Models. *Phys. Rev. Lett.*, 87:160601, 2001.
- [49] Christof Gattringer. Flux representation of an effective Polyakov loop model for QCD thermodynamics. *Nucl. Phys.*, B850:242–252, 2011, 1104.2503.
- [50] Ydalia Delgado, Hans Gerd Evertz, and Christof Gattringer. Solving the Complex Phase Problem in a QCD Related Model. *Acta Phys. Polon. Supp.*, 4:703–708, 2011, 1110.6862.
- [51] J.B. Kogut, Misha A. Stephanov, D. Toublan, J.J.M. Verbaarschot, and A. Zhitnitsky. QCD - like theories at finite baryon density. *Nucl.Phys.*, B582:477–513, 2000, hep-ph/0001171.
- [52] Simon Hands, Istvan Montvay, Susan Morrison, Manfred Oevers, Luigi Scorzato, et al. Numerical study of dense adjoint matter in two color qcd. *Eur.Phys.J.*, C17:285–302, 2000, hep-lat/0006018.
- [53] Simon Hands, Seyong Kim, and Jon-Ivar Skullerud. Deconfinement in dense 2-color QCD. *Eur.Phys.J.*, C48:193, 2006, hep-lat/0604004.
- [54] Simon Hands, Seyong Kim, and Jon-Ivar Skullerud. A Quarkyonic Phase in Dense Two Color Matter? *Phys.Rev.*, D81:091502, 2010, 1001.1682.
- [55] Takuya Kanazawa, Tilo Wettig, and Naoki Yamamoto. Chiral Lagrangian and spectral sum rules for dense two-color QCD. *JHEP*, 0908:003, 2009, 0906.3579.
- [56] Nils Strodthoff, Bernd-Jochen Schaefer, and Lorenz von Smekal. Quark-meson-diquark model for two-color QCD. 2011, 1112.5401.
- [57] K. Holland, P. Minkowski, M. Pepe, and U. J. Wiese. Exceptional confinement in G(2) gauge theory. *Nucl. Phys.*, B668:207–236, 2003, hep-lat/0302023.
- [58] M. Pepe and U. J. Wiese. Exceptional deconfinement in G(2) gauge theory. *Nucl. Phys.*, B768:21–37, 2007, hep-lat/0610076.

- [59] Sidney Coleman and Jeffrey Mandula. All possible symmetries of the  $s$  matrix. *Phys. Rev.*, 159:1251–1256, Jul 1967.
- [60] Rudolf Haag, Jan T. Lopuszanski, and Martin Sohnius. All Possible Generators of Supersymmetries of the  $s$  Matrix. *Nucl. Phys.*, B88:257, 1975.
- [61] Savas Dimopoulos and Howard Georgi. Softly Broken Supersymmetry and SU(5). *Nucl.Phys.*, B193:150, 1981.
- [62] John R. Ellis, J.S. Hagelin, Dimitri V. Nanopoulos, Keith A. Olive, and M. Srednicki. Supersymmetric Relics from the Big Bang. *Nucl.Phys.*, B238:453–476, 1984.
- [63] Gudrun Hiller and Martin Schmaltz. Solving the strong CP problem with supersymmetry. *Phys.Lett.*, B514:263–268, 2001, hep-ph/0105254.
- [64] Ugo Amaldi, Wim de Boer, and Hermann Furstenau. Comparison of grand unified theories with electroweak and strong coupling constants measured at LEP. *Phys. Lett.*, B260:447–455, 1991.
- [65] John Ellis, S. Kelley, and D.V. Nanopoulos. Precision lep data, supersymmetric guts and string unification. *Physics Letters B*, 249(34):441 – 448, 1990.
- [66] S. Ferrara, B. Zumino, and J. Wess. Supergauge multiplets and superfields. *Physics Letters B*, 51(3):239 – 241, 1974.
- [67] P. H. Dondi and H. Nicolai. Lattice supersymmetry. *Nuovo Cim.*, A41:1, 1977.
- [68] G. Veneziano and S. Yankielowicz. An effective lagrangian for the pure  $n = 1$  supersymmetric yang-mills theory. *Physics Letters B*, 113(3):231 – 236, 1982.
- [69] Paul H. Ginsparg and Kenneth G. Wilson. A remnant of chiral symmetry on the lattice. *Phys. Rev. D*, 25:2649–2657, May 1982.
- [70] G. Curci and G. Veneziano. Supersymmetry and the Lattice: A Reconciliation? *Nucl.Phys.*, B292:555, 1987.
- [71] A. Donini, M. Guagnelli, P. Hernandez, and A. Vladikas. Towards N=1 superYang-Mills on the lattice. *Nucl.Phys.*, B523:529–552, 1998, hep-lat/9710065. 25 Latex pages, 5 figures Report-no: CERN-TH/97-266.
- [72] I. Montvay. Supersymmetric Yang-Mills theory on the lattice. *Int.J.Mod.Phys.*, A17:2377–2412, 2002, hep-lat/0112007.
- [73] Joel Giedt. Progress in four-dimensional lattice supersymmetry. *Int.J.Mod.Phys.*, A24:4045–4095, 2009, 0903.2443. 64 pages.
- [74] George Tamminga Fleming, John B. Kogut, and Pavlos M. Vranas. SuperYang-Mills on the lattice with domain wall fermions. *Phys.Rev.*, D64:034510, 2001, hep-lat/0008009.

- [75] K. Demmouche et al. Simulation of 4d  $N=1$  supersymmetric Yang-Mills theory with Symanzik improved gauge action and stout smearing. *Eur. Phys. J.*, C69:147–157, 2010, 1003.2073.
- [76] F. Grsey, P. Ramond, and P. Sikivie. A universal gauge theory model based on  $e_6$ . *Physics Letters B*, 60(2):177 – 180, 1976.
- [77] Corinne A Manogue and Tevian Dray. Octonions,  $e_6$ , and particle physics. *Journal of Physics: Conference Series*, 254(1):012005, 2010.
- [78] Björn H. Wellegehausen, Andreas Wipf, and Christian Wozar. Effective Polyakov Loop Dynamics for Finite Temperature  $G(2)$  Gluodynamics. *Phys.Rev.*, D80:065028, 2009, 0907.1450.
- [79] Björn H. Wellegehausen, Andreas Wipf, and Christian Wozar. Casimir Scaling and String Breaking in  $G(2)$  Gluodynamics. *Phys.Rev.*, D83:016001, 2011, 1006.2305.
- [80] Björn H. Wellegehausen, Andreas Wipf, and Christian Wozar. Phase diagram of the lattice  $G_2$  Higgs Model. *Phys.Rev.*, D83:114502, 2011, 1102.1900.
- [81] Björn H. Wellegehausen. Confinement, Casimir scaling and phase transitions in  $G(2)$  gauge theories. *PoS, LATTICE2010*:293, 2010, 1010.5523.
- [82] Björn H. Wellegehausen. Phase diagram of the  $G(2)$  Higgs model and  $G(2)$ -QCD. *PoS, LATTICE2011*:266, 2011, 1111.0496.
- [83] Murat Günaydin and Feza Gürsey. Quark structure and octonions. *Journal of Mathematical Physics*, 14(11):1651–1667, 1973.
- [84] Andrzej Borowiec, Jerzy Lukierski, Vladimir Lyakhovsky, Marek Mozrzymas, and Valeriy N. Tolstoy. Basic twist quantization of the exceptional Lie algebra  $G(2)$ . *J.Math.Phys.*, 46:103502, 2005, hep-th/0403185.
- [85] A.J. Macfarlane. The sphere  $S(6)$  viewed as a  $G(2)/SU(3)$  coset space. *Int.J.Mod.Phys.*, A17:2595–2613, 2002.
- [86] I. Yokota. Exceptional Lie groups. *ArXiv e-prints*, February 2009, 0902.0431.
- [87] Sergio L. Cacciatori, Bianca L. Cerchiai, Alberto Della Vedova, Giovanni Ortenzi, and Antonio Scotti. Euler angles for  $G(2)$ . *J. Math. Phys.*, 46:083512, 2005, hep-th/0503106.
- [88] S. Uhlmann, R. Meinel, and A. Wipf. Ward identities for invariant group integrals. *J. Phys.*, A40:4367–4390, 2007, hep-th/0611170.
- [89] I. Montvay and G. Münster. *Quantum fields on a lattice*. Cambridge monographs on mathematical physics. Cambridge University Press, 1994.
- [90] H.J. Rothe. *Lattice gauge theories: an introduction*. World Scientific lecture notes in physics. World Scientific, 2005.

- [91] B. A. Berg. Introduction to Markov Chain Monte Carlo Simulations and their Statistical Analysis. *eprint arXiv:cond-mat/0410490*, October 2004, arXiv:cond-mat/0410490.
- [92] Ulli Wolff. Monte Carlo errors with less errors. *Comput.Phys.Commun.*, 156:143–153, 2004, hep-lat/0306017.
- [93] Bernd A. Berg. Monte carlo calculation of confidence limits for realistic least square fitting. *Computer Physics Communications*, 69(1):65–72, 1992.
- [94] George T. Duncan. An empirical study of jackknife-constructed confidence regions in nonlinear regression. *Technometrics*, 20(2):pp. 123–129, 1978.
- [95] S. Duane, A. D. Kennedy, B. J. Pendleton, and D. Roweth. Hybrid Monte Carlo. *Phys. Lett.*, B195:216–222, 1987.
- [96] Nicola Cabibbo and Enzo Marinari. A new method for updating su(n) matrices in computer simulations of gauge theories. *Physics Letters B*, 119(4–6):387–390, 1982.
- [97] Paolo Marenzoni, Luigi Pugnetti, and Pietro Rossi. Measure of autocorrelation times of local hybrid Monte Carlo algorithm for lattice QCD. *Phys.Lett.*, B315:152–156, 1993, hep-lat/9306013.
- [98] Ronald D. Ruth. A canonical integration technique. *Nuclear Science, IEEE Transactions on*, 30(4):2669–2671, aug. 1983.
- [99] J.C. Sexton and D.H. Weingarten. Hamiltonian evolution for the hybrid monte carlo algorithm. *Nuclear Physics B*, 380(3):665–677, 1992.
- [100] Tetsuya Takaishi and Philippe de Forcrand. Testing and tuning symplectic integrators for the hybrid monte carlo algorithm in lattice qcd. *Phys. Rev. E*, 73(3):036706, Mar 2006.
- [101] Haruo Yoshida. Construction of higher order symplectic integrators. *Physics Letters A*, 150(5–7):262–268, 1990.
- [102] Karl Jansen, Andrea Shindler, Carsten Urbach, and Urs Wenger. HMC algorithm with multiple time scale integration and mass preconditioning. *PoS, LAT2005*:118, 2006, hep-lat/0510064.
- [103] Alexander Laufer. The Exponential map of GL(N). *J.Phys.A*, A30:5455–5470, 1997, hep-th/9604049.
- [104] J. Greensite, K. Langfeld, S. Olejnik, H. Reinhardt, and T. Tok. Color Screening, Casimir Scaling, and Domain Structure in G(2) and SU(N) Gauge Theories. *Phys.Rev.*, D75:034501, 2007, hep-lat/0609050.
- [105] Björn Wellegehausen. Effektive Polyakov-Loop-Modelle fuer  $SU(N)$  - und  $G_2$  - Eichtheorien. Diplomarbeit, FSU Jena, 2008.
- [106] Ulli Wolff. Collective Monte Carlo Updating for Spin Systems. *Phys.Rev.Lett.*, 62:361, 1989.

- [107] Bernd Gehrman and Ulli Wolff. Efficiencies and optimization of HMC algorithms in pure gauge theory. *Nucl.Phys.Proc.Suppl.*, 83:801–803, 2000, hep-lat/9908003.
- [108] K. Symanzik. Continuum limit and improved action in lattice theories: (i). principles and 4 theory. *Nuclear Physics B*, 226(1):187–204, 1983.
- [109] K. Symanzik. Continuum limit and improved action in lattice theories: (ii). o(n) non-linear sigma model in perturbation theory. *Nuclear Physics B*, 226(1):205–227, 1983.
- [110] M. Lüscher and P. Weisz. On-Shell Improved Lattice Gauge Theories. *Commun. Math. Phys.*, 97:59, 1985.
- [111] R. Horsley, H. Perlt, P. E. L. Rakow, G. Schierholz, and A. Schiller. Perturbative determination of  $c_{SW}$  for plaquette and symanzik gauge action and stout link clover fermions. *Phys. Rev. D*, 78(5):054504, Sep 2008.
- [112] A.D. Kennedy, Ivan Horvath, and Stefan Sint. A New exact method for dynamical fermion computations with nonlocal actions. *Nucl.Phys.Proc.Suppl.*, 73:834–836, 1999, hep-lat/9809092.
- [113] Matthias Troyer and Uwe-Jens Wiese. Computational complexity and fundamental limitations to fermionic quantum monte carlo simulations. *Phys. Rev. Lett.*, 94(17):170201, May 2005.
- [114] D.H. Weingarten and D.N. Petcher. Monte Carlo Integration for Lattice Gauge Theories with Fermions. *Phys.Lett.*, B99:333, 1981.
- [115] W. Fraser. A survey of methods of computing minimax and near-minimax polynomial approximations for functions of a single independent variable. *J. ACM*, 12(3):295–314, July 1965.
- [116] Beat Jegerlehner. Krylov space solvers for shifted linear systems. 1996, hep-lat/9612014.
- [117] C.R. Allton, C.T. Sachrajda, R.M. Baxter, S.P. Booth, K.C. Bowler, S. Collins, D.S. Henty, R.D. Kenway, C. McNeile, B.J. Pendleton, D.G. Richards, J.N. Simone, A.D. Simpson, A. McKerrell, C. Michael, and M. Prisznyak. Quenched light hadron mass spectrum and decay constants: The effects of o(a) improvement at  $\beta = 6.2$ . *Nuclear Physics B*, 407(2):331–355, 1993.
- [118] M.A. Clark and A.D. Kennedy. Accelerating fermionic molecular dynamics. *Nucl.Phys.Proc.Suppl.*, 140:838–840, 2005, hep-lat/0409134.
- [119] S. Gusken, U. Low, K.H. Mutter, R. Sommer, A. Patel, et al. Nonsinglet axial vector couplings of the baryon octet in lattice QCD. *Phys.Lett.*, B227:266, 1989.
- [120] C. Best, M. Gockeler, R. Horsley, Ernst-Michael Ilgenfritz, H. Perlt, et al. Pion and rho structure functions from lattice QCD. *Phys.Rev.*, D56:2743–2754, 1997, hep-lat/9703014.
- [121] Shao-Jing Dong and Keh-Fei Liu. Stochastic estimation with Z(2) noise. *Phys.Lett.*, B328:130–136, 1994, hep-lat/9308015.

- [122] Khalil Bitar, A.D. Kennedy, Roger Horsley, Steffen Meyer, and Pietro Rossi. The qcd finite temperature transition and hybrid monte carlo. *Nuclear Physics B*, 313(2):348–376, 1989.
- [123] J. Greensite. The Confinement problem in lattice gauge theory. *Prog.Part.Nucl.Phys.*, 51:1, 2003, hep-lat/0301023.
- [124] Philippe de Forcrand and Oliver Jahn. Comparison of SO(3) and SU(2) lattice gauge theory. *Nucl.Phys.*, B651:125–142, 2003, hep-lat/0211004.
- [125] C. Ford, T. Tok, and A. Wipf. Abelian projection on the torus for general gauge groups. *Nucl.Phys.*, B548:585–612, 1999, hep-th/9809209.
- [126] L’udovit Liptak and Stefan Olejnik. Casimir scaling in G(2) lattice gauge theory. *Phys.Rev.*, D78:074501, 2008, 0807.1390.
- [127] K. Holland, M. Pepe, and U.J. Wiese. The Deconfinement phase transition of Sp(2) and Sp(3) Yang-Mills theories in (2+1)-dimensions and (3+1)-dimensions. *Nucl.Phys.*, B694:35–58, 2004, hep-lat/0312022.
- [128] S. Elitzur. Impossibility of Spontaneously Breaking Local Symmetries. *Phys.Rev.*, D12:3978–3982, 1975.
- [129] Guido Cossu, Massimo D’Elia, Adriano Di Giacomo, Biagio Lucini, and Claudio Pica. G2 gauge theory at finite temperature. *JHEP*, 10:100, 2007, 0709.0669.
- [130] Jens Braun, Astrid Eichhorn, Holger Gies, and Jan M. Pawłowski. On the Nature of the Phase Transition in SU(N), Sp(2) and E(7) Yang-Mills theory. *Eur.Phys.J.*, C70:689–702, 2010, 1007.2619.
- [131] Philippe de Forcrand and Oliver Jahn. Deconfinement transition in (2+1)-dimensional SU(4) lattice gauge theory. *Nucl.Phys.Proc.Suppl.*, 129:709–711, 2004, hep-lat/0309153.
- [132] Kieran Holland, Michele Pepe, and Uwe-Jens Wiese. Revisiting the deconfinement phase transition in SU(4) Yang-Mills theory in 2+1 dimensions. *JHEP*, 0802:041, 2008, 0712.1216.
- [133] A. Wipf, T. Kaestner, C. Wozar, and T. Heinzl. Generalized Potts-Models and their Relevance for Gauge Theories. *SIGMA*, 3:006, 2007, hep-lat/0610043.
- [134] Christian Wozar, Tobias Kaestner, Andreas Wipf, and Thomas Heinzl. Inverse Monte-Carlo determination of effective lattice models for SU(3) Yang-Mills theory at finite temperature. *Phys. Rev.*, D76:085004, 2007, 0704.2570.
- [135] Christian Wozar, Tobias Kastner, Björn H. Wellegehausen, Andreas Wipf, and Thomas Heinzl. Inverse Monte-Carlo and Demon Methods for Effective Polyakov Loop Models of SU(N)-YM. 2008, 0808.4046.

- [136] M. Lüscher, K. Symanzik, and P. Weisz. Anomalies of the free loop wave equation in the wkb approximation. *Nuclear Physics B*, 173(3):365–396, 1980.
- [137] M. Lüscher. Symmetry-breaking aspects of the roughening transition in gauge theories. *Nuclear Physics B*, 180(2):317–329, 1981.
- [138] F. Gliozzi, M. Pepe, and U.-J. Wiese. The width of the color flux tube at 2-loop order. *Journal of High Energy Physics*, 2010(11):1–16, 2010. 10.1007/JHEP11(2010)053.
- [139] Ofer Aharony and Eyal Karzbrun. On the effective action of confining strings. *Journal of High Energy Physics*, 2009(06):012, 2009.
- [140] Dimitra Karabali, V.P. Nair, and Alexandr Yelnikov. The Hamiltonian Approach to Yang-Mills (2+1): An Expansion Scheme and Corrections to String Tension. *Nucl.Phys.*, B824:387–414, 2010, 0906.0783.
- [141] Thomas Appelquist, Michael Dine, and I.J. Muzinich. The static potential in quantum chromodynamics. *Physics Letters B*, 69(2):231–236, 1977.
- [142] Jan Ambjorn, P. Olesen, and C. Peterson. Stochastic confinement and dimensional reduction. 2. Three-dimensional SU(2) lattice gauge theory. *Nucl.Phys.*, B240:533, 1984.
- [143] Dimitra Karabali, Chan ju Kim, and V.P. Nair. Planar Yang-Mills theory: Hamiltonian, regulators and mass gap. *Nucl.Phys.*, B524:661–694, 1998, hep-th/9705087.
- [144] Yu.A. Simonov. Gluelumps and Confinement in QCD. 2010, 1003.3608.
- [145] Grigorios I. Poulis and Howard D. Trottier. 'Gluelump' spectrum and adjoint source potential in lattice QCD in three-dimensions. *Phys.Lett.*, B400:358–363, 1997, hep-lat/9504015.
- [146] Jan Ambjorn, P. Olesen, and C. Peterson. Stochastic Confinement and Dimensional Reduction. 1. Four-Dimensional SU(2) Lattice Gauge Theory. *Nucl.Phys.*, B240:189, 1984.
- [147] Christopher Michael. Adjoint Sources in Lattice Gauge Theory. *Nucl.Phys.*, B259:58, 1985.
- [148] L.A. Griffiths, Christopher Michael, and Paul E.L. Rakow. The adjoint source potential. *Phys.Lett.*, B150:196–198, 1985.
- [149] Howard D. Trottier. Adjoint 'quark' color fields in four-dimensional lattice gauge theory: Vacuum screening and penetration. *Phys.Lett.*, B357:193–198, 1995, hep-lat/9503017.
- [150] M. Muller, W. Beirl, Manfred Faber, and H. Markum. Universality of the confinement string in multiplet potentials. *Nucl.Phys.Proc.Suppl.*, 26:423–425, 1992.
- [151] N.A. Campbell, I.H. Jorysz, and Christopher Michael. The adjoint source potential in SU(3) lattice gauge theory. *Phys.Lett.*, B167:91, 1986.

- [152] Christopher Michael. Hadronic forces from the lattice. *Nucl.Phys.Proc.Suppl.*, 26:417–419, 1992.
- [153] Gunnar Singh Bali. Casimir scaling of SU(3) static potentials. *Phys.Rev.*, D62:114503, 2000, hep-lat/0006022.
- [154] Carlo Piccioni. Casimir scaling in SU(2) lattice gauge theory. *Phys.Rev.*, D73:114509, 2006, hep-lat/0503021.
- [155] Owe Philipsen and Hartmut Wittig. String breaking in SU(2) Yang-Mills theory with adjoint sources. *Phys.Lett.*, B451:146–154, 1999, hep-lat/9902003.
- [156] P.W. Stephenson. Breaking of the adjoint string in (2+1)-dimensions. *Nucl.Phys.*, B550:427–448, 1999, hep-lat/9902002.
- [157] Philippe de Forcrand and Owe Philipsen. Adjoint string breaking in 4-D SU(2) Yang-Mills theory. *Phys.Lett.*, B475:280–288, 2000, hep-lat/9912050.
- [158] Slavo Kratochvila and Philippe de Forcrand. Observing string breaking with Wilson loops. *Nucl.Phys.*, B671:103–132, 2003, hep-lat/0306011.
- [159] Luigi Del Debbio, Haralambos Panagopoulos, Paolo Rossi, and Ettore Vicari. k string tensions in SU(N) gauge theories. *Phys.Rev.*, D65:021501, 2002, hep-th/0106185.
- [160] B. Lucini and M. Teper. Confining strings in SU(N) gauge theories. *Phys.Rev.*, D64:105019, 2001, hep-lat/0107007.
- [161] Slavo Kratochvila and Philippe de Forcrand. String breaking with Wilson loops? *Nucl.Phys.Proc.Suppl.*, 119:670–672, 2003, hep-lat/0209094.
- [162] M. Pepe and U.-J. Wiese. From Decay to Complete Breaking: Pulling the Strings in SU(2) Yang-Mills Theory. *Phys.Rev.Lett.*, 102:191601, 2009, 0901.2510.
- [163] Owe Philipsen and Hartmut Wittig. String breaking in nonAbelian gauge theories with fundamental matter fields. *Phys.Rev.Lett.*, 81:4056–4059, 1998, hep-lat/9807020.
- [164] Howard D. Trottier. String breaking by dynamical fermions in three-dimensional lattice QCD. *Phys.Rev.*, D60:034506, 1999, hep-lat/9812021.
- [165] Howard D. Trottier and Kit Yan Wong. Static potential and local color fields in unquenched lattice QCD(3). *Phys.Rev.*, D72:054505, 2005, hep-lat/0408028.
- [166] Carleton E. Detar, Olaf Kaczmarek, Frithjof Karsch, and Edwin Laermann. String breaking in lattice quantum chromodynamics. *Phys.Rev.*, D59:031501, 1999, hep-lat/9808028.
- [167] Gunnar S. Bali, Hartmut Neff, Thomas Duessel, Thomas Lippert, and Klaus Schilling. Observation of string breaking in QCD. *Phys.Rev.*, D71:114513, 2005, hep-lat/0505012.

- [168] Martin Lüscher and Peter Weisz. Locality and exponential error reduction in numerical lattice gauge theory. *JHEP*, 0109:010, 2001, hep-lat/0108014.
- [169] E. Eichten, K. Gottfried, T. Kinoshita, K.D. Lane, and Tung-Mow Yan. Charmonium: Comparison with Experiment. *Phys.Rev.*, D21:203, 1980.
- [170] P. Goddard, J. Goldstone, C. Rebbi, and Charles B. Thorn. Quantum dynamics of a massless relativistic string. *Nucl.Phys.*, B56:109–135, 1973.
- [171] Michael Creutz. Asymptotic-freedom scales. *Phys. Rev. Lett.*, 45(5):313–316, Aug 1980.
- [172] R. Sommer. A New way to set the energy scale in lattice gauge theories and its applications to the static force and alpha-s in SU(2) Yang-Mills theory. *Nucl. Phys.*, B411:839–854, 1994, hep-lat/9310022.
- [173] Michael J. Teper. SU(N) gauge theories in 2+1 dimensions. *Phys. Rev.*, D59:014512, 1999, hep-lat/9804008.
- [174] M. Lüscher. Symmetry Breaking Aspects of the Roughening Transition in Gauge Theories. *Nucl.Phys.*, B180:317, 1981.
- [175] Harvey B. Meyer. Static forces in d=2+1 SU(N) gauge theories. *Nucl.Phys.*, B758:204–226, 2006, hep-lat/0607015.
- [176] Barry Simon. Mean field upper bound on the transition temperature in multicomponent ferromagnets. *Journal of Statistical Physics*, 22(4):491–493, 1980. 10.1007/BF01012868.
- [177] K. Binder and D. P. Landau. Finite-size scaling at first-order phase transitions. *Phys. Rev. B*, 30(3):1477–1485, Aug 1984.
- [178] I.G. Halliday and A. Schwimmer. The Phase Structure of SU(N)/Z(N) Lattice Gauge Theories. *Phys.Lett.*, B101:327, 1981.
- [179] Biagio Lucini, Michael Teper, and Urs Wenger. Properties of the deconfining phase transition in SU(N) gauge theories. *JHEP*, 0502:033, 2005, hep-lat/0502003.
- [180] Richard C. Brower, David A. Kessler, and Herbert Levine. Monopole condensation and the lattice QCD crossover. *Phys.Rev.Lett.*, 47:621, 1981.
- [181] L. Caneschi, I.G. Halliday, and A. Schwimmer. The phase structure of mixed lattice gauge theories. *Nucl.Phys.*, B200:409, 1982.
- [182] T. Blum, Carleton E. DeTar, Urs M. Heller, Leo Karkkainen, K. Rummukainen, et al. Thermal phase transition in mixed action SU(3) lattice gauge theory and Wilson fermion thermodynamics. *Nucl.Phys.*, B442:301–316, 1995, hep-lat/9412038.

- [183] C. Bonati, G. Cossu, M. D’Elia, and A. Di Giacomo. Phase diagram of the lattice SU(2) Higgs model. *Nucl.Phys.*, B828:390–403, 2010, 0911.1721.
- [184] K. Osterwalder and E. Seiler. Gauge Field Theories on the Lattice. *Annals Phys.*, 110:440, 1978.
- [185] Eduardo H. Fradkin and Stephen H. Shenker. Phase Diagrams of Lattice Gauge Theories with Higgs Fields. *Phys.Rev.*, D19:3682–3697, 1979.
- [186] Christof Gattringer, Christian B. Lang, Christof Gattringer, and Christian Lang. Dynamical fermions. In *Quantum Chromodynamics on the Lattice*, volume 788 of *Lecture Notes in Physics*, pages 185–211. Springer Berlin / Heidelberg, 2010. 10.1007/978-3-642-01850-3\_8.
- [187] Philippe de Forcrand. Simulating QCD at finite density. *PoS*, LAT2009:010, 2009, 1005.0539.
- [188] S. Leupold, K. Redlich, M. Stephanov, A. Andronic, D. Blaschke, et al. Bulk properties of strongly interacting matter. *Lect.Notes Phys.*, 814:39–334, 2011.
- [189] Jan M. Pawłowski. The QCD phase diagram: Results and challenges. *AIP Conf.Proc.*, 1343:75–80, 2011, 1012.5075.
- [190] Michael Buballa. NJL model analysis of quark matter at large density. *Phys.Rept.*, 407:205–376, 2005, hep-ph/0402234. Habilitation Thesis.
- [191] Owe Philipsen. The QCD phase diagram at zero and small baryon density. *PoS*, LAT2005:016, 2006, hep-lat/0510077.
- [192] Z. Fodor and S.D. Katz. A New method to study lattice QCD at finite temperature and chemical potential. *Phys.Lett.*, B534:87–92, 2002, hep-lat/0104001.
- [193] Z. Fodor and S.D. Katz. Lattice determination of the critical point of QCD at finite T and  $\mu$ . *JHEP*, 0203:014, 2002, hep-lat/0106002.
- [194] Z. Fodor, S.D. Katz, and K.K. Szabo. The QCD equation of state at nonzero densities: Lattice result. *Phys.Lett.*, B568:73–77, 2003, hep-lat/0208078.
- [195] C.R. Allton, S. Ejiri, S.J. Hands, O. Kaczmarek, F. Karsch, et al. The QCD thermal phase transition in the presence of a small chemical potential. *Phys.Rev.*, D66:074507, 2002, hep-lat/0204010.
- [196] C.R. Allton, S. Ejiri, S.J. Hands, O. Kaczmarek, F. Karsch, et al. The Equation of state for two flavor QCD at nonzero chemical potential. *Phys.Rev.*, D68:014507, 2003, hep-lat/0305007.
- [197] C.R. Allton, M. Doring, S. Ejiri, S.J. Hands, O. Kaczmarek, et al. Thermodynamics of two flavor QCD to sixth order in quark chemical potential. *Phys.Rev.*, D71:054508, 2005, hep-lat/0501030.
- [198] Rajiv V. Gavai and Sourendu Gupta. Pressure and nonlinear susceptibilities in QCD at finite chemical potentials. *Phys.Rev.*, D68:034506, 2003, hep-lat/0303013.

- [199] R.V. Gvai and Sourendu Gupta. The Critical end point of QCD. *Phys.Rev.*, D71:114014, 2005, hep-lat/0412035.
- [200] R.V. Gvai and Sourendu Gupta. QCD at finite chemical potential with six time slices. *Phys.Rev.*, D78:114503, 2008, 0806.2233.
- [201] Owe Philipsen. Status of the QCD phase diagram from lattice calculations. 2011, 1111.5370.
- [202] Philippe de Forcrand and Owe Philipsen. The QCD phase diagram for small densities from imaginary chemical potential. *Nucl.Phys.*, B642:290–306, 2002, hep-lat/0205016.
- [203] P. de Forcrand and O. Philipsen. QCD phase diagram for small densities from simulations at imaginary  $\mu$ . *Nucl.Phys.Proc.Suppl.*, 119:535–537, 2003, hep-lat/0209084.
- [204] P. de Forcrand and O. Philipsen. QCD phase diagram at small densities from simulations with imaginary  $\mu$ . 2003, hep-ph/0301209.
- [205] Philippe de Forcrand and Owe Philipsen. Constraining the QCD phase diagram by tricritical lines at imaginary chemical potential. *Phys.Rev.Lett.*, 105:152001, 2010, 1004.3144.
- [206] Claudio Bonati, Philippe de Forcrand, Massimo D’Elia, Owe Philipsen, and Francesco Sanfilippo. Constraints on the two-flavor QCD phase diagram from imaginary chemical potential. 2012, 1201.2769.
- [207] D.T. Son and Misha A. Stephanov. QCD at finite isospin density. *Phys.Rev.Lett.*, 86:592–595, 2001, hep-ph/0005225.
- [208] Thomas D .Cohen. Functional integrals for QCD at nonzero chemical potential and zero density. *Phys.Rev.Lett.*, 91:222001, 2003, hep-ph/0307089.
- [209] Thomas D. Cohen. QCD functional integrals for systems with nonzero chemical potential. 2004, hep-ph/0405043. In memory of Ian Kogan, to appear in the memorial volume.
- [210] Thomas D. Cohen. Large  $N_c$  qcd at nonzero chemical potential. *Phys. Rev. D*, 70:116009, Dec 2004.
- [211] Simon Hands. Simulating dense matter. *Prog.Theor.Phys.Suppl.*, 168:253–260, 2007, hep-lat/0703017.
- [212] Simon Hands, Timothy J. Hollowood, and Joyce C. Myers. Numerical Study of the Two Color Attoworld. *JHEP*, 1012:057, 2010, 1010.0790.
- [213] Simon Hands, Philip Kenny, Seyong Kim, and Jon-Ivar Skullerud. Lattice Study of Dense Matter with Two Colors and Four Flavors. *Eur.Phys.J.*, A47:60, 2011, 1101.4961.
- [214] Luigi Del Debbio, Agostino Patella, and Claudio Pica. Higher representations on the lattice: Numerical simulations. SU(2) with adjoint fermions. *Phys.Rev.*, D81:094503, 2010, 0805.2058.

- [215] Julia Danzer, Christof Gattringer, and Axel Maas. Chiral symmetry and spectral properties of the Dirac operator in G2 Yang-Mills Theory. *JHEP*, 0901:024, 2009, 0810.3973.
- [216] Axel Maas, Lorenz von Smekal, Björn Wellegehausen, and Andreas Wipf. The phase diagram of a gauge theory with fermionic baryons. 2012, 1203.5653.
- [217] Axel Maas, Lorenz von Smekal, Björn Wellegehausen, and Andreas Wipf. to be published.
- [218] Kazuo Fujikawa. Path-integral measure for gauge-invariant fermion theories. *Phys. Rev. Lett.*, 42(18):1195–1198, Apr 1979.
- [219] Kenji Fukushima and Tetsuo Hatsuda. The phase diagram of dense QCD. *Rept.Prog.Phys.*, 74:014001, 2011, 1005.4814.
- [220] Simon Hands, Seyong Kim, and Jon-Ivar Skullerud. Quark Matter in QC(2)D. *Eur. Phys. J.*, A31:787–789, 2007, nucl-th/0609012.
- [221] R. Kirchner, I. Montvay, J. Westphalen, S. Luckmann, and K. Spanderen. Evidence for discrete chiral symmetry breaking in  $N = 1$  supersymmetric Yang-Mills theory. *Phys. Lett.*, B446:209–215, 1999, hep-lat/9810062.
- [222] I. Montvay. An Algorithm for Gluinos on the Lattice. *Nucl. Phys.*, B466:259–284, 1996, hep-lat/9510042.
- [223] I. Campos et al. Monte Carlo simulation of SU(2) Yang-Mills theory with light gluinos. *Eur.Phys.J.*, C11:507–527, 1999, hep-lat/9903014.
- [224] F. Farchioni et al. The Supersymmetric Ward identities on the lattice. *Eur.Phys.J.*, C23:719–734, 2002, hep-lat/0111008. 34 pages, 7 figures. Typo corrected, last sentence reformulated, reference added. To appear in Eur. Phys. J. C.
- [225] Roland Peetz. Spectrum of  $N=1$  Super Yang Mills Theory on the Lattice with a Light Gluino. Dissertation, Münster, 2003.
- [226] Federico Farchioni and Roland Peetz. The Low-lying mass spectrum of the  $N=1$  SU(2) SUSY Yang-Mills theory with Wilson fermions. *Eur.Phys.J.*, C39:87–94, 2005, hep-lat/0407036. 17 pages, 9 figures: improved analysis of the pseudoscalar meson mass, final published version DOI: 10.1140/epjc/s2004-02081-2.
- [227] Alexander Ferling. Numerische Methoden zur Erforschung einer  $N = 1$  Super Yang-Mills-Theorie mit SU (2)c und SU (3)c Wilson Fermionen. Dissertation, Münster, 2009.
- [228] Georg Bergner, Istvan Montvay, Gernot Munster, Dirk Sandbrink, and Umut D. Ozugurel. Supersymmetric Yang-Mills theory: a step towards the continuum. 2011, 1111.3012.

- [229] Joel Giedt, Richard Brower, Simon Catterall, George T. Fleming, and Pavlos Vranas. Lattice super-Yang-Mills using domain wall fermions in the chiral limit. *Phys.Rev.*, D79:025015, 2009, 0810.5746. 25 pages.
- [230] Michael G. Endres. Dynamical simulation of N=1 supersymmetric Yang-Mills theory with domain wall fermions. *Phys.Rev.*, D79:094503, 2009, 0902.4267.
- [231] G.R. Farrar, G. Gabadadze, and M. Schwetz. On the effective action of N=1 supersymmetric Yang-Mills theory. *Phys.Rev.*, D58:015009, 1998, hep-th/9711166.
- [232] Simon Catterall and Toby Wiseman. Towards lattice simulation of the gauge theory duals to black holes and hot strings. *JHEP*, 0712:104, 2007, 0706.3518.
- [233] Johannes Hartung. Untersuchungen zu dimensional kompaktisierten Super-Yang-Mills-Theorien. Diplomarbeit, FSU Jena, 2008.
- [234] F. Bernardoni, S. L. Cacciatori, B. L. Cerchiai, and A. Scotti. Mapping the geometry of the F4 group. *ArXiv e-prints*, May 2007, 0705.3978.
- [235] F. Bernardoni, S. L. Cacciatori, B. L. Cerchiai, and A. Scotti. Mapping the geometry of the E<sub>6</sub> group. *Journal of Mathematical Physics*, 49(1):012107, January 2008, 0710.0356.



# Zusammenfassung

Das Standardmodell der Elementarteilchen ist bis heute die erfolgreichste Theorie zur vereinheitlichten Beschreibung der elektromagnetischen, der schwachen und der starken Wechselwirkung unterhalb einer Energieskala von 1 TeV. Trotz seines großen Erfolgs in der Beschreibung der Natur der Elementarteilchen, in exzellenter Übereinstimmung mit Experimenten, beinhaltet es sowohl ungelöste Probleme in seiner Anwendung, wie z.B. das Confinement-Problem oder die Erzeugung der Massen der Elementarteilchen, als auch fundamentalere Probleme wie die Vereinheitlichung mit der Gravitation oder die Existenz von dunkler Materie. Die Theorie der starken Wechselwirkung ist die Quantenchromodynamik (QCD), die für eine Untersuchung auch nicht-störungstheoretische Methoden, wie z.B. Monte-Carlo Simulationen auf diskreten Raumzeitgittern, unbedingt erfordert. Aufgrund des Vorzeichenproblems ist diese Methode jedoch nicht bei großen Dichten und tiefen Temperaturen anwendbar. Aber gerade dieser auch experimentell schwer zugängliche Bereich des QCD-Phasendiagramms hat interessante Auswirkungen in vielen Bereichen der Physik, wie z.B. in den Eigenschaften nuklearer Materie in der Kernphysik oder der Entstehung von Neutronensternen in der Astrophysik.

In der vorliegenden Arbeit wurde die Eichgruppe  $SU(3)$  der QCD durch die exzeptionelle Lie-Gruppe  $G_2$  ersetzt. Es zeigt sich, dass  $SU(3)$  und  $G_2$  Yang-Mills Theorien viele Gemeinsamkeiten besitzen. Unter anderem konnten in dieser Arbeit *Casimir scaling* und *string breaking*, wichtige Eigenschaften der QCD in Bezug auf das Confinement-Problem, in verschiedenen Darstellungen der Eichgruppe mit hoher Präzision nachgewiesen werden. Des Weiteren konnte gezeigt werden, dass  $G_2$ -QCD kein Vorzeichenproblem besitzt, und somit war es möglich, zum ersten Mal für eine Theorie mit fermionischen Baryonen und fundamentalen Quarks das Phasendiagramm auch für niedrige Temperaturen und hohe Dichten nicht-störungstheoretisch zu untersuchen. Hierbei wurde auch die *silver-blaze* Eigenschaft, bekannt aus der QCD, nachgewiesen. Die hier durchgeführten Simulationen eröffnen viele interessante Fragestellungen in Hinblick auf die Zustandsgleichungen von kalter dichter fermionischer Materie und bilden die Grundlage für weitere Untersuchungen des  $G_2$ -QCD Phasendiagramms.

Es wird erwartet, dass das Standardmodell nur eine effektive Theorie ist, die auf höheren Energieskalen durch eine fundamentalere Theorie abgelöst wird. Ansätze für solche fundamentaleren Theorien, wie z.B. die Stringtheorie oder das minimal supersymmetrische Standardmodell (MSSM), beinhalten oft eine Verdopplung der Freiheitsgrade durch eine Erweiterung der Raumzeitsymmetrien um sogenannte Supersymmetrien. In dieser Arbeit wurde die einfachste Erweiterung, die  $\mathcal{N} = 1$  Super-Yang-Mills Theorie, dimensional reduziert in einer und drei Raumzeitdimensionen, mit Hilfe von Gitter-Monte-Carlo Simulationen untersucht. Insbesondere konnte hier gezeigt werden, dass eine Wiederherstellung der Supersymmetrie, die durch das diskrete Raumzeitgitter gebrochen wird, im Kontinuumslimites mit der gewählten Gitterformulierung möglich ist. Dieses Ergebnis erlaubt weitere Untersuchungen bezüglich des Teilchen- und Massenspektrums dieser Theorie.

Technische Aspekte dieser Arbeit beinhalteten eine Entwicklung von hocheffizienten und parallelisierten Algorithmen zur Ausführung der beschriebenen Simulationen auf Supercomputern.



# Danksagung

Ich danke allen, die zum Gelingen dieser Doktorarbeit beigetragen haben. . .

- . . . Prof. Dr. Andreas Wipf für die Themenstellung und Zusammenarbeit, für viele anregende Impulse und die Möglichkeit eines unabhängigen und freien Forschens,
- . . . den Mitgliedern der Arbeitsgruppe für die gute Zusammenarbeit und Unterstützung,
- . . . Dr. Christian Wozar für die gemeinsamen Arbeiten an  $G_2$ -Eichtheorien und für viele Diskussionen zu Algorithmen,
- . . . Dr. Georg Bergner für seine Ratschläge auf dem Gebiet der Supersymmetrie und anregenden Diskussionen auf den Lattice-Konferenzen,
- . . . Daniel Körner und Raphael Flore für die Zusammenarbeit an  $O(N)$ -Sigma-Modellen und Methoden der Monte-Carlo-Renormierungsgruppe,
- . . . Lukas Janssen für viele Anregungen und Gespräche über die Physik der funktionalen Renormierungsgruppe und dem Thirring-Modell,
- . . . Priv.Doz. Dr. Lorentz von Smekal und Dr. Axel Maas für unsere gemeinsame Arbeit an der  $G_2$ -QCD sowie der Bereitstellung von Computer-Ressourcen,
- . . . meinen Eltern für die stete Unterstützung,
- . . . ganz herzlich.



# Ehrenwörtliche Erklärung

Ich erkläre hiermit ehrenwörtlich, dass ich die vorliegende Arbeit selbstständig, ohne unzulässige Hilfe Dritter und ohne Benutzung anderer als der angegebenen Hilfsmittel und Literatur angefertigt habe. Die aus anderen Quellen direkt oder indirekt übernommenen Daten und Konzepte sind unter Angabe der Quelle gekennzeichnet. Ergebnisse, die in Zusammenarbeit mit den Mitgliedern des Lehrstuhles für Quantenfeldtheorie in Jena und anderen Kooperationen entstanden sind, sind in der Arbeit entsprechend benannt.

Weitere Personen waren an der inhaltlich-materiellen Erstellung der vorliegenden Arbeit nicht beteiligt. Insbesondere habe ich hierfür nicht die entgeltliche Hilfe von Vermittlungs- bzw. Beratungsdiensten (Promotionsberater und andere Personen) in Anspruch genommen. Niemand hat von mir unmittelbar oder mittelbar geldwerte Leistungen für Arbeiten erhalten, die im Zusammenhang mit dem Inhalt der vorgelegten Dissertation stehen.

Die Arbeit wurde bisher weder im In- noch im Ausland in gleicher oder ähnlicher Form einer anderen Prüfungsbehörde vorgelegt.

Die geltende Promotionsordnung der Physikalisch-Astronomischen Fakultät ist mir bekannt.

Ich versichere ehrenwörtlich, dass ich nach bestem Wissen die reine Wahrheit gesagt und nichts verschwiegen habe.

Jena, 16.04.2012

Björn-Hendrik Wellegehausen



# Lebenslauf

Name: Björn-Hendrik Wellegehausen  
Geburtstag: 03. Juli 1983  
Geburtsort: Großburgwedel, Deutschland  
Nationalität: deutsch

## Schule

1990-1994                    Grundschule Großburgwedel  
1994-1996                    Orientierungsstufe Großburgwedel  
1996-2003                    Gymnasium Großburgwedel  
Juni 2003                    Abitur  
Juli 2003-März 2004      Wehrdienst

## Studium

SS 2004- WS 2009      Diplomstudium (Physik), FSU Jena  
Februar 2009              Diplom (Physik), FSU Jena  
seit Februar 2009      Doktorand am Theoretisch-Physikalischen Institut, FSU Jena

Jena, 16.04.2012

Björn-Hendrik Wellegehausen